INVESTIGATION OF THE STRUCTURAL AND FUNCTIONAL PROPERTIES OF LEAD-FREE BARIUM CALCIUM ZIRCONATE TITANATE PIEZOCERAMICS

By

CHANG SHU

A thesis submitted to the University of Birmingham

for the degree of

DOCTOR OF PHILOSOPHY

School of Metallurgy and Materials

College of Engineering and Physical Sciences

The University of Birmingham

December 2017

Abstract

Piezoelectric ceramics have been widely used in sensors, actuators and ultrasonic transducers due to their ability to achieve efficient conversion between electrical and mechanical vibrations. There is an urgent desire to move to lead-free materials achieving comparable piezoelectric performance to lead-based materials. One of the most promising alternatives has been reported to be a pseudo-binary system $zBa_{0.70}Ca_{0.30}TiO_3$-(1-z) $BaZr_{0.20}Ti_{0.80}O_3$ (abbreviated as zBCT-(1-z)BZT) which, at the z=0.5 composition, has comparable piezoelectric performance to lead-based materials. However, there is a lack of systematic research to investigate the effects of fabrication on the structural and functional properties of this zBCT-(1-z)BZT system.

In this work, the end member $Ba_{1-x}Ca_xTiO_3$ (x=0-0.30) and $BaZr_yTi_{1-y}O_3$ (y=0-0.30) systems have been firstly investigated as single dopants into the parent $BaTiO_3$ phase. The phase transition diagrams of the two systems have been successfully established by measuring temperature dependent Raman spectroscopy and functional properties combined with characterisation by physical, microstructural and X-ray diffraction techniques. The fabrication of $Ba_{0.70}Ca_{0.30}TiO_3$ and $BaZr_{0.20}Ti_{0.80}O_3$ ceramics by solid-state methods has been optimised to form single phase materials, and this fabrication procedure has been applied as a novel way to form zBCT-(1-z)BZT ($0 \leq z \leq 1$ with 0.1 step) ceramics by stoichiometrically mixing and sintering the pre-calcined $Ba_{0.70}Ca_{0.30}TiO_3$ and $BaZr_{0.20}Ti_{0.80}O_3$ powders.

A new phase diagram of the zBCT-(1-z)BZT ($0 \leq z \leq 1$) has been constructed by combining structural and functional property measurements. It indicates a vertical orthorhombic phase region separating rhombohedral and tetragonal phases below the Curie temperature. The highest piezoelectric properties have been observed for z=0.5 ceramics at room temperature, with piezoelectric charge constant, d_{33}=281 pC/N and planar coupling factor, k_p=0.43 for ceramics with an average grain size of ~15 μm sintered at 1400 °C, due to the increased potential polarization directions in the vicinity of the orthorhombic to tetragonal phase boundary.

Acknowledgements

For the complement of my PhD studies, I am supported by a large group of people. First and foremost, I would like to thanks to my supervisor, Professor Tim Button, for all his support through my study. His invaluable guidance on my lab work, suggestions on personal development, offers for exchange study in Brno University of Technology and help on my thesis. His guidance has always inspired, motivated and supported me through my study. He is a very generous and patient supervisor, and my mentor.

I should thank to my parents, Mr Weiping Shu and Mrs Huiqin Liu. Their love encourages me to grow up and study abroad in UK, and their financial support helps me to complete my PhD study. I also sincerely appreciate the invaluable love and support from my husband, Mr Xi Lu.

I should also thank my co-supervisor, Dr Daniel Reed, for his support and supervision in my PhD study. I would also thank the Functional Materials Group at the University of Birmingham: thanks to Mr Carl Meggs for technical assistance and his support for my study; thanks to Dr Yun Jiang, Dr Shaun Dorey, Dr Tanikan Thongchai, Dr Hojat Pooladvand, Dr Pavel Tofel, Dr Yang Bai, Ing Martin Safar, Miss Yanlei Chen and Mr Bo Nan for their kind friendship and support; thanks to Dr Hana Hughes for her help on my exchange study in Brno University of Technology. And I would thank to the University of Birmingham, Brno University of Technology and Erasmus Traineeship Program to offering the chance, providing the funding and equipment for my PhD study.

Finally, I would like to express my sincere thanks to all the friends and family in my life, this thesis would not have been possible without their help, support and encouragement.

Table of Contents

List of Figures

List of Tables

Nomenclature and Acronyms

a	Lattice constant length (Å)
A	Area (m^2)
A'	Pre-exponential factor
b	Lattice constant length (Å)
c	Lattice constant length (Å)
C	Capacitance of ceramics (F)
C_0	Capacitance of referenced capacitor (F)
C_{0+}	Capacitance at 0 V in Capacitance-Voltage Measurement
$\boldsymbol{D}$	Dielectric displacement vector
d	Distance (m)
d_{33}	Piezoelectric charge coefficient
d_{hkl}	Interplanar spacing (Å)
D_0	Diameter of pressing die (m)
D_s	Diameter of ceramics after sintering (m)
E	Electric field (V/m)
$\boldsymbol{E}$	Electric field vector
E_C	Coercive field (V/m)
E_R	Reorientation energy
f_a	Anti-resonant frequency (Hz)
f_r	Resonant frequency (Hz)
I	Intensity of Raman mode
k	Electromechanical coupling coefficient
k_p	Electromechanical planar coupling coefficient

k_t	Electromechanical thickness coupling coefficient
k_{15}	Electromechanical shear coupling coefficient
k_{31}	Electromechanical transverse coupling coefficient
k_{33}	Electromechanical longitudinal coupling coefficient
M	Mass (g)
$n\lambda$	Multiple of incident wavelength (Å)
$\boldsymbol{P}$	Polarization vector
P_r	Remanent polarization (C/m^2)
P_{rmin}	Minimum value of remanent polarization (C/m^2)
P_s	Spontaneous polarization (C/m^2)
P_{sat}	Saturation polarization (C/m^2)
Q_0	Charge (C)
r	Radius of ceramic disc (m)
R	Universal gas constant (J/(Kmol))
R_{wp}	Weighted profile R-factor
t	Thickness of ceramic disc (m)
$tan\delta$	Dielectric loss
T	Temperature (°C or K)
T_{cal}	Calcination temperature (°C or K)
T_C	Curie temperature (°C or K)
T_m	Temperature for maximum relative permittivity (°C or K)
T_{O-T}/T_{T-O}	Phase transition temperature between tetragonal and orthorhombic phases (°C or K)
T_{R-C}/T_{C-R}	Phase transition temperature between rhombohedral and cubic phases (°C or K)

$T_{R\text{-}O}/T_{O\text{-}R}$	Phase transition temperature between rhombohedral and orthorhombic phases (°C or K)
$T_{R\text{-}T}/T_{T\text{-}R}$	Phase transition temperature between rhombohedral and tetragonal phase (°C or K)
T_s	Sintering temperature (°C or K)
$T_{T\text{-}C}/T_{C\text{-}T}$	Phase transition temperature between tetragonal and cubic phases (°C or K)
V	Unit cell volume ($Å^3$)
V_0	Voltage (V)
x	Calcium content
x^*	Calcium content in tetragonal barium calcium titanate
x^*_c	Solubility of calcium content in tetragonal barium calcium titanate at 0 K
X	Particle size value of percent particles on a cumulative distribution
y	Zirconium content
z	Barium calcium titanate content
α	Lattice constant angle (°)
β	Lattice constant angle (°)
γ	Lattice constant angle (°)
δ	Phase difference
ε_0	Vacuum permittivity (F/m)
ε_r	Relative permittivity
ε_{rmax}	Maximum relative permittivity at variable temperature
θ	Incident angle of X-ray beam (°)
σ	Total surface charge density (C/m^2)
σ_0	Surface charge density in vacuum (C/m^2)

σ_{pol}	Increased surface charge density form inserted dielectric materials (C/m^2)
χ	Electric susceptibility
ω	Peak position of Raman mode (cm^{-1})
Γ	Peak width of Raman mode (cm^{-1})
Γ_0	Peak width of Raman mode at 0 K
BCT	Barium calcium titanate with 30 at. % calcium
BTO	Barium titanate
BZT	Barium zirconate titanate with 20 at. % zirconium
CCD	Charge coupled device
CVM	Capacitance-voltage measurement
dw	Domain width
DPT	Diffuse phase transition
DSC	Differential scanning calorimetry
FWHM	Full width at half maximum
GS	Grain size
HWHM	Half width at half maximum
IFM	Impedance measurement
LO	Longitudinal optical mode
MPB	Morphotropic phase boundary
O-T/T-O	Phase transition between orthorhombic and tetragonal phases
PVA	Polyvinyl alcohol
PZM	Piezo measurement
PZT	Lead zirconate titanate

QPA	Quantitative phase analysis
R-C/C-R	Phase transition between rhombohedral and cubic phases
R-O/O-R	Phase transition between rhombohedral and orthorhombic phases
R-T/T-R	Phase transition between rhombohedral and tetragonal phases
Ref.	Reference
SEM	Scanning electron microscopy
T-C/C-T	Phase transition between tetragonal and cubic phases
TCP	Tricritical point
TGA	Thermogravimetric analysis
THM	Thermo measurement
TO	Transverse optical mode
XRD	X-ray diffraction
zBCT-(1-z)BZT	Barium calcium titanate and barium zirconate titanate pseudo-binary system

Chapter 1 Introduction

Piezoelectric ceramics have been widely used in sensors, actuators and ultrasonic transducers due to their ability to achieve efficient conversion between electric and mechanical vibrations. Among those materials, lead zirconate titanate (PZT) is most commercially popular due to its high piezoelectric properties. However, the contained lead causes concern as a potential environmental hazard. Legislation is therefore in place to ban its use, once an alternative material is found [1, 2], which inspired the drive towards lead-free alternatives. Lead-free $z(Ba_{0.70}Ca_{0.30}TiO_3)$-$(1-z)(BaZr_{0.20}Ti_{0.80}O_3)$ ceramics, abbreviated as zBCT-(1-z)BZT, have therefore been exploited in research due to their comparable piezoelectric properties to lead-based materials and similar phase diagram to the PZT system. Previous research has revealed that the functional properties of zBCT-(1-z)BZT ceramics are sensitive to processing procedures and compositions (*z* values) [3]. However, there is a lack of understanding of the resultant variations in crystal structures and the corresponding contributions to functional properties.

This project, as pioneering work in the Functional Materials Group of the University of Birmingham, was inspired by the described paucity of understanding to investigate the relationship between structural and functional properties of zBCT-(1-z)BZT ceramics. It covers systematic and consecutive studies in both end member systems (*i.e.* $Ba_{1-x}Ca_xTiO_3$ and $BaZr_yTi_{1-y}O_3$) and the desired zBCT-(1-z)BZT system. The study has encompassed the fabrication of different stoichiometric ceramics, the characterisation of structural

properties and measurement of functional properties. It provides a different approach to investigate the zBCT-(1-z)BZT system based on the systematic studies of the end member systems and finally reveals the linkage between structural and functional properties in the zBCT-(1-z)BZT system.

This thesis is presented in a logical structure: Chapter 2 covers a comprehensive literature survey for this project, consisting of the fundamental theories of piezoelectric materials (section 2.1), previous research on $BaTiO_3$ ceramics as the parent phase of the zBCT-(1-z)BZT system (section 2.2), the development in $Ba_{1-x}Ca_xTiO_3$ and $BaZr_yTi_{1-y}O_3$ materials as end member systems as well as the zBCT-(1-z)BZT system (sections 2.3-2.5), and the aims of this project (section 2.6). Chapter 3 indicates the details of experimental methodology to fabricate and characterise the materials. Chapter 4 to Chapter 7 report the main results and discussions. Where Chapter 4 illustrates the optimization of fabrication procedure for this project based on the characterisation of $Ba_{0.70}Ca_{0.30}TiO_3$ and $BaZr_{0.20}Ti_{0.80}O_3$ ceramics. Chapter 5 applies Raman spectroscopy to identify phase transitions in $Ba_{1-x}Ca_xTiO_3$ based on direct structural measurement and reveals the diffusion mechanism of Ca^{2+} into $BaTiO_3$ by creating a $BaTiO_3$-$CaTiO_3$ diffusion couple and bridges the relationship between structural and functional properties in the $Ba_{1-x}Ca_xTiO_3$ system. The functional property measurements, along with Raman spectroscopy, are applied to relate the functional performance to the corresponding crystal structure and determine phase diagrams in the $BaZr_yTi_{1-y}O_3$ (Chapter 6) and zBCT-(1-z)BZT (Chapter 7) systems. Chapter 8 concludes the entire project and proposes

potential future work.

Chapter 2 Literature Review

In this chapter, the up-to-date literature on lead-free (Ba,Ca)(Zr,Ti)O_3 piezoelectric compositions are reviewed. This review includes a brief introduction to piezoelectricity and piezoelectric material systems, followed by reviews of $BaTiO_3$ ceramics, Ca^{2+}-doped $BaTiO_3$ ceramics, Zr^{4+}-doped $BaTiO_3$ ceramics and Ca^{2+}, Zr^{4+} co-doped $BaTiO_3$ ceramics. The chapter concludes with outlining the aims and objectives of this project.

2.1 Introduction to piezoelectric materials

2.1.1 Dielectrics, piezoelectricity and ferroelectricity

Dielectric materials are able to support electric charges and the resultant electric dipole structures do not have any electric conduction. The dipole moment originates from the distant positive and negative electrically charged entities on an atomic or molecular level. As a vector, dipole moment could cancel out with each other in a unit cell, therefore a dielectric material has no net polarization.

Dielectric materials are utilized in capacitor applications due to their insulating properties and rearrangement of electric charges under the application of an electric field [4]. As shown in Figure 2.1 (A), a parallel-plate capacitor is filled in vacuum and loaded in an electric field, where the capacitance C_0 is related to the quantity of charge stored on either plate (Q_0) by Equation 2.1, where V_0 refers to the voltage applied across the capacitor [5]. If the circuit is closed, a transient surge of current will flow through the circuit, shown in

Figure 2.1 (B), and the area under the curve will be equal to the charge stored on the capacitor. If a dielectric material is inserted into the parallel capacitor (shown in Figure 2.1 (C)), it means that the dielectric material is in an electric field, and therefore the random oriented dipole moment in the dielectric material will be aligned: this process is called 'polarization'. The inserted dielectric material contributes to a greater capacitance, with a corresponding increase in stored charge (shown in Figure 2.1 (D)) [5].

$$C_0 = \frac{Q_0}{V_0} \tag{2.1}$$

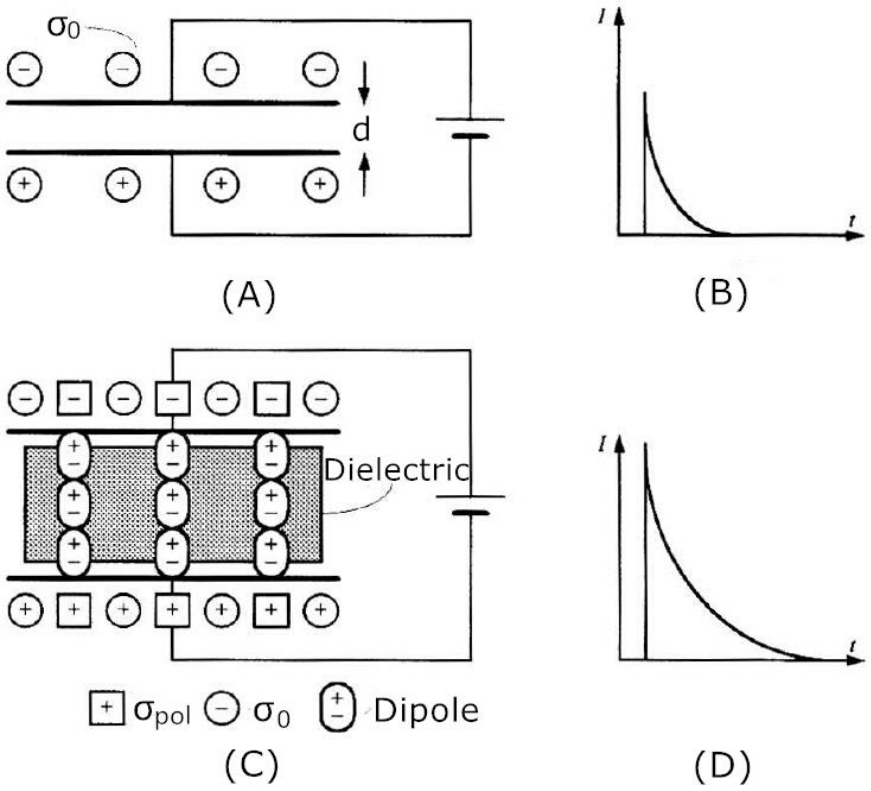

Figure 2.1. Demonstration of (A) parallel-plate capacitor filled in vacuum; (B) resultant transient current in closing circuit of (A); (C) parallel-plate capacitor with inserted dielectric material; (D) transient current in closing circuit of (C) [5].

In Figure 2.1 (A), the capacitance C_0 could also be given by Equation 2.2, where A is the

area of the plate, d is the distance between plates and ε_0 is the permittivity of free space with the value of $8.85*10^{-12}$ F/m [5]. Combining Equations 2.1 and 2.2, the surface charge density on the capacitor plate in vacuum (σ_0) is expressed by Equation 2.3, where E is the applied electric field. In Figure 2.1 (C), the capacitance C could then be expressed by Equation 2.4, where ε is the permittivity of the inserted dielectric medium. Therefore, the relative permittivity (ε_r, or dielectric constant) of the dielectric material is given by Equation 2.5, indicating the charge-storing capacity of a material compared to that of vacuum [5]. The total surface charge density (σ) in this case is given by Equation 2.7, where σ_{pol} is the increased charge density as a result of the dielectric material compared to that of vacuum. As the total surface charge density σ is equivalent to the magnitude of the dielectric displacement vector $\boldsymbol{D}$ and σ_{pol} is equivalent to the magnitude of the polarization in dielectric materials $\boldsymbol{P}$, therefore Equation 2.6 can be rewritten as Equation 2.7 [4-6].

$$C_0 = \frac{\varepsilon_0 A}{d} \tag{2.2}$$

$$\sigma_0 = \frac{Q_0}{A} = \frac{\varepsilon_0 V}{d} = \varepsilon_0 E \tag{2.3}$$

$$C = \frac{\varepsilon A}{d} \tag{2.4}$$

$$\varepsilon_r = {}^{\varepsilon}/_{\varepsilon_0} \tag{2.5}$$

$$\sigma = \sigma_0 + \sigma_{pol} \tag{2.6}$$

$$\boldsymbol{D} = \varepsilon_0 \boldsymbol{E} + \boldsymbol{P} \tag{2.7}$$

In the case of a linear dielectric, where the polarization is proportional to the electric field in the material (as shown in Figure 2.2 (A)), the relative permittivity is directly related to a dimensionless constant (electric susceptibility, χ) with the relationship as shown in Equation 2.8. The electric susceptibility defines how easily the dielectric materials are polarized in an electric field [6].

$$\varepsilon_r = \varepsilon/\varepsilon_0 = 1 + \chi \tag{2.8}$$

The dielectric loss is another characterization parameter for dielectric properties, which indicates the dissipated energy as heat when an alternating electric field is applied. This dissipation is caused by the phase difference (δ) between the applied electric field and induced polarization. The phase difference (δ) is also called the loss tangent, in the case of low loss dielectrics, δ is very small, therefore, the dissipation factor ($tan\delta$) is generally used to describe the dielectric loss [7].

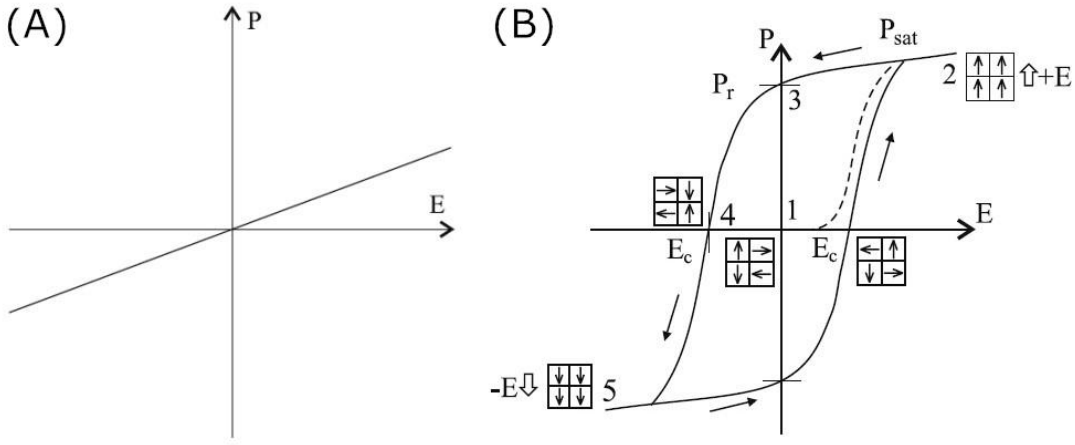

Figure 2.2. The polarization VS electric field curve of (A) linear dielectric materials; (B) ferroelectric materials [8].

Dielectric materials can be divided into subgroups of piezoelectric, pyroelectric and ferroelectric materials, as shown in Figure 2.3. When stress is applied to a piezoelectric material, polarisation is developed in the materials, the so called 'direct piezoelectric effect', where the 'converse piezoelectric effect' describes the deformation of materials under the application of an electric field [6]. There are 21 out of 32 classes of single-crystal structure that are non-centrosymmetric, and 20 of them have the potential to exhibit the piezoelectric effect [6], where the only exception is from a cubic class 432 as the piezoelectric charges along the <111> polar axes cancel each other out [9]. The piezoelectric charge coefficient (d_{33}) is used to describe the ratio of short circuit charge developed in materials' polarization direction per electrode area in response to the applied stress in the same direction (or ratio of the strain developed in polarization direction with the applied electric field). The electromechanical coupling coefficient (k) indicates the ability of piezoelectric material to achieve transformation between electrical and mechanical energy [6]. In terms of the effect of directions, the coupling coefficients as k_p (planar), k_t (thickness), k_{31} (transverse), k_{33} (longitudinal) and k_{15} (shear), are in common usage [10].

As shown in Figure 2.3, ferroelectric materials are a subgroup of piezoelectric materials, in which the direction of spontaneous polarization can be reversed by the application of an external electric field. Therefore, the relationship between the polarization and electric field of the ferroelectric materials is a hysteresis loop (*P*-*E* loop), shown in Figure 2.2 (B). When a positive electric field is applied (as the dashed line), the polarization starts to

align along the same direction as the electric field. The polarization increases with increasing electric field until reaching its maximum value (saturation or spontaneous polarization, P_{sat}), then gradually decreases with the decrease in electric field, reaching a remanent polarization value (P_r) when the electric field is totally removed. If a negative electric field is then applied, the polarization is reduced until it reaches zero at the coercive field (E_c). Further increasing the magnitude of the negative electric field changes the polarization direction to be same as the negative electric field and then finally attains the negative saturation polarization. The hysteresis loop could then be completed with the decrease of the negative electric field and application of a positive electric field. The ferroelectric behaviour will disappear above a critical temperature, the Curie temperature (T_C), where the material transforms to a centrosymmetric crystal structure [6] and becomes paraelectric.

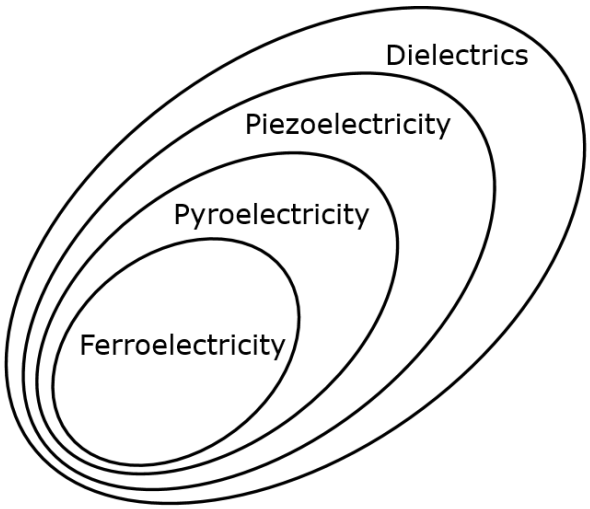

Figure 2.3. Schematics of dielectrics, piezoelectric and ferroelectrics.

2.1.2 Move from lead-based to lead-free piezoelectric systems

For many decades, lead zirconate titanate, $Pb(Zr_{1-y}Ti_y)O_3$ (PZT) has been the most frequently used commercial piezoelectric material [6]. As shown in Figure 2.4, it has a typical perovskite structure, with the general chemical composition ABO_3. The 8 A-site cations (Pb^{2+}) occupy the corners of the unit cell, 1 B-site cation (Zr^{4+}/Ti^{4+}) sits in the body centre and 6 oxygen anions (O^{2-}) are in the centres of faces, forming an octahedron around the B-site cation. PZT is a solid solution system of two materials: a ferroelectric lead titanate ($PbTiO_3$) and an anti-ferroelectric lead zirconate ($PbZrO_3$), with a phase diagram as shown in Figure 2.5 [11]. The T_c increases dramatically from $PbZrO_3$ to $PbTiO_3$ and can therefore be controlled by changing the Zr^{4+}/Ti^{4+} ratios. A morphotropic phase boundary (MPB) is a characteristic of the PZT phase diagram, which is identified as an abrupt structural changes between two ferroelectric phases (tetragonal and rhombohedral) [6]. The vertical MPB in Figure 2.5 implies that the composition (Zr^{4+}/Ti^{4+} ratio≈1) of coexisting tetragonal and rhombohedral phases is independent of temperature. In the compositional range near the MPB, the piezoelectric charge coefficient (d_{33}) and planar coupling coefficient (k_p) surge to their peak values, which is attributed to the coexistence of two ferroelectric phases increasing ease of reorientation of the polarisation directions when the electric field is applied [12]. Based on the first investigation of the PZT system [13], the fact that high piezoelectric properties could be achieved near the MPB was then exploited in commercial applications [6].

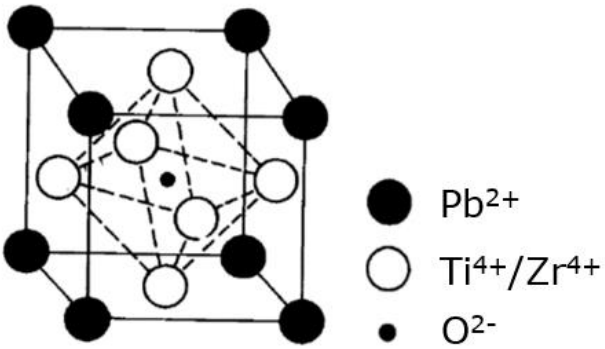

Figure 2.4. Perovskite structure of $Pb(Zr_{1-y}Ti_y)O_3$ [6].

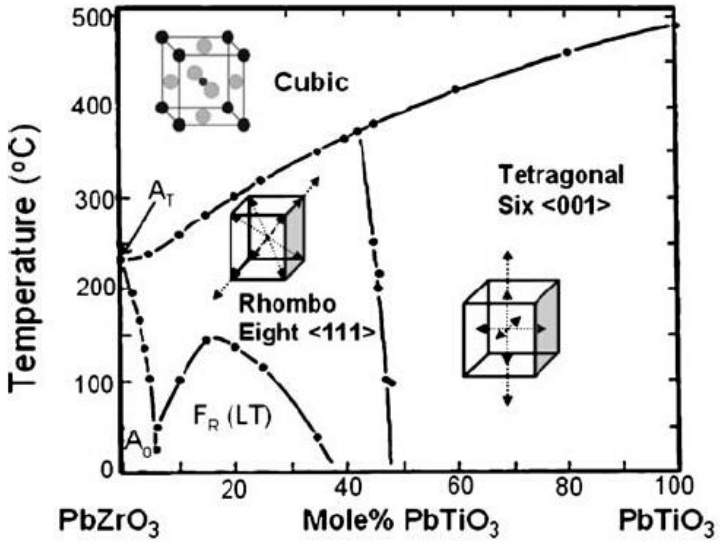

Figure 2.5. Phase diagram of PZT system [11].

However, lead is toxic, and once it is absorbed in lungs, skin or the gastro-intestinal system, it would be accumulated and stored in bone and soft tissue, which is hardly ejected [14]. Lead oxide (PbO) has been used as a reagent to fabricate PZT and other lead-based piezoceramics, resulting in lead contents of more than 60 wt.% [15]. This high lead content therefore is of particular concern as lead oxide volatilizes during high temperature fabrication processes and material disposal results in potential toxicity to the environment [15]. A series of EU directives [1, 2, 16, 17] has been published to restrict the use of lead-contained materials, therefore a lead-free alternative for PZT is demanded

for future applications and has become one of the most important research directions for piezoelectric materials.

A number of lead-free systems have been investigated as potential alternatives to PZT, including: $KNbO_3$-$NaNbO_3$, $Bi_{0.50}Na_{0.50}TiO_3$-$BaTiO_3$ and $0.5Ba_{0.70}Ca_{0.30}TiO_3$-$0.5BaZr_{0.20}Ti_{0.80}O_3$. In the $KNbO_3$-$NaNbO_3$ system, enhanced piezoelectric properties were found when the K^+/Na^+ ratio≈1 and this is analogous to the MPB in PZT [18]. The piezoelectric properties of this MPB composition ($(K_{0.50}Na_{0.50})NbO_3$) are summarised in Table 2.1 [19-22]. Its high electromechanical coupling factors and low dielectric constant make it a possible candidate for application in ultrasonic transducers [23]. However, the volatility of Na^+ or K^+ at high temperature makes the processing procedure difficult, with low sintering temperature resulting in nonstoichiometric and low density ceramics [23]. As one end member of $Bi_{0.50}Na_{0.50}TiO_3$-$BaTiO_3$ system, $Bi_{0.50}Na_{0.50}TiO_3$ has been considered as a promising lead-free piezoelectric material owing to its large remanent polarization (P_r=38 μC/cm^2) [24] and high Curie temperature (T_c=320ºC) [25]. However, the high coercive field (E_c=7.3 kV/cm) [24] results in hard poling procedure and limits the performance [23, 26]. The binary system with $BaTiO_3$ was then investigated with the observation of an MPB at 6-7% $BaTiO_3$, resulting in enhanced properties, as listed in Table 2.1 [27]. It could also be utilized in high frequency ultrasonic or piezoelectric actuator applications [27]. However, there is no prominent lead-free material found to substitute for the versatile PZT in every property or application, where most of them could only be utilized as alternatives to PZT in certain applications [23].

The $0.5Ba_{0.70}Ca_{0.30}TiO_3$-$0.5BaZr_{0.20}Ti_{0.80}O_3$ composition has been found to have comparable piezoelectric performance to soft PZT ceramics (as listed in Table 2.1), and has been considered as a promising lead-free piezoelectric material [28]. The corresponding $zBa_{0.70}Ca_{0.30}TiO_3$-(1-z)$BaZr_{0.20}Ti_{0.80}O_3$ system (abbreviated as zBCT-(1-z)BZT), whose phase diagram is shown in Figure 2.6 [28], exhibits enhanced properties within the MPB compositions around z=0.5, and has triggered more research since 2009 [29]. Therefore, in this chapter, a coherent literature survey will cover the parent $BaTiO_3$ ceramics and the end member $Ba_{1-x}Ca_xTiO_3$ and $BaZr_yTi_{1-y}O_3$ systems. The research development from Ca^{2+}, Zr^{4+} co-doped $BaTiO_3$ to this promising zBCT-(1-z)BZT system will also be reviewed.

Table 2.1. Dielectric and piezoelectric properties comparison between lead-free piezoceramics and PZT.

Composition	**Relative permittivity (ε_r)**	**Piezoelectric charge coefficient (d_{33}, pC/N)**	**Piezoelectric coupling coefficient (k)**	**Curie temperature (T_c, ºC)**	**Ref.**
Hard PZT	1700-3400	375-590	~0.7 (k_{33})	190-365	[11]
Soft PZT	~1000	225-290	~0.7 (k_{33})	~300	[11]
$BaTiO_3$	1900	191	0.38 (k_p)	130	[6]
$(K_{0.50}Na_{0.50})NbO_3$	472	80-160	0.23-0.45 (k_p)	~420	[19-22]
$0.94Bi_{0.50}Na_{0.50}TiO_3$ -$0.06BaTiO_3$	580	125	0.55 (k_{33})	288	[27]
$0.5Ba_{0.70}Ca_{0.30}TiO_3$-$0.5BaZr_{0.20}Ti_{0.80}O_3$	~3060	~620	N/A	~93	[28]

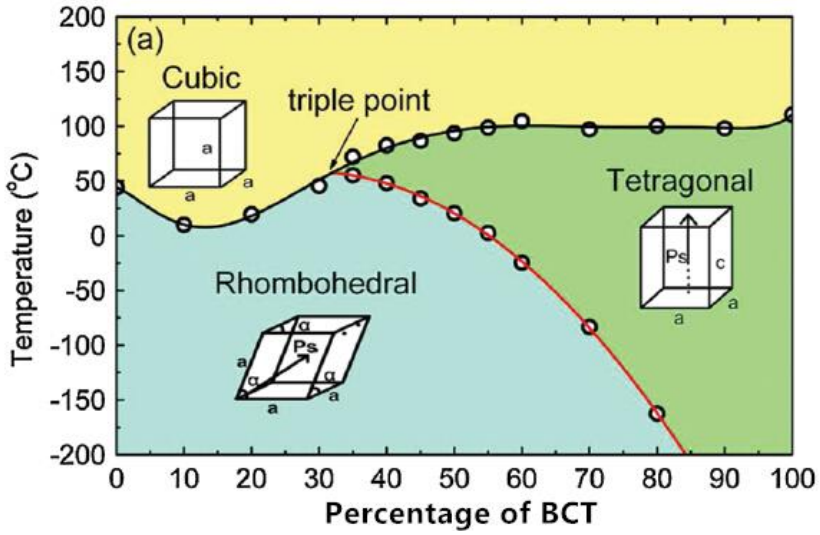

Figure 2.6. Phase diagram of $zBa_{0.70}Ca_{0.30}TiO_3$-(1-z)$BaZr_{0.20}Ti_{0.80}O_3$ system (abbreviated as zBCT-(1-z)BZT, BCT refers to $Ba_{0.70}Ca_{0.30}TiO_3$) [28].

2.2 Barium titanate ($BaTiO_3$)

2.2.1 Crystal structure and phase transitions of $BaTiO_3$

$BaTiO_3$ possesses a non-ferroelectric hexagonal structure above 1460 ºC, and reconstructively transforms to the perovskite cubic structure below 1460 ºC, which then transforms to ferroelectric phases upon cooling [30]. The perovskite-related crystal structures of $BaTiO_3$ change with temperature as shown in Figure 2.7 [30]. When the temperature is above 130 ºC, the T_C, $BaTiO_3$ has a cubic perovskite structure. At 130 ºC, the unit cell is elongated along an edge direction (*c* axis in Figure 2.7) and becomes tetragonal which is the onset of ferroelectric phases. When the temperature further drops down to 0 ºC, the cube elongates along a face diagonal direction and transforms to a 'pseudo-monoclinic' but actually orthorhombic structure [30]. The cube starts to elongate along the body diagonal direction from -90 ºC with a resulting rhombohedral structure. As the possibility of Ti^{4+} being off-centred in each direction are equivalent, there are 6,

12 and 8 spontaneous polarization directions in the tetragonal, orthorhombic and rhombohedral structures, respectively [6, 18, 31].

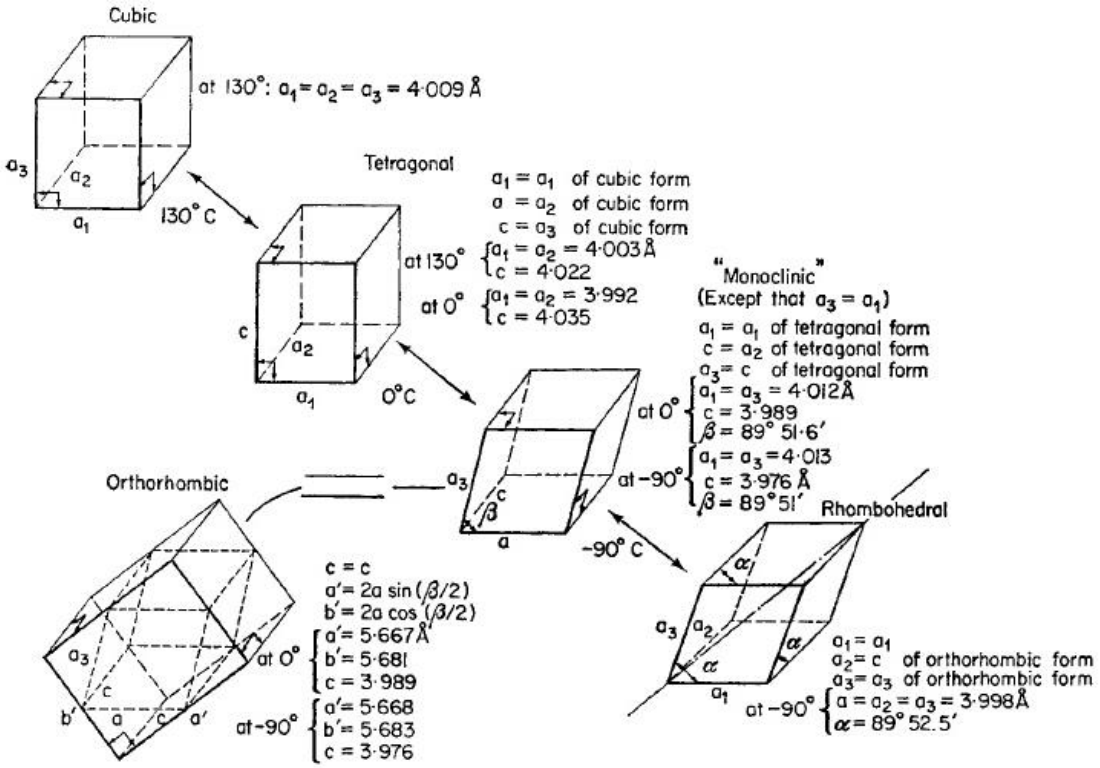

Figure 2.7. Unit cell distortion of $BaTiO_3$ polymorphs [30].

Compared with single crystals, the observed spontaneous polarization in randomly orientated polycrystalline ceramics is limited by the random directions of the crystallographic axes in the individual grains, and the materials have to be poled by the application of a high electric field at a temperature above room temperature but below T_C in order to maximise the polarisation alignment. The theoretically calculated maximum fractions of polarization in tetragonal, orthorhombic, rhombohedral perovskite ceramics compared to a single crystal are 0.83, 0.91 and 0.87 respectively, assuming that the polar axes take all possible alignments [6]. However, in reality, a tetragonal $BaTiO_3$ ceramic

possesses only about half the saturation polarization of that in a single crystal. This reduced value is caused by the inhibited rotations of 90º domains due to the involvement of strain [6]. Therefore, the spontaneous polarization as well as saturation polarization in ceramics could be affected by both the crystal structure and domain structure.

2.2.2 Formation mechanism of $BaTiO_3$ ceramics

The dielectric and ferroelectric properties of $BaTiO_3$ ceramics are dependent on the fabrication methods used and can be affected by crystal structure, microstructure and chemical homogeneity [32-34]. $BaTiO_3$ ceramics fabricated via solid-state methods often result in the presence of the impurity Ba_2TiO_4 phase. The swelling during decomposition of this impurity phase can lead to cracking or crazing in ceramics [30]. Therefore, an understanding of the reaction mechanism and resultant properties of solid-state fabricated ceramics is important in any study of $BaTiO_3$-related materials.

The reaction mechanism between $BaCO_3$ and TiO_2 can be described as occurring in three steps as shown below [35]:

(1) Formation of $BaTiO_3$ at an early stage from the reaction between $BaCO_3$ and TiO_2, which is then slowed down by step 2;

(2) Formation of an intermediate Ba_2TiO_4 phase from the reaction between $BaCO_3$ and $BaTiO_3$ formed in step 1;

(3) Formation of $BaTiO_3$ finally from the reaction between intermediate Ba_2TiO_4 and

remaining TiO_2.

The heat treatment of $BaCO_3$-TiO_2 and Ba_2TiO_4-$BaTiO_3$-TiO_2 layered samples further indicates that the diffusion of the intermediate Ba_2TiO_4 phase into $BaTiO_3$ could form $BaTiO_3$ and a titanium-free 'BaO' compound. This 'BaO' compound further reacts with TiO_2 to form more $BaTiO_3$ [36].

Felgner et al. reported the presence of orthorhombic and monoclinic Ba_2TiO_4 and minor amounts of a $BaTi_4O_9$ phase when heating $BaCO_3$ and TiO_2 [37]. A small amount of an unknown phase (2θ=26.7º) was also observed in previous studies [35, 38], which could not be defined after matching with every available JCPDS card for Ba-Ti-O compounds [38]. Therefore, the reaction mechanism between $BaCO_3$ and TiO_2 appears to be dependent on different experimental conditions and further studies would be useful.

The rate of reaction between $BaCO_3$ and TiO_2 was found to be dependent on many factors: (1) particle size and phase of starting materials, which affects the reaction rate but not the reaction mechanism [39-43]; (2) milling procedure of starting materials can produce homogeneous mixtures, reduce particle size and improve reactivity of powders, which improves the reaction rate [38, 41, 44-46] and even the reaction mechanism in step 2 [47]; (3) stoichiometric ratio of reagents, where a slight excess of TiO_2 acted as a catalyst to accelerate the $BaCO_3$ decomposition [35], however, either Ti-rich or Ba-rich compositions resulted in secondary $BaTi_2O_5$ or Ba_2TiO_4 phases, respectively [41, 48].

2.2.3 Grain size effect on functional properties of $BaTiO_3$ ceramics

Much research has focused on investigating the potential effects of grain size on the dielectric, ferroelectric and piezoelectric properties of $BaTiO_3$ at room temperature.

Arlt et al. reported a theoretical relationship between the 90º domain width (*dw*) and grain size (*GS*) where *dw* is proportional to $(GS)^{1/2}$ when *GS*<10 μm and becomes constant when *GS*>10 μm [49]. Furthermore, they observed the maximum relative permittivity value of $BaTiO_3$ ceramics for *GS*=0.7-1 μm [49]. These findings indicated a potential relationship between the grain size and/or domain size and dielectric properties of $BaTiO_3$ ceramics.

The observation of maximum relative permittivity at *GS*=0.7-1.1 μm was also confirmed by other researchers, where the maximum relative permittivity reached 4000-8000 [50-54], as shown in Figure 2.8 (A), the relative permittivity decreases for both smaller and larger grain size values [54-56]. The decreased relative permittivity in fine-grained ceramics is ascribed to the decreased tetragonality (*i.e.* decreased spontaneous tetragonal distortion) and increased density of non-ferroelectric grain boundary areas [52, 55]. This for *GS* larger than ~1.1 μm, the relative permittivity increased with decreasing grain size [50-54, 57]. As the theoretical relationship from Arlt et al. [49] has been further proved in experiments [54, 58], the decreasing grain size contributes to smaller domain size with higher domain (wall) density and increased domain wall mobility, which increased the

dipole polarization and therefore the relative permittivity [50, 54, 57].

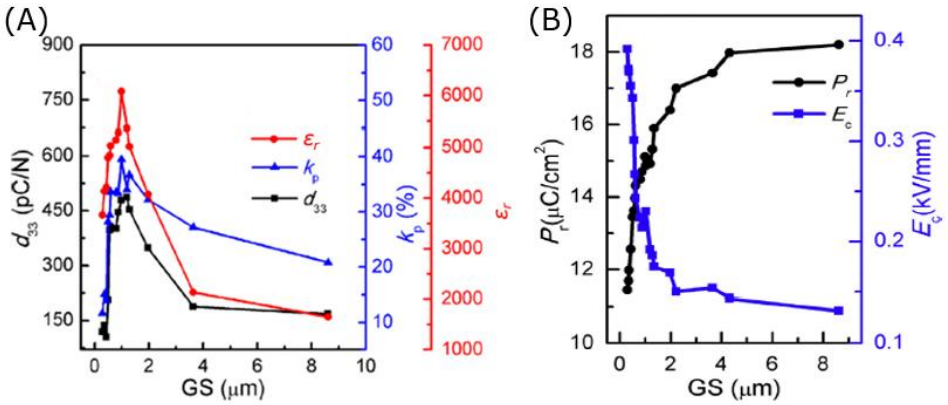

Figure 2.8. The grain size effect on functional properties of $BaTiO_3$ ceramics at room temperature: (A) ε_r, k_p, d_{33}; (B) P_r, E_c [52].

The piezoelectric charge coefficient, d_{33} showed a similar trend with changes in grain size, as shown in Figure 2.8 (A) [52]. A maximum value of d_{33} (280-519 pC/N) was observed at *GS*=0.7-1.1 μm and decreases on departure of this grain size range, as shown in Figure 2.8 (A) [51, 52, 58, 59]. This similar trend may imply the same origins of the observed dielectric and piezoelectric properties [51, 52, 58, 59]. In fine-grained ceramics (*GS*<~1.1 μm), the reduced d_{33} with decreased grain size is attributed to the monodomain and/or reduced domain density in such small grains and therefore less domain wall vibrations [58]. For relatively coarser grains (*GS*>~1.1 μm), the 90º domain width decreases with decreasing grain size. The smaller domain width then induces domain walls of smaller area dimensions with less inertial mass [51, 60], which contributes to an easier domain wall rotation and more active response to electric or stress field (*i.e.* enhanced piezoelectric properties) [52].

The ferroelectric properties (*P*-*E* loop) of $BaTiO_3$ ceramics are also affected by grain size.

Figure 2.8 (B) indicates that the remanent polarization (P_r) decreases gradually with reduction of grain size when GS>1.1 μm, followed by a dramatic drop for ceramics with GS<~1.1 μm [50, 52, 53]. In fine-grained ceramics, the decrease in grain size contributes to more non-ferroelectric grain boundaries and increased internal stress after the removal of electric field, which inhibits the orientation of polarization and therefore lower P_r [50, 52, 53]. However, for GS>1.1 μm, the "dilution" effects of grain boundary weakens its effect on the ferroelectric properties [52]. As shown in Figure 2.8 (B), the coercive field (E_c) generally increases with decreasing grain size [50, 52, 53]. When GS<~1.1 μm, the pinning effect on domain wall vibrations from grain boundaries [54, 58] leads to more difficult domain reversal (*i.e.* higher E_c). Again, the weak grain boundary effect on ferroelectric properties at GS>1.1 μm results in only slight E_c changes in this grain size region [50, 52, 53].

Grain size has also been shown to affect the phase transition temperatures of $BaTiO_3$ ceramics. Kanata et al. pointed out that the induced internal stress in smaller grains after cooling from sintering led to the presence of the orthorhombic phase at room temperature, which increased the orthorhombic-tetragonal phase transition temperature ($T_{O\text{-}T}$) of $BaTiO_3$ ceramics for GS≤20 μm [57]. This increase in $T_{O\text{-}T}$ with decreasing grain size has been further proved by other researchers [51, 52]. A decrease in Curie temperature (T_C) with reduction of grain size was also observed with accompanying decrease in tetragonality (c/a, *i.e.* decreasing stabilization of spontaneous tetragonal distortion) [51, 52, 55].

The grain size of $BaTiO_3$ ceramics could be affected by different fabrication procedures such as particle size of the reagents [56], sintering temperature [59, 60] and sintering procedure [52, 54, 58, 61]. Therefore, the corresponding functional properties of $BaTiO_3$ ceramics will also be dependent on the fabrication procedures.

2.2.4 Raman spectroscopy of $BaTiO_3$

Raman spectroscopy can provide information on chemical structures and physical forms by characterising vibrational bond energies, which enables it to detect local lattice distortions and crystallographic defects at the molecular level [62, 63]. In the case of $BaTiO_3$, when the crystal goes through the phase transitions from high temperature cubic symmetry to lower temperature ferroelectric phases, the lattice distortion mainly comes from the $[TiO_6]$ octahedra. X-ray diffraction is not very sensitive to identify phase transitions with displaced oxygen ions [63], so Raman spectroscopy has been utilized to determine the phase transition of $BaTiO_3$ based on the crystal structure information [63].

$BaTiO_3$ has the same perovskite structure as PZT, shown in Figure 2.4, with the Ba^{2+} cations occupying the A-sites. There are there are 5 atoms in each unit cell, resulting in 15 vibrational degrees of freedom in both paraelectric and ferroelectric phases. In cubic $BaTiO_3$ (O_h or *Pm3m*), these 15 vibrational modes are divided into the representations $4F_{1u}+F_{2u}$: barium and titanium atoms occupy the O_h sites, which contribute to two F_{1u} modes, and another $2F_{1u}+F_{2u}$ modes come from three oxygen atoms lying on D_{4h} sites. One of the F_{1u} symmetry modes is a translational mode, belonging to acoustical branch

and only $3F_{1u}+F_{2u}$ modes are optical branches. As the F_{2u} mode is silent and the F_{1u} modes are only infrared active, there are therefore no expected active Raman mode in cubic $BaTiO_3$ [64-69]. However, the observation of broad Raman bands around 250 and 520 cm^{-1} above the Curie temperature has been reported, which is believed to be caused by the locally displaced Ti^{4+} ions breaking the perfect cubic symmetry and forming some Raman active polar regions [63, 64, 68-71].

In tetragonal $BaTiO_3$ (C_{4v} or *P4mm*), the Ti^{4+} ion shifts off-centre in the unit cell. Each F_{1u} modes splits into a nondegenerate A_1 mode and a doubly degenerate E mode, and the F_{2u} mode splits into a B_1 and E mode. In polycrystalline $BaTiO_3$, the long-range electrostatic force resulting from the ions in the crystal structure further split the A_1 and E modes into transverse (TO) and longitudinal (LO) optical modes. Therefore, there are altogether $3[A_1(TO)+A_1(LO)]+4[E(TO)+E(LO)]+B_1$ modes in the tetragonal symmetry [68, 69]. As several of the A_1 and E modes are very close, the modes can overlap which makes unambiguous interpretation more difficult. The observed Raman modes in tetragonal $BaTiO_3$ from previous reports are summarised and listed in Table 2.2.

Table 2.2. Observed Raman modes for tetragonal $BaTiO_3$ spectra from previous reports.

Raman shifts	Raman modes	Related molecular vibrations	Ref.
~180 cm^{-1}	$[A_1(TO)]$	Ti^{4+} vibrating against the O^{2-}-cage	[72, 73]
~250 cm^{-1}	$[A_1(TO)]$	polar Ti^{4+}-O^{2-} octahedral vibrating against the Ba^{2+}-cage	[73]
~305 cm^{-1}	$[E(TO+LO), B_1]$	asymmetry within the $[TiO_6]$ octahedra	[69]
~520 cm^{-1}	$[E(TO), A_1(TO)]$	Ti-O bond movement	[74]
~720 cm^{-1}	$[E(LO), A_1(LO)]$	bending and stretching of $[TiO_6]$ octahedra	[75]

There is also a negative interference dip around 180 cm^{-1} in the Raman spectrum of tetragonal samples, which is either attributed to the anharmonic coupling of three [A_1(TO)] phonons [68, 76] or the antiresonance between the narrow [A_1(TO)] mode (~180 cm^{-1}) and the broad [A_1(TO)] mode (~250 cm^{-1}) [77]. Compared with the cubic $BaTiO_3$ Raman spectrum, the presence of intense bands at ~305 cm^{-1} and ~720 cm^{-1} have been taken as characteristic of tetragonal $BaTiO_3$ [69].

In the orthorhombic $BaTiO_3$ (C_{2v} or *Amm2*) spectrum, the presence of a distinguishing shoulder at ~190 cm^{-1} [E(TO+LO), A_1(LO)] was observed [67]. The peak position of the ~250 cm^{-1} band decreases and its intensity increases when compared with tetragonal spectra [78-80]. The position of the peak at ~305 cm^{-1} shifts to higher frequencies than that in the tetragonal spectra [78]. In addition, a weak shoulder at ~487 cm^{-1} [E(LO+TO), A_1(LO)] starts to appear, which was considered as a feature to identify the phase transition from the tetragonal to orthorhombic structure [78].

When the $BaTiO_3$ transfers from the orthorhombic to rhombohedral phase (C_{3v} or *R3m*), there are two sharp bands in the region of 170-190 cm^{-1} corresponding to the [A_1(TO)] and [E(TO+LO), A_1(LO)] mode respectively, which is reported as a rhombohedral characteristic [67, 79-81]. The intensity of the sharp band at ~305 cm^{-1} and the weak band at ~487 cm^{-1} also increase in the rhombohedral spectra [67]. The broad peak around 250 cm^{-1} drops further to lower frequency than the tetragonal or orthorhombic spectra [67, 78, 79].

The transition between the paraelectric cubic phase and the ferroelectric tetragonal phase (*C*-*T*) has therefore been successfully determined by Raman spectroscopy based on a gradual disappearance of the ~305 cm^{-1} and ~720 cm^{-1} bands as the cubic structure is approached [72, 75, 81-84]. As reviewed above, upon cooling, the discontinuous decrease in the position of the ~250 cm^{-1} band could indicate the phase transition from the tetragonal to orthorhombic (*T*-*O*) and orthorhombic to rhombohedral (*O*-*R*) phases [67, 78-80]. The onset appearance of the ~487 cm^{-1} band and double bands in the region of 170-190 cm^{-1} have been considered as characteristic of the *T*-*O* and *O*-*R* transitions respectively [67, 78-81].

Furthermore, the temperature dependent peak position (ω) and peak width (full width at half maximum, FWHM, Γ) of particular Raman modes could be obtained by in situ Raman spectroscopy measurements. Baskaran et al. have reported that the sudden decrease in peak width of the ~250 cm^{-1} or ~520 cm^{-1} bands during cooling can be ascribed to the *C*-*T* transition [70]. The changes in peak position and peak width of the ~305 cm^{-1} mode, as shown in Figure 2.9 [63], are able to identify all the phase transitions in $BaTiO_3$: upon cooling, the presence of the ~305 cm^{-1} mode is the *C*-*T* transition, the sudden increase in peak position is the *T*-*O* transition and the decrease in peak width is a result of the *O*-*R* transition [63, 85]. Therefore, it is possible to identify phase transition temperatures of $BaTiO_3$ or even $BaTiO_3$ based materials via in situ Raman spectroscopy measurements.

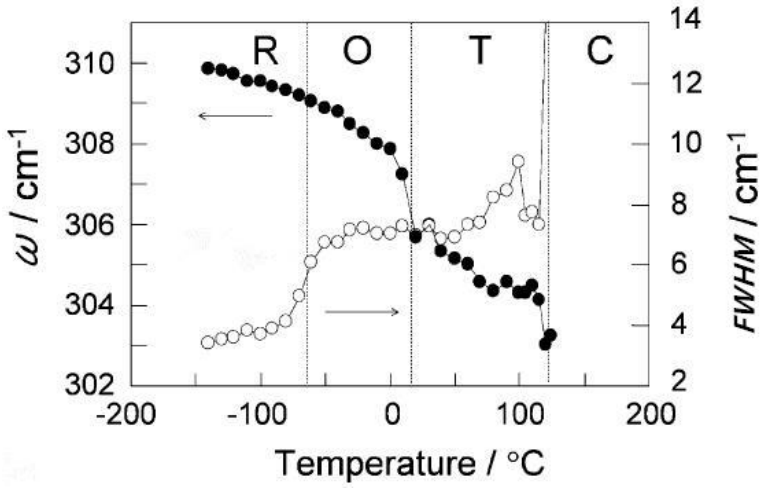

Figure 2.9. Temperature dependent peak position (ω) and peak width (full width at half maximum, FWHM, Γ) of ~305 cm^{-1} mode of $BaTiO_3$ ceramics [63].

2.3 Ca^{2+}-doped $BaTiO_3$ piezoelectric system

2.3.1 Solid solubility limit of Ca^{2+} into Ba-site of $BaTiO_3$

The solid solubility limit of Ca^{2+} into the Ba-site of $BaTiO_3$ is strongly dependent on the fabrication procedures. For $Ba_{1-x}Ca_xTiO_3$ ceramics fabricated by a solid-state method, a single tetragonal phase up to $x\approx0.23$ was observed by X-ray diffraction measurement, and it then became biphasic with a $BaTiO_3$-based tetragonal phase and $CaTiO_3$-based orthorhombic phase for $0.23<x<0.90$, and finally became a pure orthorhombic phase for $0.93\leq x\leq1$ [86, 87]. Wang et al. further confirmed that in the two phase region, the $BaTiO_3$-based tetragonal phase had a composition $Ba_{0.80}Ca_{0.20}TiO_3$ and the $CaTiO_3$-based orthorhombic phase had a composition $Ba_{0.07}Ca_{0.93}TiO_3$ indicating the solubility limits of the end members [86]. The purity of reagents, milling method and calcination and/or sintering temperature have also been reported to affect the solubility limit of Ca^{2+} in $BaTiO_3$ in solid state fabrication methods [86, 88-90]. An increased solubility limit of

Ca^{2+} (x=0.25) was also reported in solid-state fabricated $Ba_{1-x}Ca_xTiO_3$ ceramics by utilizing different fabrication processes [88, 91].

When using solid-state fabrication methods to fabricate $Ba_{0.70}Ca_{0.30}TiO_3$ ceramics, it has been observed that the microstructure comprises small orthorhombic grains dispersed amongst a matrix of larger tetragonal grains [86, 92]. Li et al. found that the average grain size of the tetragonal phase firstly increased and then decreased when increasing the sintering temperature from 1270 ºC to 1400 ºC, with the maximum grain size (~6.2 μm) observed for a sintering temperature of 1340 ºC. However, the grain size of orthorhombic phase remained nearly constant (~2.5 μm) [92]. Furthermore, Puli et al. reported that prolonged calcination at 1250 ºC for 10 hours followed by sintering at 1350 ºC for 4 hours could not supress the existence of the orthorhombic phase [93]. However, a higher sintering temperature (1500 ºC) and longer dwelling time (6 hours) could drastically reduce the amount of orthorhombic phase present, as a result of better incorporation of Ca^{2+} at the Ba-sites, and also resulted in larger overall average grain size (~40-65 μm) [93].

Other fabrication methods have also been used to form $Ba_{1-x}Ca_xTiO_3$ materials. Fu et al. used the floating-zoned method to obtain $Ba_{1-x}Ca_xTiO_3$ single crystals, where the solubility limit of Ca^{2+} was increased to x≈0.34 [94, 95]. Zhang et al. observed that the presence of single phase $Ba_{1-x}Ca_xTiO_3$ was extended to x=0.30 and a second phase started from x=0.35 in samples produced by using a low temperature direct synthesis method [96]. Tiwari et al. reported that a semi wet route reduced the compositional inhomogeneities in

$Ba_{1-x}Ca_xTiO_3$ samples compared to conventional dry routes, where the latter method also resulted in the formation of more $CaTiO_3$ [97]. A high-throughput combinatorial method was reported by Wang et al to have a similar solubility limit (x≈0.23) to the solid state method [86, 98], and using an hydrolysis method the substitutional limit of Ca^{2+} was found to be only x≈0.12, with the presence of $CaTiO_3$ observed from x=0.15 [99]. Therefore, the solubility limit of Ca^{2+} into $BaTiO_3$ and the formation of homogenous $Ba_{1-x}Ca_xTiO_3$ phases are dependent on fabrication procedures.

2.3.2 Ca^{2+} substitution into $BaTiO_3$ on Ba-site and/or Ti-site

The limited solubility of Ca^{2+} into the Ba-site in $BaTiO_3$ has led to some observations of Ca^{2+} substituting into the Ti^{4+}-site being reported, with the accompanying formation of oxygen vacancies and Ca''_{Ti} defects [91, 100, 101]. The difference in ionic charge and radius between the Ca^{2+} and Ti^{4+} ions makes the substitution of Ca^{2+} on the Ti-site difficult, and therefore Ca^{2+} prefers to substitute for Ba^{2+} rather than Ti^{4+} [99, 102]. It has been reported that Ca^{2+} mainly substitutes for Ba^{2+} when $(Ba^{2+}+Ca^{2+})/Ti^{4+}$ ratio equals to 1 [99, 102, 103]. However, when the $(Ba^{2+}+Ca^{2+})/Ti^{4+}>1$, Ca^{2+} can also occupy the Ti^{4+} site up to a value of nearly 0.02 [104-107]. Therefore, good compositional control should be exercised when fabricating $Ba_{1-x}Ca_xTiO_3$ samples.

Structural analysis of Ca^{2+}-doped $BaTiO_3$ has been used to distinguish the site occupancy of Ca^{2+} in $BaTiO_3$. Raman spectra of Ba-site substituted $BaTiO_3$ possessed the same modes as tetragonal undoped $BaTiO_3$. The ~520 cm^{-1} and ~720 cm^{-1} modes shifted to

higher frequency with increasing Ca^{2+} content due to the resulting increase of the force constant from increased Ca^{2+} occupancy at the Ba-site [93, 108]. However, the ~250 and ~305 cm^{-1} modes shifted to lower frequency with increasing addition of Ca^{2+} [108]. At room temperature, the intensity of the ~305 cm^{-1} mode decreased with increasing Ca^{2+} content on the Ba-site [108]. For $Ba_{1-x}Ca_xTiO_3$ (x=0.20), the ~305 cm^{-1} mode nearly disappeared, and the weak ~487 cm^{-1} mode was well retained below 120ºC [108]. The broad ~250 cm^{-1} and ~520 cm^{-1} modes were still present above the *T*-*C* transitions, similar to undoped $BaTiO_3$, indicating the existence of local disorder in the structure from the Ca_{Ba} defects [108, 109].

In terms of the Ti-site doped $BaTiO_3$, there would be expected to be an additional asymmetric mode ~800 cm^{-1} in the Raman spectra. This is an A_{1g} octahedral breathing mode which is only active when more than one B-site species is present. When Ca^{2+} substitutes on the Ti-site aliovalently, this asymmetric mode was also present due to the formation of Ca''_{Ti} defects [93]. Therefore, the presence and intensity of the ~800 cm^{-1} mode could be used to qualitatively determine the substituent concentrations of Ca^{2+} on the Ti-site [108, 110].

2.3.3 Deviations to Vegard's law

Vegard's law is generally applied in the solid solution of two constituents, where the lattice parameters of the system can be calculated from the lattice parameters of the two constituents by a rule of mixtures [111]. According to Vegard's law, the expected unit cell

volume (V) of a true solid solution of $Ba_{1-x}Ca_xTiO_3$ should follow the linear relationship as:

$$V = (1 - x) \cdot V_{BaTiO_3} + x \cdot V_{CaTiO_3} \quad (2.9)$$

where V_{BaTiO_3}=64.375 Å and V_{CaTiO_3}=55.935 Å [94]. However, in reality, the unit cell volume of $Ba_{1-x}Ca_xTiO_3$ system does not follow Equation 2.9 [94, 112].

Ca^{2+} substitution on the Ti-site would result in extension of the B-O bond, and therefore expansion of the [BO_6] octahedra and the unit cell volume, due to the difference in the ionic radii (Ca^{2+} ~1.00 Å, Ti^{4+} ~0.61 Å) [110, 113]. This expansion may compensate for the contraction of the unit cell caused by the smaller Ca^{2+} substituting for larger Ba^{2+} (~1.61 Å) [99, 106, 114]. Park et al. claimed that even below the Ca^{2+} solubility limit (Ca^{2+}=0.12), there was difference (around 0.15%) between the calculation (from Vegard's law) and experimental refinement (from X-ray diffraction) of the unit cell volume of Ca^{2+}-doped $BaTiO_3$ samples, indicating the existence of small amounts of Ca^{2+} on the Ti-site [91]. Lee et al. then investigated the modified Vegard's law for multi-site doped $BaTiO_3$ and found that when there was only a small amount of Ca^{2+} (≤0.02) doped in $BaTiO_3$, the $BaTiO_3$ would be multi-site occupied and the resultant unit cell volume had a slight increase [115]. With further increase of the Ca^{2+} content, the unit cell volume decreased linearly in parallel to the Vegard's law, where the difference was ascribed to the Ti-site occupancy [115]. In spite of the effects on unit cell volume, the Ti-site substitution also contributed to a decrease in tetragonality (c/a) [97, 108, 116]. Therefore, the lattice

parameters of Ca^{2+}-doped $BaTiO_3$ are sensitive to the site occupancy of Ca^{2+} on the Ba-site and/or Ti-site.

As mentioned in section 2.3.1, different fabrication procedures could broaden the Ca^{2+} solubility limit in $BaTiO_3$, and $Ba_{1-x}Ca_xTiO_3$ ($x \leq 0.34$) single crystals with Ca^{2+} only substituting on the Ba-site have been reported by Fu et al. [94, 117]. A refinement of the lattice parameters (a, c and $\sqrt[3]{a^2c}$) of these $Ba_{1-x}Ca_xTiO_3$ ($x \leq 0.34$) samples is shown in Figure 2.10. The variation of lattice constants was extremely small when the Ca^{2+} concentration was low ($x \leq 0.06$) [94]. However, with increasing Ca^{2+} concentration, the lattice constants decreased remarkably, with the tetragonality nearly unchanged [94]. Based on raw data from Fu et al.'s work, the compositional change of unit cell volume could be expressed as Equation 2.10, and its pseudo-cubic lattice constant $\sqrt[3]{a^2c}$ is shown as the blue solid line in Figure 2.10 [94]. This relationship also deviated from the Vegard's law (green dotted line) with a larger overall cell volume, which was ascribed to the greater atomic polarizability of Ca^{2+} increasing its space compared to an ideal solid solution [112].

$$V = 64.568 - 7.4836x \tag{2.10}$$

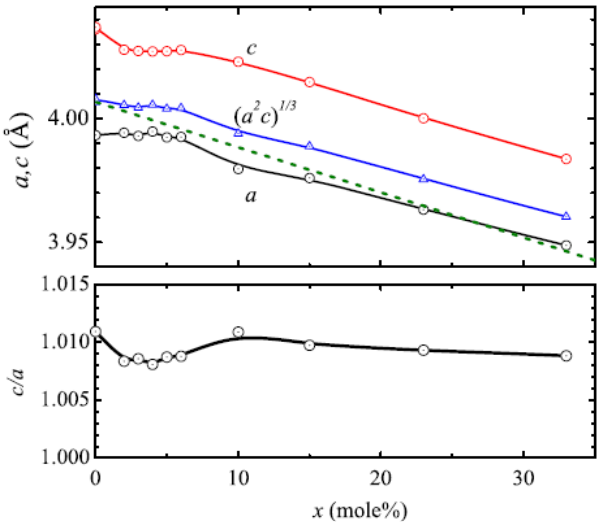

Figure 2.10. Compositional dependence of the lattice constants (upper) and tetragonality (*c/a*, lower) in $Ba_{1-x}Ca_xTiO_3$ ($x \leq 0.34$) [94].

Dawson et al. applied computer simulation to investigate compositional dependence of the volume of the [TiO_6] octahedra. With increasing Ca^{2+} content the [TiO_6] octahedra generally shrunk and the variation amongst all volumes increased, indicating that the distortion or relaxation of the [TiO_6] octahedra was not uniform [118]. When increasing the neighbouring Ca^{2+} content of sites adjacent to a [TiO_6] octahedron, the volume of the [TiO_6] octahedron decreased, and the variation increased [118]. Therefore, these complex distortions would also deviate the unit cell volume from Vegard's law.

Considering all these effects on the unit cell volume of the $Ba_{1-x}Ca_xTiO_3$ system, care has to be taken when using Vegard's relationship in the $Ba_{1-x}Ca_xTiO_3$ system.

2.3.4 Phase transition behaviour of $Ba_{1-x}Ca_xTiO_3$

The phase transition behaviour of $Ba_{1-x}Ca_xTiO_3$ system was determined by dielectric property measurements, where the peaks in the relative permittivity against temperature

curves were observed and associated with phase transitions. The obtained phase diagram is shown in Figure 2.11 [117]. A similar phase diagram of this system was also published by other researchers [112, 119]. The transition temperature of *R-O* and *O-T* decreased monotonically with Ca^{2+} addition in the Ba-site, whereas the *T-C* transition was not sensitively affected. Li and Wu related the decreased T_{R-O} and T_{O-T} to the Ca^{2+} addition inducing closer packing of O^{2-} along <111> and <110>, and the corresponding movement of Ti^{4+} was retarded [120]. The decreased T_{O-T} then contributed to an increased tetragonal symmetry region [121].

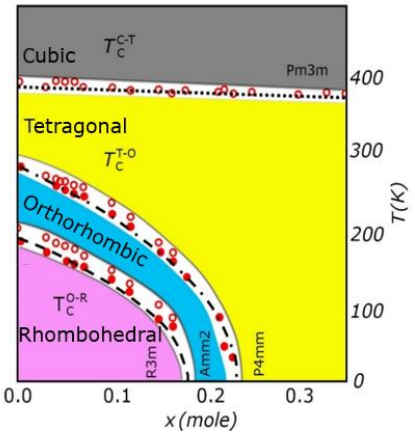

Figure 2.11. A temperature-composition phase diagram of $Ba_{1-x}Ca_xTiO_3$ ($x \leq 0.34$) system determined by dielectric measurements [117].

Figure 2.12 indicates the unit cell volume effects on the phase transition temperature of the $Ba_{1-x}Ca_xTiO_3$ system under high pressure [117]. The black dots and lines refer to the expected phase transition behaviour of pure $BaTiO_3$ under high hydrostatic pressure, where all the phase transition temperatures, T_{R-O}, T_{O-T} and T_{T-C}, decreased with the $BaTiO_3$ unit cell contraction [117, 119]. The measured phase transition temperatures of $Ba_{1-x}Ca_xTiO_3$ single crystals from temperature dependent relative permittivity (as shown

in Figure 2.11) were added as red dots and lines to Figure 2.12 [117]. The red dashed line represents the predicated decrease in T_C from Ca^{2+} addition based on Vegard's law for a solid solution system [117]. Fu et al. then also suggested that the unexpected stability in T_C was also attributed to the existence of a polarization component (off-centre displacement of Ca^{2+}) in the $Ba_{1-x}Ca_xTiO_3$ crystals stabilizing the ferroelectric tetragonal phase (*i.e.* the invariant tetragonality in Figure 2.10) [94, 117].

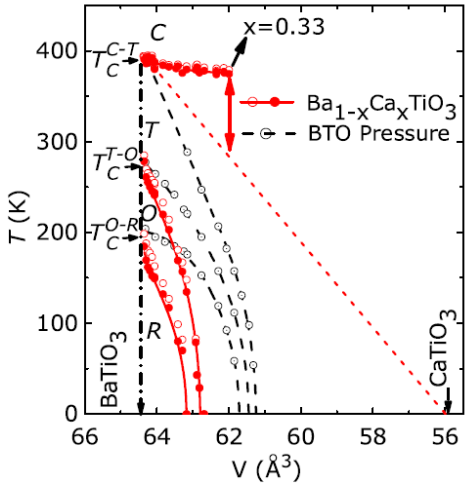

Figure 2.12. Unit-cell volume effects on the phase transition of $Ba_{1-x}Ca_xTiO_3$ single crystals and $BaTiO_3$ crystal under high pressure [117].

Levin et al. related the stabilised tetragonal phase and T_C to the enhanced polarization from Ca^{2+} addition inducing the highly strained Ca-O and Ba-O bonds and the local Ti^{4+} displacements along directions close to the tetragonal axis [114]. Wang et al. found that further Ca^{2+} addition only changed T_C negligibly in the range of x=0.20-0.50, however, leading to a decreasing ε_{rmax} value and diffuse phase transition (DPT) between the tetragonal and cubic phases [86]. Sinclair and Attfield suggested that T_C was mostly affected by the average size of A-site cations (*i.e.* Ba^{2+} and Ca^{2+}) and their size variance

[122]. Reducing the average size of the A-site cations by adding Ca^{2+} contributed to tilts and rotations of the [TiO_6] octahedra, weakening the stability of ferroelectric phase. However, the resultant increased size variance led to local disorder, enhancing the ferroelectric distortions. The combining of these two opposite effects contributed to the invariance of T_C [122]. Furthermore, Mitsui and Westphal ascribed the compositional independence of T_C to the combination of greater atomic polarizability of Ca^{2+} increasing T_C and the shrinkage of unit cell volume decreasing T_C [112].

2.3.5 Functional properties of $Ba_{1-x}Ca_xTiO_3$

At room temperature, tetragonal $BaTiO_3$ (*P4mm*) is ferroelectric, however, orthorhombic $CaTiO_3$ (*Pcmn*) does not have ferroelectric behaviour [123]. In the $CaTiO_3$ crystal, as shown in Figure 2.13, the regular [TiO_6] octahedra rotate with respect to their cubic positions and the coordination number of Ca^{2+} reduces from 12 to 8. Therefore, these displacements of the Ca^{2+} and the surrounding [TiO_6] octahedra are cancelled out and yield no ferroelectricity [123, 124]. This non-ferroelectric orthorhombic $CaTiO_3$ has low relative permittivity (ε_r=160-170) at room temperature [98].

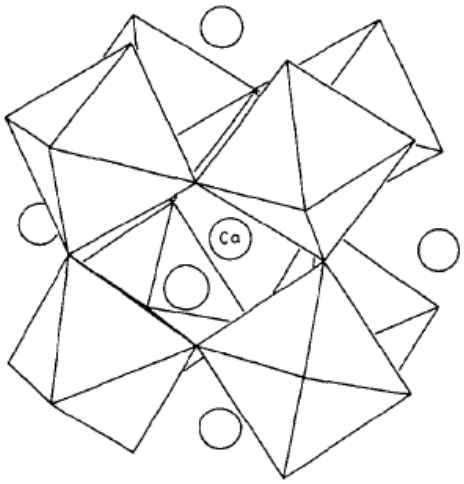

Figure 2.13. Impression of $CaTiO_3$ structure, where the [TiO_6] octahedral are rotated with respect to their positions in the ideal perovskite structure [124].

For $Ba_{1-x}Ca_xTiO_3$ ceramics, at room temperature, the addition of Ca^{2+} also leads to a decrease of relative permittivity (ε_r) [30, 87, 98, 125]. The temperature dependence of relative permittivity (ε_r-T) curve shows decreased ε_{rmax} values and DPT behaviour with increasing Ca^{2+} concentrations [86, 90, 96, 126]. Kumar et al. believed that compositional fluctuations in $Ba_{1-x}Ca_xTiO_3$ ceramics generated this DPT behaviour with various local transition temperatures and lower ε_{rmax} values [126]. Additionally, the DPT behaviour was probably related to the existence of polar clusters in the critical regimes [90]. The frequency dependent ε_r-T curve of $Ba_{1-x}Ca_xTiO_3$ ceramics indicated a slight relaxor behaviour, where the ε_r-T peak shifted slightly to higher temperatures with lower ε_{rmax} values when increasing frequency [86, 127]. Han et al. reported that the ε_{rmax} of $Ba_{0.70}Ca_{0.30}TiO_3$ ceramics was 4851 at T_C~398 K and ε_r was ~2100 at room temperature [128]. Li et al. further reported that the value of ε_{rmax} was also affected by sintering temperature when using a solid-state fabrication method and the largest ε_{rmax} (6890) at T_C was achieved after sintering at 1340 ºC, with a value at room temperature just above

1000 [92].

In terms of ferroelectric properties, the *P-E* loop of the $Ba_{1-x}Ca_xTiO_3$ system has been widely investigated. Fu et al. related the invariance of the saturation polarization of $Ba_{1-x}Ca_xTiO_3$ ($x \leq 0.34$) single crystals to its compositionally independent tetragonality [94]. However, a decreasing spontaneous polarization (P_S) with the doping of non-ferroelectric Ca^{2+} was observed in Varatharajan et al.'s work, where P_S decreased from 6.18 μC/cm^2 at x=0.12 to 2.7 μC/cm^2 at x=0.20 [125]. The same decreasing trend of remanent polarization (P_r) was observed for solid-state fabricated ceramics (x=0.23-0.5), which was also attributed to the presence and increasing amount of Ca^{2+} [86]. A higher coercive field (E_C) in $Ba_{1-x}Ca_xTiO_3$ (x=0.07) single crystals compared to $BaTiO_3$ was reported by Imura et al., and they believed that the large structural distortion around Ca^{2+} (*i.e.* the rotation of [TiO_6] octahedra around the Ca^{2+} ions) generated higher E_C [123]. The in-situ temperature *P-E* loop measurement (T=273-433 K) of $Ba_{1-x}Ca_xTiO_3$ ceramics indicated that P_S, P_r and E_C decreased during heating due to the transformation from ferroelectric to paraelectric phases [127, 128]. The *P-E* loop measurements of $Ba_{0.70}Ca_{0.30}TiO_3$ ceramics have indicated that P_S=16.73 μC/cm^2, P_r=4.15-4.37 μC/cm^2, E_C=6.67-9.10 kV/cm at room temperature, where the difference was attributed to the different fabrication procedures of ceramics via the solid-state and sol-gel methods [93, 128].

In spite of obtaining largest ε_{rmax} when sintering $Ba_{0.70}Ca_{0.30}TiO_3$ ceramics at 1340 ºC, the enhanced ferroelectric properties (P_r=8 μC/cm^2) as well as piezoelectric properties

(d_{33}~126 pC/N and k_p~0.29) were also observed [92]. Li et al. further pointed out that the functional properties of $Ba_{0.70}Ca_{0.30}TiO_3$ ceramics were sensitive to the sintering temperature, which was also affecting the grain size, where the largest tetragonal grains (~6.2 μm) were observed in ceramics sintered at 1340 ºC [92]. Therefore, the functional properties of $Ba_{0.70}Ca_{0.30}TiO_3$ ceramics were related to the grain size and fabrication procedure.

2.4 Zr^{4+}-doped $BaTiO_3$ piezoelectric system

2.4.1 Formation mechanism of Zr^{4+}-doped $BaTiO_3$

There are a number of reports of the formation of $BaZr_yTi_{1-y}O_3$ ceramics via solid-state routes. Bera and Rout found that $BaTiO_3$ and $BaZrO_3$, which both have a perovskite structure, were formed separately without the observation of any intermediate phase such as BaO, Ba_2TiO_4 or $BaTi_3O_7$ [129, 130]. The desired $BaZr_{0.40}Ti_{0.60}O_3$ phase was then formed only through diffusing $BaTiO_3$ into $BaZrO_3$ but not the diffusion from $BaZrO_3$ into $BaTiO_3$ [129]. This is evidenced by unchanged peak positions of $BaTiO_3$ and shifted peak positions of $BaZrO_3$ to higher 2θ angle towards $BaTiO_3$ in X-ray diffraction studies, which resulted from a lower diffusion coefficient of Zr^{4+} with higher ionic radius (~0.72 Å) compared to Ti^{4+} (~0.61 Å) [129].

However, the observation of intermediate Ba_2TiO_4 phase has been reported by Vasilecu et al. who suggested a two-step formation mechanism for $BaZr_yTi_{1-y}O_3$ ceramics [131, 132]: the individual $BaTiO_3$ (from intermediate Ba_2TiO_4 phase) and $BaZrO_3$ were formed

initially; followed by inter-diffusion phenomena between these two phases with the incorporation of Zr^{4+} into the $BaTiO_3$ lattice and simultaneously diffusion of Ti^{4+} into the $BaZrO_3$ lattice [131]. Suslov et al., on the other hand, believed that $BaTiO_3$ was formed firstly from $BaCO_3$ and TiO_2, which then reacted with unreacted TiO_2 to form intermediate Ba_2TiO_4. The Ba_2TiO_4 then reacted with ZrO_2 to yield $BaZrO_3$ and more $BaTiO_3$, and finally the $BaZr_yTi_{1-y}O_3$ phase was produced from reaction between $BaTiO_3$ and $BaZrO_3$ [132]. This difference in the presence of intermediate Ba_2TiO_4 phase could be attributed to different particle size of powders, which resulted in different reaction temperature ranges of the solid-state reaction and therefore the formation of the intermediate phase [132, 133].

In addition, Vasilescu reported that single $BaZr_yTi_{1-y}O_3$ (y=0.05 and 0.10) phase could be formed after sintering at 1400 ºC, whereas for y=0.15 and 0.20 there were distinct majority $BaTiO_3$ and minority $BaZrO_3$ phases. A single phase with the desired composition was only observed for samples sintered at 1500 ºC [131]. Therefore, increasing Zr^{4+} content induced a lower sinterability due to the higher energy required for Zr^{4+} diffusion, and it was more difficult to obtain dense $BaZr_yTi_{1-y}O_3$ ceramics with finer grains and higher Zr^{4+}concentrations [129, 134, 135]. It has also been reported that increasing sintering temperature promoted the diffusion coefficient of Zr^{4+} and extending holding time at sintering temperature increased the crystallinity of the $BaZr_yTi_{1-y}O_3$ phase [135-138].

2.4.2 Phase transitions of $BaZr_yTi_{1-y}O_3$

The phase diagram of $BaZr_yTi_{1-y}O_3$ (y=0-0.30) system is shown in Figure 2.14 [139], where the phase transition behaviour is strongly dependent on Zr^{4+} concentrations. Temperature dependent dielectric property measurements (ε_r-T curve) have been commonly used to identify phase transitions in $BaZr_yTi_{1-y}O_3$ ceramics. In the range of $0 \leq y \leq 0.10$, there were three relatively abrupt peaks in the ε_r-T curve referring to phase transitions from rhombohedral to orthorhombic (R-O) to tetragonal (O-T) and finally to the paraelectric cubic phase (T-C), where the T_{R-O} and T_{O-T} increased and T_{T-C} decreased with increasing Zr^{4+} amount [135, 140-143]. When substituting more Zr^{4+} into $BaZr_yTi_{1-y}O_3$ ($y \geq 0.10$), these three phase transition peaks merged into one broad peak at the ferroelectric to paraelectric phase transition [141, 144, 145].

The decrease of $T_{R-C/T-C}$ was reported to follow a linear relationship with Zr^{4+} content for y=0-0.16 [146]. The Zr^{4+} induced reduction of $T_{R-C/T-C}$ was attributed to larger Zr^{4+} ion substituting into the Ti-site weakening the bonding force between B-site ions and oxygen ions in the $BaZr_yTi_{1-y}O_3$ crystal. The induced Zr-O bonds were also thought to break the Ti-O chains, which contributed to distortions in the structure and decreased $T_{R-C/T-C}$ [135, 137, 138, 147].

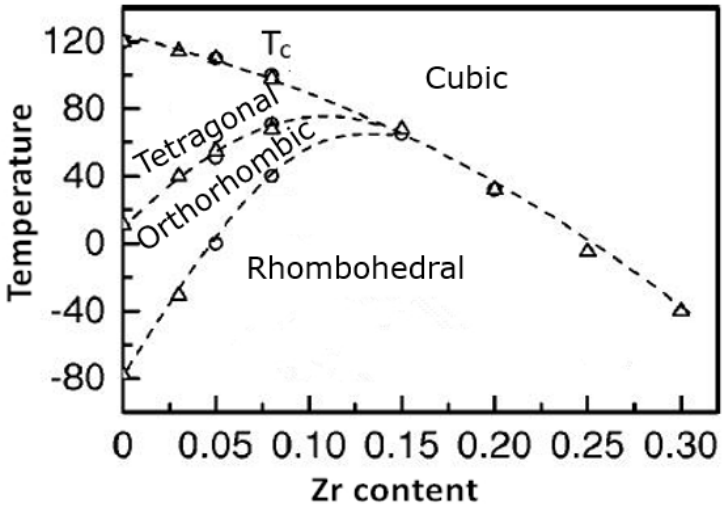

Figure 2.14. Temperature dependent phase diagram of $BaZr_yTi_{1-y}O_3$ (y=0-0.30) ceramics [139].

A broadening of the ε_r-T peaks in $y \geq 0.15$ compositions were observed and believed to be attributed to the melting peaks of three phase transitions and/or DPT behaviour [140]. This diffusive nature was caused by compositional fluctuations in the Zr^{4+}-doped ceramics, resulting in microscopic inhomogeneity and a random distribution of local $T_{R\text{-}C}$ [131, 140, 147-149].

Vasilescu et al. observed DPT behaviour even for lower Zr^{4+}-containing $BaZr_yTi_{1-y}O_3$ (y=0.05 and 0.10) ceramics, which was attributed to their small grain size (~10 μm) [131]. Tang et al. observed that the phase transition temperature ($T_{R\text{-}C}$) of $BaZr_yTi_{1-y}O_3$ (y=0.20) ceramics decreased with the reduction of grain size from 60 μm to 2 μm, with the broadening of the ε_r-T peak [150]. This indicated that DPT behaviour of $BaZr_yTi_{1-y}O_3$ ceramics can be induced by both Zr^{4+} additions and small grain size [131]. The DPT behaviour in fine-grained $BaZr_yTi_{1-y}O_3$ ceramics was induced by internal stress [151], and were more susceptible than $BaTiO_3$ to the grain size effect on DPT behaviour [134]. A frequency dependent ε_r-T curve (*i.e.* relaxor behaviour) was reported in $BaZr_yTi_{1-y}O_3$

($y \geq 0.20$) ceramics, which became more pronounced with increasing Zr^{4+} content. The relaxor behaviour resulted from microscopic compositional fluctuations and the $BaTiO_3$ macro domains being divided into micro domains induced by the introduction of dopants [135, 145, 150].

The temperature dependent *P-E* hysteresis loop of $BaZr_yTi_{1-y}O_3$ ceramics were also investigated and reported, where P_r and E_c had a general decreasing trend during heating, as a result of approaching the paraelectric cubic phase [135, 147, 152]. When the temperature was above the Curie temperature, the value of P_r was not zero and the *P-E* loop was not a complete straight line, indicating the presence of nano-polar domains in ceramics even with a nominally cubic structure [135].

The ferroelectric to paraelectric phase transitions in $BaZr_yTi_{1-y}O_3$ ceramics (as shown in Figure 2.14) were also reported from Raman spectroscopy measurements with big temperature gaps (≥ 10 ºC) [139]. In low Zr^{4+}-content ceramics ($y \leq 0.08$), the disappearance of the 310 cm^{-1} mode was considered as a signature of the ferroelectric tetragonal to paraelectric phase transition [153]. With increasing Zr^{4+} content to $y \geq 0.10$, the intensity of the 520 cm^{-1} mode, 129 cm^{-1} dip and relative intensity of the 720 cm^{-1} and 800 cm^{-1} modes (I_{720}/I_{800}) as a function of temperature have been used to determine the ferroelectric-paraelectric phase transitions [72, 75, 153-155]. The presence of ferroelectric modes above the Curie temperature also indicated the DPT behaviour in higher Zr^{4+}-content ceramics ($y \geq 0.10$) [72, 75, 144, 154, 155].

However, the changes in Raman modes for the various ferroelectric phases were relatively harder to distinguish. The *O-T* transition was identified by the disappearance of the 125 cm^{-1} dip during heating [72, 153, 154]. Miao et al. and Deluca et al. considered the onset of the broad 260 cm^{-1} mode as the *R-O* transition [144, 155]. Thus, Raman spectroscopy has the potential to determine all phase transitions in $BaZr_yTi_{1-y}O_3$ ceramics.

2.4.3 Crystal structure of $BaZr_yTi_{1-y}O_3$ at room temperature

It has been shown in Figure 2.14, that the crystal structure of $BaZr_yTi_{1-y}O_3$ at room temperature changes with Zr^{4+} concentration. It was widely accepted that undoped $BaTiO_3$ (y=0) possesses a tetragonal structure at room temperature [6]. The tetragonal structure of $BaZr_yTi_{1-y}O_3$ (y=0.025) ceramics and orthorhombic structure of $BaZr_yTi_{1-y}O_3$ (y=0.05) ceramics were suggested by Jha and Jha [137, 138]. Mahajan et al. found that $BaZr_yTi_{1-y}O_3$ (y=0.15) ceramics had a rhombohedral structure [142], whereas, the phase transition from tetragonal to orthorhombic phase was also reported in the range of y=0-0.15 [146]. Dong et al. believed that $BaZr_yTi_{1-y}O_3$ transferred from the tetragonal to orthorhombic phase in $0<y<0.06$ and further transferred to the rhombohedral phase in $0.06<y\leq0.18$ [145]. Parida et al. believed $BaZr_yTi_{1-y}O_3$ (y=0.10) had a tetragonal phase [156]. Moura et al. suggested that the $BaZr_yTi_{1-y}O_3$ transferred from orthorhombic phase (in y=0.05) to rhombohedral phase (in y=0.10 and 0.15) [157]. It has been widely accepted that $BaZr_yTi_{1-y}O_3$ becomes cubic at room temperature when $y\geq0.20$ [72, 154, 156, 158]. Thus, in the region of y=0-0.20, the identifications of phase structure were still contradictory, and the variations in the determination of the compositional induced phase

transitions could be related to the sensitivity to measured room temperature due to the curved phase boundaries (as shown in Figure 2.14).

2.4.4 Fulfilment of Vegard's law

In contrast to the Ca^{2+} substituted $BaTiO_3$ system (section 2.3.3), a better fulfilment of Vegard's law was achieved in the $BaZr_yTi_{1-y}O_3$ (y=0-1) system [159]. Chen et al. suggested the lattice parameter a increased and c decreased with the addition of Zr^{4+} due to the larger size of Zr^{4+} [160]. They also observed the lattice parameter a and c nearly reaching the same value at y=0.20, as if approaching a cubic phase [160]. As shown in Figure 2.15 (A), the relationship between lattice parameter a and Zr^{4+} content was nearly linear with slight deviation, even with $BaZr_yTi_{1-y}O_3$ transferring from the tetragonal to orthorhombic structure in y=0-0.15 [146]. Huang et al. further reported a perfectly fulfilled (correlation coefficient as 0.9988) linear relationship as a=0.0179y+0.4017 (y=0-0.10) based on the cubic structure of $BaZr_yTi_{1-y}O_3$ [161]. Furthermore, Miao et al. proposed a nonlinear relationship between unit cell volume and Zr^{4+} concentration in the range of y=0-0.35 with the assumption that $BaZr_yTi_{1-y}O_3$ ($y\neq0$) phase had a pseudo-cubic structure [144], and Pokony et al. plotted a nearly linear relationship (shown in Figure 2.15 (B)) for the dependence of unit cell volume on Zr^{4+} content in the range y=0-0.35 [110]. Therefore, previous literature suggested a good fulfilment of Vegard's law in the $BaZr_yTi_{1-y}O_3$ system, which is independent to the identified crystal structure changes. However, a well-correlated relationship between unit cell volume and Zr^{4+} concentration was not established.

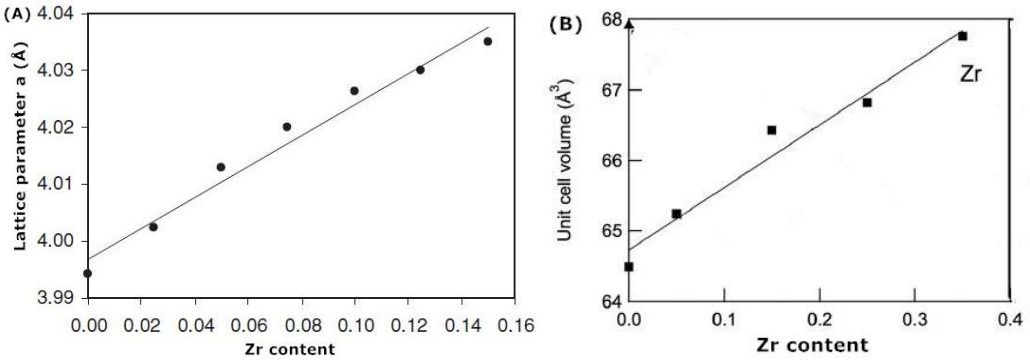

Figure 2.15. The lattice parameter *a* (A) and unit cell volume (B) as a function of Zr^{4+} content (*y* value) in $BaZr_yTi_{1-y}O_3$ (*y*=0-0.40) at room temperature [110, 146].

2.4.5 Functional properties of $BaZr_yTi_{1-y}O_3$ at room temperature

For certain $BaZr_yTi_{1-y}O_3$ ceramics, similar to $BaTiO_3$ (section 2.2.3), the dielectric properties were affected by microstructure. The larger grain size and less porous structure in $BaZr_yTi_{1-y}O_3$ ceramics contributed to higher relative permittivity (ε_r) [133, 134, 137, 138, 147, 149, 151, 162]. This was attributed to easier domain motion in larger grains and the reduction of grain boundary areas as low-permittivity regions [137, 138, 149, 151]. The increase in grain size and densification of ceramics induced a decrease in dielectric loss (*tan δ*) due to the reduction of number of defects and disorders [147, 162].

In addition, the *P-E* hysteresis loop of $BaZr_yTi_{1-y}O_3$ ceramics was also affected by grain size. The Jhas observed unsaturated *P-E* loop for low temperature sintered *y*=0.025 and 0.05 ceramics with small grains (0.62 μm and 0.39 μm) [137, 138]. The poor ferroelectric characteristics were induced by the existence of a large number of grain boundaries, which led to smaller remanent polarization (P_r<3 μC/cm^2) due to the polarization discontinuity between grain boundary and grain surface [137, 138]. Increasing sintering

temperature resulted in larger grain size (2.82 μm and 6.15 μm respectively), which enabled an easier polarization reversal in ferroelectric domains and therefore a decrease in coercive field (E_c) [137, 138]. Therefore, the larger grain size contributed to increase of P_r and decrease of E_c in the measured *P*-*E* loop. The piezoelectric properties of y=0.20 ceramics was also promoted in larger grained ceramics (~6 μm) as a result of lower electrical conductivity and sufficient polarization [162].

The effect of Zr^{4+} concentration on the functional properties of $BaZr_yTi_{1-y}O_3$ ceramics is complex, as the grain size and crystal structure change with the amount of Zr^{4+}. When increasing Zr^{4+} concentration, a decrease in grain size was reported, which was attributed to Zr^{4+} addition inhibiting grain growth in $BaZr_yTi_{1-y}O_3$ due to the slower diffusion of Zr^{4+} [142, 163, 164]. However, the increase of grain size with more Zr^{4+} addition was also reported in many studies [140, 141, 143, 165], which was caused by the presence of the $BaZrO_3$ phase enhancing the grain growth of $BaZr_yTi_{1-y}O_3$ [165]. Yu et al., on the other hand, suggested that the changes of grain size was not obviously dependent on the Zr^{4+} concentration [166].

A reduction of ε_r by increasing Zr^{4+} content was reported [132, 134, 167]. Hoshina et al. related this reduction to the decreased grain size in $BaZr_yTi_{1-y}O_3$ ceramics [134]. However, the increased ε_r with more Zr^{4+} addition was also reported in earlier studies [141-143, 145, 149, 168]. Mahajan et al. found out that $BaZr_yTi_{1-y}O_3$ (y=0.15) had a higher ε_r value (10586 at 1 kHz) than undoped $BaTiO_3$ (1675) and the increased ε_r value was caused by different crystal structures [142]. Binhayeeniyi et al. further pointed out that the Zr^{4+}

substitution expanded the unit cell of $BaZr_yTi_{1-y}O_3$, which increased net polarization and therefore a higher ε_r [168]. Huang et al. considered $BaZr_yTi_{1-y}O_3$ ($y \leq 0.20$) to have a tetragonal phase where the tetragonality decreased with increasing Zr^{4+} additions [143]. The decreasing tetragonality then induced increased formation of 90º domains to reduce the internal stress, and therefore ε_r increased [143].

The ferroelectric properties (*P*-*E* loop) of $BaZr_yTi_{1-y}O_3$ ceramics was also affected by Zr^{4+} additions. Huang et al. observed that P_r was enhanced by increasing Zr^{4+} content in $BaZr_yTi_{1-y}O_3$ ceramics (y=0-0.15), owing to larger grains (20-100 μm) in Zr^{4+}-doped ceramics [143]. However, the weakening of P_r from Zr^{4+} additions was also reported [147, 160, 163, 169]. Zhai et al. related the decrease in P_r to smaller grain size induced by Zr^{4+} additions [163]. In the range of $y \geq 0.05$, the decrease in P_r was attributed to the different ionic radii of Zr^{4+} and Ti^{4+} and the crystal structure approaching the cubic symmetry [160, 169]. Chen et al. further suggested that E_c decreased with increasing Zr^{4+} substitution due to the resultant larger grain size and easier polarization reversal process [160]. Additionally, in many previous studies, the best piezoelectric properties (d_{33}=126-208 pC/N) and highest P_r (~2.3 μC/cm^2) value were observed in $BaZr_yTi_{1-y}O_3$ (y=0.05) ceramics [141, 145, 147, 160, 168]. These enhanced responses resulted from its orthorhombic structure and its composition at the vicinity of the orthorhombic to rhombohedral phase transition boundaries at room temperature [139, 145, 168].

Therefore, the functional properties of $BaZr_yTi_{1-y}O_3$ ceramics were related to Zr^{4+} concentration, due to the corresponding variations in grain size and crystal structure, but

there was no agreed dependence of grain size to Zr^{4+} content based on previous literature.

2.5 Ca^{2+}, Zr^{4+} co-doped $BaTiO_3$ piezoelectric system

The simultaneous substitution of Ca^{2+} and Zr^{4+} into $BaTiO_3$ has been investigated by a number of researchers. The resultant (Ba,Ca)(Zr,Ti)O_3 ceramics could be formed and expressed in a number of different ways:

(1) doping Ca^{2+} (x) into $BaZr_yTi_{1-y}O_3$ at specific values of y,

(2) doping Zr^{4+} (y) into $Ba_{1-x}Ca_xTiO_3$ at specific values of x,

(3) doping Ca^{2+} (x) and Zr^{4+} (y) simultaneously with random ratios (x/y) into $BaTiO_3$ to form $(Ba_{1-x}Ca_x)(Zr_yTi_{1-y})O_3$,

(4) mixing of two $Ba_{1-x}Ca_xTiO_3$ and $BaZr_yTi_{1-y}O_3$ compositions with fixed x and y values. This is the basis of the of $0.5Ba_{0.70}Ca_{0.30}TiO_3$-0.5 $BaZr_{0.20}Ti_{0.80}O_3$, solid solution that has been shown to have promising functional properties, which in turn is a particular composition in a more general series of $zBa_{0.70}Ca_{0.30}TiO_3$-(1-z)$BaZr_{0.20}Ti_{0.80}O_3$ (zBCT-(1-z)BZT) ceramics where z varies between 0 and 1.

2.5.1 Ca^{2+}-doped $BaZr_yTi_{1-y}O_3$ (for specific values of y)

Small amounts of Ca^{2+} substitution ($0 \leq x \leq 0.20$) into $BaZr_yTi_{1-y}O_3$ (y=0.02, 0.04 and 0.05) have been widely investigated. Undoped $BaZr_yTi_{1-y}O_3$ (y=0.02, 0.04 and 0.05) ceramics

possessed orthorhombic symmetry at room temperature, which then transformed into tetragonal symmetry upon Ca^{2+} addition [170-178]. In Ca^{2+}-doped $BaZr_yTi_{1-y}O_3$ (y=0.02), the orthorhombic and tetragonal phases coexisted at room temperature for $0<x<0.03$, and a pure tetragonal phase was observed at x=0.03 [177]. However, in Ca^{2+}-doped $BaZr_{0.04}Ti_{0.96}O_3$ and $BaZr_{0.05}Ti_{0.95}O_3$, the Ca^{2+}-induced room temperature polymorphic phase transition from orthorhombic to tetragonal phase was observed at x=0.03 and 0.08, respectively [170-176]. Therefore, Zr^{4+} addition (y=0.02-0.05) stabilised the orthorhombic symmetry at room temperature, whereas Ca^{2+} addition unstablised the orthorhombic symmetry in doped $BaTiO_3$.

The orthorhombic-to-tetragonal phase transition temperature (T_{O-T}) was shown to decrease with Ca^{2+} addition, whereas Ca^{2+} addition only induced slight variations in the Curie temperature (T_C) [170-178]. The phase diagram of $Ba_{1-x}Ca_xZr_{0.05}Ti_{0.95}O_3$ (x=0-0.15) is shown in Figure 2.16 (A), where the phase boundary between the rhombohedral and orthorhombic phases (T_{R-O}) also shown to decrease with the introduction of Ca^{2+} [173, 178]. Therefore, Ca^{2+} substitution shifted the orthorhombic phase to lower temperatures without changing its temperature range [173, 178]. This Ca^{2+}-induced phase transition behaviour in Ca^{2+}-doped $BaZr_yTi_{1-y}O_3$ are similar to those described for Ca^{2+}-doped $BaTiO_3$ (section 2.3.4).

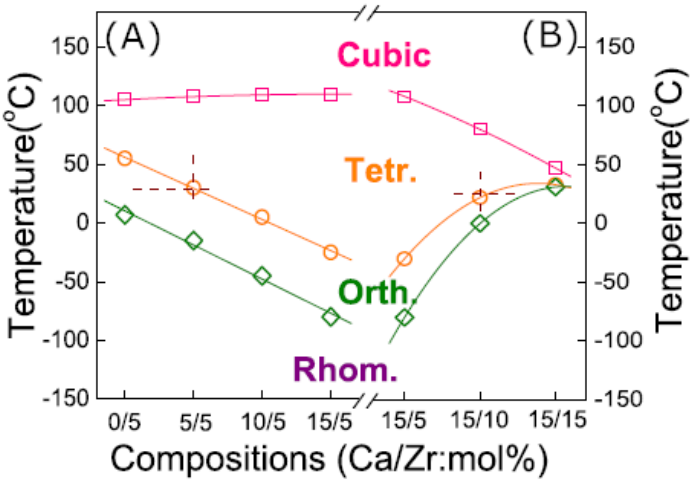

Figure 2.16. Phase diagram of (A) $Ba_{1-x}Ca_xZr_{0.05}Ti_{0.95}O_3$ (x=0-0.15) and (B) $Ba_{0.85}Ca_{0.15}Zr_yTi_{1-y}O_3$ (y=0.05-0.15) [173, 178].

Li et al. extended the compositional range for Ca^{2+}dopants to x=0.40. They reported the solubility limit for Ca^{2+} in $Ba_{1-x}Ca_xZr_{0.05}Ti_{0.95}O_3$ was 30 mol. % based on the appearance of secondary $CaTiO_3$ phase when $x \geq 0.30$ [172]. When this solubility limit was exceeded, a rapid drop in T_C and DPT behaviour was observed [172]. DPT behaviour was also observed in Ca^{2+}-doped $BaZr_{0.04}Ti_{0.96}O_3$ ($x \geq 0.06$) [170].

It is noticeable that for each Ca^{2+}-doped $BaZr_yTi_{1-y}O_3$ (y=0.02, 0.04 and 0.05) system, the coexistence of the orthorhombic and tetragonal phases at room temperature enhanced the dielectric and piezoelectric properties due to easier polarization rotation under the application of an external electric field [170, 171, 173-175, 177]. Values of ε_{rmax}=12716 in $Ba_{0.97}Ca_{0.03}Zr_{0.04}Ti_{0.96}O_3$ and ε_r=2320 in $Ba_{0.92}Ca_{0.08}Zr_{0.05}Ti_{0.95}O_3$ have been reported [170, 173, 175]. The highest piezoelectric properties were reported as d_{33}=365-392 pC/N and k_p=0.441-0.485 (in x=0.01, y=0.02; x=0.03, y=0.04; x=0.08, y=0.05) [170, 171, 173, 177]. These properties were strongly temperature dependent and dramatic decreases occurred near T_C [171, 174, 175].

Since Liu and Ren reported the comparable piezoelectric properties to PZT (d_{33}=620 pC/N) in lead-free $0.5Ba_{0.70}Ca_{0.30}TiO_3$-$0.5BaZr_{0.20}Ti_{0.80}O_3$ ($Ba_{0.85}Ca_{0.15}Zr_{0.10}Ti_{0.90}O_3$) ceramics [28], there has been much more research focusing on Ca^{2+}-doped $BaZr_{0.10}Ti_{0.90}O_3$ ceramics. $BaZr_{0.10}Ti_{0.90}O_3$ is rhombohedral at room temperature, however there was a debate on the compositional induced phase transition behaviour by Ca^{2+} addition in this system. Ye et al. claimed that $Ba_{1-x}Ca_xZr_{0.10}Ti_{0.90}O_3$ (x=0-0.20) only went through one phase transition from rhombohedral to tetragonal phase at room temperature, where the coexistence of these two phases occurred at $0.10<x<0.20$ [179]. The highest relative permittivity (ε_r=5800) was observed in x=0.15, which was ascribed to the existence of an MPB between the rhombohedral and tetragonal phases enhancing the mobility of domains and domain walls [179]. The enhanced ferroelectric properties (P_r=6.2 μC/cm^2, E_c=2.2 kV/cm) and largest piezoelectric response (d_{33}=350 pC/N, k_p=0.33) were also obtained in this composition (x=0.15), which displayed a homogeneous microstructure with large grain size (~11 μm) [179].

However, successive polymorphic phase transitions from rhombohedral to orthorhombic to the tetragonal phase in $Ba_{1-x}Ca_xZr_{0.10}Ti_{0.90}O_3$ (x=0-0.25) have also been reported [178, 180-183]. Li et al. suggested the coexistence of rhombohedral and orthorhombic phases at room temperature when x=0.14-0.18, and they observed the highest dielectric properties (ε_r=4800), ferroelectric properties (P_r=9.0 μC/cm^2, E_c=5.0 kV/cm) and piezoelectric properties (d_{33}=328 pC/N, k_p=0.376) at x=0.16 [182]. Tian et al. detected the coexistence of rhombohedral and tetragonal phases in $Ba_{1-x}Ca_xZr_{0.10}Ti_{0.90}O_3$ (x=0.15),

however, the rhombohedral phase was later on clarified to be asymmetric orthorhombic phase, which was evolved from orthorhombic phase in $Ba_{1-x}Ca_xZr_{0.10}Ti_{0.90}O_3$ (x=0.05) but with lower symmetry, and which was difficult to be distinguished from rhombohedral phase and existed as a narrow region bridging rhombohedral and tetragonal phases [178, 181]. The best functional properties were attained when x=0.15, where ε_r=4821, d_{33}=572 pC/N and k_p=0.57 [178, 181]. As shown in Figure 2.17, Fu et al. considered the phase transition from orthorhombic to tetragonal phase occurring at x=0.11-0.13 at room temperature, and T_{R-O} and T_{O-T} decreased with Ca^{2+} addition while T_C was nearly constant [180, 183]. This similarity to the $Ba_{1-x}Ca_xTiO_3$ system was attributed to the Ca^{2+} off-centred displacement stabilizing the tetragonality of adjacent Ti^{4+} [94, 117, 180, 183]. Large piezoelectric response have been observed in all $Ba_{1-x}Ca_xZr_{0.10}Ti_{0.90}O_3$ (x=0.10-0.18) ceramics, as a result of the ferroelectric phase transition temperatures (T_{R-O} and T_{O-T}) lying in the vicinity of room temperature, with a minimum energy difference between the ferroelectric phases [180, 183]. The solubility limit of Ca^{2+} in $Ba_{1-x}Ca_xZr_{0.10}Ti_{0.90}O_3$ was found to be ~18 mol. %, beyond which a secondary $CaTiO_3$-based phase started to present [180, 181, 183].

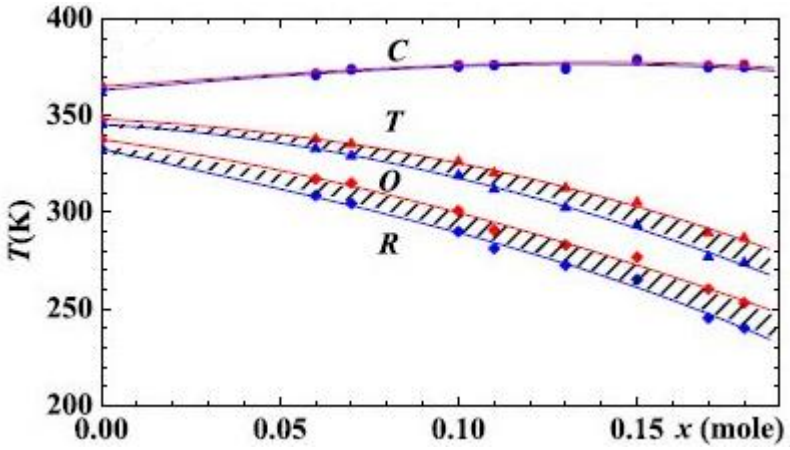

Figure 2.17. Phase diagram of $Ba_{1-x}Ca_xZr_{0.10}Ti_{0.90}O_3$ (x=0-0.18), the red and blue dots were measured upon heating and cooling respectively [180, 183].

In $Ba_{1-x}Ca_xZr_{0.10}Ti_{0.90}O_3$, a slight DPT behaviour was also observed with broad ε_r-T peak due to Ca^{2+} addition (x>0.05) [179, 181, 182]. Ye et al. further reported the relaxor behaviour in $Ba_{1-x}Ca_xZr_{0.10}Ti_{0.90}O_3$ (x=0.25): Ca^{2+} substitution induced large distortion in crystal due to large ionic radii difference between Ca^{2+} and Ba^{2+}, which hindered long-range dipole alignment and formed polar nanoregions and therefore enhanced relaxor behaviour [179].

In summary, the introduction of Ca^{2+} into $BaZr_yTi_{1-y}O_3$ (y=0.02, 0.04, 0.05 and 0.10) yielded successive phase transitions at room temperature, contributing to enhancement of functional properties. The Ca^{2+} addition also induced distortion in long-range order, resulting in DPT and even relaxor behaviour.

2.5.2 Zr^{4+}-doped $Ba_{1-x}Ca_{1-x}TiO_3$ (for specific values of x)

Zr^{4+} substitution into the $Ba_{1-x}Ca_xTiO_3$ system has also been studied. Zhang et al. investigated the Zr^{4+}-doped $Ba_{0.95}Ca_{0.05}TiO_3$ (y=0-0.15) and considered the an

orthorhombic to pseudo-cubic phase transformation at room temperature at y=0.05-0.07 [184]. They ascribed this phase transition to the distortion of the crystal structure induced by the existence of multiple ions on both the A- and B-sites [184]. In $Ba_{0.95}Ca_{0.05}Zr_yTi_{1-y}O_3$ system, the phase transition behaviour was analogous to $BaZr_yTi_{1-y}O_3$, with decreased T_C, DPT behaviour (identified by broad ε_r-T peaks) as well as pinched phase transition temperatures, all induced by the Zr^{4+} addition [184]. Good functional properties (ε_r=2070, d_{33}=338 pC/N and k_p=0.36) were obtained in $Ba_{0.95}Ca_{0.05}Zr_yTi_{1-y}O_3$ (y=0.04), which originated from its T_{O-T} lying around room temperature [184]. The highest relative permittivity at room temperature (ε_r=2838) was found in $Ba_{0.95}Ca_{0.05}Zr_yTi_{1-y}O_3$ (y=0.15), as a result of this being close to its Curie temperature [184].

A detailed structural analysis of $Ba_{0.90}Ca_{0.10}Zr_yTi_{1-y}O_3$ ceramics was carried out by Sindhu et al which revealed that the rhombohedral (*R3m*) and tetragonal (*P4mm*) phase coexisted for $0.05<y<0.10$, which was considered as the location of MPB in this system [185]. They also found a decrease in T_C accompanied by DPT and relaxor behaviour caused by the Zr^{4+} addition believed to result from structural disorders due to the presence of nonpolar [ZrO_6] clusters destroying long-range-ordered polar [TiO_6] clusters [185]. The Zr^{4+} addition contributed to a slimmer P-E loop with reduced P_r and E_c [185].

Figure 2.16 (B) shows that $Ba_{0.85}Ca_{0.15}Zr_yTi_{1-y}O_3$ (y=0.05-0.15) transferred from tetragonal to orthorhombic to rhombohedral structure at room temperature. Analogous to the $BaZr_yTi_{1-y}O_3$ system, Zr^{4+} addition yielded convergence of the rhombohedral, orthorhombic, tetragonal and cubic phases and the phase transitions pinched at y=0.15

[178]. The highest piezoelectric response was also observed in the $Ba_{0.85}Ca_{0.15}Zr_{0.10}Ti_{0.90}O_3$ composition, as its T_{O-T} is close to room temperature [178].

In summary, the substitution of Zr^{4+} in $Ba_{1-x}Ca_xTiO_3$ (x=0.05-0.15, y=0-0.15) system induced phase transformation at room temperature. However, it is unclear whether these phase transitions are polymorphic or morphotropic in nature. The Zr^{4+}-induced changes in dielectric properties (*e.g.* decreased T_C, pinched phase transitions, DPT and relaxor behaviour), reduction of P_r and E_c, enhanced piezoelectric properties in phase boundaries compositions, were similar to Zr^{4+}-doped $BaTiO_3$ ceramics (sections 2.4.2 and 2.4.5).

2.5.3 Ca^{2+}, Zr^{4+} co-doped $BaTiO_3$ ($(Ba_{1-x}Ca_x)(Zr_yTi_{1-y})O_3$) with random *x*/*y* ratios

Ravez and Simon have investigated more general $(Ba_{1-x}Ca_x)(Zr_yTi_{1-y})O_3$ compositions part of the $BaTiO_3$-$BaZrO_3$-$CaTiO_3$ ternary system, and produced a phase diagram as shown in Figure 2.18 [186, 187]. The compositions in Zone I (close to the $Ba_{1-x}Ca_xTiO_3$ solid solution) were normal ferroelectrics with three dielectric anomalies observed upon heating, representing phase transitions from rhombohedral-orthorhombic-tetragonal-cubic. These phase transitions were similar to the reviewed Zr^{4+} doped or undoped $Ba_{1-x}Ca_xTiO_3$ and Ca^{2+} doped or undoped $BaZr_yTi_{1-y}O_3$ ($0\leq x\leq 0.15$, $0\leq y\leq 0.15$) systems in sections 2.3.4, 2.4.2, 2.5.1 and 2.5.2. In Zone II, compositions were close to the $BaZr_yTi_{1-y}O_3$ (y=0.12-0.27) solid solution, possessing only one dielectric anomaly at T_C with DPT behaviour but not of relaxor type, which was similar to the $BaZr_yTi_{1-y}O_3$

($0.15 \leq y \leq 0.20$) solid solution, as described in section 2.4.2. However, there was ferroelectric relaxor behaviour observed in compositions close to the $BaZr_yTi_{1-y}O_3$ (y=0.275-0.42) solid solution (Zone III), similar to the observed relaxor behaviour in $BaZr_yTi_{1-y}O_3$ ($y \geq 0.20$, section 2.4.2). In region B, as the wide boundary between Zones II and III, the composition behaved as a ferroelectric relaxor at T_m (temperature for ε_{rmax}) which transformed to normal ferroelectric behaviour at lower temperature [186, 187]. They further pointed out that the relaxor behaviour started to appear when y>0.15, where both increasing Ca^{2+} and Zr^{4+} contents (x and y values) yielded an increase in relaxor behaviour due to strong compositional heterogeneity [186]. This stronger heterogeneity from the co-doped system compared to the individually doped $BaZr_yTi_{1-y}O_3$ system reduced the Zr^{4+} concentration for the onset of relaxor behaviour from ~0.20 to ~0.12. Tang et al. reported that the mechanical stress in grains also contributed to the broad ε_r-T peak in $(Ba_{0.90}Ca_{0.10})(Zr_{0.25}Ti_{0.75})O_3$ ceramics [188]. High internal stresses in fine-grained ceramics induced by the presence of more phase boundary regions, which might enhance DPT and even relaxor behaviour [188]. This is similar to the observed DPT in fine-grained $BaZr_yTi_{1-y}O_3$ (y=0.05 and 0.10) ceramics [151]. The investigation of the crystal structure of $(Ba_{0.92}Ca_{0.08})(Zr_{0.25}Ti_{0.75})O_3$ ceramics indicated that there was only one apparent phase transition from rhombohedral to cubic symmetry at around 208 K whereas no symmetry changes were observed during the relaxor ferroelectric to paraelectric phase transition [186, 187]. In contrast, Zeng et al. reported the phase transition in $(Ba_{0.92}Ca_{0.08})(Zr_{0.26}Ti_{0.74})O_3$ was from tetragonal to cubic phase at 200-250 K, based on

Raman spectroscopy measurements [189]. Therefore, for $(Ba_{1-x}Ca_x)(Zr_yTi_{1-y})O_3$ ceramics with high Zr^{4+} content ($y \geq 0.25$), the variations in Ca^{2+} and/or Zr^{4+} concentrations give rise to changes in phase structure as well as changes in ferroelectric characteristics between classical ferroelectrics and ferroelectric relaxors.

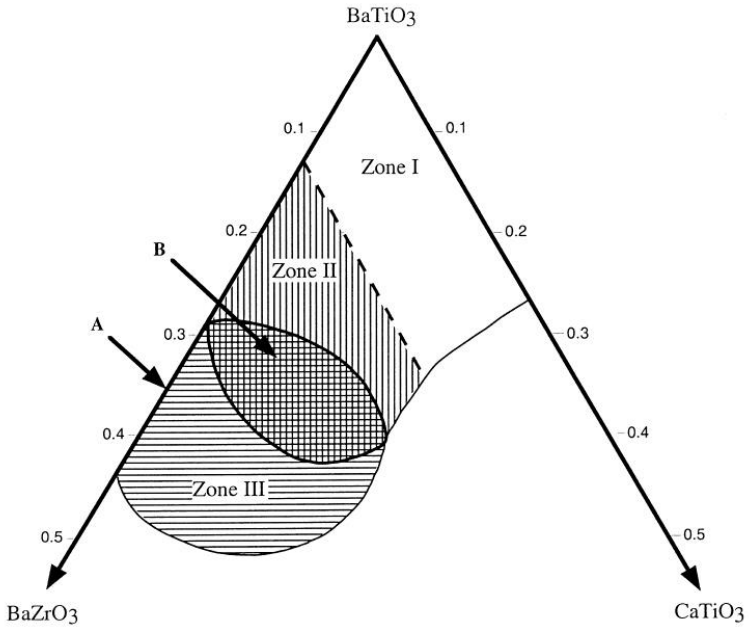

Figure 2.18. Schematic representation of $BaTiO_3$-$BaZrO_3$-$CaTiO_3$ ternary diagram [186, 187].

A series of $(Ba_{1-x}Ca_x)(Zr_yTi_{1-y})O_3$ ceramics with x/y=3:2 ($0 \leq x \leq 0.2625$, $0 \leq y \leq 0.175$) was investigated by Liu et al, where they found the solubility limit of Ca^{2+} for this system was around 19 mol.% [190]. Within the solubility region, they observed that the crystal structure at room temperature transferred from a tetragonal to a rhombohedral phase with increasing Ca^{2+} and Zr^{4+} contents. The resultant phase boundary was then considered as an MPB between tetragonal and rhombohedral phases, lying in the composition range $0.1125<x<0.15$ and $0.075<y<0.10$ [190]. Those compositions close to the MPB exhibited outstanding functional properties, with the highest properties obtained in

$(Ba_{0.89}Ca_{0.11})(Zr_{0.08}Ti_{0.92})O_3$ composition, with ε_r=2200, d_{33}=420 pC/N and k_p=0.57 [190]. However, Tian et al. questioned whether a true MPB was possible in the $(Ba_{1-x}Ca_x)(Zr_yTi_{1-y})O_3$ system by adjusting the Ca^{2+} and/or Zr^{4+} contents due to the polymorphic phase transition nature of $BaTiO_3$ [178]. They ascribed the observed large piezoelectric response in $(Ba_{0.85}Ca_{0.15})(Zr_{0.10}Ti_{0.90})O_3$ to easier domain wall motion and lattice strain in a softened lattice with pinched orthorhombic symmetry at room temperature [178, 181].

Therefore, there was no general agreement achieved on the compositional-induced phase transitions in the $(Ba_{1-x}Ca_x)(Zr_yTi_{1-y})O_3$ system. The multiple variations in Ca^{2+} and Zr^{4+} concentrations (x and y) make it very difficult to identify the crystal structure and optimise the functional properties for all $(Ba_{1-x}Ca_x)(Zr_yTi_{1-y})O_3$ compositions, and making it hard to find relationships between crystal structure and functional properties in this system. Therefore, many investigations have focused on considering $(Ba_{1-x}Ca_x)(Zr_yTi_{1-y})O_3$ as a pseudo-binary system between $(Ba_{0.70}Ca_{0.30})TiO_3$ and $Ba(Zr_{0.10}Ti_{0.90})O_3$ with single variation (z) as considered in the next section.

2.5.4 $zBa_{0.70}Ca_{0.30}TiO_3$-(1-z)$BaZr_{0.20}Ti_{0.80}O_3$ (zBCT-(1-z)BZT) system

2.5.4.1 Initial phase diagram

As mentioned in section 2.1.2, Liu and Ren firstly reported zBCT-(1-z)BZT as a promising pseudo-binary lead-free system in 2009, because of its high piezoelectric

response (d_{33}=620 pC/N) at z=0.5 which was attributed to the existence of an MPB stemming from a tricritical point (z~0.32, T=330 K) and separating rhombohedral and tetragonal phases in the phase diagram (shown in Figure 2.6). These characteristics were analogous to the PZT system and make it a promising lead-free system [28].

The tricritical point (TCP) was further characterised based on the highest ε_{rmax} at z=0.3 due to the absence of an energy barrier between the rhombohedral, tetragonal and cubic phases [28]. The MPB composition at room temperature (z=0.50) deviated a little from the TCP (z=0.32), resulting in a very weak polarization anisotropy and low energy barrier for polarization rotation between $<001>_T$ and $<111>_R$ states, and therefore yielding the highest dielectric and piezoelectric response in this composition [28]. Damjanovic further deduced that the enhanced dielectric and piezoelectric properties for z=0.5 originated from the two-dimensional flattening of the energy profile: the polarization rotation at the MPB and the polarization extension due to the proximity of *R*-*C* and *T*-*C* Curie temperatures [191].

X-ray diffraction analysis has been used to confirm the coexistence of the rhombohedral and tetragonal symmetry in z=0.50 at room temperature as the MPB composition and the coexistence of these two ferroelectric phases and paraelectric cubic phase in z=0.32 near 65 °C as the TCP composition [192, 193]. Benabdallah et al. ascribed the high piezoelectric properties in these compositions to their high polarization flexibility and the weak preferential polarization orientations in the TCP and MPB compositions [192].

Further investigations have focussed on the MPB compositions (z=0.40-0.60) to reveal other potential contributions to the anomalies observed. Elastic softening of the lattice has been considered as another contributory factor to the high piezoelectric response at z=0.50, which was evidenced by its large unipolar electrostrain (0.06%) [194]. Neutron scattering analysis for the z=0.50 composition indicated that random local polarization and strain, resulting from size mismatch and difference in the average tilt angle between [TiO_6] and [ZrO_6] octahedra, were also responsible for the high piezoelectric properties in the MPB region [195].

Microstructural analyses of compositions around the MPB were reported by Gao et al. who observed typical rhombohedral and tetragonal domain structures for z=0.40 and 0.60 respectively, whereas there was a more complex domain hierarchy for the z=0.50 composition comprising micron-sized domain lamellas and miniaturized nanodomains on lamellae at room temperature [196-199]. The presence of miniaturized nanodomain structures at the MPB have been seen in lead-based piezoelectric system and are thought to be associated with a drastic reduction of domain wall energy and the resultant enhanced properties [196, 197]. They further concluded that domain wall motion (*i.e*. extrinsic piezoelectric response) at the MPB composition was a major contribution to the high piezoelectric response [198]. Tutucu et al. reported that the higher 90º domain wall motion in compositions with lower tetragonality (z=0.60) when approaching the MPB from the $Ba_{0.70}Ca_{0.30}TiO_3$-rich end (z=0.90) also promoted the dielectric and piezoelectric properties near the MPB [200].

2.5.4.2 Revised phase diagram

With the development of the structural studies in this lead-free system, there was a debate regarding the crystal structures of the MPB region. Three possibilities were proposed: (1) the MPB was a single phase boundary separating the rhombohedral and tetragonal phases; (2) the MPB was a phase coexistence region with rhombohedral and tetragonal phases in a relative narrow compositional range; (3) the MPB region was actually a separate phase with orthorhombic (*Amm2*) symmetry bridging the polymorphic phase transition between the rhombohedral and tetragonal phases.

At temperatures lower than the reported *R*-*T* and *T*-*C* transitions for the z=0.50 composition, Damjanovic et al. detected two additional anomalies in the dielectric loss around -60 ºC and just below room temperature [28, 201]. They proposed that the first anomaly (at -60 ºC) was attributed to a phase transition from a low temperature phase to the rhombohedral phase reported by Liu and Ren, and the other anomaly was caused by a reappearance of the low temperature phase (<-60 ºC) mixing with tetragonal phase, or appearance of a new lower symmetry phase [28, 201]. Haugen et al. also detected a phase transition at -60 ºC via high energy X-ray diffraction, and considered it to be a phase transformation from a single rhombohedral *R3m* phase to a mixed phase region with tetragonal *P4mm* and rhombohedral *R3m* symmetry. In contrast, a phase change from coexisted phases to single tetragonal phase was observed just above room temperature [201, 202].

Ehmke et al. reported a further study of materials with compositions adjacent to the MPB (z=0.40-0.50) using in situ high energy X-ray diffraction and dielectric permittivity measurements and confirmed the compositional coexistence of rhombohedral and tetragonal phases covering the MPB and coexistence of rhombohedral and tetragonal and cubic phases in the vicinity of the TCP, as shown in Figure 2.19 [203].

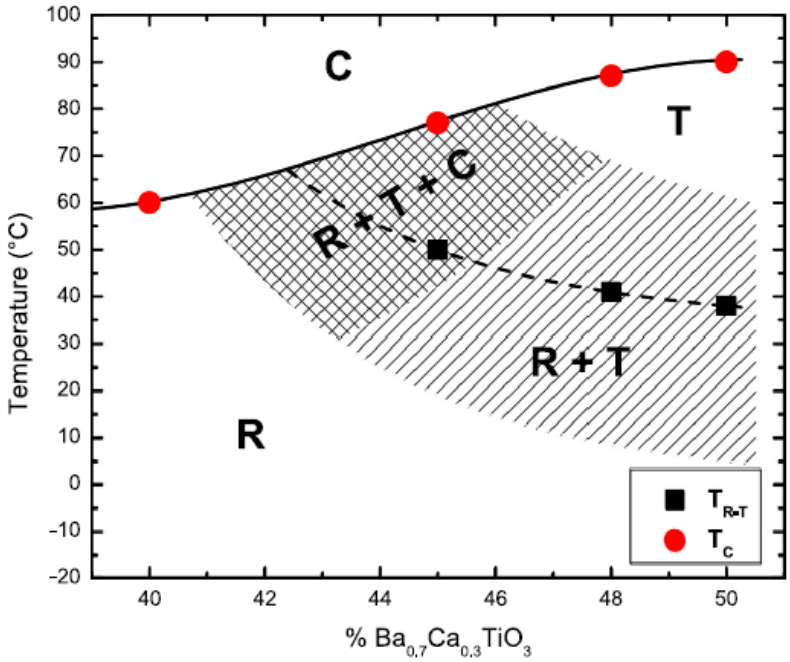

Figure 2.19. A detailed phase diagram of $zBa_{0.70}Ca_{0.30}TiO_3$-(1-z)$BaZr_{0.20}Ti_{0.80}O_3$ close to MPB region [203].

Subsequently, as shown in Figure 2.20, a revised phase diagram of the zBCT-(1-z)BZT system showing the existence of an orthorhombic phase was published by Keeble et al in 2013 [204]. Using high resolution synchrotron experiments they confirmed the presence of a phase with orthorhombic (*Amm2*) symmetry for the z=0.50 composition at 260-300 K, based on the splitting of the (111) peak consistent with $\sqrt{2}a^*\sqrt{2}a^*a$ orthorhombic supercell. The Rietveld refinements of temperature dependent diffraction patterns of z=0.40 and 0.50 compositions indicated that samples went through phase transitions from

rhombohedral (*R3m*) to orthorhombic (*Amm2*) to tetragonal (*P4mm*) and finally to cubic (*Pm3m*) upon heating [204]. They ascribed the absence of the orthorhombic phase in previous studies to a small dielectric anomaly at the *O*-*T* transition and its high instability gradient [204].

It was noticeable that both the TCP in the initial phase diagram (Figure 2.6) and the phase convergence region in this revised phase diagram (Figure 2.20) occurred at $z \approx 0.32$, where the Zr^{4+} concentration was around 0.136 (y value), analogous to the pinching effect at $y=0.15$ observed in the $BaZr_yTi_{1-y}O_3$ system (section 2.4.2). Keeble et al. further proposed that the shift of the pinching effect to lower Zr^{4+} contents in the zBCT-(1-z)BZT system compared to the $BaZr_yTi_{1-y}O_3$ system, was probably a result of the reduced stabilities of the intermediate orthorhombic phase by Ca^{2+} substitution [204].

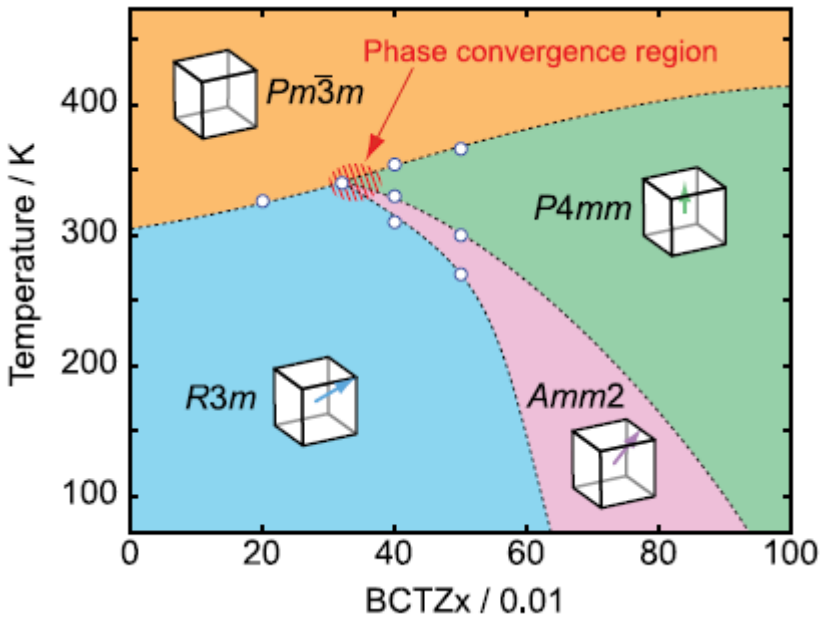

Figure 2.20 Revised phase diagram of $zBa_{0.70}Ca_{0.30}TiO_3$-(1-z)$BaZr_{0.20}Ti_{0.80}O_3$ system with orthorhombic (*Amm2*) symmetry [204].

The existence of the orthorhombic phase has been confirmed via dynamic mechanical analysis [205], and further X-ray diffraction and dielectric permittivity measurements [208]. The latter study identified the symmetry of the orthorhombic phase (*Amm2*) by comparison to $BaTiO_3$, and proposed that the large piezoelectric response observed at the MPB in other studies actually originated from easier polarization rotation and larger lattice softening at the *O-T* transition rather than *R-O* transition [206]. This is similar to the anomalous properties observed at the polymorphic *O-T* phase transition around room temperature for the $BaTiO_3$ and co-doped $Ba_{1-x}Ca_xZr_yTi_{1-y}O_3$ systems (sections 2.2.1 and 2.5.1-2.5.3).

Despite these many confirmations of the orthorhombic symmetry, there still remains some controversy of its existence, and of other phases in the zBCT-(1-z)BZT system. For example, Gao et al. only observed the coexistence of tetragonal (*P4mm*) and rhombohedral (*R3m*) symmetry in domains imaged by convergent beam electron diffraction and ruled out the existence of local orthorhombic symmetry for the z=0.50 composition [197]. Also, Puli et al. detected the coexistence of rhombohedral and tetragonal phases in z=0.10-0.20 ceramics at room temperature via X-ray diffraction and Raman spectroscopy [207-209]. Thus a systematic study of the whole phase system would be beneficial.

2.5.4.3 Factors affecting the functional properties of the z=0.50 (MPB) composition

Since the first report on comparable piezoelectric properties (d_{33}=620 pC/N) of lead-free zBCT-(1-z)BZT (z=0.50) ceramics to lead-based ceramics [28], many investigations on optimising its functional properties have been carried out. Functional properties have been shown to be very sensitive to fabrication procedure, similar to its $BaTiO_3$ parent as discussed in section 2.2.3.

Hao et al. fabricated z=0.50 ceramics by spark plasma sintering, two-step sintering and conventional sintering, reporting that different sintering methods yielded ceramics with different grain sizes. Good functional properties (d_{33}>470 pC/N, k_p>0.48) were only achieved using conventional sintering resulting in grain size ≥10 μm [210]. Hot-pressing was reported to improve densification and weaken the DPT behaviour of the sintered ceramics [211], whereas sol-gel synthesized ceramics with grain size of 10-20 μm and d_{33}≈490 pC/N exhibited lower T_C≈72 ºC compared to the more usual reported value (90 ºC), which was ascribed to an increase of internal stress after high temperature sintering (1550 ºC) [212]. Castkova et al. investigated the fabrication of z=0.50 ceramics via various wet chemical methods, and reported the best piezoelectric properties (d_{33}≈410 pC/N) in sol-gel derived ceramics with sintered grain size of around 36 μm [213]. Those reports indicate that the fabrication method, and in particular the resulting grain size, has a primary impact on the functional properties.

In general, smaller grain sizes lead to pinning of domain walls at grain boundaries and a reduced number of grains contributing polarization reversal, whereas larger grains facilitate domain wall motion with a reduced grain boundary density. It has been suggested that grain size values >10 μm are required for z=0.50 ceramics [210, 214]. Bharathi et al. further proposed that the relationship between grain size and domain size for z=0.50 ceramics was similar to that for $BaTiO_3$ ceramics: larger grain size resulted in larger domain size and the possibility to have a greater number of domain (wall) motions [215]. Therefore, grain size was a predominant factor on the resulting electrical properties.

Another possible effect on grain size and the corresponding electrical properties is the heat treatment temperatures used in the calcination and sintering processes. Temperatures should be high enough to complete the necessary chemical reactions and yield pure perovskite structures with the Ca^{2+} and Zr^{4+} fully homogeneous in the $BaTiO_3$ structure. Secondary phases have been observed in ceramics sintered below 1500 ºC [216, 217]. Both calcination and sintering temperature play significant roles in the microstructural development of ceramics and, therefore, the resultant dielectric and piezoelectric properties. Increasing calcination temperature contributes to increased chemical homogeneity throughout the grain and grain boundaries in sintered ceramics, where the atomic arrangement is more similar to that in the grains (*i.e.* good continuity of strain and domains across grain boundary), improving the resultant piezoelectric response. On the other hand, sintering temperature has a large effect on the final grain size [217]. Higher sintering temperatures result in ceramics with larger grain size as well as denser

microstructure, which then enhance the dielectric properties by decreasing the non-ferroelectric grain boundary layer [214, 215, 218, 219]. The enhancement of ferroelectric properties has been observed by increasing sintering temperature, which was originated from increasing number of grains contributing towards polarization reversal in larger grains [210, 214, 215, 218, 219]. The increase of remanent polarization (P_r) was accompanied by a reduction in coercive field (E_c) with increasing sintering temperature, as a result of easier domain switching during the polarization reversal process [214, 218]. Thus, heat treatment (calcination temperature and sintering temperature) procedure was another major effect on grain size and the resultant functional properties. A summary of the optimised properties reported in previous studies is listed in Table 2.3.

Table 2.3. Functional properties of zBCT-(1-z)BZT (z=0.50) ceramics in previous studies: T_{cal} and T_s referred to calcination temperature and sintering temperature respectively.

T_{cal} (°C)	T_s (°C)	d_{33} (pC/N)	k_p	P_r (μC/cm^2)	E_c (kV/cm)	ε_r	Average *GS* (μm)	Ref.
N/A	1450	563	N/A	9.62	2.2	2740 (10 kHz)	30	[215]
1300	1400	281	N/A	3.18	2.3	3900 (1 kHz)	7.76	[219]
N/A	1550	617	0.54	10.7	1.85	5067 (1 kHz)	~10	[214]
N/A	1440	422	0.49	~7.0	~2.5	~3000	~20	[218]
1300	1540	650	0.53	11.69	1.9	4500	~16	[217]

As mentioned in section 2.2.3, the phase structure and phase transition behaviour of $BaTiO_3$ ceramics varied in different studies, this phenomenon was also observed for z=0.50 ceramics. Wu et al. reported that increasing sintering temperature to above 1350 °C induced a transition from rhombohedral to tetragonal phase at room temperature,

where ceramics sintered at lower temperature (1300-1350 °C) only possessed one *R-C* phase transition whereas those sintered at higher temperature had a two-step transition (*R-T-C*) [218]. They also observed that T_C increased firstly with increasing sintering temperature from 1300 °C to 1410°C and then decreased when further increasing sintering temperature to 1500 °C [218]. There have also been other observations of reduced T_C (~85 °C) in larger grain size (20-32 μm) ceramics, which were attributed to the materials having denser microstructure and/or cell distortions [210, 214, 215]. Furthermore, DPT behaviour has also been observed in z=0.50 ceramics, reportedly caused by compositional fluctuations and structural disordering, as well as internal stresses in the grains [216, 220, 221]. Enhanced DPT behaviour was observed in fine-grained ceramics (~0.5 μm), as a result of weakening of long-range ferroelectric interactions, higher space charge effect in more porous structure and higher inner stress [210, 214, 215]. Hao et al. even detected ferroelectric relaxor behaviour in fine-grained z=0.50 ceramics (0.4 μm), which was confirmed by much slimmer and narrower *P-E* loop with lower P_r (<9 μC/cm^2) than coarse-grained ceramics at room temperature [210]. On the other hand, Mishra et al. found out that increasing sintering temperature from 1300 °C to 1400 °C yielded stronger DPT behaviour because of more compositional fluctuations from the competition between Zr^{4+} and Ti^{4+} at high sintering temperature [219]. Conclusively, the phase transition behaviour of z=0.50 ceramics was determined by local symmetry and microstructure, which could be affected by heat treatment conditions.

Thus, in summary, even though z=0.50 ceramics possess the best functional properties in

the zBCT-(1-z)BZT system, the optimum synthesis and fabrication conditions are far from clear. Previous studies have not clarified the debate on composition-induced and temperature-induced phase transition behaviour, and there is a lack of studies on crystal structure and functional property relationships across the compositional range.

2.6 Aims and objectives

The overall aim of this project is to carry out systematic and consecutive studies in the lead-free zBCT-(1-z)BZT piezoelectric system, based on initial investigations of its end member systems (*i.e.* $Ba_{1-x}Ca_xTiO_3$ and $BaZr_yTi_{1-y}O_3$). These include the fabrication of ceramics with different compositions and the characterisation of the resultant structural and functional properties. The detailed objectives can be summarised as follows:

- To optimise fabrication procedure of $Ba_{0.70}Ca_{0.30}TiO_3$ and $BaZr_{0.20}Ti_{0.80}O_3$ bulk ceramics as end members of the zBCT-(1-z)BZT system.

- To investigate reaction and diffusion mechanisms of Ca^{2+} into $BaTiO_3$ to form $(Ba,Ca)TiO_3$ compounds.

- To investigate the effect of Ca^{2+} or Zr^{4+} addition into $BaTiO_3$ on the crystal structure, microstructure, functional properties and phase transition behaviour.

- To fabricate zBCT-(1-z)BZT (z=0-1) bulk ceramics from preformed $Ba_{0.70}Ca_{0.30}TiO_3$ and $BaZr_{0.20}Ti_{0.80}O_3$ ceramic powders.

- To investigate the effect of sintering temperature and compositional variations (z

value) on phase compositions, microstructure and functional properties of zBCT-(1-z)BZT (z=0-1) bulk ceramics and elucidate the linkage between structural and functional properties.

- To apply Raman spectroscopy to determine structural phase diagrams of the $Ba_{1-x}Ca_xTiO_3$ (x=0-0.30), $BaZr_yTi_{1-y}O_3$ (y=0-0.30) and zBCT-(1-z)BZT (z=0-1) piezoelectric systems and clarify the debate on the crystal structure of the morphotropic phase boundary (MPB) region in the zBCT-(1-z)BZT (z=0-1) system.

- To determine the phase transitions of bulk $Ba_{1-x}Ca_xTiO_3$ (x=0-0.30), $BaZr_yTi_{1-y}O_3$ (y=0-0.30) and zBCT-(1-z)BZT (z=0-1) ceramics from temperature dependent dielectric and ferroelectric properties.

Chapter 3 Experimental Methods

The experimental methodology of this project can be broadly divided into three parts: fabrication of piezoceramics, characterisation of structural and functional properties of ceramics at room temperature, and finally determination of phase transition behaviour of ceramics by applying temperature dependent measurements. Three piezoceramic systems were investigated in this project: $Ba_{1-x}Ca_xTiO_3$, $BaZr_yTi_{1-y}O_3$ and $z(Ba_{0.70}Ca_{0.30})TiO_3$-$(1-z)Ba(Zr_{0.20}Ti_{0.80})O_3$ (zBCT-(1-z)BZT).

3.1 Fabrication of piezoceramics

In this project, piezoceramics were generally fabricated using a conventional solid-state method. There were two fabrication methods for $Ba_{0.70}Ca_{0.30}TiO_3$, one for $BaZr_yTi_{1-y}O_3$ (y=0-0.30, with 0.05 step) and one for $z(Ba_{0.70}Ca_{0.30})TiO_3$-$(1-z)Ba(Zr_{0.20}Ti_{0.80})O_3$ (z=0-1, with 0.1 step) ceramics. The used reagents were listed in Table 3.1 and the designed size for each batch was 30 g powders. The specific processing routes were detailed in this section.

Table 3.1. Reagents for fabricating piezoceramics.

Material	Purity	Company
$BaCO_3$	99.5%	Dakram
$CaCO_3$	99.4%	Lachner
TiO_2	99.9+%	PI-KEM
ZrO_2	99.82%	Dakram

3.1.1 Fabrication of $Ba_{0.70}Ca_{0.30}TiO_3$ piezoceramics

3.1.1.1 Fabrication method 1 for $Ba_{0.70}Ca_{0.30}TiO_3$ piezoceramics

Fabrication of $Ba_{0.70}Ca_{0.30}TiO_3$ ceramics was achieved by two key steps, calcination where the reagents reacted together to form a $(Ba,Ca)TiO_3$ compound, followed by sintering of the pressed calcined powder to form a ceramic, as detailed in Figure 3.1. As shown in Figure 3.1, characterisation was carried out on the formed compounds after each step: the individual techniques will be described in more detail in section 3.2.

The raw materials for preparing $Ba_{0.70}Ca_{0.30}TiO_3$ ceramics were $BaCO_3$, $CaCO_3$ and TiO_2. Stoichiometric quantities ($BaCO_3$: $CaCO_3$: TiO_2=0.7:0.3:1) of these dried raw powders were weighed (±0.01 g) and roller ball milled in ethanol ($M_{ethanol}$: M_{powder}=1.5:1) for 12h at the speed of 100 rpm. A 125 mL plastic bottle was used in conjunction with zirconia balls ($M_{ZrO2\ balls}$: M_{powder}=2:1). After milling the slurry was dried in air using an oven (Lenton WF60) at 80ºC for 24h. The dried powders were then calcined in an alumina crucible, heating up to 1100 ºC or 1250 ºC at 5 ºC/min, dwelled for 2h, before being cooled to 40 ºC at 5 ºC/min in air in a furnace (Lenton Muffle Furnace).

Before sintering, both roller ball milling and vibro milling have been used to break the agglomerations of calcined powders, shown in the blue dotted box in Figure 3.1. The calcined powders were mixed with distilled water ($M_{distilled\ water}$: M_{powder}=2:1) in 125 mL (roller ball milling) and 75 mL (vibro milling) plastic bottles for 22h, using ZrO_2 balls ($M_{ZrO2\ balls}$: M_{powder}=2:1) as milling media. The milling method for this project was

optimised in this step.

After ball milling, 10 wt. % of a combined water-based polyvinyl alcohol (PVA) binder from Duramax B-1000 and B-1007 (Chesham Chemical Ltd., UK) was added into the plastic bottle and the slurry was milled for another 15 minutes. The slurry was then dried in an oven at 90 ºC for 24h and the dried powders were ground in a mortar and pestle and then sieved to pass through a 300 μm sieve. The fine powders (~0.5 g) were then pressed into discs under a load of 12-13 kN (90-98 MPa) for one minute on a load frame (5507 Instron, UK), using a stainless-steel die with 13 mm diameter (Specac, UK). The shaped "green body" (thickness ~0.9 mm) was then formed.

Finally, the green bodies were sintered in air as follows: heating at 1 ºC/min to 325 ºC; dwell for 1h; heating at 1 ºC/min to 500 ºC for 1h, in order to burn out the binder [3]; 5 ºC/min heating to the sintering temperature (1300 ºC, 1400 ºC or 1500 ºC); dwell for 4h; and finally cooled at 5 ºC/min to 40 ºC.

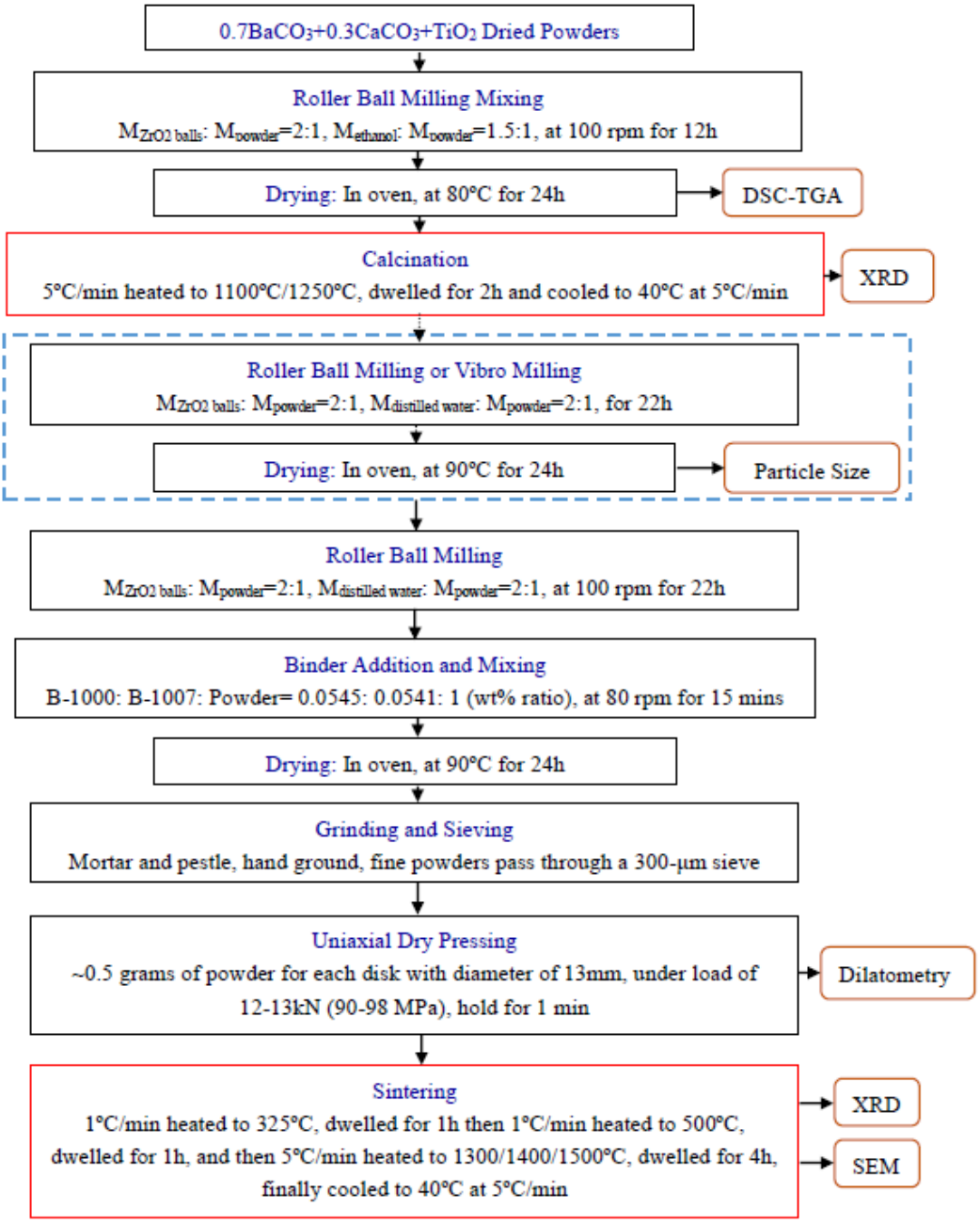

Figure 3.1. Experimental methodology for fabrication method 1 for $Ba_{0.70}Ca_{0.30}TiO_3$ piezoceramics.

3.1.1.2 Fabrication method 2 for $Ba_{0.70}Ca_{0.30}TiO_3$ piezoceramics

As the aimed single $Ba_{0.70}Ca_{0.30}TiO_3$ phase was only formed at high calcination and sintering temperatures in fabrication method 1 (detailed in section 4.2), another fabrication method was also applied to form $Ba_{0.70}Ca_{0.30}TiO_3$. Instead of mixing all

reagents together as in method 1, $BaTiO_3$ and $CaTiO_3$ ($BaTiO_3$: $CaTiO_3$=0.7:0.3) were formed first as precursor powders in method 2. The fabrication procedure of method 2 is shown in Figure 3.2, where there are two different routes for calcining the mixture of the formed $BaTiO_3$ and $CaTiO_3$ powders: (A) without further calcination step; (B) a second calcination step was carried out at 1100 ºC.

Firstly, $BaTiO_3$ and $CaTiO_3$ were formed individually by calcining $BaCO_3$ and TiO_2 at 1100 ºC for 2h and calcining $CaCO_3$ and TiO_2 at 850 ºC or 1100 ºC for 2h. In route A, after milling the calcined $BaTiO_3$ and $CaTiO_3$ in water for 22h, the rest of the process followed the same processing route as for method 1. In route B (shown in the yellow box in Figure 3.2), the ball milled slurry was dried at 90 ºC for 24h before using the same heating and cooling calcination program as used previously to double calcine the powder at 1100 ºC, followed by another ball milling step for 22h. The remaining fabrication processes were the same as the 1100 ºC calcined powder in method 1. In spite of dwelling for 4 hours during sintering, a longer dwell time (10 hours) was also used for sintering ceramics at 1300 ºC, in order to achieve good homogeneity.

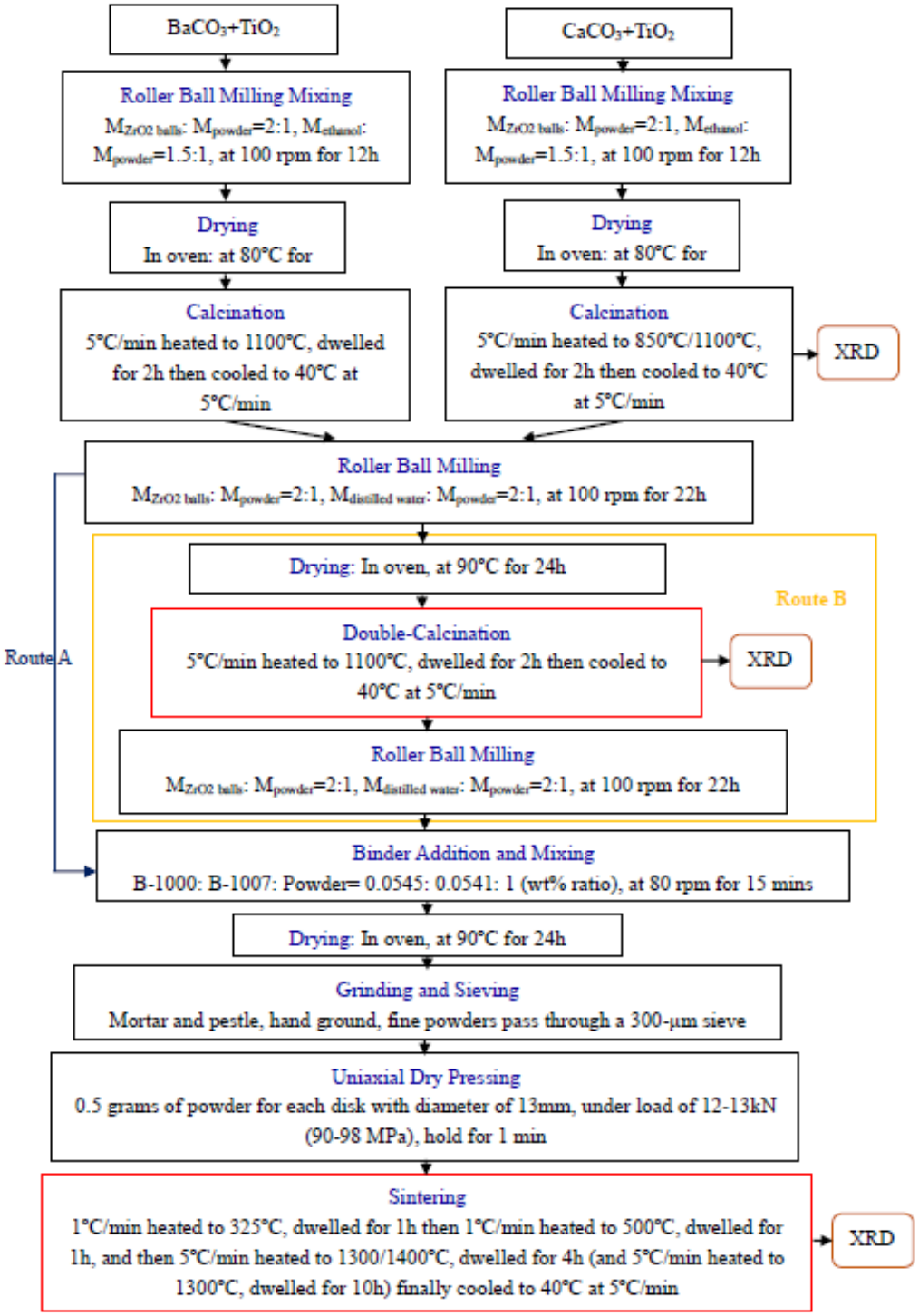

Figure 3.2. Experimental methodology for fabrication method 2 for $Ba_{0.70}Ca_{0.30}TiO_3$ piezoceramics.

3.1.2 Fabrication of $BaZr_{0.20}Ti_{0.80}O_3$ piezoceramics

The fabrication procedure for $BaZr_{0.20}Ti_{0.80}O_3$ is shown in Figure 3.3. Compared with the

fabrication method 1 for $Ba_{0.70}Ca_{0.30}TiO_3$ (Figure 3.1), the starting materials were changed to be stoichiometric quantities of $BaCO_3$, ZrO_2 and TiO_2 ($BaCO_3$: ZrO_2: TiO_2=1:0.2:0.8) with all the subsequent steps remaining the same.

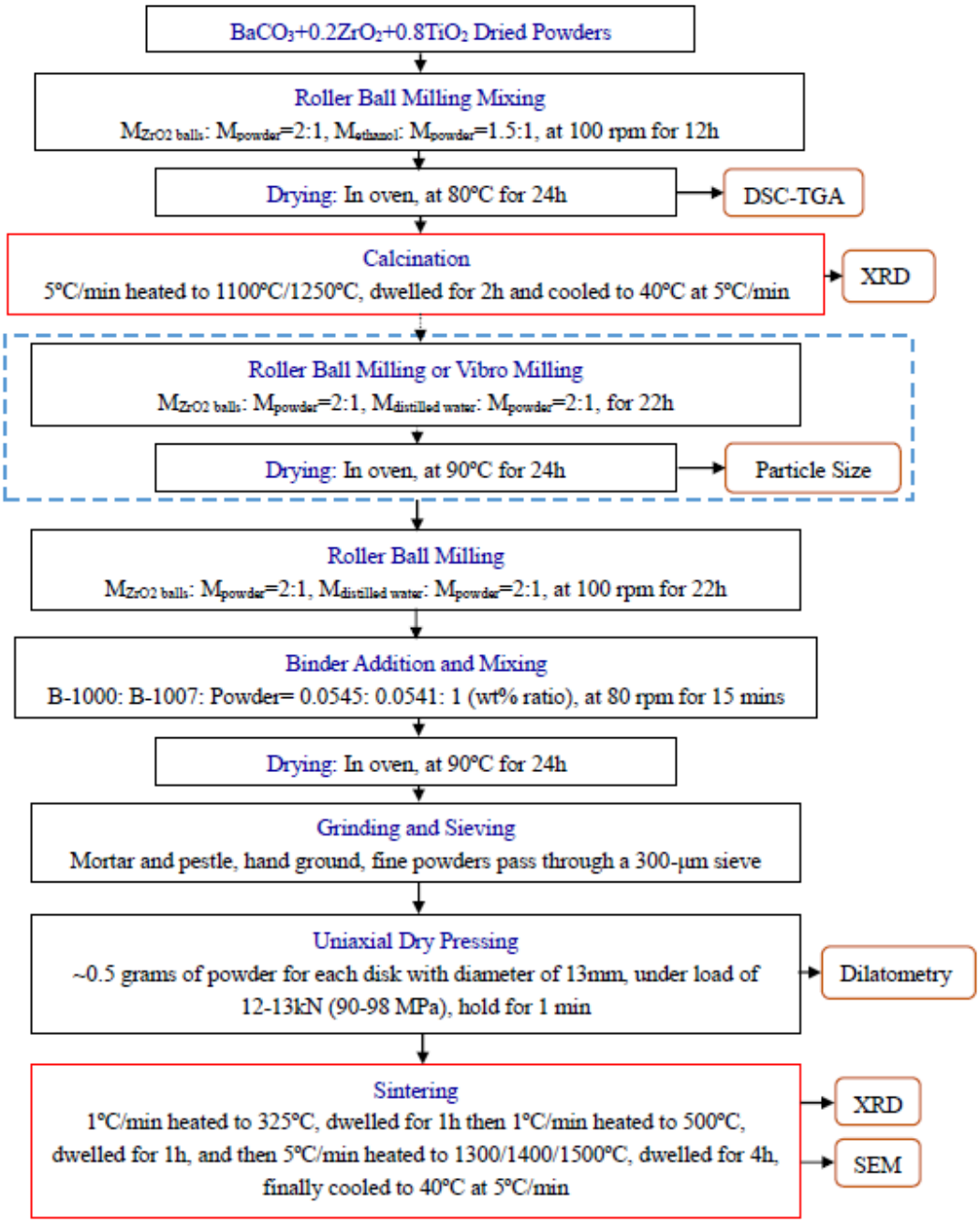

Figure 3.3. Experimental methodology for the fabrication method of $BaZr_{0.20}Ti_{0.80}O_3$ piezoceramics.

3.1.3 Fabrication of $BaZr_yTi_{1-y}O_3$ (y=0-0.30) piezoceramics

The optimised fabrication conditions for $BaZr_{0.20}Ti_{0.80}O_3$ (discussed in section 4.4) were chosen to form a series of $BaZr_yTi_{1-y}O_3$ (y=0, 0.05, 0.10, 0.15, 0.20, 0.25, 0.30) ceramics. The basic procedure followed the same steps as Figure 3.3, where the stoichiometric quantities of raw powders ($BaCO_3$: ZrO_2: TiO_2=1:y:(1-y)) were firstly mixed and calcined at 1250 ºC, followed by roller ball milling and finally sintering at 1500 ºC.

3.1.4 Fabrication of $zBa_{0.70}Ca_{0.30}TiO_3$-(1-z)$BaZr_{0.20}Ti_{0.80}O_3$ (zBCT-(1-z)BZT) ceramics

In this project, individual $Ba_{0.70}Ca_{0.30}TiO_3$ and $BaZr_{0.20}Ti_{0.80}O_3$ compounds were firstly calcined, and then mixed in appropriate proportions and sintered to produce $zBa_{0.70}Ca_{0.30}TiO_3$-(1-z)$BaZr_{0.20}Ti_{0.80}O_3$ (zBCT-(1-z)BZT) ceramics, as shown in Figure 3.4.

Stoichiometric quantities of $BaCO_3$, $CaCO_3$ and TiO_2 (0.7:0.3:1) as well as $BaCO_3$, ZrO_2 and TiO_2 (1:0.2:0.8) were mixed to prepare for the formation of $Ba_{0.70}Ca_{0.30}TiO_3$ and $BaZr_{0.20}Ti_{0.80}O_3$ phases, respectively. The mixed powders were then calcined at 1250 ºC for 2 hours (optimised in sections 4.2 and 4.4). To attain the desired zBCT-(1-z)BZT composition, stoichiometric quantities of calcined $Ba_{0.70}Ca_{0.30}TiO_3$ and $BaZr_{0.20}Ti_{0.80}O_3$ powders (with ratio as z:(1-z)) were mixed by roller ball milling, followed by the same processing steps as shown in Figure 3.1 to form bulk ceramics. The sintering temperatures were also chosen as 1300 ºC, 1400 ºC and 1500 ºC to investigate changes of the phase

compositions, microstructures and properties, and to keep the sintering temperatures consistent with the fabrication of $Ba_{0.70}Ca_{0.30}TiO_3$ and $BaZr_{0.20}Ti_{0.80}O_3$ ceramics.

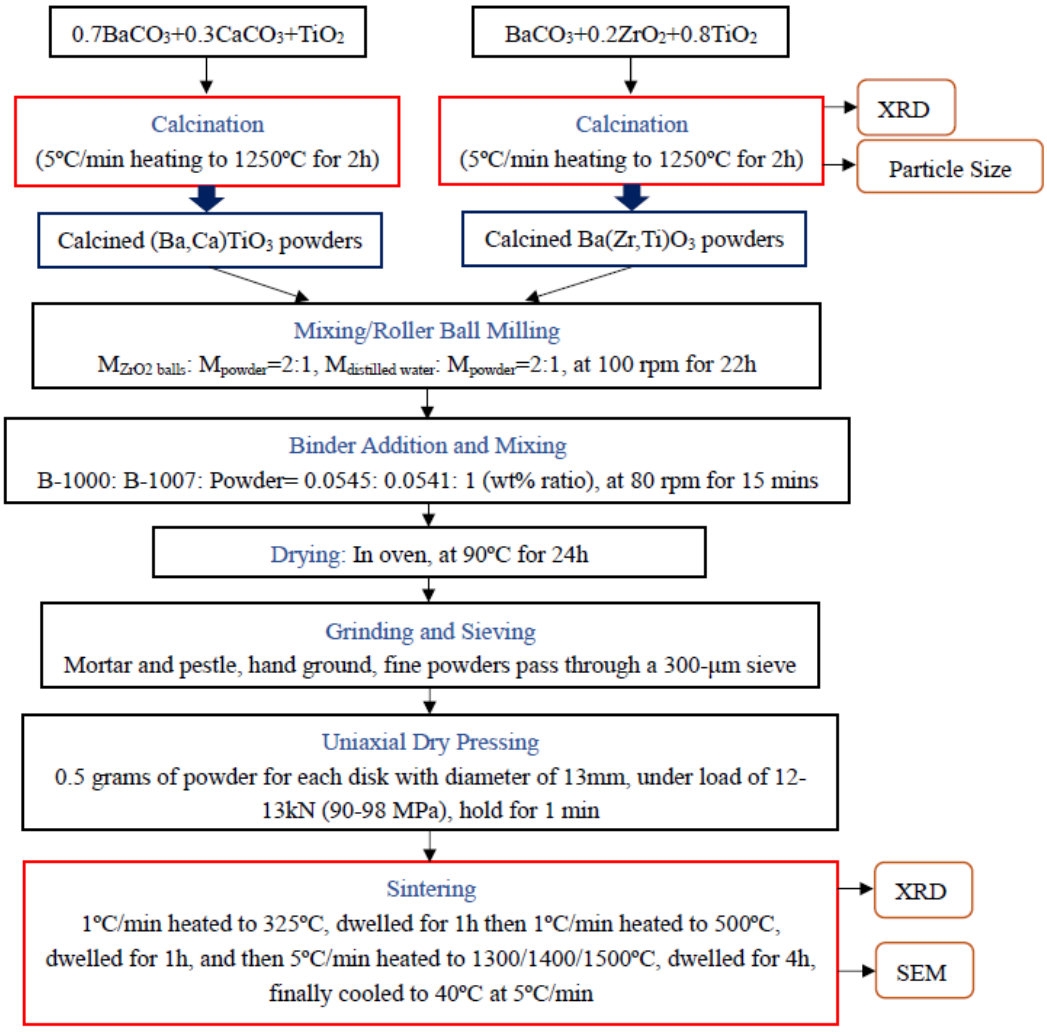

Figure 3.4. Experimental methodology for the fabrication method for $zBa_{0.70}Ca_{0.30}TiO_3$-(1-z)$BaZr_{0.20}Ti_{0.80}O_3$ piezoceramics.

3.2 Characterisation techniques

As shown in Figure 3.1-Figure 3.4, a range of techniques have been used at various stages in the fabrication of the piezoceramics to characterise and optimise their formation. The characterisations for powder samples include thermal characteristics from differential

scanning calorimetry (DSC) and thermogravimetric analysis (TGA), particle size analysis, X-ray diffraction (XRD) and Raman spectroscopy. The dilatometry of shaped green bodies was also measured. As for sintered ceramics, the density and shrinkage were measured as physical properties. The structure of ceramics was characterised by XRD, Raman spectroscopy and scanning electron microscopy (SEM). The functional properties (dielectric properties, ferroelectric properties and piezoelectric properties) of sintered ceramics were also characterised.

The thermal characteristics and XRD were only carried out once on each powder sample, however, the particle size analysis was averaged from three measurements. There were five ceramic discs sintered at each condition: two for structural characterisation; three for measuring physical properties and functional properties, where the measurements were repeated three times for each ceramic disc. Therefore, the corresponding properties and error bars were calculated from all measurements. In this project, the fabrication procedure of 1500 °C sintered $BaZr_{0.20}Ti_{0.80}O_3$ ceramics was repeated (in section 3.1.2 and 3.1.3), where the corresponding properties and error bars were averaged from two sets of ceramics. The detailed results will be discussed in Chapter 6 and Chapter 7.

It should be noted that no record of actual room temperature was made in this project. In practice, measurements were done in a number of different laboratories in two countries, and it is estimated that room temperature could vary between 15-25 ºC. These variations would be taken into consideration in later discussion (Chapter 5-7) due to their potential effects on determining the crystal structure of certain compositional ceramics at room

temperature.

3.2.1 Characterisations of powders

3.2.1.1 Thermal analysis

As shown in Figure 3.1 and Figure 3.3, the thermal analysis from differential scanning calorimetry (DSC) and thermogravimetric analysis (TGA) was carried out on mixed dried reagents. The NETZSCH simultaneous thermal analyser (STA 449C Cell) was used to observe the reaction behaviour of mixed reagents upon heating: DSC measured the amount of absorbed or released heat from powders reactions; TGA indicated the decompositions of carbonates in reagents.

After loading 35 mg of mixed powders into an alumina crucible, DSC-TGA measurements were conducted in flowing air (100 ml/min) at atmospheric pressure, using heat rate of 10 ºC/min to 1400 ºC. Based on the reaction temperatures measured from DSC-TGA, the calcination temperatures of mixed dried reagents for forming $Ba_{0.70}Ca_{0.30}TiO_3$ and $BaZr_{0.20}Ti_{0.80}O_3$ were therefore designed at higher temperatures (detailed in section 4.2.1 and 4.4.1).

3.2.1.2 Particle size analysis

The particle size distribution of starting materials (Table 3.1) and milled calcined powders was measured by using a laser diffraction particle size analyser (Sympatec, Bury, UK). As shown in Figure 3.1 and Figure 3.3, the milling method of calcined $Ba_{0.70}Ca_{0.30}TiO_3$

and $BaZr_{0.20}Ti_{0.80}O_3$ powders was optimised based on particle size distribution results (discussed in section 4.2.2 and 4.4.2).

~0.5 g measuring powder, ~3 g distilled water and one drop of $Na_4P_2O_7$ (as dispersant) were firstly loaded into a 5 ml vial to prepare a suspension. After a reference measurement, the suspension was then added into the integral ultrasonic bath of the analyser (with concentration ~26 %). The soft agglomerates in the suspension were broken by the following sonication for 15 s. During the measurement, the laser beam passed through the dispersed particles and the light was scattered onto a lens. The particle size distributions were then obtained by calculating from measured angular variation in intensity of scattered light.

3.2.1.3 X-ray diffraction (XRD)

X-ray diffraction is a powerful technique for determining the crystal structure of materials. As shown in Figure 3.5, the atoms in crystalline materials are arranged as a periodic array. When the X-ray beam is incident to a plane (with incident angle as θ), a portion of scattered X-rays (with constructive interference) then produced diffraction based on Bragg's law (Equation 3.1): the path difference of two scattered waves is equal to a multiple of the incident wavelength ($n\lambda$). Therefore, the atoms arrangement (interplanar spacing, d_{hkl}) could be obtained from diffraction pattern.

$$2d_{hkl}sin\theta = n\lambda \tag{3.1}$$

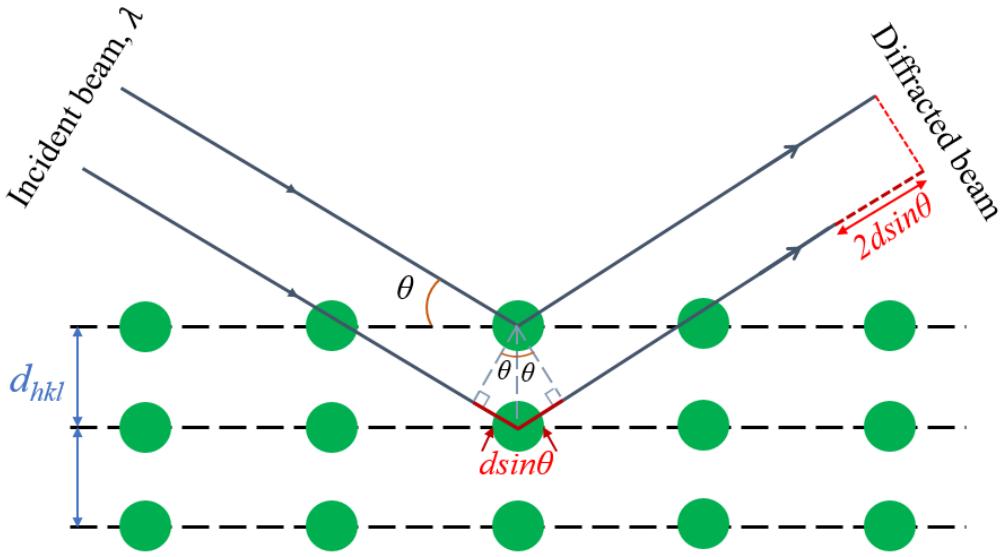

Figure 3.5. Diffraction of X-rays in a crystalline material.

In this project, the samples for XRD measurements were in powdered form for starting materials (Table 3.1) and calcined compounds whereas in bulked form for sintered ceramics. The corresponding randomly arranged crystal structure in those powders and polycrystalline ceramics then allowed the diffraction to occur across all available crystallographic planes.

The XRD measurements were performed by using a Bruker D8 advance X-ray diffractometer with Cu-Kα ($K\alpha_1$=1.5406 Å, $K\alpha_2$=1.5444 Å) radiation. The diffraction pattern was then collected by measuring the variations in intensity of X-rays against moving the X-ray source (40 kV, 40 mA) and detector between 10° to 140° 2θ range with step size as 0.0142°. The initial analysis of diffraction patterns was achieved by comparing with reference data in the crystal structure database to approximately estimate the phase composition. The reference data used in this project was crystallographic information file (.cif) from the Inorganic Crystal System Database (ICSD). However, in

this study, a further structural refinement (via pseudo-Rietveld method) was necessary to investigate the desired zBCT-(1-z)BZT system, where the Ca^{2+} and Zr^{4+} diffused into $BaTiO_3$ simultaneously. This pseudo-Rietveld refinement was achieved by using jEdit and Topas-Academic software [222]. The reference data (.cif) was firstly input into jEdit to generate a calculated reference pattern in Topas. The refinement then adjusted the parameters of this calculated pattern (*e.g*. unit cell lattice parameters, phase compositions etc.) to minimise its difference to the measured pattern. The refinement therefore enabled the more precise identifications of lattice parameters (to 0.0001 Å) by analysing multiple diffracted peaks simultaneously and refining data to have higher resolution than step size (0.0142°). In addition, the consistent performance of the incident X-rays (40 kV, 40 mA) and detector contributed to the accurate identification of phase compositions (to 0.1 wt. %) in refinement. Therefore, the precise crystallographic structure information was obtained from refinement in Topas-Academic and shown in jEdit.

In this project, the refinement of identifying the Ca^{2+} or Zr^{4+} concentrations in $BaTiO_3$ were based on Vegard's law for binary solid solution system [111]. A revised linear relationship (V=64.568-7.4836x) as anomaly to Vegard's law was used for $Ba_{1-x}Ca_xTiO_3$ system (reviewed in section 2.3.3) [94]. In $BaZr_yTi_{1-y}O_3$ system, where the Vegard's law was fulfilled (section 2.4.4), a linear relationship (V=9.2799y+64.543) was calculated based on previous research and was used for calculating Zr^{4+} content [223]. More detailed examples of refinement for $Ba_{1-x}Ca_xTiO_3$, $BaZr_yTi_{1-y}O_3$ and zBCT-(1-z)BZT system in jEdit and Topas-Academic are shown in Appendix I. Although the Rietveld refinement

was precise on calculating lattice parameters, in this project, the accuracy of elemental concentrations was related to the accuracy of used linear relationships and the unrefined atomic coordinates.

3.2.1.4 Raman spectroscopy

Raman spectroscopy was also used to determine if it is cubic, tetragonal, orthorhombic or rhombohedral phase based on direct measuring molecular vibrations in samples. In Raman spectroscopy, a single frequency of radiation was used to irradiate the sample. When light interacted with the molecule and distorted the electron cloud to form virtual states without the movement of nuclei. If the scattered energy was similar to the incident beam (*i.e*. elastic scattering), this elastic scattering was dominant and called as Rayleigh scattering (shown in Figure 3.6). However, Raman spectroscopy detects the different scattered energies from the incident beam (*i.e.* inelastic scattering), where the nuclear motion was induced by transferring the energy from incident photons to molecular (Stokes in Figure 3.6) or from molecular to scattered photons (anti-Stokes in Figure 3.6). Raman scattering was a weak process, which only occurred one in every 10^6-10^8 photons. At room temperature, as the expectation of molecular at excited vibrational states (n) other than ground state (m) was relatively small, therefore, the Raman scattering usually recorded Stokes scattering.

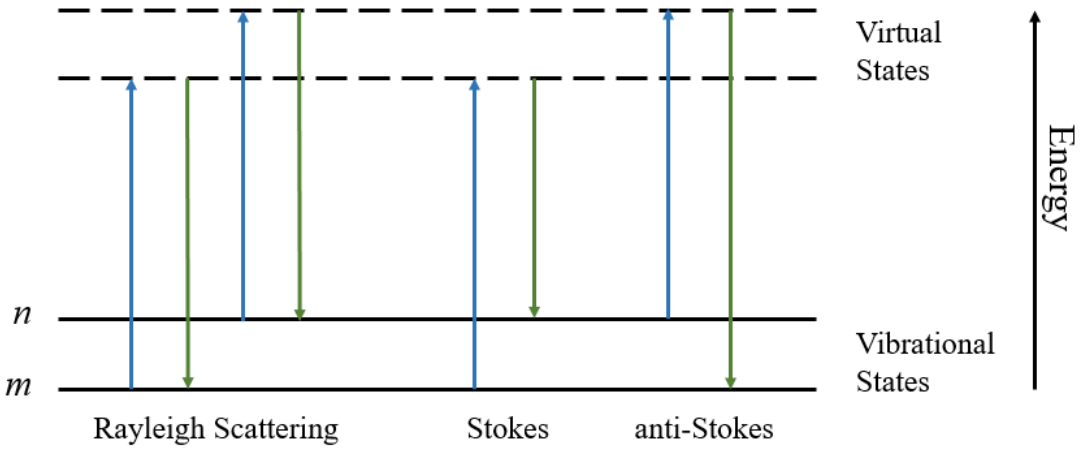

Figure 3.6. Diagram of Rayleigh and Raman scattering processes.

In this project, all samples were in powdered form for Raman spectroscopy measurement, where sintered ceramics were hand grounded in an agate mortar and pestle. The Raman spectra of each compositions were obtained using a Renishaw InVia Reflex Raman spectrometer with a 488 nm excitation laser (~2 mW power). A x20 microscope objective was used to focus the laser beam onto the powder samples with a spot-diameter of approximately 50 μm. Once the laser interacted with the sample, the scattered light went through a filter to remove the Rayleigh scattering. The remaining Raman scattering was separated by a grating (2400 grooves/mm) and then detected by a charge-coupled device (CCD). The information of vibrational modes (*e.g.* peak position, peak intensity, peak width etc.) in Raman spectra were obtained by Renishaw Wire 4.1 and Igor Pro software.

3.2.2 Characterisations of green body--dilatometry

The onset of sintering of $Ba_{0.70}Ca_{0.30}TiO_3$ and $BaZr_{0.20}Ti_{0.80}O_3$ green bodies were determined by measuring dilatometry in a NETZSCH 402E-1600 °C furnace. The calcined $Ba_{0.70}Ca_{0.30}TiO_3$ and $BaZr_{0.20}Ti_{0.80}O_3$ powders (with binders) were first pressed

and shaped as a cuboid of 8 mm*8 mm*11 mm (5507 Instron, UK) under a pressure of 90-98 MPa. The cuboid was put into the furnace to burn off the binders (heating to 325 ºC at 1 ºC/min for 1 hour and 1 ºC/min to 500 ºC for 1 hour) [3]. The cuboid samples were then put into the dilatometer, using a heating profile from room temperature to 1500 ºC at 5 ºC/min in nitrogen (50 ml/min), whilst measuring the dimensional changes against temperature. After heating to the set temperature (1500 °C), the sample was cooled down directly to room temperature at 5 ºC/min. The highest measured real temperature in the dilatometer was recorded as 1470 °C. The sintering temperatures for $Ba_{0.70}Ca_{0.30}TiO_3$ and $BaZr_{0.20}Ti_{0.80}O_3$ green bodies were then chosen at higher temperature than the onset of shrinkage (discussed in section 4.2.3 and 4.4.3).

3.2.3 Characterisation of sintered ceramics

3.2.3.1 Physical properties

The dimensions of the ceramics were measured to calculate the density and shrinkage. For each ceramic disc, the diameter (D_s) was obtained by averaging the measured diameters of 3 random positions (Electronic Digital Calliper 0-150 mm/0.01 mm/±0.02 mm, RS, UK). The thickness of ceramics (t) was measured by a micrometre (Electronic Digital Micrometre IP54, 0-30 mm/0.001 mm/±0.002 mm, TESA, Switzerland), averaging thickness of 5 random positions.

As the sintered ceramics were shaped as discs with flat surfaces, therefore their densities could be calculated by dividing mass by volume (calculated from measured dimensions

as $\frac{t*\pi D_S^2}{4}$). The mass of samples was measured by an electronic balance (R300S, Sartorius) to 0.0001g. The theoretical density of ceramics was obtained from XRD measurements (section 3.2.1.3). The relative density of ceramics was then calculated as the percentage of measured density (from mass and dimensions) over theoretical density (from XRD).

As for the shrinkage, the radial shrinkage was calculated by Equation 3.2, where the D_0 referred to the diameter of green body (13 mm, same as the diameter of the die).

$$Shrinkage = \frac{D_0 - D_S}{D_0} * 100\% \quad (3.2)$$

3.2.3.2 Microstructure

Scanning electron microscopy was performed to observe the microstructure (*e.g.* grain size, porosity etc.) of sintered ceramics. The sintered ceramics were initially polished and then thermally etched at 100 ºC below the sintering temperature for 10 minutes. After adhering the prepared sample to an aluminium stub through a conductive carbon adhesive tape, the sample along with the stub was then coated with a gold layer (100 nm) by a sputter coater (K575X, Emitech). The circular surfaces of sintered ceramics were imaged by using secondary electrons in the scanning electron microscope (Phillips XL30 ESEM-FEG). The grain sizes of the sintered ceramics were then obtained using the linear intercept method [224].

3.2.3.3 Dielectric properties

Before investigating the functional properties of sintered ceramics, an electrode

deposition stage was required. The sintered ceramics were firstly coated with a chromium layer (40 nm) and then two gold layers (200 nm) on both circular surfaces by the same sputter coater as in section 3.2.3.2. The electrode coated ceramics could then be poled in a silicone oil bath at room temperature for 10 minutes under a direct current electric field of 3 kV/mm.

After loading ceramics on a bespoke jig for low frequency measurement (Advanced functional materials, UK), the capacitance (C) and dielectric loss factor ($tan\delta$) at 1 kHz and room temperature of unpoled and poled ceramics were measured by an impedance analyser (4294A, Agilent, USA). The relative permittivity (ε_r) was then calculated by Equation 3.3 and 2.5, where t and r refer to thickness and radius ($r=D_s/2$) of the ceramics respectively.

$$\varepsilon = C \cdot \frac{t}{\pi \cdot r^2} \tag{3.3}$$

3.2.3.4 Ferroelectric properties

The ferroelectric hysteresis loops (P-E loop) were measured on unpoled ceramics from a piezoelectric evaluation system (aixPES, aixACCT, Germany). The photo of this system was shown in Figure 3.7 (A), where a piezo sample holder or a thick-/thin film sample holder was connected to a variety of additional hardware components (shown in Figure 3.7 (B)). In this study, the piezo sample holder (Figure 3.7 (C)) was used to measure all sintered bulk ceramics. Before the measurement, the unpoled ceramic disc was centred onto the bump of the bottom contact. The silicon oil was then injected into the chamber

to slightly cover the ceramics (to increase the spark-over voltage), followed by closing the lid of sample holder carefully. The Piezo Measurement (PZM) was then chosen to perform hysteresis measurements, where the applied signal was the triangular voltage with the maximum amplitude as E=3 kV/mm and frequency as 1 Hz. The aixPlorer 3.0 software was used to analyse measured data, where the coercive field (E_C) and remanent polarization (P_r) of ceramics were worked out directly.

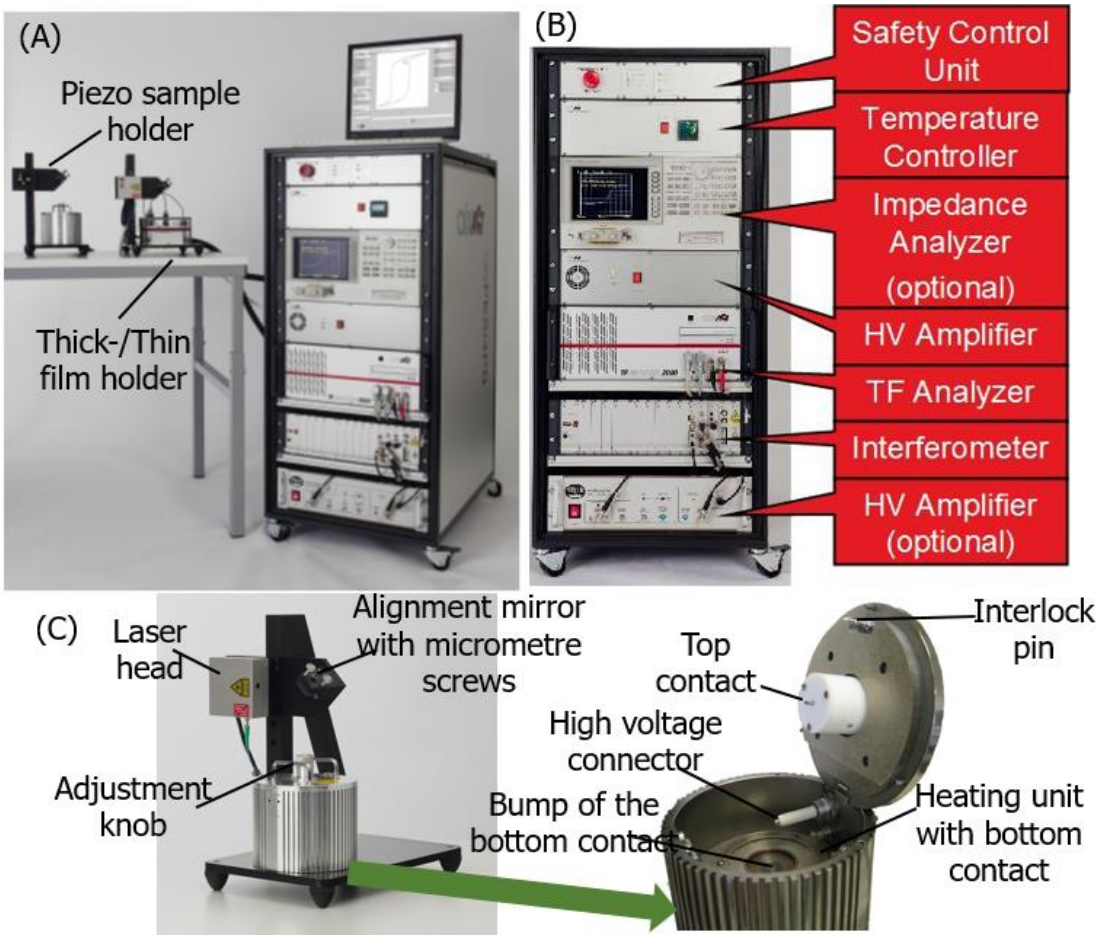

Figure 3.7. Photos of aixACCT piezoelectric evaluation system: (A) integral system; (B) hardware components; (C) piezo sample holder.

3.2.3.5 Piezoelectric properties

In this project, the frequency method [10] was used to measure the piezoelectric

parameters of the ceramics. The resonant frequency (f_r) and anti-resonant frequency (f_a) of poled ceramics were obtained by the same impedance analyser (with the same jig) as described in section 3.2.3.3 at room temperature. The planar electromechanical coupling coefficients (k_p) were then calculated by the equation below [6]:

$$k_p^2 \approx 2.51 \cdot \frac{f_r}{f_a - f_r} - \left(\frac{f_r}{f_a - f_r}\right)^2 \quad (3.4)$$

The piezoelectric charge coefficient (d_{33}) of poled ceramics was measured at room temperature by quasi-static (or Berlincourt) method in this project [10], using a Berlincourt d_{33} meter (YE2730A, Sinocera, China) to read the d_{33} values directly. When measuring each ceramics disc, six random points were measured and averaged to be the d_{33} value.

3.3 Temperature dependent characterisation techniques

The temperature dependent characterisations, including measuring Raman spectroscopy, dielectric and ferroelectric properties, were used to determine the phase transitions in samples based on both structural and functional property measurements. The measured samples were $Ba_{0.70}Ca_{0.30}TiO_3$ ceramics (as a global composition, fabricated in section 3.1.1) containing tetragonal $Ba_{1-x*}Ca_{x*}TiO_3$ (x*=0, 0.03, 0.05, 0.10, 0.15, 0.20 and 0.30, x* referred to the Ca^{2+} concentrations in tetragonal phase) compositions; $BaZr_yTi_{1-y}O_3$ (y=0-0.30) ceramics, which were fabricated in section 3.1.3; 1500 °C sintered zBCT-(1-z)BZT (z=0-1) ceramics, as fabricated in section 3.1.4. For each composition, only one

sample was selected to perform measurements and some measurements were repeated. Therefore, the error bars for phase transition temperatures derived from single set measurement were not displayed. As for those phase transition temperatures determined from several Raman modes or thermal loop functional property measurements, the corresponding error bars were calculated and displayed.

3.3.1 Temperature dependent Raman spectroscopy

The same Raman spectrometer as described in section 3.2.1.4 was used to perform the temperature dependent measurements. The powdered ceramics or ground bulked ceramics were firstly placed into an aluminium crucible in an Instec HCS621V sample cell, where the atmosphere and temperature environment was controlled during the measurement. The 488 nm laser (2 mW power) was focused onto the sample with a ~50 μm diameter spot. In the case of $Ba_{0.70}Ca_{0.30}TiO_3$ ceramics, only tetragonal $Ba_{1-x*}Ca_{x*}TiO_3$ phase areas were firstly detected and focused at room temperature, ensuring that observed molecular vibrations and phase transition behaviour were from tetragonal $Ba_{1-x*}Ca_{x*}TiO_3$. Then heating the sample from -190 °C to 240 °C at 1 °C/min in 1 bar Ar flowing at 100 ml/min in the sample cell. Simultaneously, the obtained Raman scattering upon heating were detected by CCD and collected at every 30 seconds. The data were exported from Renishaw Wire 4.1 to MATLAB R2013a to investigate the changes in vibrational modes (in peak position, intensity, width etc.) against temperature (as detailed in Appendix II). The obtained phase transition temperatures were calibrated by comparing the transition temperatures of $BaTiO_3$ from Raman spectroscopy

measurement to those from reference [225].

3.3.2 Temperature dependent dielectric and ferroelectric properties

The electrode coated and unpoled bulk ceramics were used to measure the temperature dependent dielectric and ferroelectric properties. In the case of $Ba_{0.70}Ca_{0.30}TiO_3$ ceramics, only two compositions containing tetragonal $Ba_{1-x*}Ca_{x*}TiO_3$ (x*=0.20 and 0.30) phases were bulk samples, therefore the measurements were only carried out on those two samples. The same piezoelectric evaluation system as described in section 3.2.3.4 was performed to measure temperature dependent functional properties. Before the measurement, the sample was also located in the centre of bump of the bottom contact in piezo sample holder (shown in Figure 3.7 (C)). The silicon oil was injected for measuring ferroelectric properties but not for measuring dielectric properties, after which the lid of sample holder was closed carefully.

The Thermo Measurement (THM) was then chosen to perform dielectric or ferroelectric measurement on consecutive temperature steps (gapped by 2 ºC) between -100 ºC to 150 ºC at 1 ºC/min. In the THM mode, the Impedance Measurement (IFM) was applied to measure capacitance and dielectric loss of ceramics at 1 kHz and variable temperatures, by using the external Impedance Analyser components (shown in Figure 3.7 (B)). The relative permittivity was calculated from Equation 3.3 and 2.5 and its relationship to temperature was obtained.

The temperature dependent ferroelectric hysteresis loops were measured by applying PZM in THM mode. In this PZM measurement, the maximum amplitude of applied voltage was E=2 kV/mm. After measurement, the coercive field (E_C) and remanent polarization (P_r) as a function of temperatures could be obtained in aixPlorer 3.0 software. Another CV Measurement (CVM) was applied alternatively with the PZM in the THM mode to perform small signal capacitance vs voltage measurements on sample. The maximum amplitude of the applied signal was E=1.5 kV/mm and the frequency was 1 kHz, the measured capacitance at 0 V (C_{0+}) could then be shown in aixPlorer 3.0 and used to work out the relative permittivity upon heating by CVM measurement (with silicon oil present). The obtained phase transition temperatures from all functional property measurements (incl. THM+IFM, THM+PZM+CVM) were calibrated by comparing to the transition temperatures of $BaTiO_3$ in the same reference as section 3.3.1 [225].

3.4 Reaction mechanism study of $BaTiO_3$-$CaTiO_3$

3.4.1 Fabrication of samples

The reagents chosen for this study were $BaCO_3$, $CaCO_3$ and TiO_2 (listed in Table 3.1). Similar to the mixing procedure outlined in Figure 3.1, stoichiometric quantities of these reagents were weighed to form mixtures of $CaCO_3$+TiO_2, $BaCO_3$+TiO_2 and 0.7$BaCO_3$+0.3$CaCO_3$+TiO_2. A homogeneous slurry of each mixture was formed by roller

ball milling in ethanol for 12h. Subsequent drying of the slurry was carried out in an oven at 80 ºC for 24h to produce the desired mixtures.

The 1100 ºC formed $BaTiO_3$ powder in section 3.1.1.2 as well as $CaTiO_3$ powder (99%, Sigma-Aldrich) was roller ball milled in distilled water separately. The combined PVA binder (as described in section 3.1.1.1) were added into slurries at the same ratios in Figure 3.1 before ball milling the slurries for another 15 minutes. The slurries were then dried in oven at 90 ºC for 24 hours. The dried $BaTiO_3$ and $CaTiO_3$ were pressed at 90-98 MPa in a 13 mm die to form a diffusion couple (shown in Figure 3.8). The diffusion couple was sintered using the sintering profile defined in Figure 3.1 and sintered at 1500 ºC (for 4 hours) to investigate the diffusion mechanism between $BaTiO_3$ and $CaTiO_3$.

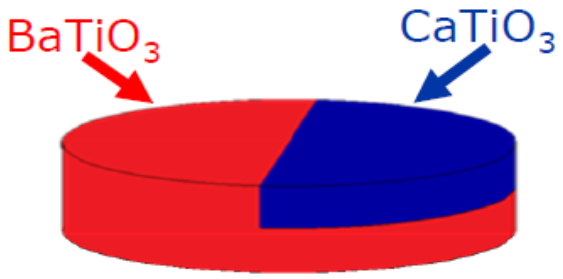

Figure 3.8. Schematic diagram of $BaTiO_3$-$CaTiO_3$ diffusion couple.

3.4.2 Characterisation of mixed powders

Thermal analysis (DSC-TGA) of the dried mixtures of $CaCO_3$+TiO_2, $BaCO_3$+TiO_2 and 0.7$BaCO_3$+0.3$CaCO_3$+TiO_2 were carried out using the same NETZSCH STA 449C Cell as in section 3.2.1.1 from 500 ºC to 1500 ºC at 5 ºC/min under flowing argon (100 ml/min). XRD was performed using the same Bruker D8 advance X-ray diffractometer as described in section 3.2.1.3, and in situ measurements were carried out

in an Anton Paar XRK900 cell from room temperature to 800 ºC at 5 ºC/min, under flowing helium (at 1.5 bar and 100 ml/min). The XRD pattern was collected isothermally before heating to next set temperature point.

3.4.3 Characterisation of diffusion couple

Raman imaging of the sintered diffusion couple was performed using the same Renishaw InVia Raman microscope as section 3.2.1.4. The 488 nm laser was focused through a x50 long working distance objective by StreamLine line focus tool onto the diffusion couple. Then a line of laser light was scanned on sample with the simultaneous collection of multiple points data, followed by the moving of the x-y mapping stage for next scanning. Therefore, the chemical imaging of diffusion couple could be obtained.

Chapter 4 Optimising the fabrication of $Ba_{0.70}Ca_{0.30}TiO_3$ and $BaZr_{0.20}Ti_{0.80}O_3$ ceramics

The characterisation results of the fabricated $Ba_{0.70}Ca_{0.30}TiO_3$ and $BaZr_{0.20}Ti_{0.80}O_3$ ceramics (as described in section 3.1.1 and 3.1.2) would be stated and discussed in this chapter. Based on those results, the fabrication conditions were optimised at each step and the optimised fabrication procedure for later study would be concluded.

4.1 Starting Materials

The XRD patterns of the starting materials are shown in Figure 4.1. As received $BaCO_3$, $CaCO_3$ and ZrO_2 are shown in (A), (B) and (D), and it can be seen that the respective patterns can be indexed completely using reference spectra for Witherite ($BaCO_3$), Calcite ($CaCO_3$) and Baddeleyite (ZrO_2). Refinement of the pattern of as received TiO_2 (shown in (C)), shows that it is comprised of 95.8 wt. % Rutile and 4.2 wt. % Anatase forms of TiO_2.

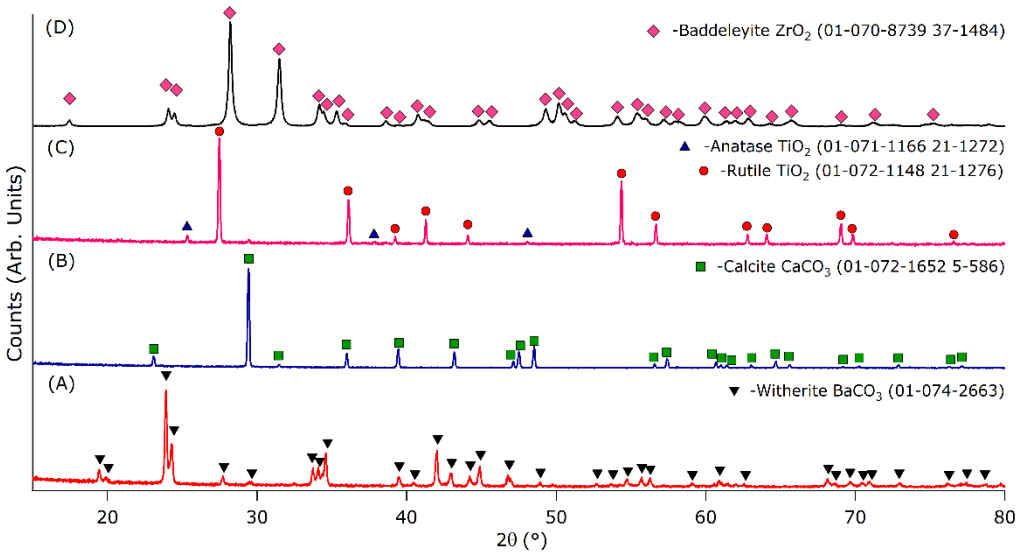

Figure 4.1. The XRD patterns of reagents: (A) $BaCO_3$; (B) $CaCO_3$; (C) TiO_2; (D) ZrO_2.

The particle size of as received powders (after breaking agglomerations in ultrasonic bath) is listed in Table 4.1, where X_{50} and X_{90} indicate the particle size values of 50 % and 90 % particles on a cumulative volume distribution. The starting $BaCO_3$, TiO_2 and ZrO_2 powders are fine powders (X_{50}<4 μm), whereas $CaCO_3$ powders have large particle size with X_{50}>50 μm. As shown in Figure 4.2 (A), (C) and (D), the small particles (with agglomerations) of $BaCO_3$, TiO_2 and ZrO_2 powders are also observed by scanning electron microscopy (SEM). Figure 4.2 (B) further indicates that $CaCO_3$ powders are coarser with averaged particle size around 50 μm.

Table 4.1. Particle size of reagents.

Materials	X_{50} **(μm)**	X_{90} **(μm)**
$BaCO_3$	3.83±0.03	8.65±0.16
$CaCO_3$	55.48±0.55	80.22±0.68
TiO_2	3.81±0.02	8.52±0.04
ZrO_2	3.73±0.02	8.27±0.07

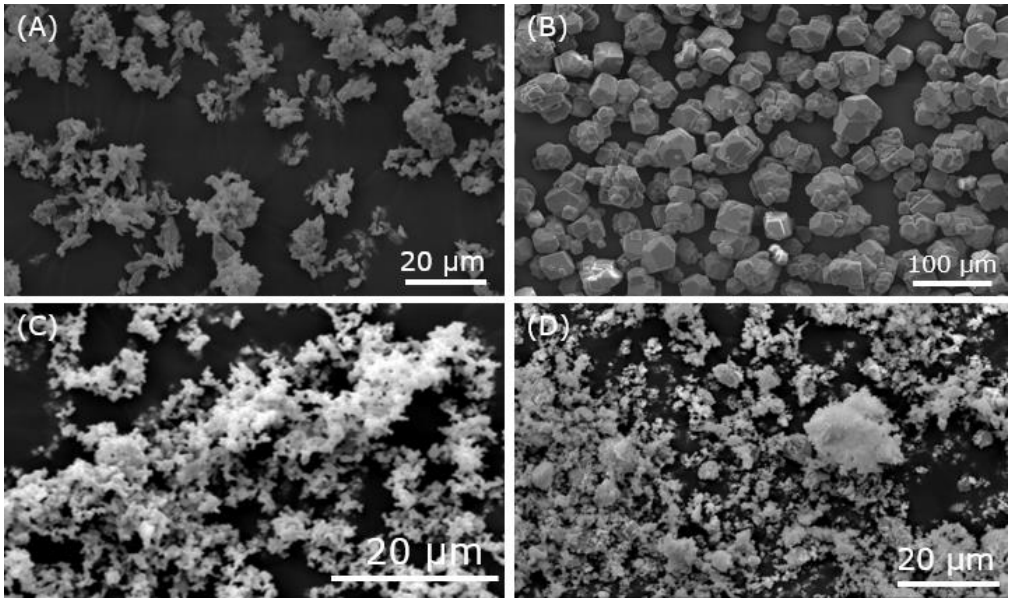

Figure 4.2. The SEM images of reagents: (A) $BaCO_3$; (B) $CaCO_3$; (C) TiO_2; (D) ZrO_2.

4.2 Fabrication method 1 of $Ba_{0.70}Ca_{0.30}TiO_3$ ceramics

In this method, the $Ba_{0.70}Ca_{0.30}TiO_3$ ceramics were fabricated following the procedure in Figure 3.1, where $BaCO_3$, $CaCO_3$ and TiO_2 were mixed and calcined, followed by sintering the pressed pellets. The optimisation of calcination temperature, milling method of calcined powders and sintering temperature was necessary to ensure the formation of the desired $Ba_{0.70}Ca_{0.30}TiO_3$ phase.

4.2.1 Optimising the calcination temperature

The reaction temperature of mixtures of the reagents ($BaCO_3$, $CaCO_3$ and TiO_2) were tested by DSC-TGA, and the data are shown in Figure 4.3.

Theoretically, for a mixture of $0.7BaCO_3 + 0.3CaCO_3 + TiO_2$ the total mass loss is expected

to be 17.74 % through the released CO_2, of which 5.32 % can be attributed to $CaCO_3$ and 12.42 % to $BaCO_3$. Previous studies have shown that the decomposition of individual $CaCO_3$ occurred from 924 ºC followed by the reaction with TiO_2 to form $CaTiO_3$ from 1038 ºC. While individual $BaCO_3$ decomposed at 987 ºC and formed $BaTiO_3$ at 1090 ºC [226].

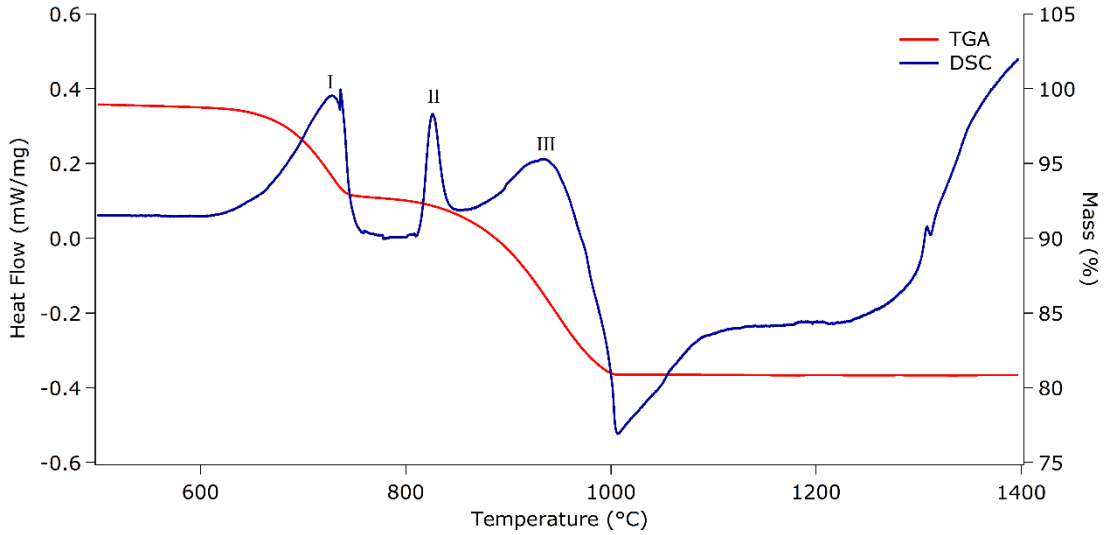

Figure 4.3. The DSC-TGA curve of heating $0.7BaCO_3+0.3CaCO_3+TiO_2$ mixture to 1400 °C at 10 °C/min.

The TGA in Figure 4.3 shows two steps of mass losses: the first mass loss starts at 605 ºC with a loss of around 6 % corresponding to the decomposition of $CaCO_3$. The second mass loss of 12 % corresponds to $BaCO_3$ with an onset temperature 756 ºC. These mass losses are in agreement with theoretical values. The expected reduction in onset temperature of the mixture compared to the individual compounds is observed. When the temperature exceeds 1030 ºC, the mass of the system remains stable, indicating that $CaCO_3$ and $BaCO_3$ have fully decomposed.

In the DSC curve, there are three exothermic peaks observed in the ranges 605-756 ºC (peak I), 811-857 ºC (II) and 857-973 ºC (III), as well as an endothermic peak around 1000 ºC. The exothermic peaks I and III correspond with large reductions in mass and could therefore be considered to be the decomposition of $CaCO_3$ and $BaCO_3$, respectively. The endothermic peak has no associated mass loss, indicating that decompositions and reactions finished around 1000 ºC. A detailed discussion of reaction mechanism for peak II and exothermic peak will be investigated in Chapter 5 (section 5.3.1).

From the DSC-TGA results, the reactions between $BaCO_3$, $CaCO_3$ and TiO_2 are all completed at 1100 ºC. Therefore, samples were calcined at two temperatures in method 1, 1100 ºC and 1250 ºC (see section 3.1.1.1).

Figure 4.4 shows the XRD patterns and analysed phase compositions of $Ba_{0.70}Ca_{0.30}TiO_3$ powders calcined at 1100 ºC (pattern A) and 1250 ºC (pattern B) prepared using method 1. After calcination, instead of the expected single phase of $Ba_{0.70}Ca_{0.30}TiO_3$, the powders contain two discrete phases: a Ba-rich tetragonal phase (fitted by PDF-number: 01-081-0042) and a Ca-rich 'pseudo-cubic' phase (01-075-2100 42-423). The precise quantitative phase analysis was achieved by refining XRD data on jEdit and Topas-Academic (section 3.2.1.3 and Appendix I). The powder calcined at 1100 ºC (for 2 hours) contains 84.1±0.2 wt. % tetragonal $Ba_{0.90}Ca_{0.10}TiO_3$ and 15.9±0.2 wt. % 'pseudo-cubic' $Ba_{0.15}Ca_{0.85}TiO_3$. When calcined at 1250 ºC (for 2 hours) the powder contains 85.9±0.2 wt. % tetragonal $Ba_{0.85}Ca_{0.15}TiO_3$ and 14.1±0.2 wt. % pseudo-cubic $Ba_{0.18}Ca_{0.82}TiO_3$. Thus, higher calcination temperatures contribute to a better

homogeneity for these two distinct phases.

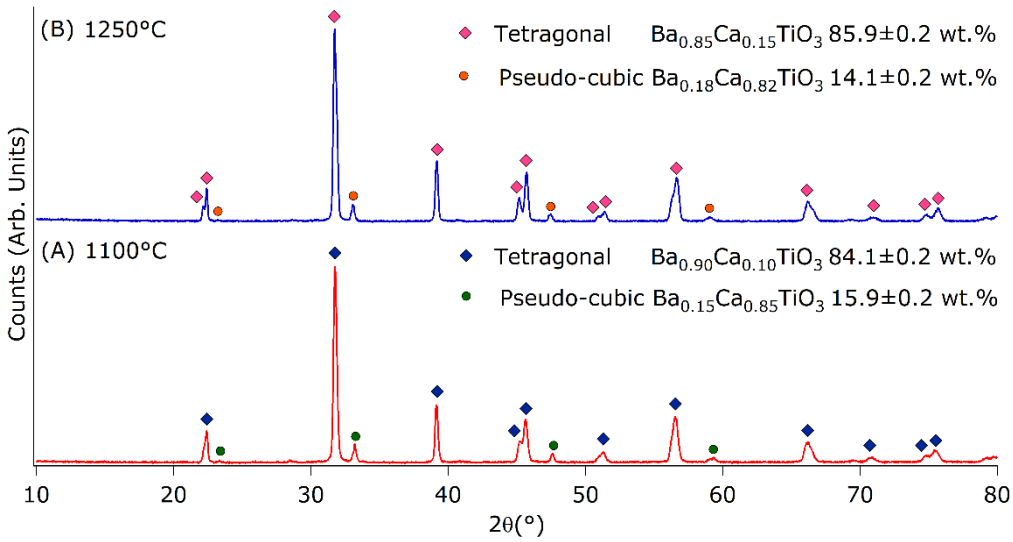

Figure 4.4. XRD patterns of (A) 1100 ºC; (B) 1250 ºC calcined mixture of $BaCO_3$, $CaCO_3$ and TiO_2.

4.2.2 Optimising the milling method

Table 4.2 demonstrates the particle size of ball-milled and vibro-milled calcined powders prepared using method 1. All the milling and calcination conditions result in similar particle size distributions. Hence, roller ball milling was chosen as the milling method for subsequent fabrications.

Table 4.2. Particle size of different milled calcined $Ba_{0.70}Ca_{0.30}TiO_3$ powders.

Powder Name		X_{50}**(µm)**	X_{90}**(µm)**
1100 ºC Calcined	Ball Milled	2.83(±0.01)	5.43(±0.02)
	Vibro Milled	2.54(±0.02)	5.13(±0.02)
1250 ºC Calcined	Ball Milled	2.82(±0.01)	4.79(±0.01)
	Vibro Milled	2.81(±0.01)	5.12(±0.02)

4.2.3 Optimising the sintering temperature

The optimum sintering temperature of calcined $Ba_{0.70}Ca_{0.30}TiO_3$ was determined by measuring the dimensional change in powder pressed green bodies (with binder burnt out first) of the two calcined powders as a function of increasing temperature using a dilatometer. The sample was heated at 5 ºC/min to 1500 °C and cooled directly to room temperature (as described in section 3.2.2). In Figure 4.5, the blue line indicates the temperature and the brown line indicates the percentage changes in length. As shown in (A), the length of the green body made with powder calcined at 1100 ºC remains stable until 1156 ºC at which point there is a sharp decrease, which suggests the sintering temperature of 1100 ºC calcined $Ba_{0.70}Ca_{0.30}TiO_3$ should be higher than 1156 ºC. In Figure 4.5 (B), the green body made with powder calcined at 1250 ºC starts to shrink at 1141 ºC, where the sintering temperature should be higher. Therefore, in this work, 1300 ºC, 1400 ºC and 1500 ºC were chosen as appropriate sintering temperatures (100 ºC gap) for both 1100 ºC and 1250 ºC calcined $Ba_{0.70}Ca_{0.30}TiO_3$ powders, and initial trials were undertaken.

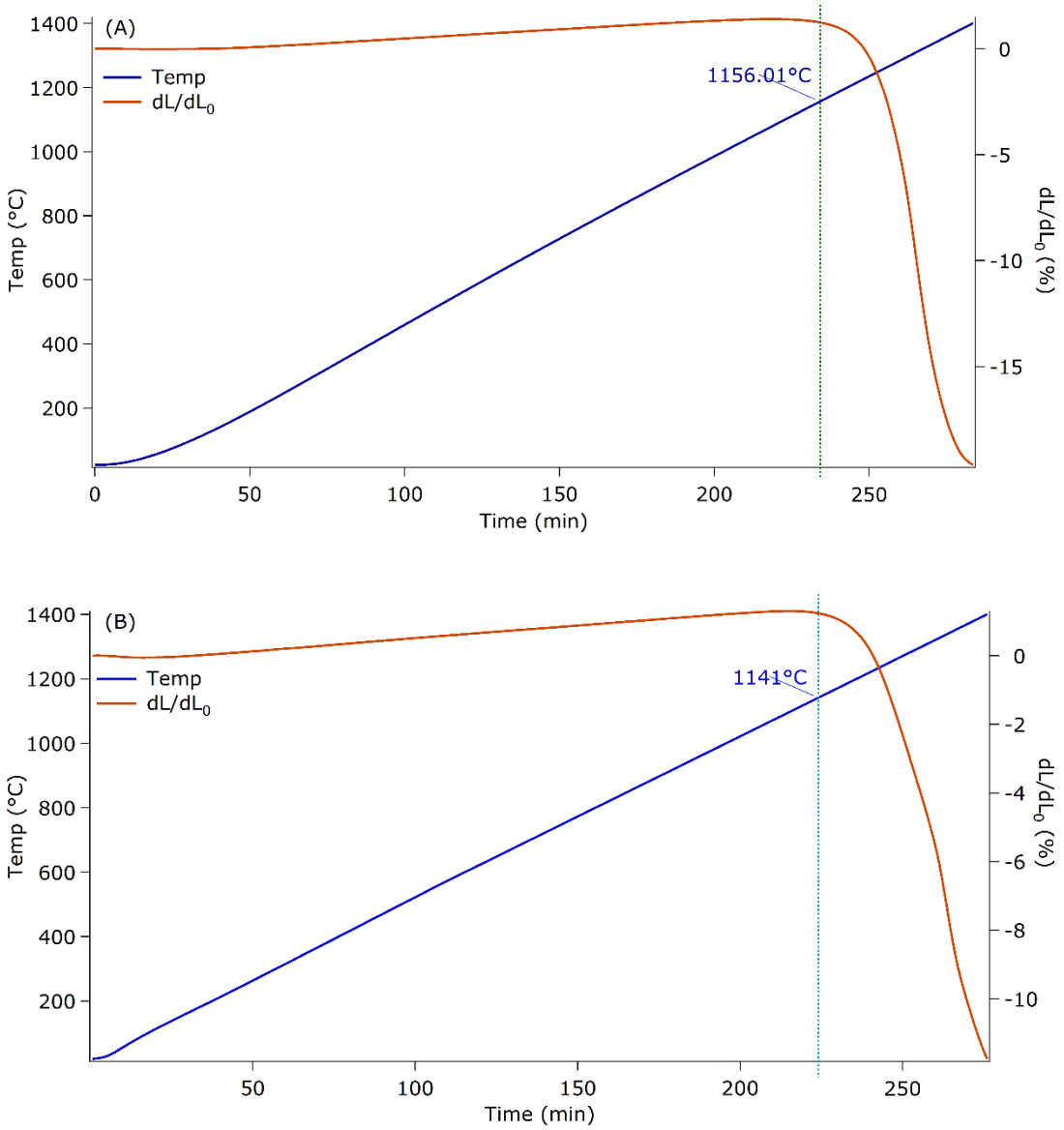

Figure 4.5. Dimension changes of (A) 1100 ºC calcined; (B) 1250 ºC calcined $Ba_{0.70}Ca_{0.30}TiO_3$ green body during heating to 1500 °C at 5 °C/min in dilatometer.

Photographs of sintered ceramics are shown in Figure 4.6. There are only photographs for 1300 ºC and 1400 ºC sintered ceramics for 1100 ºC calcined powders (Figure 4.6 (A)), as the 1500 ºC sintered ceramics melted during the sintering procedure. Whereas the higher calcination temperature (1250 ºC) avoids this melting phenomenon at the same sintering temperature (1500 ºC, Figure 4.6 (B)). With reference to XRD determination

(Figure 4.4), the lower temperature calcination (1100 ºC) contributes to less Ca^{2+} content in Ba-rich phase (10 at. %). During sintering, the homogeneity is promoted and the consequent higher Ca^{2+} content in the $(Ba,Ca)TiO_3$ phase then reduces its melting point close to 1500°C [89]. On the contrary, as for the greater Ca^{2+}-contained Ba-rich phase (15 at. %) in 1250 ºC calcined powders, the melting point increases with increasing Ca^{2+} content during sintering, therefore the corresponding melting point becomes much higher than 1500 ºC [89]. It is interesting to notice that both photographs show darker colour in higher temperature sintered ceramics, which may be related to homogeneity and density.

The physical properties of the sintered ceramics are listed in Table 4.3. The ceramics fabricated from powders calcined at 1100 ºC have similar values of shrinkage and density. While for ceramics fabricated from powders calcined at 1250 ºC, the shrinkage and density increase with increasing sintering temperature from 1300 ºC to 1400 ºC, and keep constant when increasing further to 1500 ºC. Furthermore, the shrinkage of the sample sintered at 1400 ºC is in good agreement with the values in Figure 4.5.

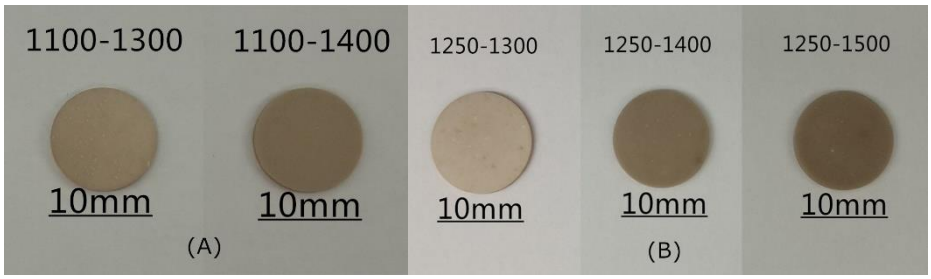

Figure 4.6. Photos of sintered ceramics. (A) photos of discs from powders calcined at 1100 ºC; (B) photos of discs from powders calcined at 1250 ºC (Sample Name: Calcination temperature (ºC)-Sintering temperature (ºC)).

Table 4.3. Physical properties of sintered ceramics (Sample Name: Calcination temperature (ºC)-Sintering temperature (ºC)).

Sample Name	**1100-1300**	**1100-1400**	**1250-1300**	**1250-1400**	**1250-1500**
Diameter shrinkage (%)	19.17 (±0.20)	19.14 (±0.22)	10.98 (±0.02)	13.84 (±0.22)	13.87 (±0.25)
Bulk density (g/cm^3)	5.14 (±0.02)	5.12 (±0.04)	4.61 (±0.08)	5.12 (±0.02)	5.02 (±0.06)
Relative density (%)	93.58 (±0.36)	95.11 (±0.74)	84.37 (±1.46)	95.08 (±0.37)	92.59 (±1.11)

The XRD patterns of sintered $Ba_{0.70}Ca_{0.30}TiO_3$ ceramics are shown in Figure 4.7 and the refined lattice parameters were listed in Table 4.4. As shown in Figure 4.7 (A), both 1300 ºC and 1400 ºC sintered ceramics from 1100 ºC calcined powders have a majority of Ba-rich tetragonal phase and a minority of Ca-rich pseudo-cubic phase, which is not the desirable homogeneous $Ba_{0.70}Ca_{0.30}TiO_3$ phase. However, a higher sintering temperature contributes to more tetragonal phase with a higher content of Ca^{2+}, *i.e.* better homogeneity. The sintered ceramics from 1250 ºC calcined powders have the same trend (Figure 4.7 (B)), however, the desirable single phase could be formed when sintering samples at 1500 ºC (Table 4.4). Therefore, better homogeneity could be achieved by higher calcination and sintering temperatures.

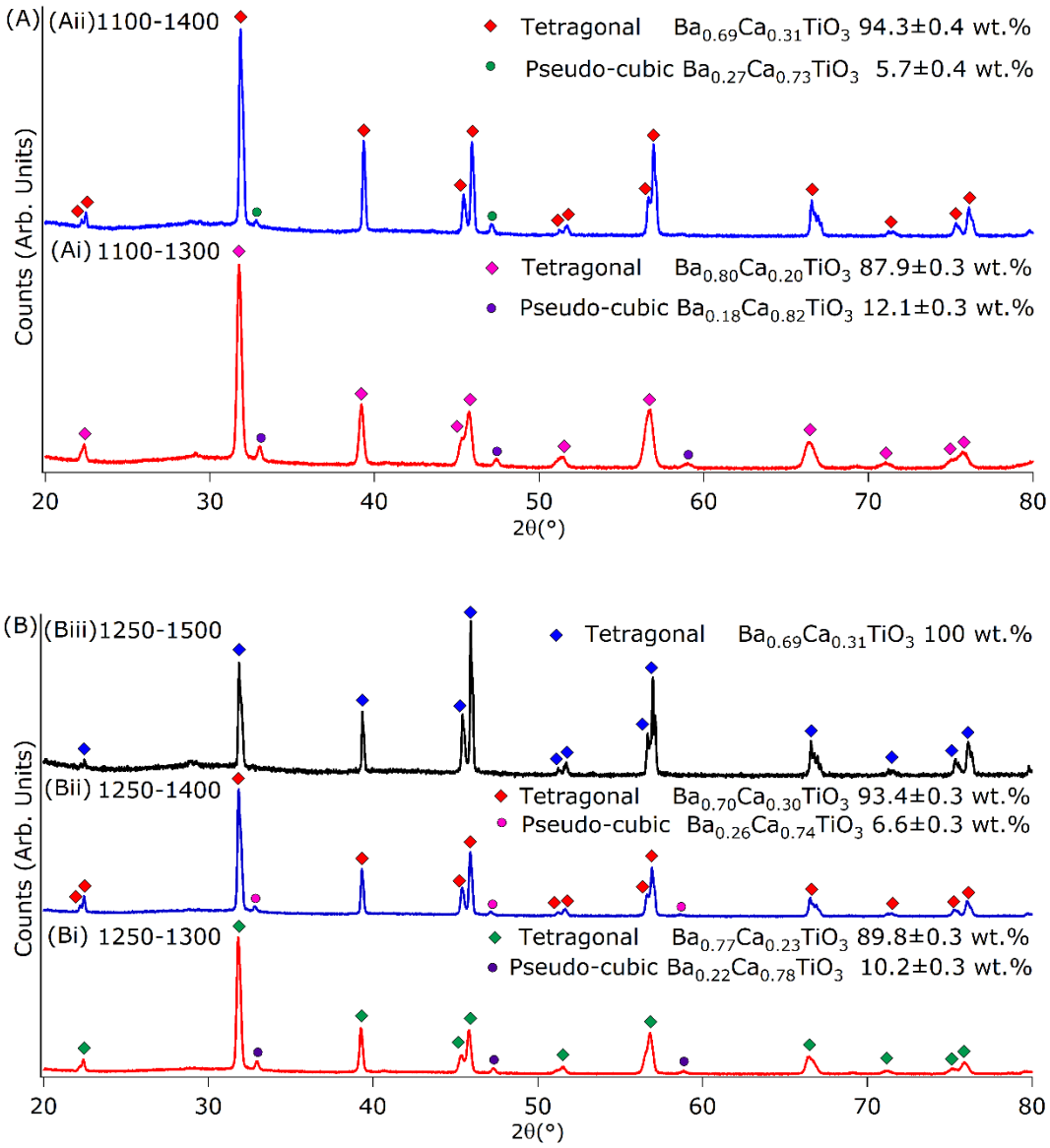

Figure 4.7. XRD patterns of sintered $Ba_{0.70}Ca_{0.30}TiO_3$ ceramics from (A) 1100ºC calcined powders; (B) 1250ºC calcined powders: (Ai) 1100-1300, (Aii) 1100-1400, (Bi) 1250-1300, (Bii) 1250-1400 and (Biii) 1250-1500 (Sample Name: Calcination temperature (ºC)-Sintering temperature (ºC)).

Table 4.4. The unit cell parameters of sintered $Ba_{0.70}Ca_{0.30}TiO_3$ ceramics (fabricated by method 1) from XRD (Sample Name: Calcination temperature (ºC)-Sintering temperature (ºC)).

Sample Name	Tetragonal phase			Pseudo-cubic phase	
	***a*=*b* (Å)**	***c* (Å)**	**Unit cell volume (Å^3)**	***a*=*b*=*c* (Å)**	**Unit cell volume (Å^3)**
1100-1300	3.9685 (±0.0002)	4.0045 (±0.0002)	63.068 (±0.006)	3.8362 (±0.0004)	56.456 (±0.017)
1100-1400	3.9501 (±0.0001)	3.9913 (±0.0001)	62.278 (±0.003)	3.8553 (±0.0007)	57.304 (±0.029)
1250-1300	3.9629 (±0.0001)	3.9996 (±0.0001)	62.813 (±0.005)	3.8452 (±0.0003)	56.855 (±0.014)
1250-1400	3.9511 (±0.0001)	3.9917 (±0.0001)	62.316 (±0.003)	3.8533 (±0.0005)	57.214 (±0.022)
1250-1500	3.9504 (±0.0001)	3.9908 (±0.0001)	62.279 (±0.004)	--	--

The microstructure of the sintered ceramics is shown in Figure 4.8. In Figure 4.8 (A) and (B) it can be seen that the sintered ceramics from 1100 ºC calcined powders have a bimodal grain size distribution with uniform larger grains (1-2 μm) and a small amount of smaller grains (<1 μm). As shown in Figure 4.8 (C) and (D), the 1300 ºC and 1400 ºC sintered ceramics from 1250 ºC calcined powders also exhibit a similar bimodal grain size, however, the 1500 ºC sintered ceramics only have large grains (10-20 μm). Based on XRD results (Figure 4.7) and literature [92], the large grains have been interpreted as the tetragonal phase and small grains the pseudo-cubic phase.

Combining the physical properties (Table 4.3) and the microstructure of the 1100 ºC calcined ceramics (Figure 4.8 (A) and (B)) it would appear that lower porosity and higher density (≥93 %) can be obtained using these conditions. However, Figure 4.8 (C) shows the porous microstructure of 1250 ºC calcined 1300 ºC sintered ceramics, with a corresponding lower shrinkage (~11 %) and density (~84 %). With increased sintering

temperatures (1400 and 1500 ºC), as shown in Figure 4.8 (D) and (E), the ceramics become denser, with constant shrinkage and density (Table 4.3).

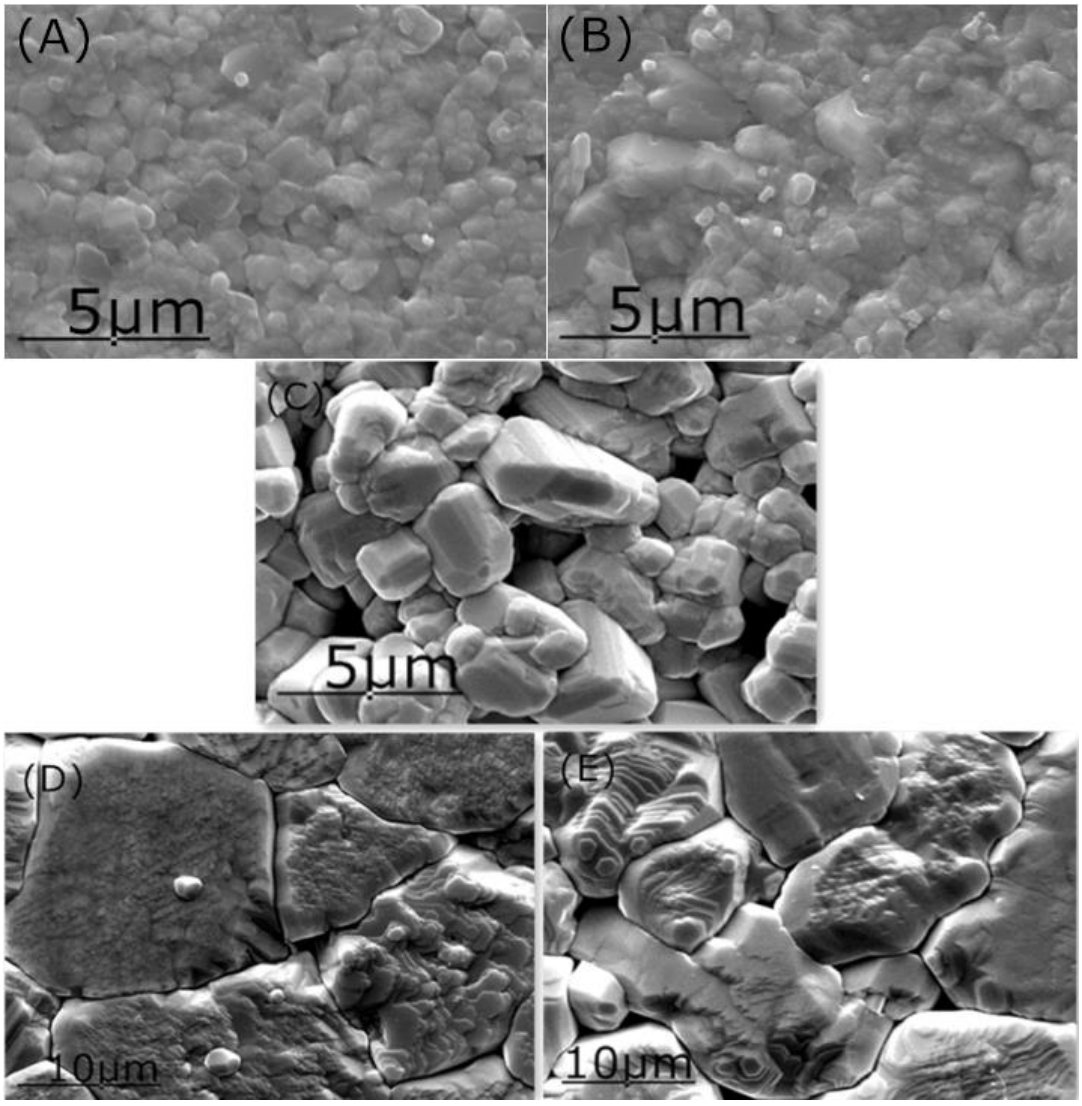

Figure 4.8. SEM images of sintered $Ba_{0.70}Ca_{0.30}TiO_3$ ceramics: (A) 1100-1300; (B) 1100-1400; (C) 1250-1300; (D) 1250-1400; (E) 1250-1500 (Sample Name: Calcination temperature (ºC)-Sintering temperature (ºC)).

4.3 Fabrication method 2 of $Ba_{0.70}Ca_{0.30}TiO_3$ ceramics

It has been shown above that the expected single $Ba_{0.70}Ca_{0.30}TiO_3$ phase could not be

formed by calcination or lower sintering temperatures in fabrication method 1, therefore another fabrication method (method 2) was investigated to form $Ba_{0.70}Ca_{0.30}TiO_3$ ceramics, using $BaTiO_3$ and $CaTiO_3$ as reagents. The corresponding fabrication procedure was described in section 3.1.1.2.

4.3.1 Fabrication of $BaTiO_3$ and $CaTiO_3$

The pure tetragonal $BaTiO_3$ could be formed by calcining $BaCO_3$ and TiO_2 at 1100 ºC for 2h, as shown in Figure 4.9. This shows that a calcination temperature of 1100 ºC (for 2 hours) is suitable for the formation of $BaTiO_3$. However, when $CaCO_3$ and TiO_2 are calcined at 850 ºC, a mixture of unreacted 18.4 wt. % CaO (fitted with PDF-number: 01-070-5490), 11.7 wt. % $CaCO_3$ (01-071-2392 41-1475), 44.2 wt. % Rutile TiO_2 and 1.9 wt. % Anatase TiO_2 (measured at room temperature) is found with only 23.9 wt. % orthorhombic $CaTiO_3$ (01-081-0561 42-423) formed (shown in Figure 4.10 (A)). Therefore, 850 ºC (for 2 hours) is insufficient temperature to form pure $CaTiO_3$ and a higher temperature (1100 ºC) has been chosen to form $CaTiO_3$. Where more $CaTiO_3$ phase (64.9 wt. %) could be formed with less unreacted CaO (15.2 wt. %) and Rutile TiO_2 (19.9 wt. %), as shown in Figure 4.10 (B). Therefore, higher calcination temperature contributes to better formation of $CaTiO_3$ and the pure $CaTiO_3$ phase is hard to be produced by calcination. As the ultimate aim is to form pure $Ba_{0.70}Ca_{0.30}TiO_3$ phase, both 850 ºC and 1100 ºC calcined $CaTiO_3$ reacting with $BaTiO_3$ could be used to study the formation of pure $Ba_{0.70}Ca_{0.30}TiO_3$ phase.

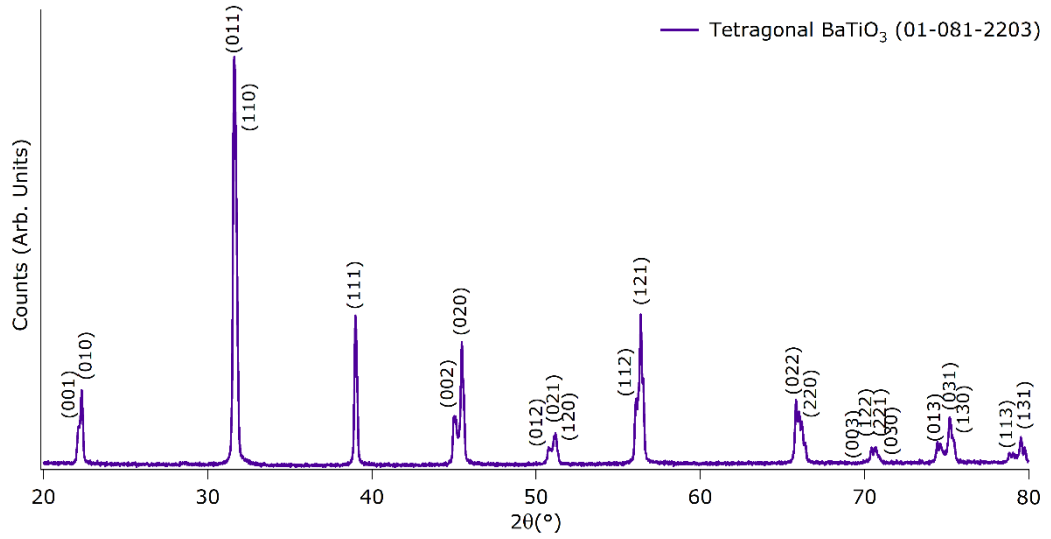

Figure 4.9. XRD pattern of 1100 ºC calcined $BaCO_3$+TiO_2.

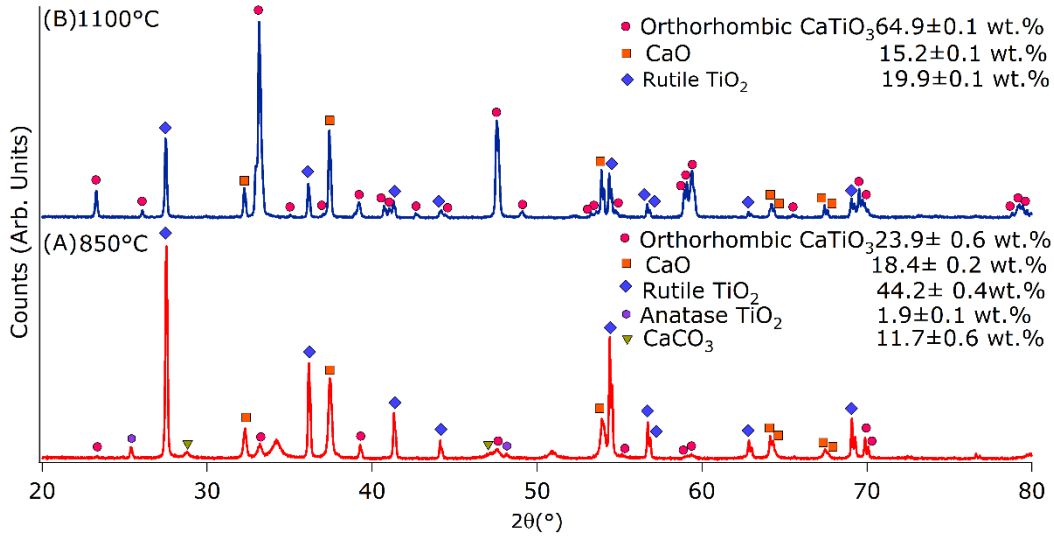

Figure 4.10. XRD pattern of (A) 850 ºC and (B) 1100 ºC calcined $CaCO_3$+TiO_2.

4.3.2 850 ºC formed $CaTiO_3$ reacted with $BaTiO_3$

4.3.2.1 Optimising the fabrication route

In Chapter 3 (Figure 3.2), two routes were outlined for the fabrication of $Ba_{0.70}Ca_{0.30}TiO_3$. In Route A the ceramics are formed by sintering a mixture of 850 ºC calcined $CaTiO_3$ and 1100 ºC calcined $BaTiO_3$, and the XRD patterns corresponding to 1300 ºC and 1400 ºC

sintered ceramics are shown in Figure 4.11. The refined lattice parameters are detailed in Table 4.5. A better homogeneity was achieved by using a higher sintering temperature (1400 ºC) with more Ca^{2+} substitution and more Ba-rich tetragonal phase. However, as the fully homogeneity could not be achieved by either sintering temperature, therefore, a double calcination step (Route B in Figure 3.2) was investigated to form the $Ba_{0.70}Ca_{0.30}TiO_3$ phase.

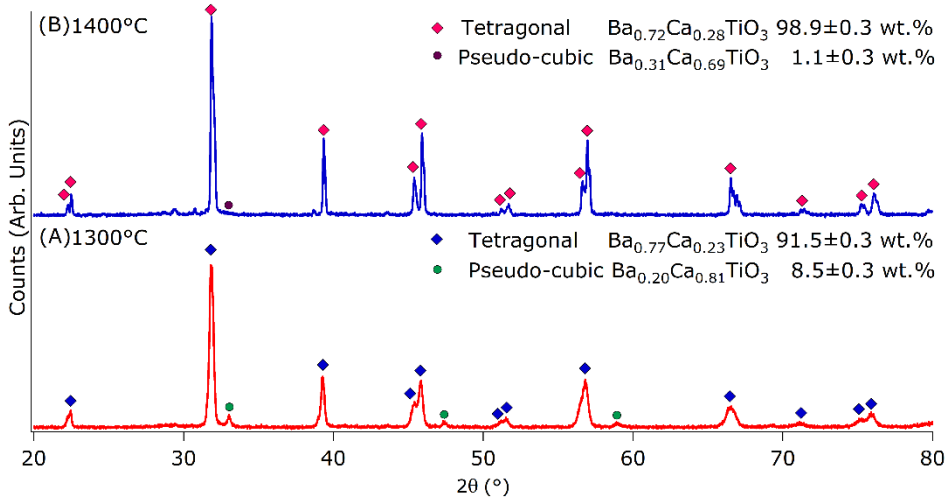

Figure 4.11. XRD patterns of (A) 1300 ºC and (B) 1400 ºC sintered ceramics from 850 ºC calcined $CaTiO_3$ and 1100 ºC calcined $BaTiO_3$ (Route A).

The XRD patterns of 1100 ºC double calcined powders from the mixture of 850 ºC calcined $CaTiO_3$ and 1100 ºC calcined $BaTiO_3$ (Route B) are shown in Figure 4.12 (A). And the XRD patterns of sintered ceramics from the double calcined powders are shown in Figure 4.12 (B), with lattice parameters listed in Table 4.5. Compared with Route A (Figure 4.11), double calcination yields better homogeneity at each sintering temperature. Therefore, the double calcination step was the chosen fabrication procedure for a study of the reaction between 1100 ºC calcined $CaTiO_3$ and 1100 ºC calcined $BaTiO_3$.

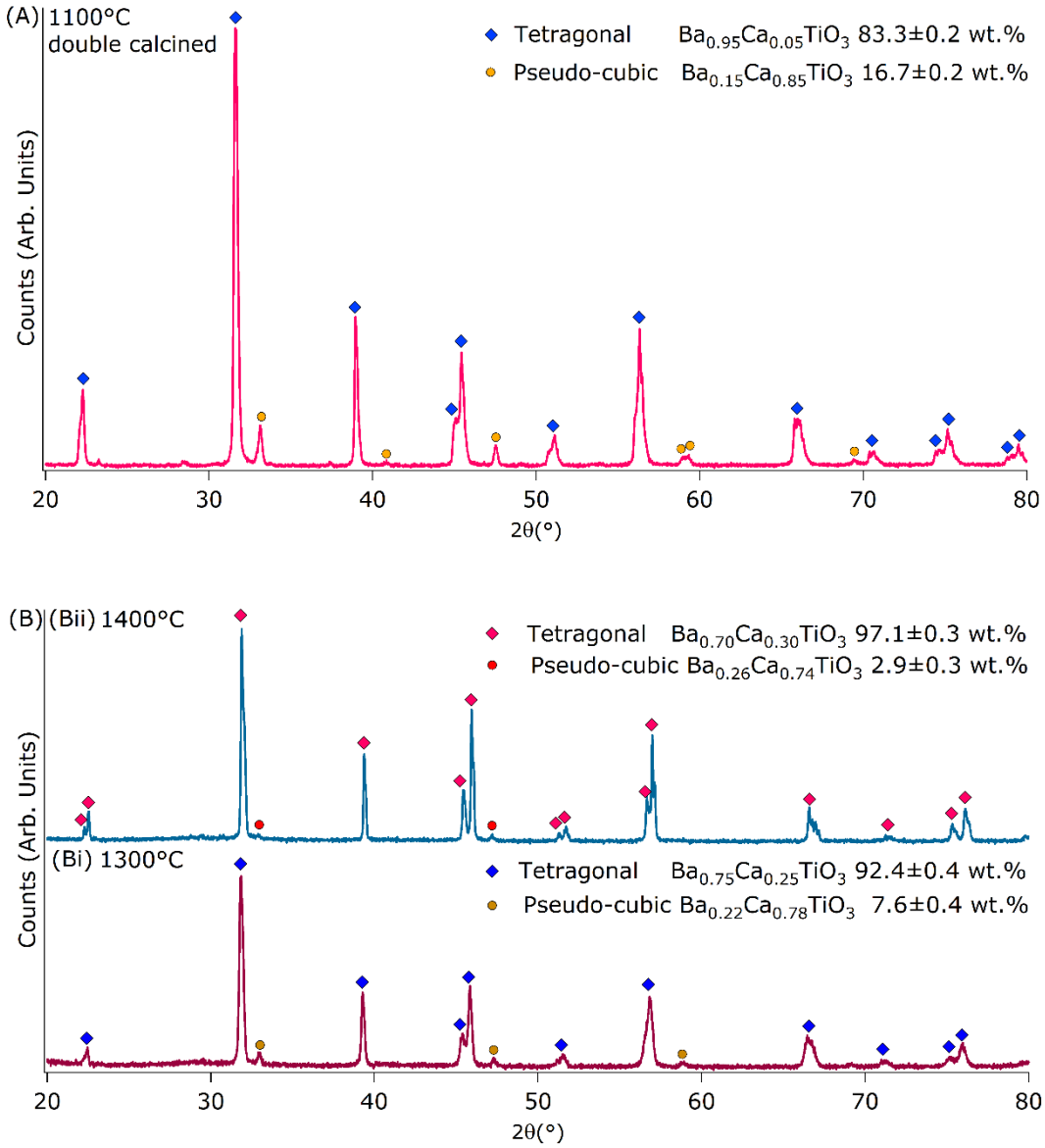

Figure 4.12. XRD patterns of (A) 1100 ºC double calcined powders from mixture of 850 ºC calcined $CaTiO_3$ and 1100 ºC calcined $BaTiO_3$; (B) 1300 ºC (Bi) and 1400 ºC (Bii) sintered ceramics from double calcined powders (Route B).

4.3.2.2 Optimising the sintering time

In has been shown above that neither fabrication route produced the desired pure tetragonal $Ba_{0.70}Ca_{0.30}TiO_3$ phase. This could be attributed to either not high enough calcination/sintering temperatures and/or insufficient time. In order to investigate the effect of sintering time, a longer sintering time (10 hours) was used for sintering powders

at 1300 ºC in both Routes A and B.

The XRD patterns and refined lattice parameters of 1300 ºC sintered ceramics (10 hours) by each route are shown in Figure 4.13 and Table 4.5. Compared with the ceramics sintered for 4 hours, as shown in Figure 4.11 and Figure 4.12 (B), longer sintering time has not resulted in further homogenisation, with similar Ca^{2+} content in the tetragonal phase and similar amount of tetragonal phase observed. Therefore, all subsequent fabrications used 4 hours as the sintering time.

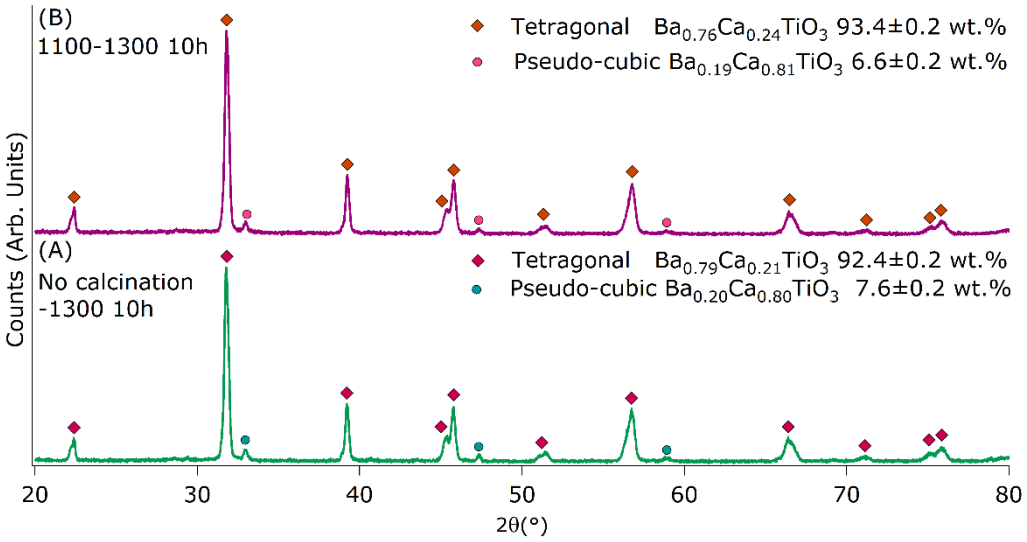

Figure 4.13. XRD patterns of 1300 ºC sintered (10 hours) ceramics from (A) no double calcined (Route A) and (B) 1100 ºC double calcined mixture of 850 ºC calcined $CaTiO_3$+1100 ºC calcined $BaTiO_3$ (Route B).

4.3.3 1100 ºC formed $CaTiO_3$ reacted with $BaTiO_3$

The XRD pattern of 1100 ºC double calcined powders from 1100 ºC calcined $CaTiO_3$ and $BaTiO_3$ is shown in Figure 4.14 (A). And the XRD patterns of sintered ceramics from the double calcined powders are shown in Figure 4.14 (B), with the corresponding lattice

parameters listed in Table 4.5. Compared with the double calcined powders or sintered ceramics from 850 ºC calcined $CaTiO_3$ and 1100 ºC $BaTiO_3$ (shown in Figure 4.12), the 1100 ºC calcined $CaTiO_3$ does not produce a more homogeneous Ba-rich tetragonal phase. The presence of unreacted $CaO/CaCO_3$ in the 850 ºC calcined $CaTiO_3$ could contribute to a better mobility for Ca^{2+} into $BaTiO_3$ than 1100 ºC calcined $CaTiO_3$.

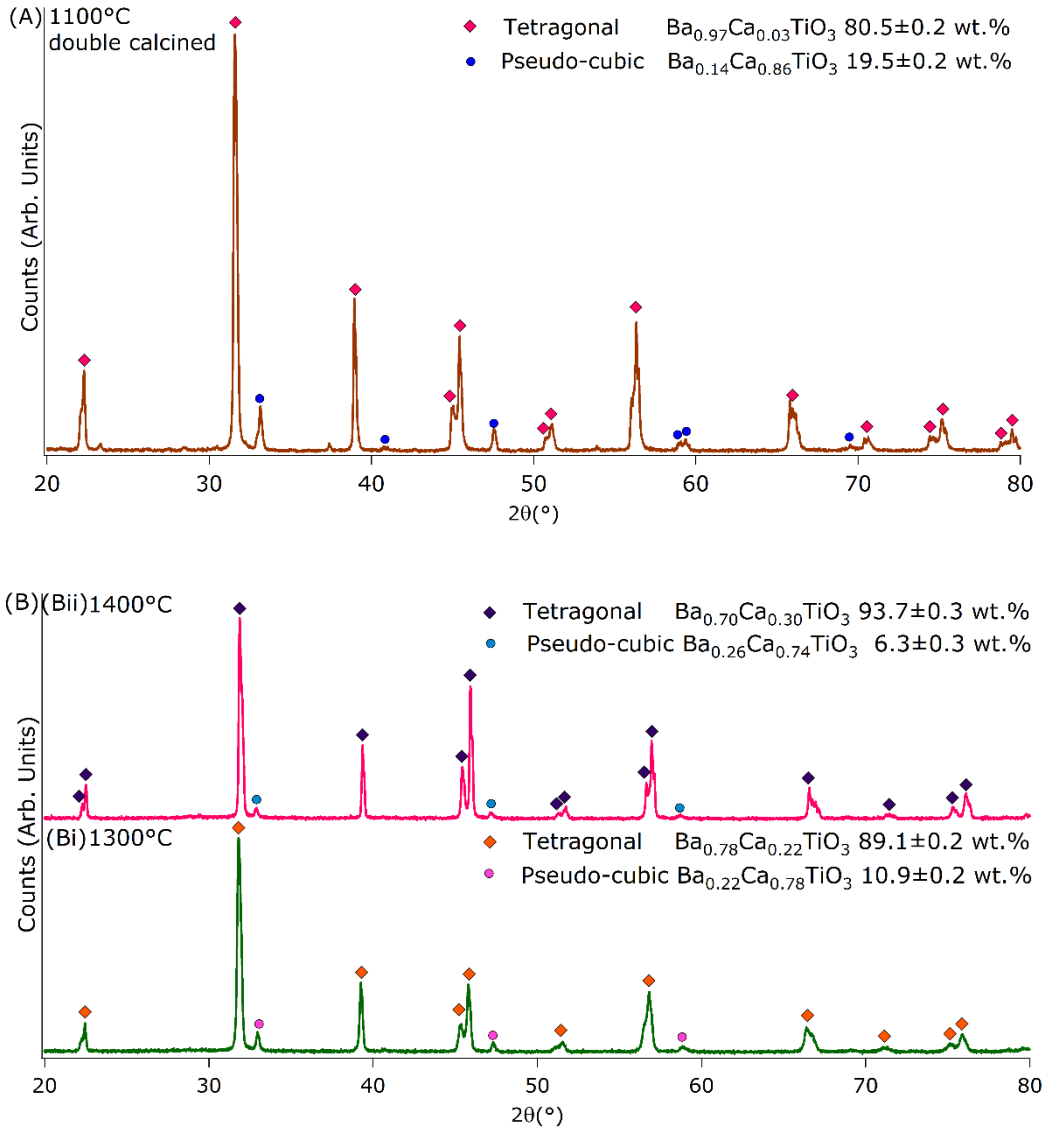

Figure 4.14. The XRD patterns of (A) 1100 ºC double calcined powders from 1100 ºC calcined $CaTiO_3$ and $BaTiO_3$; (B) 1300 ºC (Bi) and 1400 ºC (Bii) sintered ceramics from 1100 ºC double calcined powders.

Table 4.5. The unit cell parameters of sintered $Ba_{0.70}Ca_{0.30}TiO_3$ ceramics (fabricated by method 2) from XRD (Route B1 and B2 refer to 1100 °C double calcination of 850 °C calcined $CaTiO_3$+1100 °C calcined $BaTiO_3$ and 1100 °C calcined $CaTiO_3$+1100 °C calcined $BaTiO_3$ respectively).

Fabrication route & sintering of ceramics	**Tetragonal phase**			**Pseudo-cubic phase**	
	***a*=*b* (Å)**	***c* (Å)**	**Unit cell volume (Å^3)**	***a*=*b*=*c* (Å)**	**Unit cell volume (Å^3)**
Route A 1300 °C (4h)	3.9638 (±0.0009)	4.0007 (±0.0009)	62.858 (±0.031)	3.8380 (±0.0009)	56.536 (±0.041)
Route A 1300 °C (10h)	3.9658 (±0.0010)	4.0032 (±0.0010)	62.961 (±0.035)	3.8407 (±0.0010)	56.652 (±0.044)
Route A 1400 °C (4h)	3.9538 (±0.0003)	3.9966 (±0.0003)	62.477 (±0.011)	3.8644 (±0.0044)	57.709 (±0.197)
Route B1 1300 °C (4h)	3.9601 (±0.0009)	3.9966 (±0.0010)	62.676 (±0.033)	3.8437 (±0.0010)	56.786 (±0.045)
Route B1 1300 °C (10h)	3.9625 (±0.0011)	3.9984 (±0.0011)	62.780 (±0.037)	3.8391 (±0.0011)	56.582 (±0.047)
Route B1 1400 °C (4h)	3.9518 (±0.0001)	3.9932 (±0.0001)	62.360 (±0.003)	3.8535 (±0.0009)	57.222 (±0.042)
Route B2 1300°C (4h)	3.9641 (±0.0005)	4.0026 (±0.0005)	62.896 (±0.017)	3.8448 (±0.0005)	56.834 (±0.022)
Route B2 1400 °C (4h)	3.9518 (±0.0001)	3.9924 (±0.0001)	62.348 (±0.003)	3.8544 (±0.0005)	57.263 (±0.020)

4.4 Fabrication method of $BaZr_{0.20}Ti_{0.80}O_3$ ceramics

The $BaZr_{0.20}Ti_{0.80}O_3$ ceramics were fabricated as described in section 3.1.2. The characterisations of formed powders and ceramics after each step were discussed in this section, in order to conclude the optimised fabrication condition for $BaZr_{0.20}Ti_{0.80}O_3$ ceramics.

4.4.1 Optimising the calcination temperature

The DSC-TGA of a mixture of the $BaCO_3$, ZrO_2 and TiO_2 starting materials was measured to observe the reaction temperature of reagents, and the results are shown in Figure 4.15.

The mixture of $BaCO_3+0.2ZrO_2+0.8TiO_2$ is expected to have 15.39 % mass loss during heat treatment due to the released CO_2 from the $BaCO_3$ decomposition. In the TGA curve, it can be seen that the loss in mass starts at 756 ºC with an overall 15.17 % mass loss, which agrees with the theoretical value. The mass becomes stable again at 1050 ºC, indicating that the $BaCO_3$ has fully decomposed.

In the DSC curve, there are two exothermic peaks in the ranges of 811-857 ºC (peak I) and 857-973 ºC (II), and an endothermic peak with lowest heat flow at 1055 ºC. Similar to the mixture of $0.7BaCO_3+0.3CaCO_3+TiO_2$, shown in Figure 4.3, the exothermic peak II is attributed to the decomposition of $BaCO_3$ and the origination of peak I would be discussed in Chapter 5 (section 5.3.1). The endothermic peak is assigned to the formation

of $Ba(Zr,Ti)O_3$. As shown in Figure 4.15, the reagents complete reaction at 1055 ºC, therefore, the calcination temperatures of reagents were chosen as 1100 ºC and 1250 ºC, consistent with the values chosen for $Ba_{0.70}Ca_{0.30}TiO_3$.

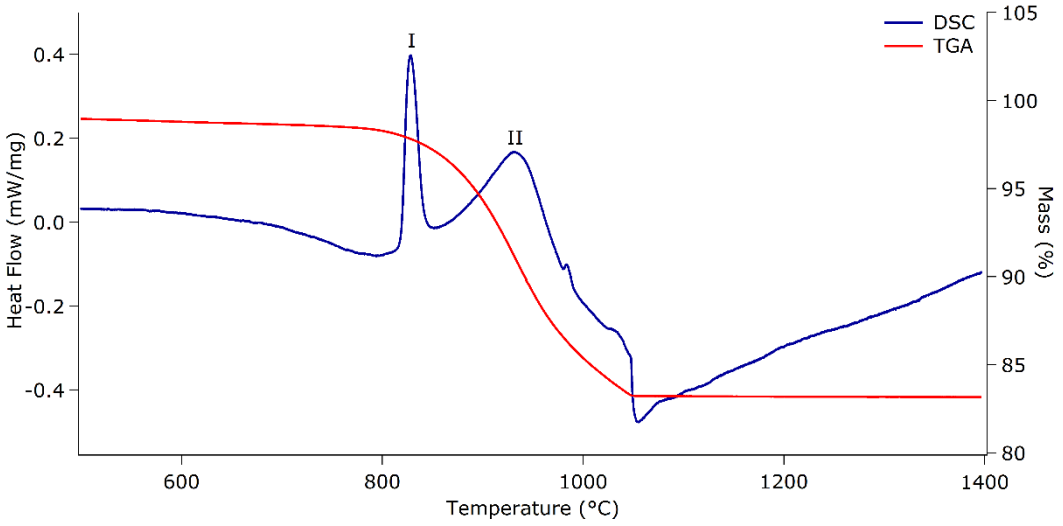

Figure 4.15. The DSC-TGA curve of heating $BaCO_3$+0.2ZrO_2+0.8TiO_2 mixture to 1400 °C at 10 °C/min.

The XRD patterns and analysed phase compositions of 1100 ºC (Figure 4.16 (A)) and 1250 ºC (Figure 4.16 (B)) calcined powders are shown in Figure 4.16. Neither of the calcination temperatures resulted in single $BaZr_{0.20}Ti_{0.80}O_3$ phase products. A tetragonal $BaTiO_3$ phase is formed as the predominant phase at both calcination temperatures. This is proved by the unit cell volume of this phase (64.449 $Å^3$) being similar to $BaTiO_3$ without any expansion from substituted Zr^{4+}. A Zr-rich cubic $Ba(Zr,Ti)O_3$ (PDF-number: 01-070-3667) and a Ti-rich cubic $Ba(Zr,Ti)O_3$ (01-079-2263) phases are also formed. As shown in Figure 4.16 (B), the higher calcination temperature yields more $BaTiO_3$ phase and more Zr^{4+} diffusion into Ti-rich $Ba(Zr,Ti)O_3$ phase (*i.e.* better homogeneity) [131].

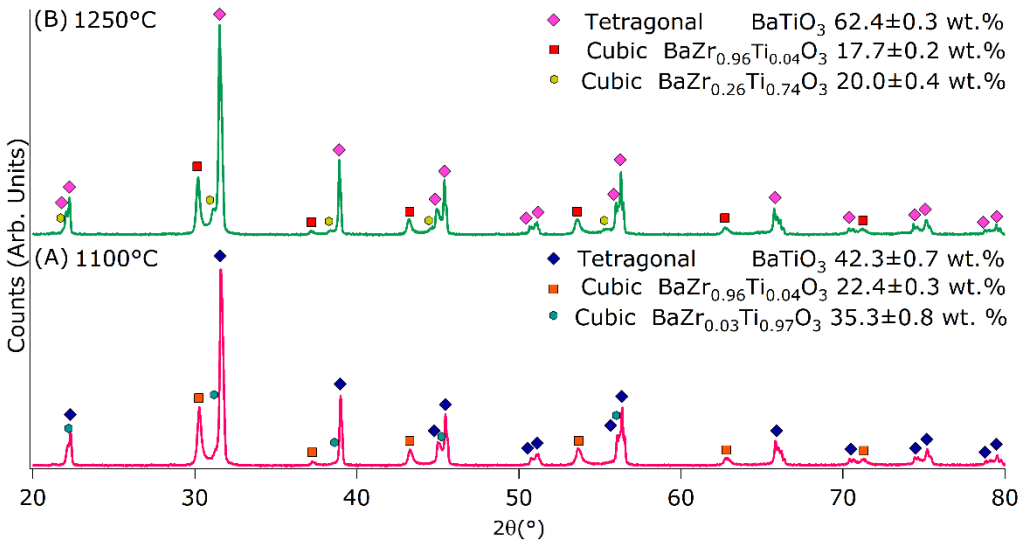

Figure 4.16. XRD patterns of (A) 1100 ºC; (B) 1250 ºC calcined mixture of $BaCO_3$, ZrO_2 and TiO_2.

4.4.2 Optimising the milling method

Table 4.6 shows the particle size of calcined $BaZr_{0.20}Ti_{0.80}O_3$ powders after milling via different methods. As shown in table, the roller ball milling method contributes to smaller particles of both temperature calcined powders than vibro milling method. Therefore, roller ball milling method was chosen for the fabrication of $BaZr_{0.20}Ti_{0.80}O_3$ ceramics in this study.

Table 4.6. Particle size of different milled calcined $BaZr_{0.20}Ti_{0.80}O_3$ powders.

Powder Name		X_{50}**(μm)**	X_{90}**(μm)**
1100ºC Calcined	Ball Milled	1.64(±0.03)	4.59(±0. 02)
	Vibro Milled	1.81(±0.04)	6.16(±0.03)
1250ºC Calcined	Ball Milled	1.52(±0.01)	2.91(±0.01)
	Vibro Milled	1.86(±0.01)	3.88(±0.04)

4.4.3 Optimising the sintering temperature

The sintering temperature of $BaZr_{0.20}Ti_{0.80}O_3$ ceramics was optimised by measuring the dimension changes of calcined $BaZr_{0.20}Ti_{0.80}O_3$ green bodies (without containing binder) upon heating, and the results are shown in Figure 4.17. As the green bodies of samples from both the 1100 ºC (A) and 1250 ºC (B) calcined powders start shrinking when the temperature is increased to around 1300 ºC, sintering temperatures of 1300 ºC-1500 ºC were used for sample fabrication.

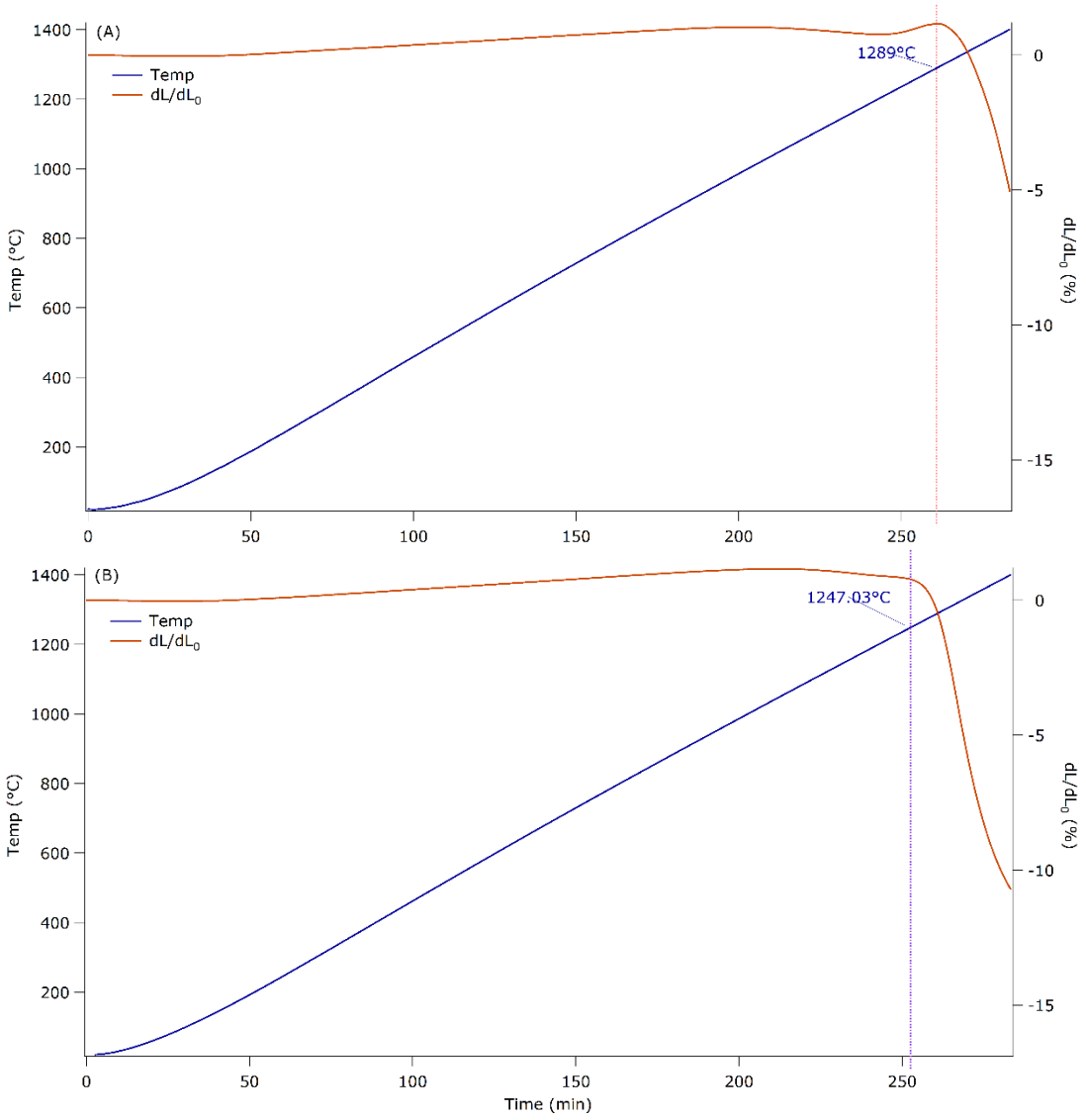

Figure 4.17. Dimension changes of (A) 1100 ºC calcined; (B) 1250 ºC calcined $BaZr_{0.20}Ti_{0.80}O_3$ green body during heating to 1500 °C at 5 °C/min in dilatometer.

Photographs of sintered $BaZr_{0.20}Ti_{0.80}O_3$ ceramics fabricated from both 1100 ºC and 1250 ºC calcined powders are shown in Figure 4.18. As shown in (A), the 1300 ºC sintered ceramics have not fully sintered or shrunk. This agrees with the corresponding physical properties (listed in Table 4.7), as 1300 ºC is just above 1289 ºC where the green body starts shrinking, this ceramic has not fully sintered with little shrinkage and low density. Therefore, no further characterisation was carried out for this ceramic. In both

photographs, the higher temperature sintered $BaZr_{0.20}Ti_{0.80}O_3$ ceramics show darker colour, being similar to the observation in $Ba_{0.70}Ca_{0.30}TiO_3$ ceramics (Figure 4.6).

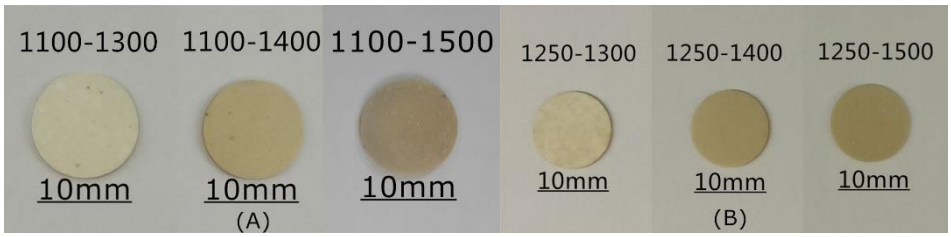

Figure 4.18. Photos of sintered ceramics. (A) photos of discs from powders calcined at 1100 ºC; (B) photos of discs from powders calcined at 1250 ºC (Sample Name: Calcination temperature (ºC)-Sintering temperature (ºC)).

Table 4.7. Physical properties of sintered ceramics (Sample Name: Calcination temperature (ºC)-Sintering temperature (ºC)).

Sample Name	**1100-1300**	**1100-1400**	**1100-1500**	**1250-1300**	**1250-1400**	**1250-1500**
Diameter Shrinkage (%)	10.51 (±0.10)	17.52 (±0.44)	16.79 (±0.08)	13.43 (±0.80)	13.23 (±0.19)	13.50 (±0.01)
Bulk density (g/cm^3)	4.44 (±0.01)	5.47 (±0.10)	5.51 (±0.05)	5.02 (±0.13)	5.23 (±0.03)	5.16 (±0.04)
Relative density (%)	--	90.53 (±1.66)	91.21 (±0.83)	83.06 (±2.15)	86.59 (±0.36)	85.38 (±0.66)

The XRD patterns of sintered ceramics are shown in Figure 4.19. A single phase is formed after sintering rather than three different phases in the calcined powders. Sintered ceramics from powders calcined at 1100 ºC (shown in (A)) form a rhombohedral $BaZr_{0.18}Ti_{0.82}O_3$ phase where the Zr^{4+} content is lower than expected from the stoichiomentric proportions of the mixed regeants. This could be attributed to the accuracy of calulation based on the referenced linear relationship of $BaZr_yTi_{1-y}O_3$ (as described in section 3.2.1.3) [223]. A systematic investigation of Vegard's relationship

for $BaZr_yTi_{1-y}O_3$ (y=0-0.30) would be studied in Chapter 6 (section 6.1), based on which the Zr^{4+} concentrations are refined as 19-20 at. % in these ceramics.

A same single phase has been found in 1300 ºC and 1400 ºC sintered ceramics from 1250 ºC calcined powders, as shown in Fig 4.18 (B). As the angle of the rhomboheral unit cell increases from 89.94º to 89.98º for ceramics sintered at 1300 ºC and 1400 ºC respectively (Table 4.8), giving rise to broader peaks in the 1300 ºC sintered ceramics rather than split sharper peaks observed in the1400 ºC sintered ceramics. When sintering samples at 1500 ºC, the peaks of XRD patterns become sharper and similar to those of the cubic phase. If the pattern is refined as a rhombohedral phase, then the angle of unit cell would be 90.03º (shown in Table 4.8). Therefore, it is not possible to distinguish between the rhombohedral and cubic structures using these patterns. This difficulty is increased as the phase boundary between rhombohedral and cubic phases occurs around 20 at. % Zr^{4+} at room temperature [227], making it therefore hard to determine the accurate phase information of the 1500 ºC sintered ceramics here. A later study of $Ba(Zr,Ti)O_3$ ceramics fabricated using the same conditions will be detailed in Chapter 6.

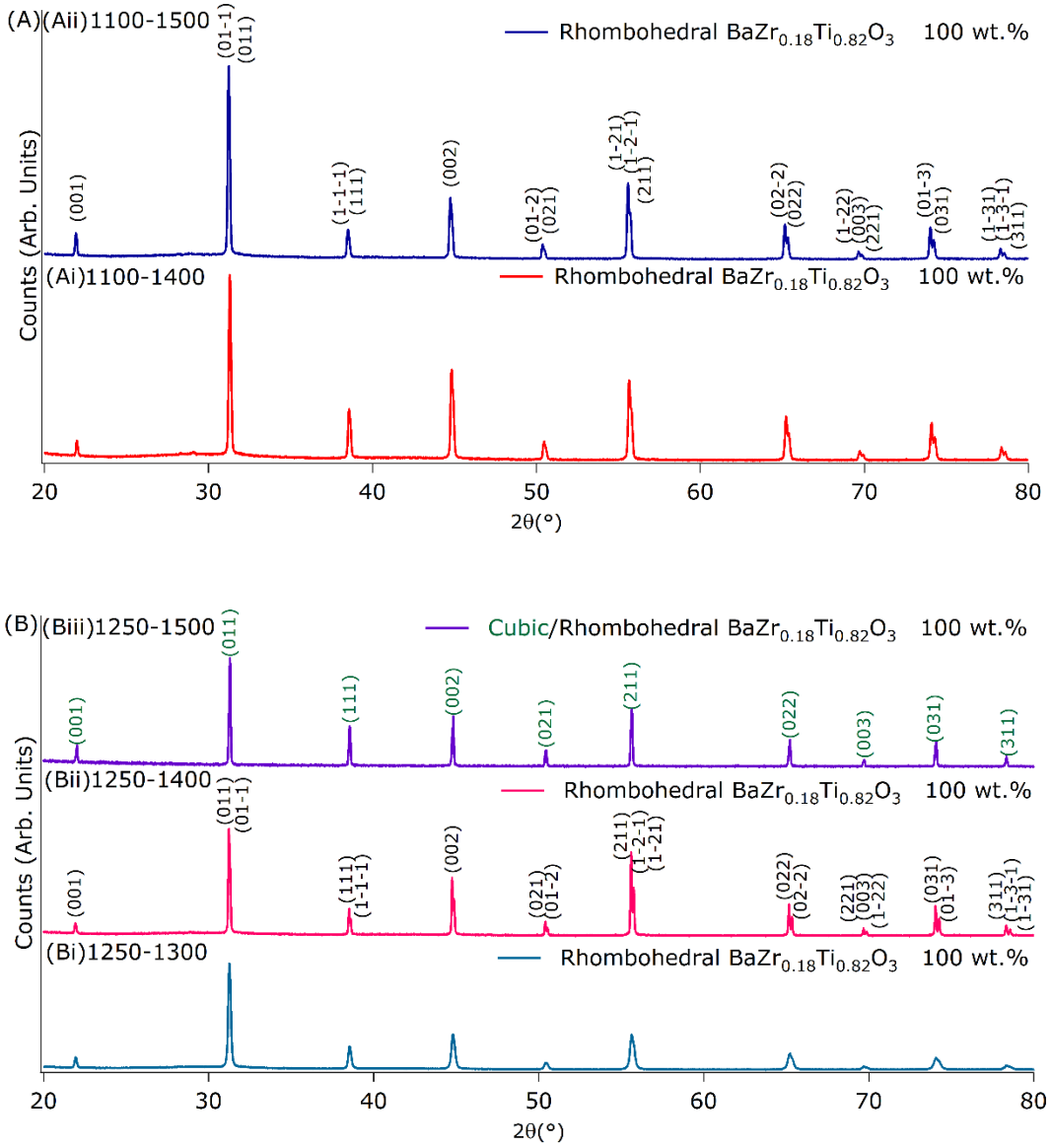

Figure 4.19. XRD patterns of sintered $BaZr_{0.20}Ti_{0.80}O_3$ from (A) 1100 ºC calcined powders; (B) 1250 ºC calcined powders: (Ai) 1100-1400, (Aii) 1100-1500, (Bi) 1250-1300, (Bii) 1250-1400 and (Biii) 1250-1500 (Sample Name: Calcination temperature (ºC)-Sintering temperature (ºC)).

Table 4.8. The unit cell parameters of sintered rhombohedral $BaZr_{0.20}Ti_{0.80}O_3$ from XRD (Sample Name: Calcination temperature (ºC)-Sintering temperature (ºC)).

Sample Name	**1100-1400**	**1100-1500**	**1250-1300**	**1250-1400**	**1250-1500**
a/b/c (Å)	4.0460 (±0.0001)	4.04629 (±0.0001)	4.04552 (±0.0001)	4.04647 (±0.0001)	4.0457 (±0.0001)
α/β/γ (º)	89.960 (±0.001)	90.036 (±0.001)	89.936 (±0.002)	89.975 (±0.001)	90.032 (±0.001)
Unit cell volume ($Å^3$)	66.233 (±0.002)	66.248 (±0.001)	66.210 (±0.003)	66.256 (±0.001)	66.216 (±0.002)

The microstructure of sintered $BaZr_{0.20}Ti_{0.80}O_3$ ceramics are shown in Figure 4.20. As shown in (A), there are some small grains (grain size around 2 μm) in the 1400 ºC sintered ceramics from 1100 ºC calcined powders, which are absent in 1500 ºC sintered ceramics (shown in (B)). As for 1250 ºC calcined samples, sintering samples at 1300 ºC results in small grains (1-2 μm) and porous structure in ceramics (shown in (C)). When sintering samples at 1400 ºC and 1500 ºC, as shown in (D) and (E), the ceramics ends up with larger grains with grain size over 20 μm.

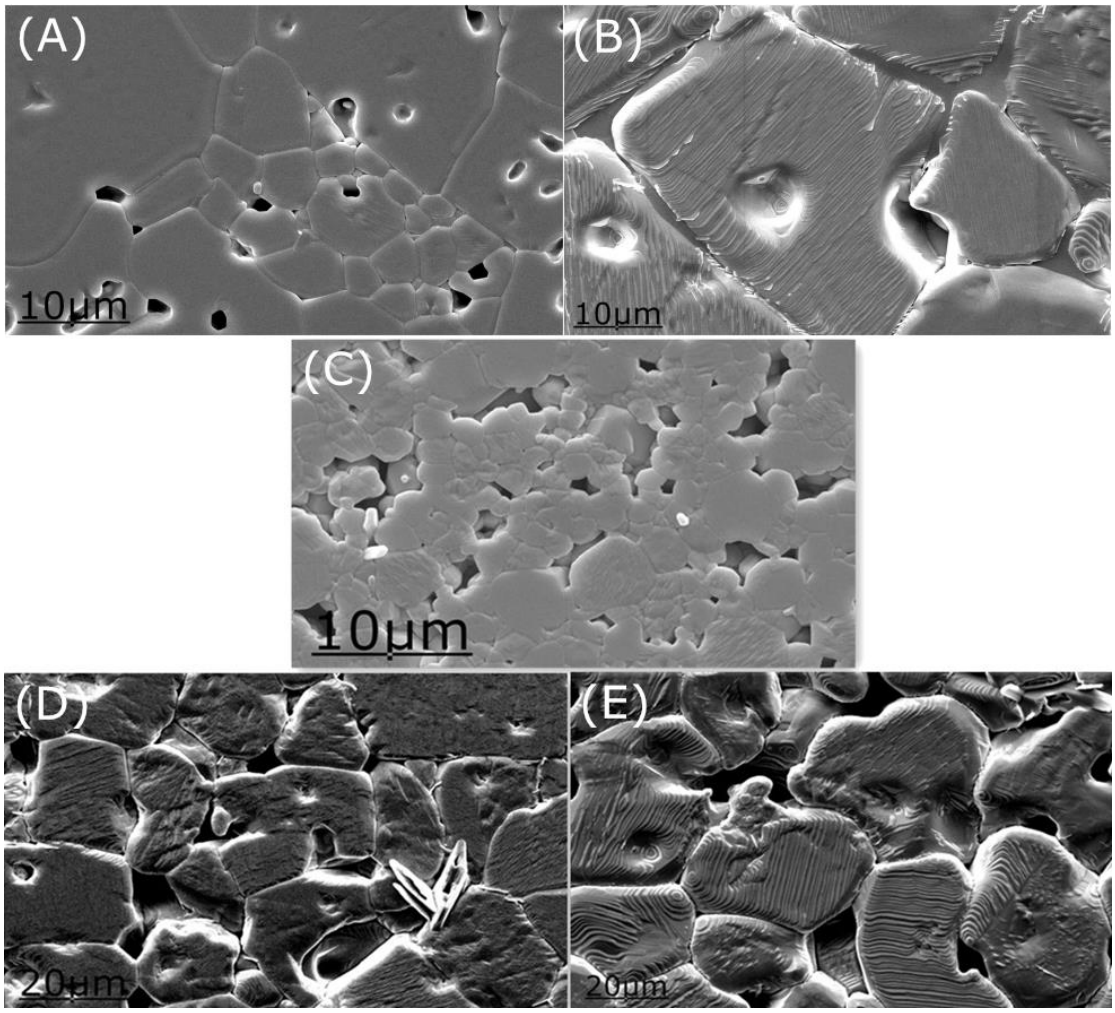

Figure 4.20. SEM images of sintered $BaZr_{0.20}Ti_{0.80}O_3$ ceramics: (A) 1100-1400; (B) 1100-1500; (C) 1250-1300; (D) 1250-1400; (E) 1250-1500 (Sample Name: Calcination temperature (ºC)-Sintering temperature (ºC)).

Combining with physical properties of the ceramics (as listed in Table 4.7), the less homogenous calcined powders (1100 ºC calcined) contributes to higher shrinkage and density of 1400 ºC and 1500 ºC sintered ceramics compared to those from 1250 ºC calcined powders. This could be caused by more reaction/homogeneity occurring during the initial sintering stage of the 1100 ºC calcined samples, which promotes densification. However, the sintered ceramics from 1250 ºC calcined powders are more porous with similar shrinkage and densities after sintering at different temperatures. The observed

larger grains in the porous structure indicate that grains grow before achieving densification in the initial sintering stage.

4.5 Summary

In conclusion, the single Ba-rich tetragonal phase with complete stoichiometric substitution of Ca^{2+} for Ba^{2+}, $Ba_{0.70}Ca_{0.30}TiO_3$, was only formed when the powders were calcined at 1250 ºC and sintered at 1500 ºC. Therefore, the fabrication method 1 (section 3.1.1.1) was used to form $Ba_{0.70}Ca_{0.30}TiO_3$ in later work. The formed tetragonal $Ba_{1-x*}Ca_{x*}TiO_3$ (x*=0, 0.03, 0.05, 0.10, 0.15, 0.20, 0.30) phases in fabricated $Ba_{0.70}Ca_{0.30}TiO_3$ ceramics from these two methods (in section 4.2 and 4.3) could be used to study the phase diagram of $Ba_{1-x*}Ca_{x*}TiO_3$ (x*=0-0.30) system (reported and discussed in section 5.1). In addition, the observed difficulty of diffusion between Ba^{2+} and Ca^{2+}, will be further investigated in section 5.3.

Compared with the fabrication of $Ba_{0.70}Ca_{0.30}TiO_3$, when fabricating $BaZr_{0.20}Ti_{0.80}O_3$, the Zr^{4+} substitution into the Ti-site is easier to achieve. The higher calcination and sintering temperatures contribute to better homogeneity but to a more porous microstructure. In this study, the fabrication of $BaZr_{0.20}Ti_{0.80}O_3$ ceramics aims to produce a homogeneous single phase. Therefore, the optimized fabrication procedure is 1250 ºC calcination and 1500 ºC sintering. A proposed future work is to investigate another fabrication methods to produce the homogeneous and dense $BaZr_{0.20}Ti_{0.80}O_3$ ceramics.

According to the optimized fabrication conditions, the formation of monophasic

$BaZr_yTi_{1-y}O_3$ (y=0-0.30) ceramics was aimed to further investigate the effects of Zr^{4+} addition into $BaTiO_3$ on: crystal structure, microstructure, phase transition behaviour and functional properties (discussed in Chapter 6).

Based on the optimized fabrication conditions for end member ceramics ($Ba_{0.70}Ca_{0.30}TiO_3$ and $BaZr_{0.20}Ti_{0.80}O_3$), the calcination temperature for forming zBCT-(1-z)BZT ceramics would also be set as 1250 ºC. Sintering temperature steps would be chosen as 1300 ºC, 1400 ºC and 1500 ºC to systematically investigate the relationship between phase compositions, microstructure and properties of all zBCT-(1-z)BZT ceramics.

Chapter 5 A study of the $Ba_{1-x*}Ca_{x*}TiO_3$ system

With reference to sections 4.2 and 4.3, the formed $Ba_{0.70}Ca_{0.30}TiO_3$ ceramics (fabrication followed section 3.1.1) contain a majority of Ba-rich tetragonal phase and a minority of Ca-rich pseudo-cubic phase. Those tetragonal compositions were written as $Ba_{1-x*}Ca_{x*}TiO_3$ with $x*$ referring to the corresponding Ca^{2+} concentrations.

In this chapter, the samples with tetragonal $Ba_{1-x*}Ca_{x*}TiO_3$ ($x*$=0, 0.03, 0.05, 0.10, 0.15, 0.20 and 0.30) compositions were studied. As described in sections 3.1.1, 4.2 and 4.3, the pure $BaTiO_3$ ($x*$=0) was produced by a calcination reaction of $BaCO_3$ with TiO_2 at 1100 °C for 2h. The two-step process of calcining $CaCO_3$ with TiO_2 at either 1100 °C or 850 °C (for 2h) and subsequent addition of $BaTiO_3$ ($BaTiO_3$:$CaTiO_3$=0.7:0.3) at 1100 °C yielded $Ba_{1-x*}Ca_{x*}TiO_3$ with $x*$=0.03 and 0.05. The $Ba_{1-x*}Ca_{x*}TiO_3$ with $x*$=0.10 and 0.15 were produced by a single calcination reaction of $BaCO_3$, $CaCO_3$ and TiO_2 (with ratios as 0.7:0.3:1) at 1100 °C and 1250 °C, respectively. The $Ba_{1-x*}Ca_{x*}TiO_3$ where $x*$=0.20 and 0.30 were produced by sintering the 1100 °C calcined samples (pressed as 13-mm discs) at 1300 °C and 1400 °C for 4h, respectively. The fabrication details are summarised in Table 5.1, where only $x*$=0.20 and 0.30 compositions were bulk ceramics and other compositions were powders.

Table 5.1. Conditions used for the synthesis of the $Ba_{1-x*}Ca_{x*}TiO_3$ samples.

Sample Name	First-step calcination of $BaCO_3$ + TiO_2	First-step calcination of $CaCO_3$ + TiO_2	Second-step calcination of $0.7BaTiO_3$+ $0.3CaTiO_3$	$0.7BaCO_3 + 0.3CaCO_3$+ TiO_2	
				Calcination	Sintering
x*=0	1100 °C	-	-	-	-
x*=0.03	1100 °C	1100 °C	1100 °C	-	-
x*=0.05	1100 °C	850 °C	1100 °C	-	-
x*=0.10	-	-	-	1100 °C	-
x*=0.15	-	-	-	1250 °C	-
x*=0.20	-	-	-	1100 °C	1300 °C
x*=0.30	-	-	-	1100 °C	1400 °C

5.1 $Ba_{1-x*}Ca_{x*}TiO_3$ (x*=0-0.30) phase diagram by Raman spectroscopy

5.1.1 Characterisation of $Ba_{1-x*}Ca_{x*}TiO_3$ (x*=0-0.30)

The room temperature XRD patterns of these $Ba_{0.70}Ca_{0.30}TiO_3$ samples with tetragonal $Ba_{1-x*}Ca_{x*}TiO_3$ (x*=0, 0.03, 0.05, 0.10, 0.15, 0.20 and 0.30) compositions are combined and shown in Figure 5.1. As discussed in sections 4.2 and 4.3, the XRD patterns (x*=0.03-0.30) show reflections corresponding to predominantly a Ba-rich tetragonal phase and a minor Ca-rich pseudo-cubic phase. In the refinement (as described in section 3.2.1.3 and Appendix I), the degree of substitution of Ca^{2+} in the tetragonal phase (x*, $\leq \pm 0.007$) was determined using the relationship with the unit cell volume proposed by Fu et al. [94]. The substitution of Ba^{2+} in the pseudo-cubic phases was refined by unit cell volumes

based on Vegard's law. The calculated compositions and quantitative phase analysis (QPA) are summarised in Table 5.2.

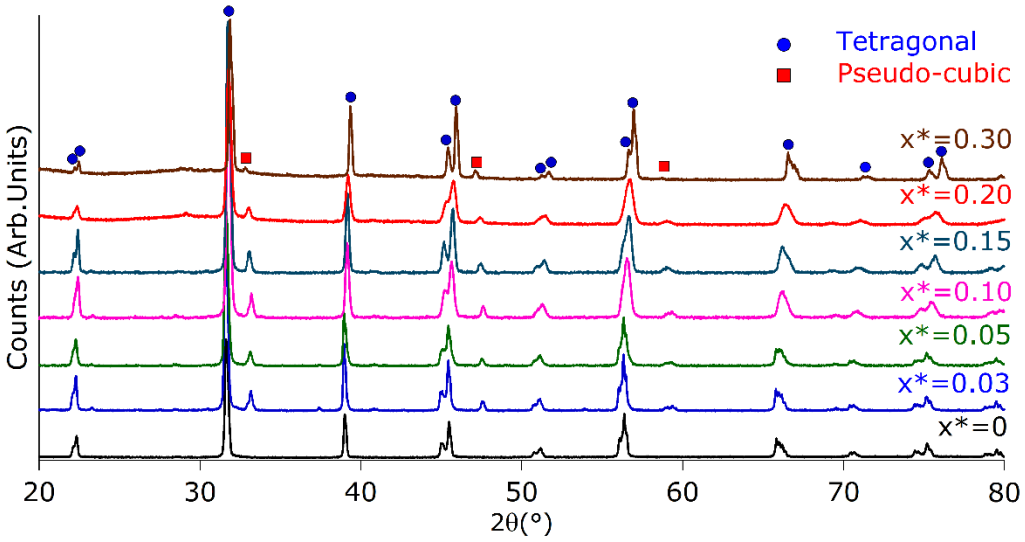

Figure 5.1. The room temperature XRD patterns of $Ba_{1-x^*}Ca_{x^*}TiO_3$ (x^*=0-0.30) samples.

Table 5.2. Quantitative phase analysis results of XRD measurements (at room temperature) of $Ba_{1-x*}Ca_{x*}TiO_3$ ($x*$=0-0.30) samples.

Sample Name	XRD QPA Results
$x*$=0	Tetragonal: $BaTiO_3$ 100 wt.%
$x*$=0.03	Tetragonal: $Ba_{0.97}Ca_{0.03}TiO_3$ 80.5±0.2 wt.% Pseudo-cubic: $Ba_{0.14}Ca_{0.86}TiO_3$ 19.5±0.2 wt.%
$x*$=0.05	Tetragonal: $Ba_{0.95}Ca_{0.05}TiO_3$ 83.3±0.2 wt.% Pseudo-cubic: $Ba_{0.15}Ca_{0.85}TiO_3$ 16.7±0.2 wt.%
$x*$=0.10	Tetragonal: $Ba_{0.90}Ca_{0.10}TiO_3$ 84.1±0.2 wt.% Pseudo-cubic: $Ba_{0.15}Ca_{0.85}TiO_3$ 15.9±0.2 wt.%
$x*$=0.15	Tetragonal: $Ba_{0.85}Ca_{0.15}TiO_3$ 85.9±0.2 wt.% Pseudo-cubic: $Ba_{0.18}Ca_{0.82}TiO_3$ 14.1±0.2 wt.%
$x*$=0.20	Tetragonal: $Ba_{0.80}Ca_{0.20}TiO_3$ 87.9±0.3 wt.% Pseudo-cubic: $Ba_{0.18}Ca_{0.82}TiO_3$ 12.1±0.3 wt.%
$x*$=0.30	Tetragonal: $Ba_{0.69}Ca_{0.31}TiO_3$ 94.3±0.4 wt.% Pseudo-cubic: $Ba_{0.27}Ca_{0.73}TiO_3$ 5.7±0.4 wt.%

As shown in Figure 4.8 (A) and (B), both large tetragonal grains and small pseudo-cubic grains are observed in the SEM micrographs of sintered $Ba_{1-x*}Ca_{x*}TiO_3$ ($x*$=0.20 and 0.30) bulk ceramics (discussed in section 4.2.3) [92]. In this project, it is therefore possible to target the tetragonal grains, using Raman imaging and comparing the obtained spectra against the reference tetragonal $BaTiO_3$ spectra (as described in sections 3.4.1 and 3.4.3). Then only the identified tetragonal grains were focused and used for the phase diagram study.

5.1.2 Raman spectra of $BaTiO_3$ powders

Figure 5.2 shows the Raman spectra of $BaTiO_3$ powders measured at four temperatures:

(A) 108 K, (B) 200 K, (C) 298 K and (D) 483 K. These four temperatures relate to the rhombohedral, orthorhombic, tetragonal and the cubic phases, respectively [80]. The Raman spectra of $BaTiO_3$ ceramics were also measured for comparison and will be discussed in section 6.2.1. As mentioned in section 2.2.4, the ideal cubic P*m3m* (O_h) perovskite has $3F_{1u}+F_{2u}$ modes which are not Raman active, however, broad peaks at 270 cm^{-1} and 528 cm^{-1} are observed, Figure 5.2 (D), the presence of these modes in the cubic phase stems from the displacement of Ti^{4+} ions from the average position which distort the perfect cubic symmetry [70].

The tetragonal P*4mm* (C_{4v}) phase of $BaTiO_3$ would give rise to $3A_1+B_1$ and 4E Raman active modes. Splitting of the Raman active A_1 and E phonons into longitudinal (along *a* direction of the unit cell, LO) and transverse (along *b* direction of the unit cell, TO) components is caused by long range electrostatic forces, giving rise to $3[A_1(LO)+A_1(TO)]+B_1$ and 4[E(LO)+E(TO)]. The Raman spectrum, Figure 5.2 (C), has 4 peaks with a sharp peak at around 310 cm^{-1} [E(TO+LO), B_1] and broader peaks at 270 cm^{-1} [A_1(TO)], 528 cm^{-1} [E(TO), A_1(TO)] and 720 cm^{-1} [E(LO), A_1(LO)], which account for 8 of the 15 active modes. Cooling to 200 K gives rise to the orthorhombic A*mm2* (C_{2v}) phase, Figure 5.2 (B), along with the 8 modes observed in the tetragonal phase, an additional peak at 188 cm^{-1} [E(TO+LO), A_1(LO)] and a weak shoulder at 489 cm^{-1} [E(TO+LO), A_1(LO)] are observed. There is also a shift in the [A_1(TO)] peak from 270 cm^{-1} to 260 cm^{-1}. Continued cooling to 108 K yields the rhombohedral R*3m* (C_{3v}) phase, Figure 5.2 (A), the shoulder at 489 cm^{-1} [E(TO+LO), A_1(LO)] has become a

distinct peak and a peak at 168 cm^{-1} [A_1(TO)] is now observed. The 260 cm^{-1} [A_1(TO)] peak further shifts to 250 cm^{-1}.

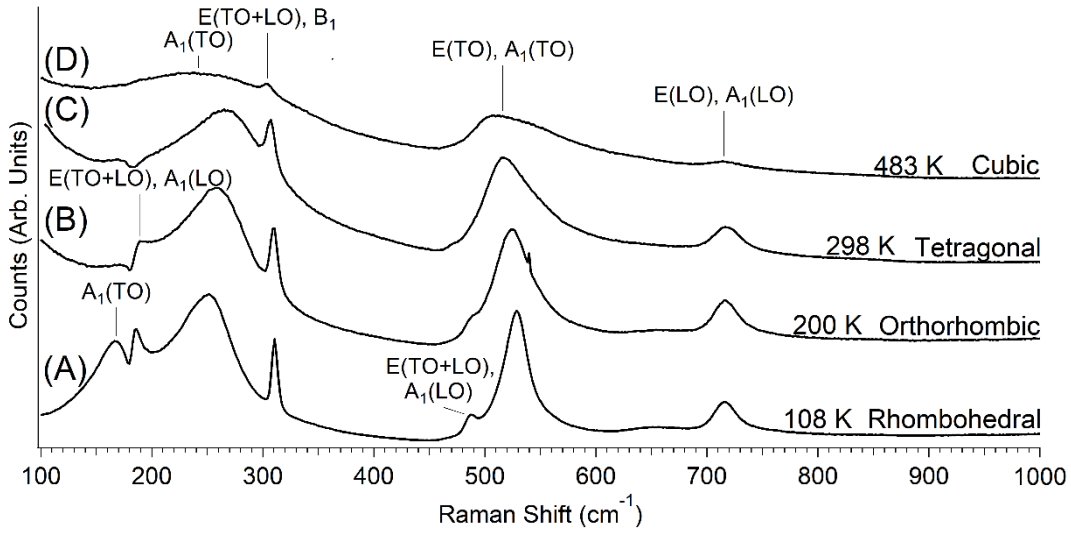

Figure 5.2. Raman spectra of $BaTiO_3$ phase at (A) 108 K (Rhombohedral), (B) 200 K (Orthorhombic), (C) 298 K (Tetragonal) and (D) 483 K (Cubic).

For this work the most significant modes are associated with the peaks at around 270 cm^{-1} [A_1(TO)] and 310 cm^{-1} [E(TO+LO), B_1] in the tetragonal phase. Figure 5.3 (A) shows the [A_1(TO)] vibrational mode, where A-site ions (Ba^{2+}) move against the Ti-O 'framework'. The peak around 310 cm^{-1} is comprised of three overlapping modes: B_1, E(TO) and E(LO), shown in Figure 5.3(B), (C) and (D), respectively. Previous research [85] has shown that the position and width of the peak around 310 cm^{-1} can be used to identify all the phase transition temperatures for $BaTiO_3$.

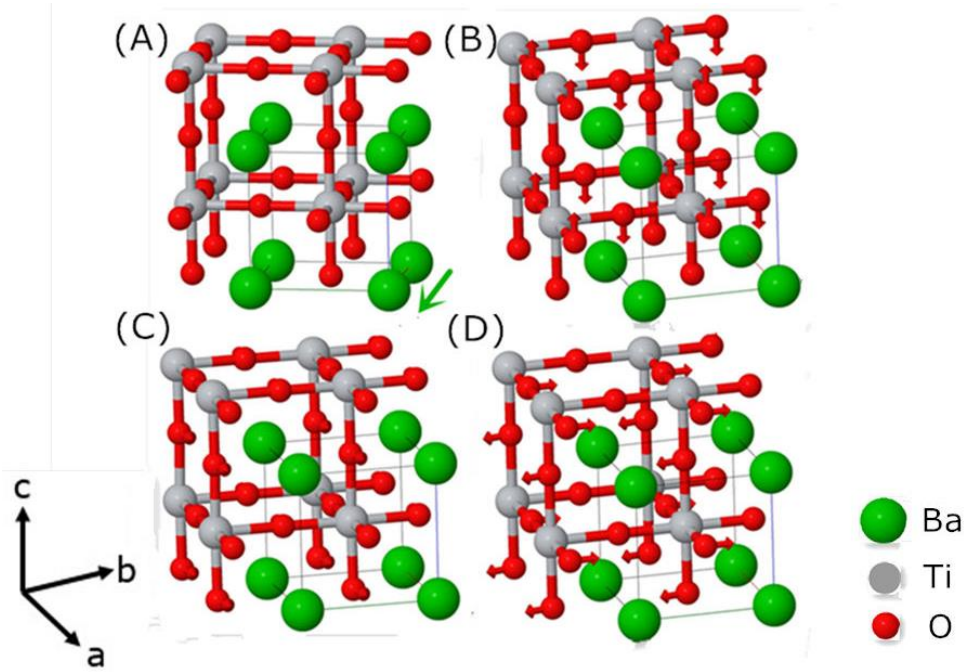

Figure 5.3. Vibrational modes for tetragonal $BaTiO_3$: (A) [A_1 (TO)] at 270 cm^{-1}, (B) B_1 at 310 cm^{-1}, (C) [E(TO)] at 310 cm^{-1} and (D) [E(LO)] at 310 cm^{-1} [63].

5.1.3 Raman spectra of tetragonal $Ba_{1-x^*}Ca_{x^*}TiO_3$ (x^*=0-0.30)

Figure 5.4 shows the room temperature (tetragonal phase) Raman spectra for $Ba_{1-x^*}Ca_{x^*}TiO_3$ (x^*=0-0.30). The absence of the 800 cm^{-1} mode indicates a complete substitution of Ca^{2+} on the Ba-site [110]. A shift to lower energy is observed for the [A_1(TO)] peak centred around the 270 cm^{-1} peak and a broadening of the [E(TO+LO), B_1] peak centred around the 310 cm^{-1} with increasing Ca^{2+} content. These peak shifts are consistent with a previous report, and may be attributed to the changes of phonon vibrations of Ti-O bonds from Ca^{2+} substitution [108]. It is noticeable that the peak broadening of the 310 cm^{-1} band is linearly dependent on the Ca^{2+} concentrations in x^*=0-0.20, and this relationship is shown in Figure 5.5. The shift of the ~520 and ~720 cm^{-1} modes to higher frequency is also observed with increasing Ca^{2+} content. This is ascribed

to the increase of force constant from increased Ca^{2+} incorporation on the Ba-site [93, 108]. Local disorder associated with the position of Ti^{4+} in cubic $BaTiO_3$ phase is observed when it is transferred from a tetragonal phase [63, 85], a similar effect is believed to be present with greater degrees of Ca^{2+} substitution, disordering the position of Ti^{4+} in the tetragonal $Ba_{1-x*}Ca_{x*}TiO_3$ giving rise to the shift and broadenings in the observed peaks.

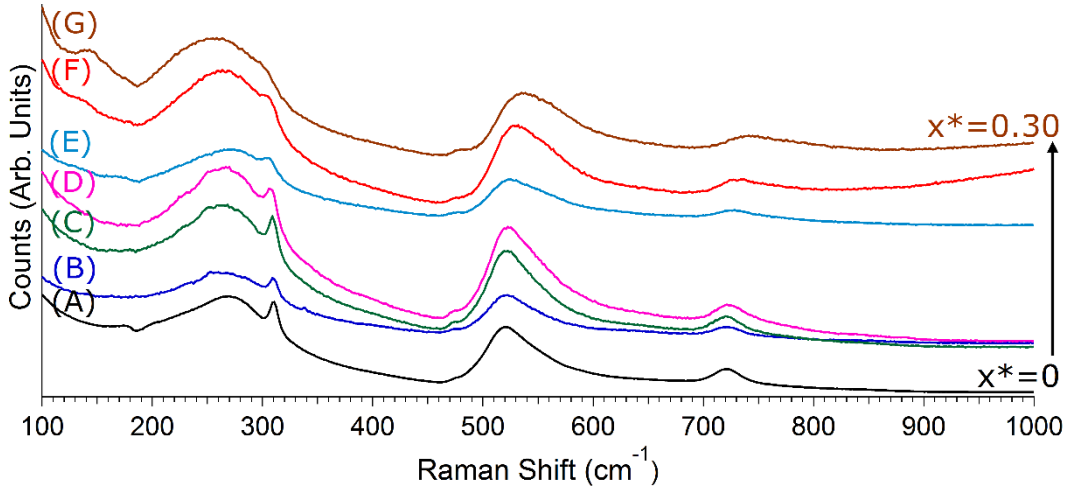

Figure 5.4. Raman spectra of $Ba_{1-x*}Ca_{x*}TiO_3$ ($x*$=0-0.30) at room temperature: (A) $x*$=0, (B) $x*$=0.03, (C) $x*$=0.05, (D) $x*$=0.10, (E) $x*$=0.15, (F) $x*$=0.20, (G) $x*$=0.30.

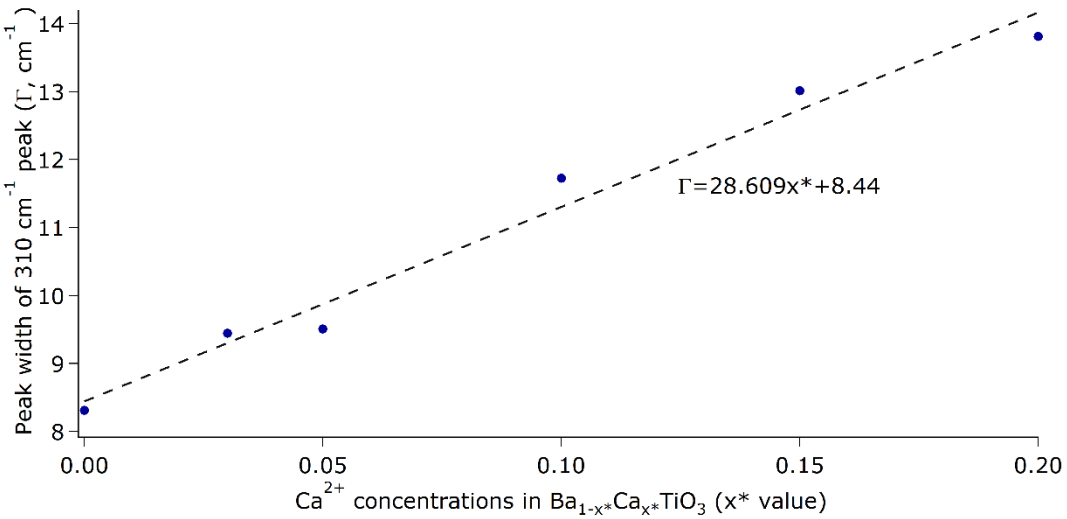

Figure 5.5. Variation in the peak width of the 310 cm^{-1} Raman peak with Ca^{2+} content in $Ba_{1-x}*Ca_{x}*TiO_3$ ($x*$=0-0.20) at room temperature.

5.1.4 Variable temperature Raman spectra of $Ba_{1-x^*}Ca_{x^*}TiO_3$ (x^*=0-0.30)

To identify the phase transitions T_{R-O}, T_{O-T} and T_{T-C} the peak position (ω) and half width half maximum (HWHM) (Γ) for the overlapping [E(TO+LO), B_1] modes at 310 cm^{-1} were measured and compared as a function of temperature for $BaTiO_3$, and are shown in Figure 5.6. Upon heating from 100 K the T_{R-O} can be observed as an increase in the peak width between 184.5 and 206.3 K for $BaTiO_3$, which is attributed to asymmetry of the perovskite primitive cell in the orthorhombic phase. The onset temperature is determined by the intercept of lines of best fit below the phase change (110-170 K) and during the phase change (180-203 K), with a transition observed for the $Ba_{1-x^*}Ca_{x^*}TiO_3$ (x^*=0.03-0.10) samples. The T_{O-T} is seen as a softening of the modes between 275.3 and 287.1 K for $BaTiO_3$, the T_{O-T} is observed in $Ba_{1-x^*}Ca_{x^*}TiO_3$ samples x^*=0.03-0.15. The [E(TO+LO), B_1] modes start to disappear in the cubic phase, therefore T_{T-C} is observed as a sudden increase in peak position and an increase in peak width at 394.2 K for $BaTiO_3$, as it is no longer possible to curve fit the peak.

As all the phase transitions here are first order [30, 81], the onset temperature is considered to be the phase transition temperature. The calibrated phase transition temperatures (detailed in section 3.3.1) for all $Ba_{1-x^*}Ca_{x^*}TiO_3$ compositions are shown in Table 5.3.

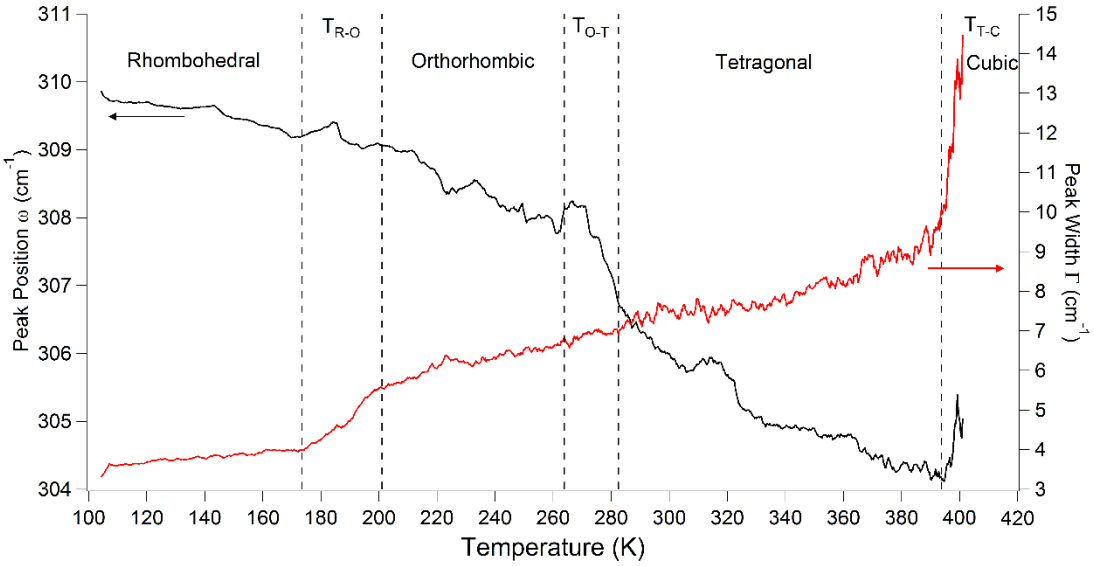

Figure 5.6. Peak width (red) and peak position (black) vs temperature for the 310 cm^{-1} Raman peak of $BaTiO_3$ ceramic.[1]

Table 5.3. Onset temperatures for the phase transition of $Ba_{1-x*}Ca_{x*}TiO_3$ (x*=0-0.30) determined by analysis of Raman spectra.[2]

Sample Name	T_{R-O} (K)	T_{O-T} (K)	T_{T-C} (K)
x*=0	184.5	275.3	394.2
x*=0.03	172.9	270.9	390.9
x*=0.05	156.1	256.9	389.5
x*=0.10	108.1	208.5	380.7
x*=0.15		168.2	375.2
x*=0.20			368.3
x*=0.30			360.1

A structural phase diagram of $Ba_{1-x*}Ca_{x*}TiO_3$ ($0 \leq x* \leq 0.30$), has been constructed using

[1] This figure is formed from peak fitting the 310 cm^{-1} peak in 640 Raman spectra during dynamic heating from 100 K to 420 K. During heating, switching off the liquid nitrogen pump can result in a temporary loss of focus on the surface of the sample. It was possible to determine this anomaly on automatic peak fitting by inspection of the individual Raman spectrum.

[2] In this table, the phase transition temperature of each composition was determined from single set measurements, therefore no error bar is displayed (as described in section 3.3).

the phase transition temperatures determined by the analysis of the Raman spectra, and is shown in Figure 5.7. The transition temperatures $T_{R\text{-}O}$ and $T_{O\text{-}T}$ decrease significantly as x^* increases, however, the Curie temperature ($T_{T\text{-}C}$) shows only a small decrease over the whole range of x^* values investigated. The relationship between the temperatures of the *R-O* or *O-T* phase boundaries and x^* value has been reported to follow the formula:

$$T \propto (x*_c - x*)^{\frac{1}{2}} \tag{5.1}$$

where x^*_C is the solubility of Ca^{2+} in $Ba_{1-x^*}Ca_{x^*}TiO_3$ at 0 K [117]. Using the structural data derived from the Raman spectroscopy measurements presented here, values of $x^*_{C(R\text{-}O)}$=0.152±0.004 and $x^*_{C(O\text{-}T)}$ =0.237±0.01 have been calculated. These values agree well with values of 0.180 and 0.233 respectively from previous work [117] based on the measurement of dielectric properties.

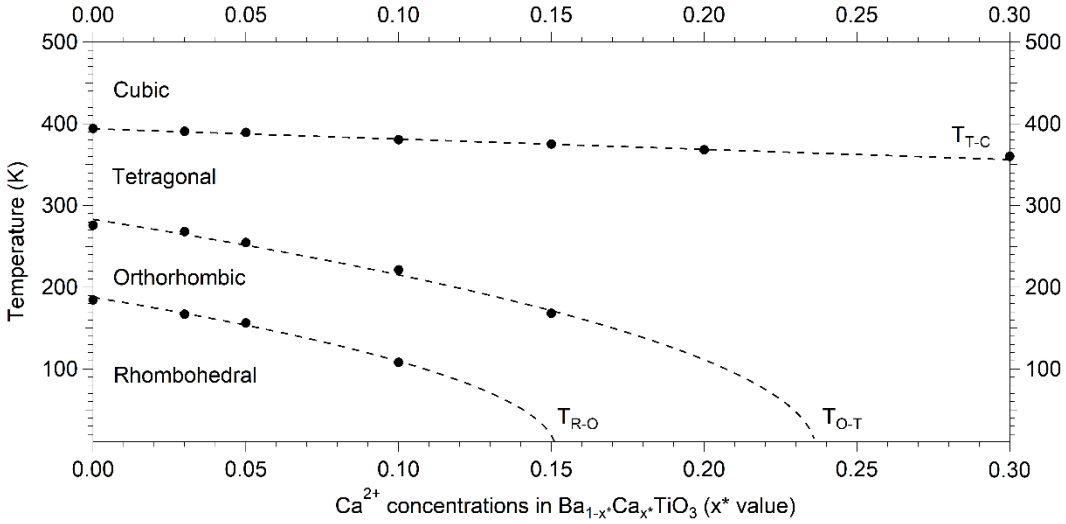

Figure 5.7. Phase diagram of $Ba_{1-x^*}Ca_{x^*}TiO_3$ ($0 \leq x^* \leq 0.30$) derived from Raman spectroscopy measurements.

5.2 Functional properties of $Ba_{1-x^*}Ca_{x^*}TiO_3$ (x^*=0.20, 0.30) bulk ceramics

The functional properties of sintered $Ba_{1-x^*}Ca_{x^*}TiO_3$ (x^*=0.20 and 0.30) ceramics at room temperature and variable temperature were measured as detailed in sections 3.2.3.3, 3.2.3.4, 3.2.3.5 and 3.3.2. The measured properties as well as their relationship to the structural information from Raman spectroscopy are reported and discussed in this section.

5.2.1 Functional properties of $Ba_{1-x^*}Ca_{x^*}TiO_3$ (x^*=0.20, 0.30) bulk ceramics (measured at room temperature)

The dielectric properties of unpoled and poled $Ba_{1-x^*}Ca_{x^*}TiO_3$ (x^*=0.20 and 0.30) bulk ceramics at room temperature are listed in Table 5.4. The $Ba_{1-x^*}Ca_{x^*}TiO_3$ (x^*=0.20) has higher relative permittivity (ε_r) than $Ba_{1-x^*}Ca_{x^*}TiO_3$ (x^*=0.30) before and after poling, which agrees with previous work that the relative permittivity decreases with increased Ca^{2+} substitution [30, 125]. This phenomenon may be caused by the presence of low permittivity $CaTiO_3$-rich phase in ceramics [125]. However, the dielectric loss ($tan\delta$) of $Ba_{1-x^*}Ca_{x^*}TiO_3$ (x^*=0.20) was lower than $Ba_{1-x^*}Ca_{x^*}TiO_3$ (x^*=0.30) before poling but higher after poling. In both cases, the lower dielectric loss has been found in poled ceramics due to the better aligned polarization achieved in the poling procedure.

Table 5.4. Dielectric properties of unpoled and poled $Ba_{1-x*}Ca_{x*}TiO_3$ ($x*$=0.20 and 0.30) bulk ceramics at room temperature.

Dielectric properties	**$Ba_{1-x*}Ca_{x*}TiO_3$ ($x*$=0.20)**		**$Ba_{1-x*}Ca_{x*}TiO_3$ ($*x$=0.30)**	
	Unpoled	**Poled**	**Unpoled**	**Poled**
Relative permittivity (ε_r)	1049±12	1035±2	607±7	618±11
Dielectric loss ($tan\delta$)	0.019±<0.001	0.018±<0.001	0.023±0.003	0.009±0.001

Figure 5.8 shows the polarization-electric field (*P*-*E*) loop of unpoled $Ba_{1-x*}Ca_{x*}TiO_3$ ($x*$=0.20 and 0.30) bulk ceramics at 25 ºC. The $Ba_{1-x*}Ca_{x*}TiO_3$ ($x*$=0.30) ceramics have higher values of remanent polarization (P_r=7.22±0.40 μC/cm^2) and coercive field (E_c=7.81±0.69 kV/cm) than $Ba_{1-x*}Ca_{x*}TiO_3$ ($x*$=0.20) ceramics, where P_r=1.95±0.02 μC/cm^2 and E_c=4.82±0.28 kV/cm. As the $Ba_{1-x*}Ca_{x*}TiO_3$ ($x*$=0.30) ceramics were sintered at higher temperature (1400 ºC) than the $Ba_{1-x*}Ca_{x*}TiO_3$ ($x*$=0.20) ceramics (1300 ºC), a better homogeneity with more tetragonal phase (see section 4.2.3) as well as a higher tetragonality (see Table 5.5) were achieved. Therefore, the $Ba_{1-x*}Ca_{x*}TiO_3$ ($x*$=0.30) ceramics have higher spontaneous polarization, resulting in higher remanent polarization.

Table 5.5. Tetragonality of $Ba_{1-x*}Ca_{x*}TiO_3$ ($x*$=0.20 and 0.30) from XRD analysis (detailed lattice parameters shown in Table 4.4).

Sample Name	***a* (Å)**	***c* (Å)**	***c/a***
$Ba_{1-x*}Ca_{x*}TiO_3$ ($x*$=0.20)	3.9685 (±0.0002)	4.0045 (±0.0002)	1.0091
$Ba_{1-x*}Ca_{x*}TiO_3$ ($x*$=0.30)	3.9501 (±0.0001)	3.9913 (±0.0001)	1.0104

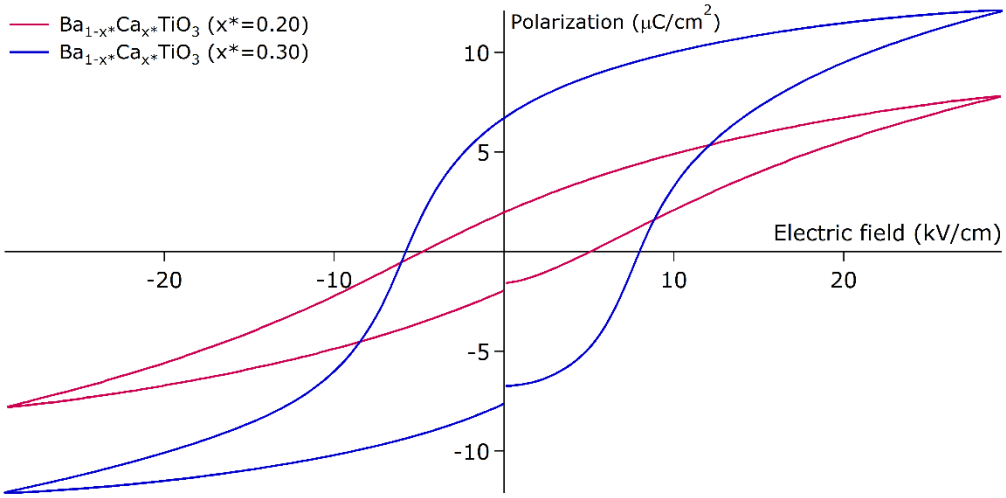

Figure 5.8. The polarization-electric field (*P-E*) loop of unpoled $Ba_{1-x*}Ca_{x*}TiO_3$ ($x*$=0.20 and 0.30) bulk ceramics at 25 ºC.

The measured values of the piezoelectric charge coefficient (d_{33}) and planar electromechanical coupling coefficient (k_p) are 78±2 pC/N and 0.22 for $Ba_{1-x*}Ca_{x*}TiO_3$ ($x*$=0.30) ceramics, and 8±2 pC/N and 0.15 for $Ba_{1-x*}Ca_{x*}TiO_3$ ($x*$=0.20) ceramics respectively. The higher values for the $Ba_{1-x*}Ca_{x*}TiO_3$ ($x*$=0.30) ceramics are consistent with the *P-E* data presented above.

5.2.2 Reorientation energy and piezoelectric properties of $Ba_{1-x*}Ca_{x*}TiO_3$ ($x*$=0.20, 0.30) bulk ceramics

Previous studies have shown that the activation energy (reorientation energy) of B-H bond vibrations in borohydride materials [228-230] could be calculated from Equation 5.2, where Γ_0 is the peak width Γ at 0 K, A' is a constant, and E_R is the reorientation energy.

$$\Gamma = \Gamma_0 + A' e^{-\frac{E_R}{RT}} \tag{5.2}$$

The relationships between the peak width (Γ) of the 310 cm^{-1} peak and temperature

reciprocal (*1/T*) of the tetragonal phase in $Ba_{1-x*}Ca_{x*}TiO_3$ ($x*$=0.20 and 0.30) ceramics are shown in Figure 5.9 (A) and (B) respectively, where the red dots are original data. The reorientation energy (E_R) then refers to the vibration energy of the Ti-O bond (Figure 5.3). The curve fitting results based on Equation 5.2 are shown as black lines in Figure 5.9, with E_R=18.65±0.01 kJ/mol for $Ba_{1-x*}Ca_{x*}TiO_3$ ($x*$=0.20) and E_R=2.53±0.05 kJ/mol for $Ba_{1-x*}Ca_{x*}TiO_3$ ($x*$=0.30).

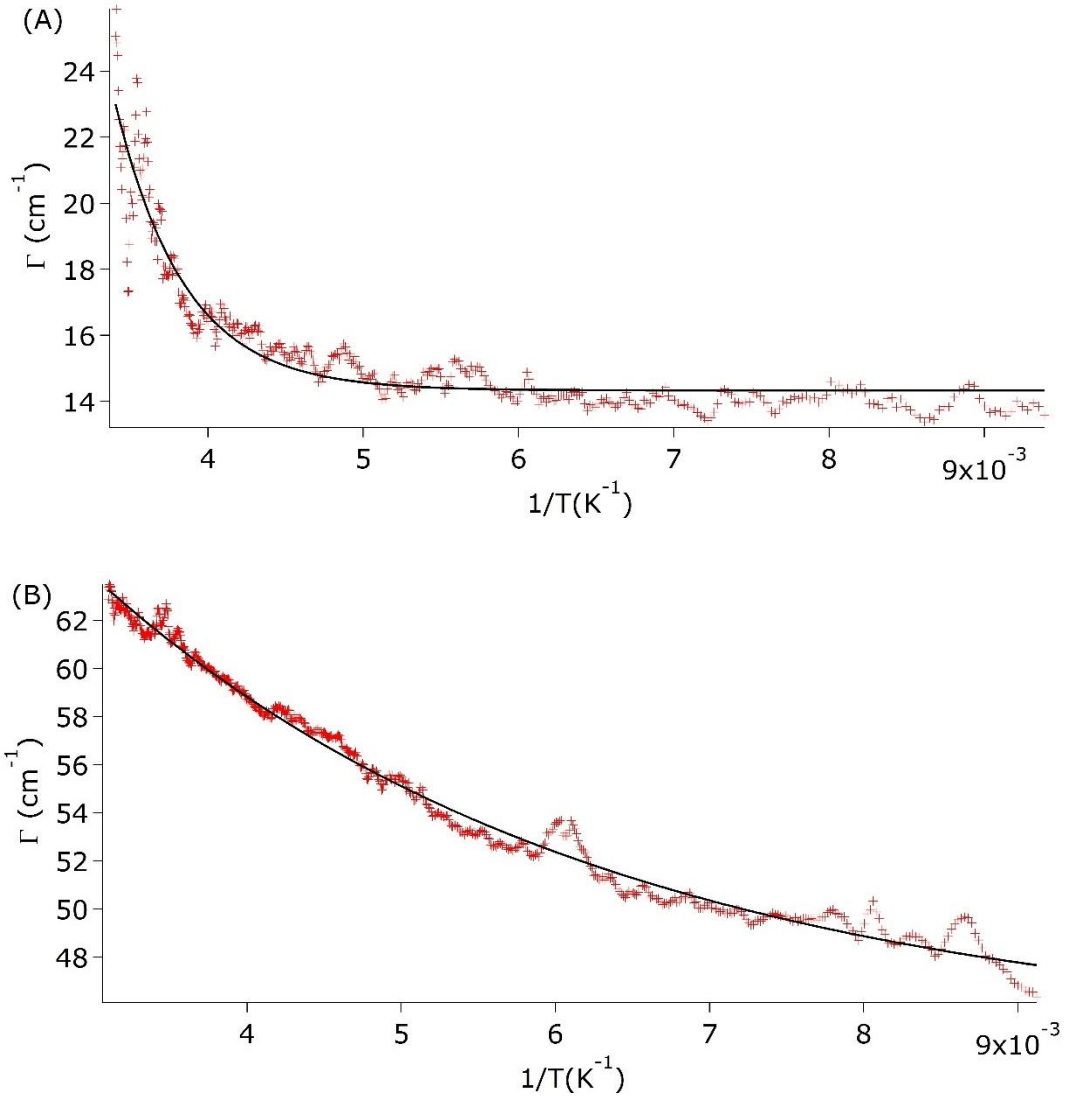

Figure 5.9. The relationship between peak width (*Γ*) and the temperature reciprocal (*1/T*) of tetragonal (A) $Ba_{1-x*}Ca_{x*}TiO_3$ ($x*$=0.20) and (B) $Ba_{1-x*}Ca_{x*}TiO_3$ ($x*$=0.30): original data (red) and fitting curve (black).

In the tetragonal $Ba_{1-x*}Ca_{x*}TiO_3$ structure, the reorientation energy (E_R) of the Ti-O bond is believed to refer to the energy barrier for Ti^{4+} switching between off-centred directions. The lower E_R in the tetragonal $Ba_{1-x*}Ca_{x*}TiO_3$ ($x*$=0.30) phase implies an easier reorientation and depolarization procedure of Ti^{4+}. However, in Figure 5.8, the corresponding coercive field of $Ba_{1-x*}Ca_{x*}TiO_3$ ($x*$=0.30) ceramics is higher than that of the $Ba_{1-x*}Ca_{x*}TiO_3$ ($x*$=0.20) ceramics. This difference between the structural and functional property measurements could be attributed to the fact that the Raman spectroscopy was only measured on discreet tetragonal $Ba_{1-x*}Ca_{x*}TiO_3$ phase, whereas the *P-E* loop was measured on the whole bulk sample containing both the $CaTiO_3$ rich and $Ba_{1-x*}Ca_{x*}TiO_3$ phases.

5.2.3 Temperature dependent functional properties of $Ba_{1-x*}Ca_{x*}TiO_3$ ($x*$=0.20, 0.30) bulk ceramics

The temperature dependence of the dielectric and ferroelectric properties of $Ba_{1-x*}Ca_{x*}TiO_3$ ($x*$=0.20 and 0.30) ceramics was measured between 300-430 K to observe changes between the ferroelectric and paraelectric phases. As described in section 3.3.2, the measured remanent polarization (P_r) recorded in the *P-E* loop by PZM, the calculated relative permittivity (ε_r) from the measured capacitance by the CVM measurement and impedance analyser (IFM, 1kHz) are shown in Figure 5.10. Good agreement between the heating and cooling curves in PZM and CVM was achieved.

Upon heating, the remanent polarization (P_r) of both ceramics decreases to zero (at T_1)

before increasing again. The decrease of P_r is attributed to the ceramics undergoing the phase transition from the ferroelectric tetragonal phase to the paraelectric cubic phase, when the P_r drops to zero (T=T_1), the ceramics possesses the cubic phase on average. However, the reappearance of a positive P_r value with further heating could potentially indicate the existence of some tetragonal clusters from off-centred Ti^{4+} in the disordered cubic structure. Therefore, combined with the appearance of Raman modes in cubic phases (similar to $BaTiO_3$ as discussed in section 5.1.2), these results could confirm literature reports that the tetragonal to cubic phase transition is an order-disorder phase transition and the high temperature structure is only cubic on average [70, 231]. The $Ba_{1-x*}Ca_{x*}TiO_3$ (x*=0.30) ceramics have generally higher P_r values due to its higher sintering temperature as discussed in section 5.2.1.

The maximum values of relative permittivity (ε_{rmax}) by the CVM and IFM methods are observed at T=T_2 and T=T_3, respectively. The calibrated values of T_1, T_2 and T_3 are listed in Table 5.6. The difference between these temperatures could be attributed to the different measurement methods. When approaching the phase transition to the paraelectric phase, the Ti^{4+} ions are close to the centres of the unit cells, resulting in weak polarization and a reduction in remanent polarization. Therefore, the observed T_1 should be lower than actual the phase transition temperature. As for T_2 and T_3, previous work has reported that the ε_{rmax} are observed at the highest phase transition rate between tetragonal and cubic phases [70]. One possible explanation for observing the lower phase transition temperature at T_2 by CVM than T_3 by IFM could be that the higher applied electricity in

CVM measurement accelerates the mobility of ions and therefore achieves highest phase transition rate at lower temperature. The broader peak of ε_{rmax} in $Ba_{1-x*}Ca_{x*}TiO_3$ ($x*$=0.20) indicates a diffusive phase transition procedure between the tetragonal and cubic phase. Due to its lower sintering temperature, $Ba_{1-x*}Ca_{x*}TiO_3$ ($x*$=0.20) ceramics have a lower relative density (93.58 %) compared to 95.11 % for $Ba_{1-x*}Ca_{x*}TiO_3$ ($x*$=0.30) ceramics (detailed in Table 4.3), which indicates a more porous structure (see Figure 4.8 (A) and (B)), thus increasing space charge field in the $x*$=0.20 ceramics and therefore a more diffusive phase transition [215]. The less homogeneity in $Ba_{1-x*}Ca_{x*}TiO_3$ ($x*$=0.20) ceramics could be another possible origination of diffusive phase transition with the presence of microscopic composition fluctuation [148].

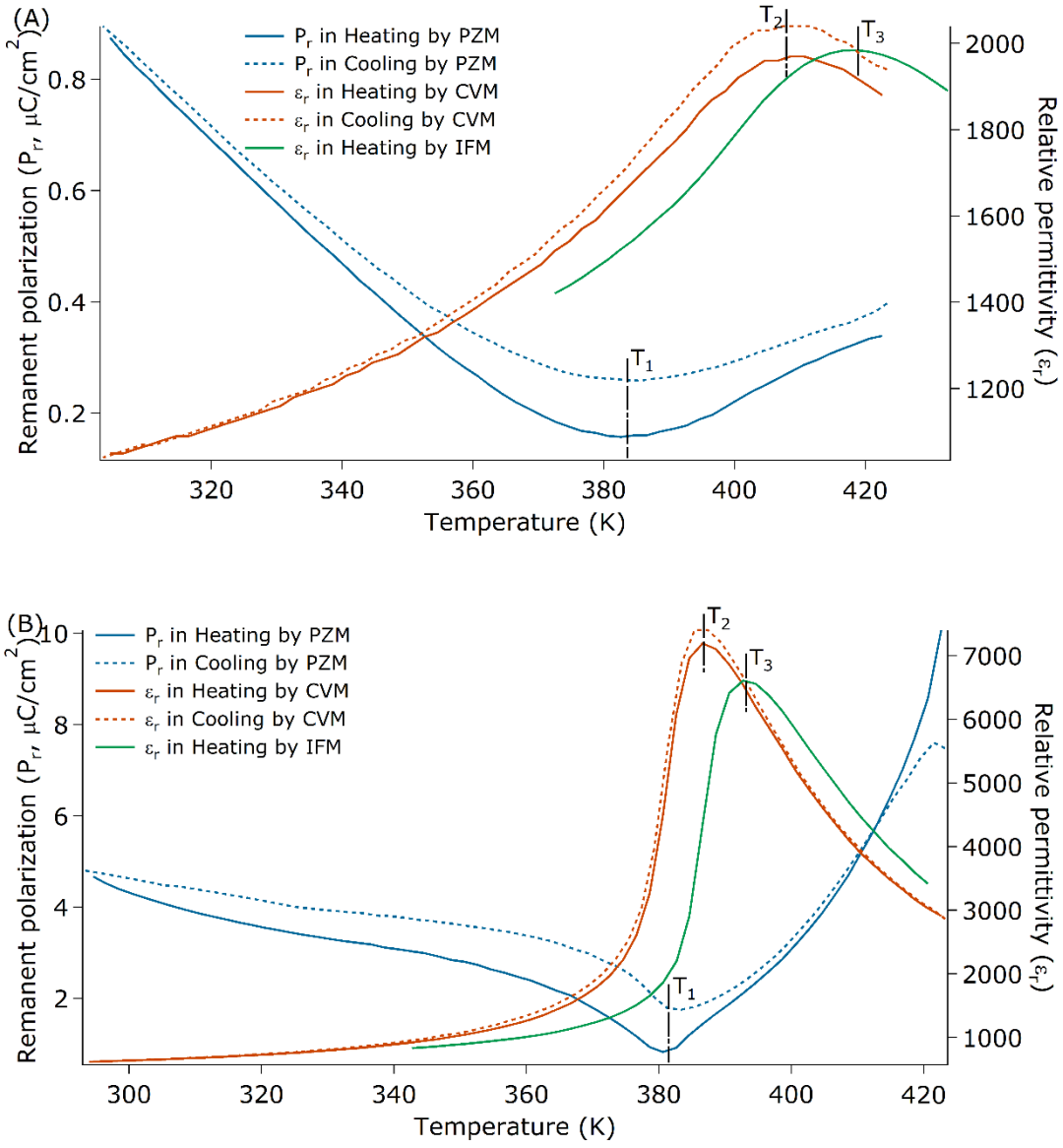

Figure 5.10. Functional property measurements of (A) $Ba_{1-x^*}Ca_{x^*}TiO_3$ (x^*=0.20) and (B) $Ba_{1-x^*}Ca_{x^*}TiO_3$ (x^*=0.30) ceramics at variable temperature.

Table 5.6. Calibrated phase transition temperatures of $Ba_{1-x*}Ca_{x*}TiO_3$ ($x*$=0.20 and 0.30) ceramics from PZM (T_1), CVM (T_2) and IFM (T_3).

Sample Name	T_1 (K)	T_2 (K)	T_3 (K)[3]
$x*$=0.20	362.0±2.0	386.0±2.2	392.3
$x*$=0.30	360.0±1.9	364.8±0.5	367.0

The temperature dependence of the relative permittivity (ε_r) of $Ba_{1-x*}Ca_{x*}TiO_3$ ($x*$=0.20 and 0.30) ceramics calculated from the measured capacitance by IFM is shown in Figure 5.11. When the temperature is lower than 375 K, the ε_r of the $Ba_{1-x*}Ca_{x*}TiO_3$ ($x*$=0.20) ceramics is higher than that of the $Ba_{1-x*}Ca_{x*}TiO_3$ ($x*$=0.30) ceramics, however at higher temperatures the situation is reversed. According to Figure 5.11, at room temperature, the lower ε_r of the $Ba_{1-x*}Ca_{x*}TiO_3$ ($x*$=0.30) ceramics coincides with the trend between the Ca^{2+} content and dielectric properties discussed in section 5.2.1, and literature reports [30]. As the relative permittivity is dependent on phase structure and temperature [30], the thermal energy could affect the Ti^{4+} movement [70]. In the lower temperature range ($T \leq 375$ K), it was shown in section 5.2.2 that the reorientation energy of Ti^{4+} movement in $Ba_{1-x*}Ca_{x*}TiO_3$ ($x*$=0.30) ceramics is smaller than for $Ba_{1-x*}Ca_{x*}TiO_3$ ($x*$=0.20) ceramics. A possible explanation to the smaller relative permittivity in $Ba_{1-x*}Ca_{x*}TiO_3$ ($x*$=0.30) ceramics at $T \leq 375$ K could be that the movement of the Ti^{4+} ion will be stuck with low thermal energy. When increasing the temperature over 375 K, the thermal energy is high enough to active the Ti^{4+} movement, therefore the $Ba_{1-x*}Ca_{x*}TiO_3$ ($x*$=0.30) ceramics with lower reorientation energy could have easier mobility of Ti^{4+}, and the

[3] The phase transition temperature (T_3) of each composition was determined from single set measurement on IFM, therefore no error bar is displayed (as described in section 3.3).

consequently higher relative permittivity.

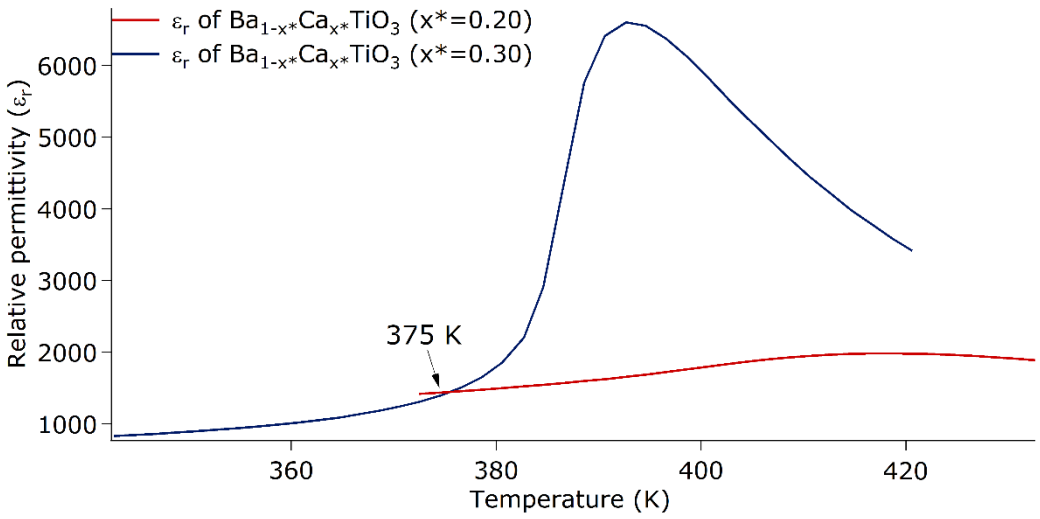

Figure 5.11. The temperature dependence of relative permittivity of $Ba_{1-x*}Ca_{x*}TiO_3$ ($x*$=0.20 and 0.30) ceramics measured by IFM.

The phase transition temperatures of $Ba_{1-x*}Ca_{x*}TiO_3$ ($x*$=0.20 and 0.30) ceramics determined by in situ functional properties can be added into the $Ba_{1-x*}Ca_{x*}TiO_3$ phase diagram (Figure 5.7). In the PZM measurement, the temperature with minimum remanent polarization (T_1) is taken as phase transition temperature between tetragonal and cubic phase. The transition temperatures in CVM and IFM measurement are recorded at the highest relative permittivity (T_2 and T_3). These phase transition temperatures from functional properties measurement (as listed in Table 5.6) are shown in Figure 5.12, which is in good agreement with the Raman spectroscopy data.

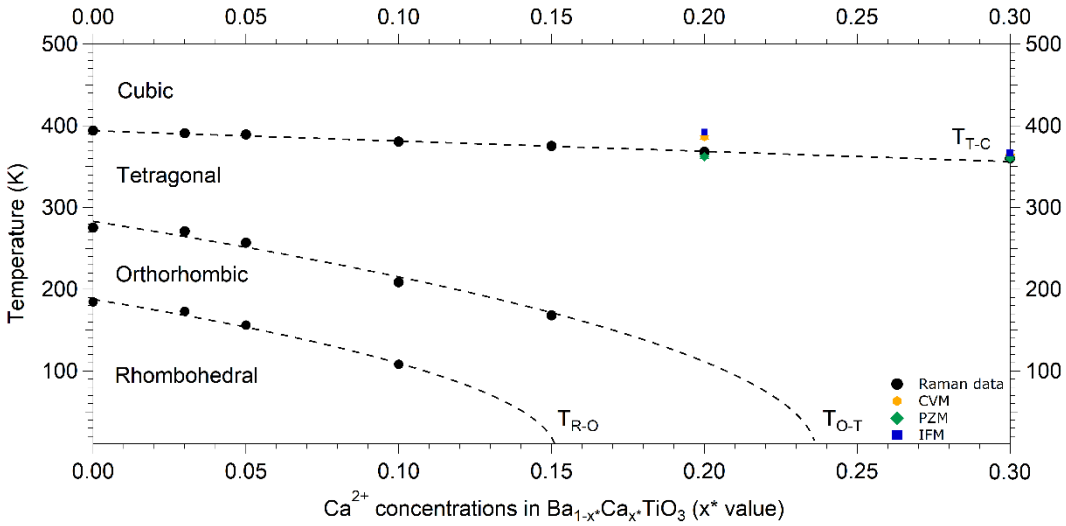

Figure 5.12. Phase diagram of $Ba_{1-x*}Ca_{x*}TiO_3$ ($0 \leq x* \leq 0.30$) derived from temperature dependent Raman spectroscopy and functional property measurements.

5.3 Mechanism of Ca-Ba diffusion in (Ba,Ca)TiO_3 ceramics

As detailed in Chapter 4, the pure $Ba_{0.70}Ca_{0.30}TiO_3$ phase is hard to attain due to the difficulty of Ca^{2+} substitution and homogenisation. Therefore, a study of the reaction mechanism between $BaTiO_3$ and $CaTiO_3$ was initiated in order to understand the mechanism of Ca^{2+} substitution onto the Ba^{2+} site.

As described in section 3.4.2, the thermal analyses by DSC-TGA were also carried out for $0.7BaCO_3+0.3CaCO_3+TiO_2$ mixture in this section. However, compared with previous study (section 4.2.1) that heating mixture at 10 °C/min in flowing air, a slower heating rate (5 °C/min) and the flowing argon were chosen, in order to maintain sufficient reaction time for mixtures and provide inert atmosphere. The in situ XRD measurement for mixed powders therefore used the same heating rate (5 °C/min) in flowing helium.

5.3.1 Reaction mechanism of $BaCO_3$, $CaCO_3$ and TiO_2

Mixtures of $CaCO_3$+TiO_2, $BaCO_3$+TiO_2 and 0.7$BaCO_3$+0.3$CaCO_3$+TiO_2 were heated to study the reaction mechanism of $BaCO_3$, $CaCO_3$ and TiO_2 as reagents to form $Ba_{0.70}Ca_{0.30}TiO_3$ ceramics. Thermal analyses of these mixtures are shown in Figure 5.13.

The mixture of $CaCO_3$+TiO_2, Figure 5.13 (A), exhibit a weight loss of 28.54 wt. % between 572 and 775 ºC corresponding to an exothermic peak (I) at 748 ºC, which is caused by the decomposition of $CaCO_3$. There is a broad endothermic peak in the DSC curve, with the minimum at 961 ºC. This peak is attributed to the formation of $CaTiO_3$.

As shown in Figure 5.13 (B), a mixture of $BaCO_3$+TiO_2 starts to decompose slowly from 737 ºC and finishes decomposition at 991 ºC with an overall mass loss of 15.50 wt. %. A broad exothermic peak at 899 ºC (III) in the DSC curve is attributed to the decomposition of $BaCO_3$. A sharp exothermic peak (II) at 824 ºC is also observed, without a change in mass, suggesting the formation of a new phase or solid-state phase transition. An endothermic peak at 991 ºC is due to the formation of $BaTiO_3$.

Figure 5.13 (C) shows the mixture of 0.7$BaCO_3$+0.3$CaCO_3$+TiO_2 and exhibits two steps of mass loss, starting at 572 ºC (5.21 wt. %) and 717 ºC (12.36 wt. %) attributed to the release of CO_2 from $CaCO_3$ and $BaCO_3$ respectively, with complete decomposition achieved at 996 ºC. Compared with mixtures $CaCO_3$+TiO_2 and $BaCO_3$+TiO_2, there is no change in the onset temperature for $CaCO_3$ decomposition. However, a reduction of 20 ºC in the $BaCO_3$ decomposition temperature is thought to be associated with the exothermic

decomposition of $CaCO_3$. Compared with Figure 4.3 (10 ºC/min heating rate), a lower heating rate in the mixture of $0.7BaCO_3+0.3CaCO_3+TiO_2$ (5 ºC/min) could contribute to longer time for releasing CO_2 from $CaCO_3$, which makes less CO_2 atmosphere in crucible and $BaCO_3$ start to release CO_2 at lower temperature. In the DSC curve, exothermic peaks at 705 ºC (I), and 899 ºC (III) correspond to the decomposition of $CaCO_3$, and $BaCO_3$ respectively as observed as in mixtures $CaCO_3+TiO_2$ and $BaCO_3+TiO_2$. The exothermic reaction at 826 ºC (II) seen in the mixture of $BaCO_3+TiO_2$ can also be seen. The broad endothermic peak at 1089ºC corresponds to the formation of $BaTiO_3$ and $CaTiO_3$, and/or $(Ba,Ca)TiO_3$.

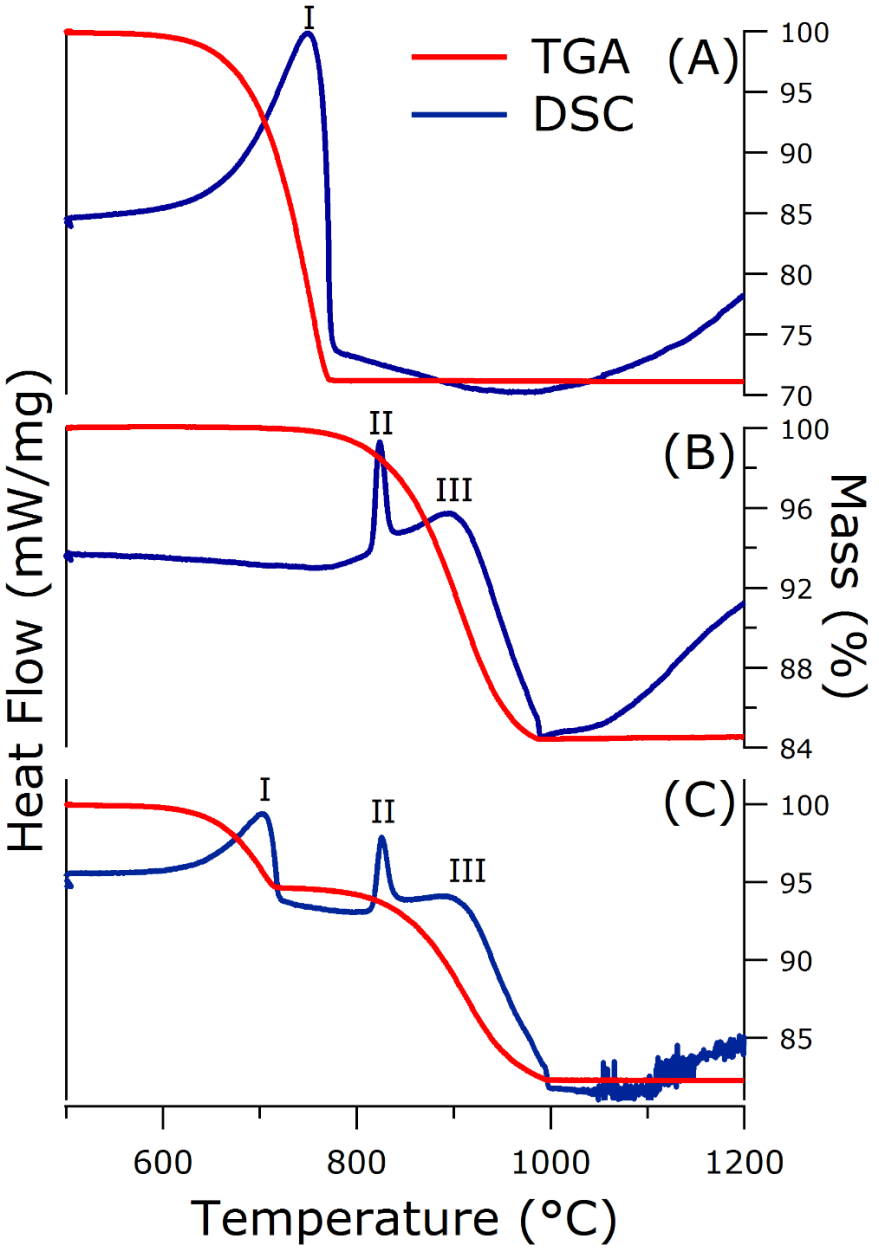

Figure 5.13. DSC-TGA curve of mixture (A) $CaCO_3$+TiO_2; (B) $BaCO_3$+TiO_2; (C) 0.7$BaCO_3$+0.3$CaCO_3$+TiO_2, heated at 5 °C/min in flowing argon.

The in situ XRD patterns of mixtures of $CaCO_3$+TiO_2, $BaCO_3$+TiO_2 and 0.7$BaCO_3$+0.3$CaCO_3$+TiO_2 heated at 5 °C/min in flowing helium are shown in Figure 5.14. Note that all patterns contain reflections corresponding to the Al_2O_3 sample container. At room temperature, all mixtures show reflections attributed to the corresponding starting materials (TiO_2, $CaCO_3$ and $BaCO_3$). For the mixture of

$CaCO_3$+TiO_2, the presence of CaO is detected at 600 ºC, further heating to 700 ºC intensifies the CaO reflections and $CaCO_3$ is no longer observed, and the presence of $CaTiO_3$ is observed at 800 ºC. The mixture of $BaCO_3$+TiO_2 shows the decomposition of $BaCO_3$ has started at 600 ºC, yielding the intermediate Ba_2TiO_4 phase above 650 ºC. The formation of cubic $BaTiO_3$ from 700 ºC corresponds to a reduction in the intensity of the Ba_2TiO_4 phase. A small amount of unknown phase (2θ=26.7º) is present between 600 ºC and 700 ºC, which cannot be matched with any available Ba-Ti-O compound. This unidentified phase has been reported in previous studies and believed to transfer into $BaTiO_3$ at high temperature [35, 38].

The in situ XRD pattern for mixture 0.7$BaCO_3$+0.3$CaCO_3$+TiO_2 shows similar reactions to those of mixtures $CaCO_3$+TiO_2 and $BaCO_3$+TiO_2. The decomposition of $CaCO_3$ yielding CaO occurs between 600 and 700 ºC, and the decomposition of $BaCO_3$ and the formation of Ba_2TiO_4 starting at 700 ºC. The unknown phase observed in mixture $BaCO_3$+TiO_2 (2θ=26.7º) is also present until 750 ºC. The formation of $BaTiO_3$ is first observed at a higher temperature in the mixture of 0.7$BaCO_3$+0.3$CaCO_3$+TiO_2 (750 ºC). At 800 ºC, $BaCO_3$ is no longer observed and the Ba_2TiO_4 phase appears to be present in a higher concentration compared to mixture $BaCO_3$+TiO_2. The absence of reflections due to the $CaTiO_3$ phase could be due either to concentrations below the detection limit of the XRD and/or to the reaction with BaO or $BaTiO_3$ to form (Ba,Ca)TiO_3.

In general, the in situ XRD detected reactions occurring at lower temperature than DSC-TGA measurement. This difference could be attributed to that XRD patterns were

collected isothermally before heating to next set temperature (section 3.4.2), resulting in slower heating process (*i.e.* longer reaction time) for mixtures than that in DSC-TGA measurement.

The combination of DSC-TGA and XRD results allows the reaction mechanisms to be understood. The decomposition of $CaCO_3$, peak I on the DSC-TGA between 572 and 775 ºC occurs with the release of CO_2 is shown in Equation 5.3. $BaCO_3$ also decomposes with the evolution of CO_2 between 650 and 750 ºC, peak III on the DSC-TGA, and is represented by Equation 5.4. The exothermic at 899 ºC (peak II) corresponds to the reaction between BaO and the surface of TiO_2 particles to yield the Ba-rich Ba_2TiO_4 phase, Equation 5.5. Further reaction of TiO_2 with Ba_2TiO_4 allows the formation of cubic $BaTiO_3$ (Equation 5.6) [35]. The formation of the $CaTiO_3$, Equation 5.7, is only observed in the mixture $CaCO_3$+TiO_2 above 800 ºC, and is not observed in the mixture $0.7BaCO_3$+$0.3CaCO_3$+TiO_2. The formation of Ba_2TiO_4, $BaTiO_3$ and/or $(Ba,Ca)TiO_3$ appear to be slowed down in the mixture $0.7BaCO_3$+$0.3CaCO_3$+TiO_2, this may be due to the presence of CaO or $CaTiO_3$ preventing or slowing reactions 5.5 and 5.6. This assumption agrees with the previous observation and discussion in section 4.3.3 that the mobility of Ca^{2+} into $BaTiO_3$ is higher in unreacted $CaCO_3$ than $CaTiO_3$.

$$CaCO_3 \rightarrow CaO + CO_2 \tag{5.3}$$

$$BaCO_3 \rightarrow BaO + CO_2 \tag{5.4}$$

$$2BaO + TiO_2 \rightarrow Ba_2TiO_4 \tag{5.5}$$

$$Ba_2TiO_4 + TiO_2 \rightarrow 2BaTiO_3 \quad (5.6)$$

$$CaO + TiO_2 \rightarrow CaTiO_3 \quad (5.7)$$

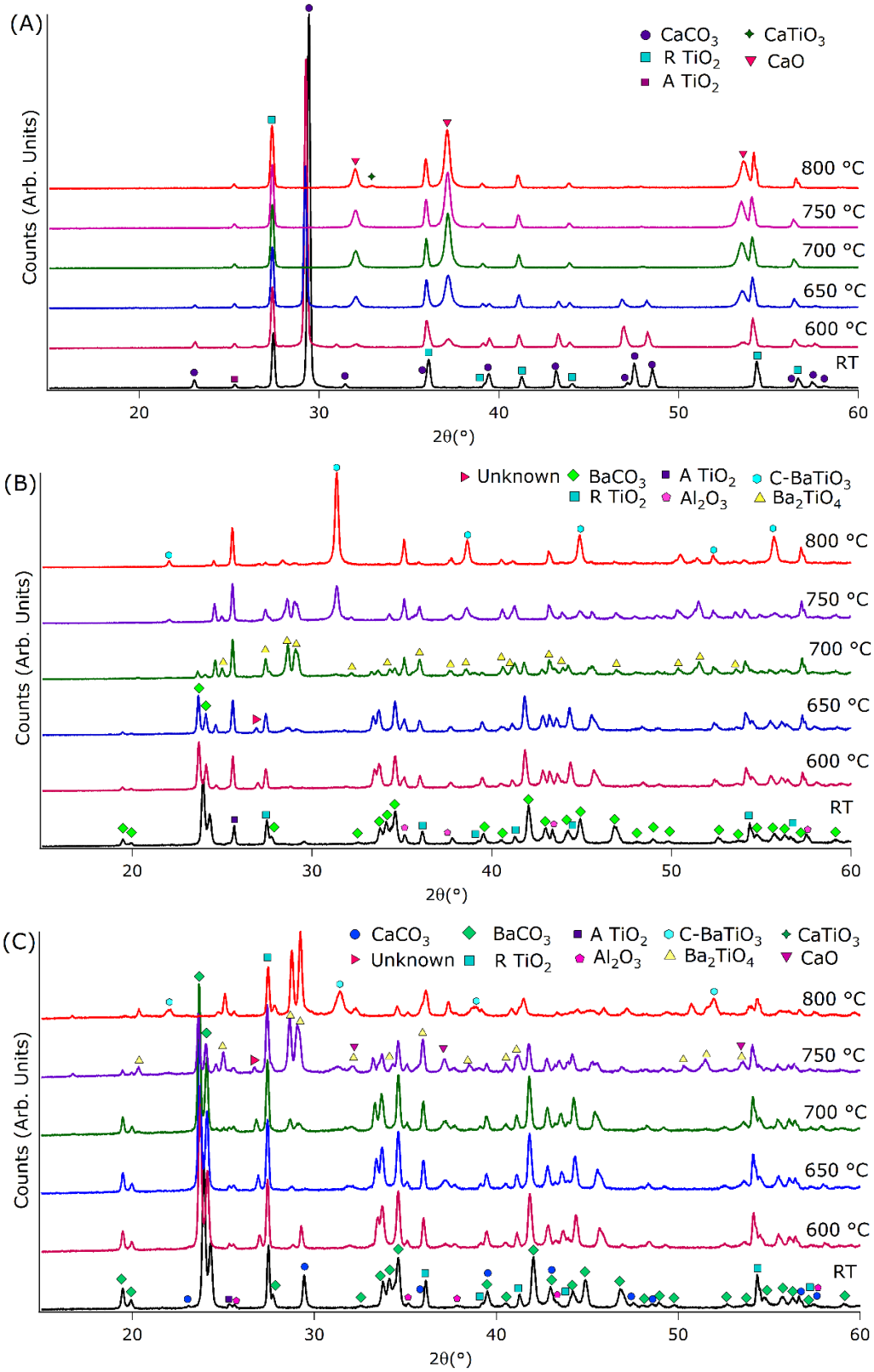

Figure 5.14. The in situ XRD patterns of mixture: (A) $CaCO_3$+TiO_2; (B) $BaCO_3$+TiO_2; (C) 0.7$BaCO_3$+0.3$CaCO_3$+TiO_2, heated isothermally at 5 °C/min in flowing helium.

5.3.2 Diffusion mechanism of Ca^{2+} into $BaTiO_3$

A $BaTiO_3$-$CaTiO_3$ diffusion couple (as shown in Figure 3.8) was produced following the description in section 3.4.1, in order to investigate the diffusion mechanism of Ca^{2+} from $CaTiO_3$ into $BaTiO_3$. The Raman imaging has been taken on the surface of diffusion couple before and after sintering at 1500 ºC, shown in Figure 5.15. By comparing the obtained spectra against reference spectra, it is possible to identify $CaTiO_3$ (green) and $BaTiO_3$ (red) (Figure 5.15 (A)). Before sintering there is a clear $BaTiO_3$-$CaTiO_3$ phase boundary and some $BaTiO_3$ on the top of $CaTiO_3$ side (red spots), which is attributed to some $BaTiO_3$ powder left on the $CaTiO_3$ side during pressing. After sintering the clear distinction between the $CaTiO_3$ and $BaTiO_3$ based phases remains present (Figure 5.15 (C)). This indicates that the $BaTiO_3$ rich phase has retained the tetragonal crystal structure.

Previous investigation in section 5.1.3 has shown that the [E(LO+TO), B_1] mode (observed ~310 cm^{-1}) peak becomes broader with more Ca^{2+} substitution in the tetragonal phase. Before sintering the peak width of the [E(LO+TO), B_1] mode shows a sharp and consistent peak across the whole $BaTiO_3$ area (Figure 5.15 (B)). After sintering, there is a range of peak widths (Figure 5.15 (D)). The blue areas indicate a sharpening of the peak, due to the sintering process forming larger, better ordered grains. The red areas with broader peaks indicate higher Ca^{2+} concentration, *i.e.* greater substitution. The highest substitution occurs as expected along the $BaTiO_3$-$CaTiO_3$ interface, with Ca^{2+} diffusion appearing to occur along the $BaTiO_3$ grain boundaries. The Ca^{2+} concentrations at any positions in diffusion areas could potentially be identified based on the local peak width

and the linear relationship shown in Figure 5.5.

This would suggest that to form (Ba,Ca)TiO_3 from $BaTiO_3$ and $CaTiO_3$, the Ca^{2+} diffuses along the grain boundaries to leave a core of $BaTiO_3$ surrounded by a (Ba,Ca)TiO_3 shell. Subsequently there is the slower process of Ca^{2+} diffusion into the core. Previous research in core ($BaTiO_3$)-shell ($SrTiO_3$, $BaZrO_3$) structure suggested the possibility to modulate dielectric properties of final materials by controlling the overall compositions of the $BaTiO_3$ and $SrTiO_3$/$BaZrO_3$ [232]. However, in this project, the core-shell structure as $BaTiO_3$-(Ba,Ca)TiO_3 limits the further diffusion of Ca^{2+} into $BaTiO_3$, therefore this core-shell structure is not desired to achieve homogeneous (Ba,Ca)TiO_3 phase. Combining sections 4.3.3 and 5.3.1, the mobility of Ca^{2+} into $BaTiO_3$ is limited in $CaTiO_3$, thus $CaCO_3$ rather than $CaTiO_3$ will be chosen as the reagent to fabricate homogeneous $Ba_{0.70}Ca_{0.30}TiO_3$ (discussed in sections 4.2 and 4.3) and zBCT-(1-z)BZT ceramics in this project (as detailed in sections 3.1.1.1 and 3.1.4).

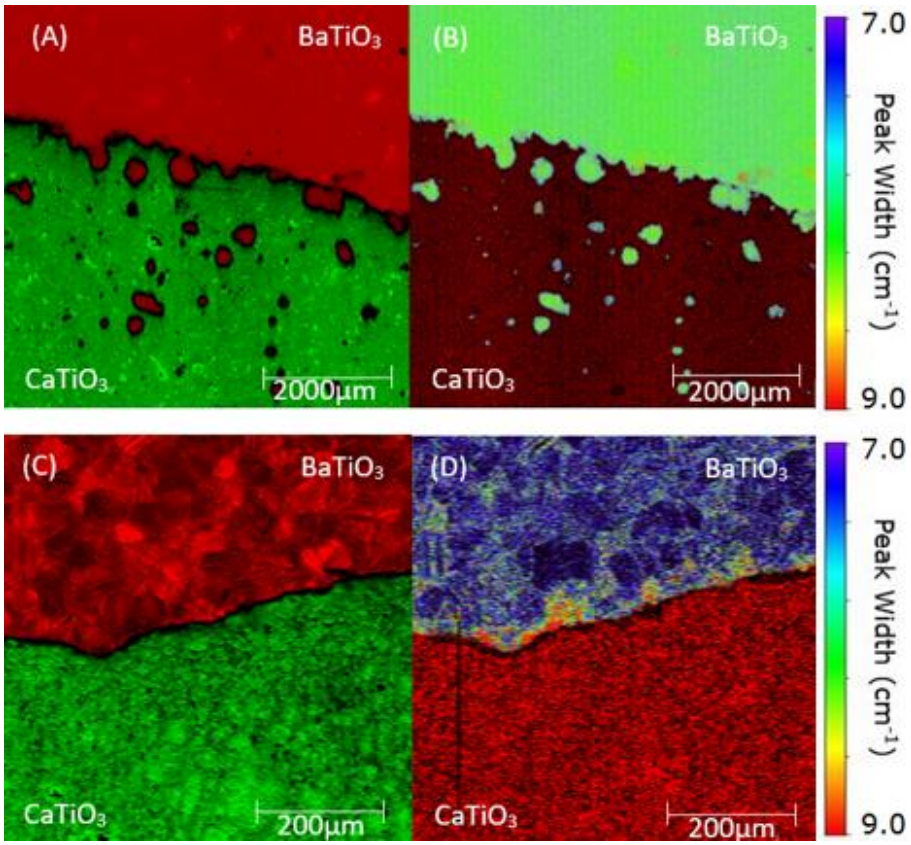

Figure 5.15. Raman imaging spectral of $BaTiO_3$-$CaTiO_3$ diffusion couple. (A) component map before sintering; (B) peak width map of [E(LO+TO), B_1] peak before sintering; (C) component map after sintering; (D) peak width map of [E(LO+TO), B_1] peak after sintering.

5.4 Summary

In this chapter, the fabricated $Ba_{0.70}Ca_{0.30}TiO_3$ ceramics (described in sections 3.1.1, 4.2 and 4.3), which contain tetragonal $Ba_{1-x*}Ca_{x*}TiO_3$ (x*=0-0.30) phases, were investigated as a Ca^{2+} substituting $BaTiO_3$ system. At room temperature, Raman spectroscopy of those tetragonal $Ba_{1-x*}Ca_{x*}TiO_3$ (x*=0-0.30) phases indicates that Ca^{2+} substitution into Ba-site contributes to the shift of the 270 cm^{-1} [A_1(TO)] peak to a lower frequency, whereas the ~520 cm^{-1} [E(TO), A_1(TO)] and ~720 cm^{-1} [E(LO), A_1(LO)] modes shift to a higher frequency. A linear relationship between Ca^{2+} concentrations and the broadening of

310 cm^{-1} [E(LO+TO), B_1] peak is established as Γ=28.609x*+8.44. Those Ca^{2+}-induced variations in Raman modes will be referenced for later study in the more complicated zBCT-(1-z)BZT system (section 7.1.2).

The temperature dependent Raman spectroscopy (targeted only on the tetragonal phases) determines the phase transitions (T_{R-O}, T_{O-T} and T_{T-C}) in all $Ba_{1-x*}Ca_{x*}TiO_3$ (x*=0-0.30) compositions, based on the variations in peak width and peak position of 310 cm^{-1} [E(LO+TO), B_1] peak upon heating. Therefore, the phase diagram of $Ba_{1-x*}Ca_{x*}TiO_3$ ($0 \leq x* \leq 0.30$) derived from Raman spectroscopy is constructed, achieving good agreements with reported literature based on dielectric property measurements [117].

The functional property measurements were carried out on two bulk samples: $Ba_{1-x*}Ca_{x*}TiO_3$ (x*=0.20 and 0.30). The $Ba_{1-x*}Ca_{x*}TiO_3$ (x*=0.30) ceramics with greater homogeneity (*i.e.* more tetragonal phase present) and higher tetragonality contribute to better ferroelectric and piezoelectric properties than $Ba_{1-x*}Ca_{x*}TiO_3$ (x*=0.20) ceramics. The tetragonal-cubic phase transitions of $Ba_{1-x*}Ca_{x*}TiO_3$ (x*=0.20 and 0.30) ceramics are also determined by temperature dependent functional property measurements, where $Ba_{1-x*}Ca_{x*}TiO_3$ (x*=0.20) ceramics show diffusive phase transition behaviour, due to its lower density and presence of microscopic composition fluctuation [148, 215]. The identified phase transition temperatures from functional property measurements agree with the Raman spectroscopy measurements.

The aim is to establish a linkage between the structural properties and functional

properties. The reorientation energy (E_R) obtained from Raman spectroscopy measurements indicates an easier reorientation and depolarization procedure for Ti^{4+} in $Ba_{1-x*}Ca_{x*}TiO_3$ (x*=0.30) ceramics. However, the *P-E* loop show the reverse trend. This difference could be attributed to the presence of Ca-rich pseudo-cubic phase in *P-E* loop measurement. Therefore, future work on fabrication and investigation of monophasic $Ba_{1-x}Ca_xTiO_3$ is needed to further build this linkage.

Compared with reactions in $CaCO_3$+TiO_2 and $BaCO_3$+TiO_2 mixtures upon heating, the presence of $CaTiO_3$ slows down the formation of $BaTiO_3$ in mixture $0.7BaCO_3$+$0.3CaCO_3$+TiO_2. Raman imaging of a $BaTiO_3$-$CaTiO_3$ diffusion couple reveals that Ca^{2+} diffuses from $CaTiO_3$ to $BaTiO_3$ by forming a (Ba,Ca)TiO_3 shell surrounding the $BaTiO_3$ core, which slows further diffusion. In this core-shell structure, the homogeneity is limited. This further confirms that $CaTiO_3$ is not the desirable reagent to produce homogeneous $Ba_{0.70}Ca_{0.30}TiO_3$ and zBCT-(1-z)BZT ceramics. In this project, the $CaCO_3$ with the contribution to better homogeneity (sections 4.2 and 4.3) is therefore chosen as the reagent.

Chapter 6 A study of the $BaZr_yTi_{1-y}O_3$ system

In section 2.4 it was shown that the introduction of Zr^{4+} into $BaTiO_3$ affects the corresponding physical properties, microstructure, phase compositions, functional properties and phase transition behaviour. However, no agreed effect has been concluded in the reported literature. Therefore, a detailed study of the $BaZr_yTi_{1-y}O_3$ (y=0, 0.05, 0.10, 0.15, 0.20, 0.25 and 0.30) ceramics was undertaken in order to reveal the Zr^{4+}-induced effects on the structural and functional properties, and the results are reported and discussed in this chapter.

As discussed and optimised in Chapter 4 (sections 4.4 and 4.5), Zr^{4+} is able to substitute onto the Ti-site during sintering yielding a single homogenous phase. In this project, the fabrication route used for $BaZr_yTi_{1-y}O_3$ (y=0-0.30) samples was to calcine the stoichiometric mixed reagents ($BaCO_3$, ZrO_2 and TiO_2) at 1250 ºC for 2 hours, followed by sintering at 1500 ºC for 4 hours (as described in section 3.1.3). The characterisations of fabricated ceramics (as described in sections 3.2 and 3.3) are shown and discussed.

6.1 Characterisation of $BaZr_yTi_{1-y}O_3$ (y=0-0.30) ceramics

The room temperature XRD patterns of $BaZr_yTi_{1-y}O_3$ (y=0-0.30) ceramics are shown in Figure 6.1 (A), where each $BaZr_yTi_{1-y}O_3$ (y=0-0.30) ceramic exhibits reflections consistent with a single perovskite structure phase. The refined lattice parameters of each

composition at room temperature are summarised in Table 6.1. There is an increase in both lattice constants and unit cell volume with increasing Zr^{4+} content (Table 6.1), observed as a shift to higher *d*-spacings (lower 2θ) in the XRD patterns (Figure 6.1 (B)). This is attributed to the expansion of the unit cell by Zr^{4+} substitution with larger ionic radius (~0.72 Å) than Ti^{4+} (~0.605 Å). The (002) peak for all $BaZr_yTi_{1-y}O_3$ (y=0-0.30) ceramics are shown in Figure 6.1 (B) with a closer view of the 2θ=44-46º range. Refinement of the patterns has indicated: the $BaZr_yTi_{1-y}O_3$ (y=0) has tetragonal symmetry with splitting of (002) and (020) peaks; the $BaZr_yTi_{1-y}O_3$ (y=0.05) is an orthorhombic phase with splitting of (022) and (200) peaks; the $BaZr_yTi_{1-y}O_3$ (y=0.10-0.20 and y=0.25-0.30) respectively possess rhombohedral and cubic symmetry with only a single (002) peak. The splitting in each Miller plane peak is caused by the different wavelength of $K_{\alpha 1}$ and $K_{\alpha 2}$ X-ray radiation (section 3.2.1.3). These observations are consistent with a previous study [227] where the crystal structure of $BaZr_yTi_{1-y}O_3$ changes with Zr^{4+} content (y value) at room temperature: $0 \leq y \leq 0.025$ is tetragonal, $0.025 \leq y \leq 0.08$ is orthorhombic, $0.08 \leq y \leq 0.21$ is rhombohedral and $y \geq 0.21$ is cubic.

As shown in Table 6.1, in the rhombohedral phase (y=0.10-0.20), the lattice angles increase with increasing Zr^{4+} content, which makes the crystal structure become more similar to the cubic phase. Subsequently, substituting more Zr^{4+} ($y \geq 0.20$), the crystal structure becomes cubic. Figure 6.2, based on the data in Table 6.1, demonstrates that the relationship between Zr^{4+} content (y) in $BaZr_yTi_{1-y}O_3$ (y=0-0.30) ceramics and unit cell volume (V) is linear, and independent of the crystal structure. Therefore, in the

$BaZr_yTi_{1-y}O_3$ system, quantitative phase analysis from XRD data could be investigated by using this linear relationship:

$$V = 9.3721y + 64.402 \quad (6.1)$$

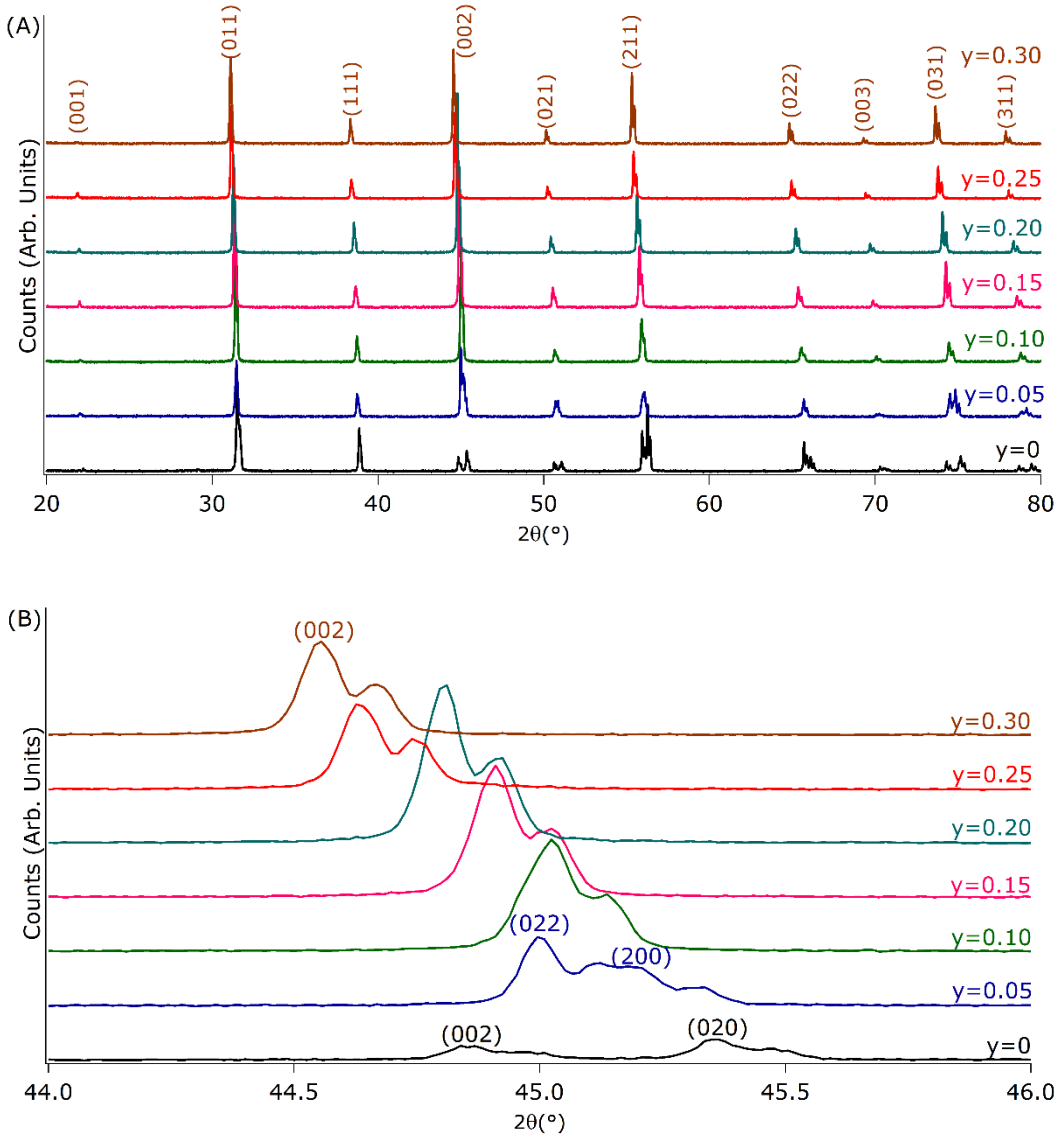

Figure 6.1. The XRD patterns of sintered $BaZr_yTi_{1-y}O_3$ (y=0-0.30) ceramics: (A) 2ϑ=20-80º; (B) 2ϑ=44-46º.

Table 6.1. Lattice parameters of sintered $BaZr_yTi_{1-y}O_3$ (y=0-0.30) ceramics from XRD analysis.

Sample name	**Phase name**	***a/b/c* (Å)**	***α/β/γ* (°)**	**Unit cell volume (Å^3)**
y=0	Tetragonal	a=c=3.9945 (±0.0001) b=4.0377 (±0.0001)	90	64.425 (±0.003)
y=0.05	Orthorhombic[4]	a=c=4.0240 (±0.0002) b=4.0060 (±0.0001)	α =γ=90 β~89.89	64.866 (±0.005)
y=0.10	Rhombohedral	4.0280 (±0.0001)	89.941 (±0.001)	65.351 (±0.003)
y=0.15	Rhombohedral	4.0366 (±0.0001)	89.959 (±0.002)	65.775 (±0.003)
y=0.20	Rhombohedral	4.0463 (±0.0001)	89.977 (±0.002)	66.246 (±0.002)
y=0.25	Cubic	4.0561 (±0.0001)	90	66.728 (±0.003)
y=0.30	Cubic	4.0668 (±0.0001)	90	67.260 (±0.003)

[4] The a, b, c in orthorhombic phase from XRD measurement refer to a, c, a_3 parameters in the orthorhombic unit cell in Figure 2.7.

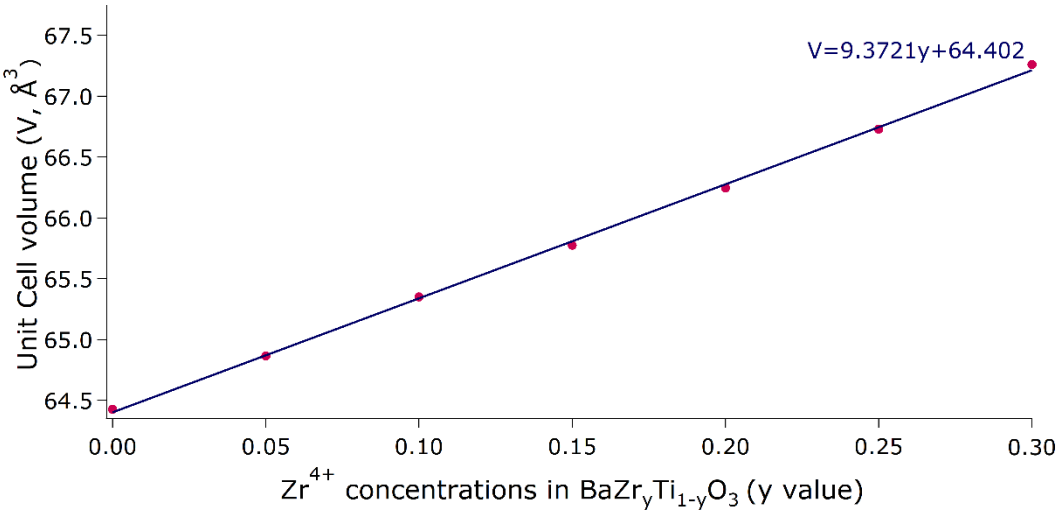

Figure 6.2. The linear relationship between Zr^{4+} content and unit cell volume from sintered $BaZr_yTi_{1-y}O_3$ (y=0-0.30) ceramics.

SEM micrographs of sintered $BaZr_yTi_{1-y}O_3$ (y=0-0.30) ceramics are shown in Figure 6.3 and the changes in average grain size with Zr^{4+} concentration are shown in Figure 6.4. It can be seen that the average grain size is between 18-95 µm and exhibits an overall decrease with Zr^{4+} addition with a small variation at y=0.25. This reduction of grain size indicates that Zr^{4+} addition inhibits the grain growth as a result of the larger Zr^{4+} ion diffusing slower than smaller Ti^{4+} ion [164]. As for $BaZr_yTi_{1-y}O_3$ (y=0.20) ceramics, as one end member of zBCT-(1-z)BZT system, the measured grain size is 30.0±9.7 µm in general agreement with other reports of 40 µm for materials produced by a solid-state fabrication method [151].

It is interesting to note that the variations in relative density against Zr^{4+} content (shown in Figure 6.5) have the same trend as that in grain size (Figure 6.4), where the $BaZr_yTi_{1-y}O_3$ (y=0.15 and 0.20) ceramics possessed lowest relative density (~87 %) and smallest grain size (~30 µm). Reasons for this similar trend and apparent peak at y=0.25

are unclear. With reference to lattice parameters identified by XRD (Figure 6.2) and crystal symmetry determined by Raman spectroscopy (discussed later in section 6.3), it would appear that the composition of sample fabrication is correct. And the fact that groups of samples were sintered together also rules out sample fabrication issues.

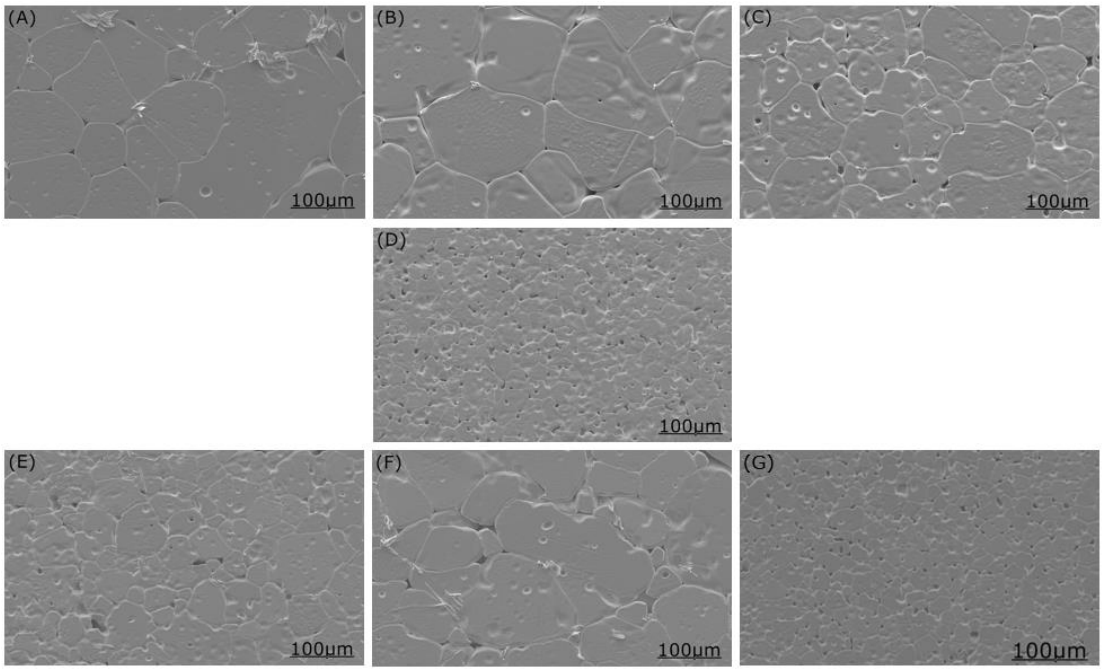

Figure 6.3. SEM images of sintered $BaZr_yTi_{1-y}O_3$ ceramics: (A) y=0; (B) y=0.05; (C) y=0.10; (D) y=0.15; (E) y=0.20; (F) y=0.25 and (G) y=0.30.

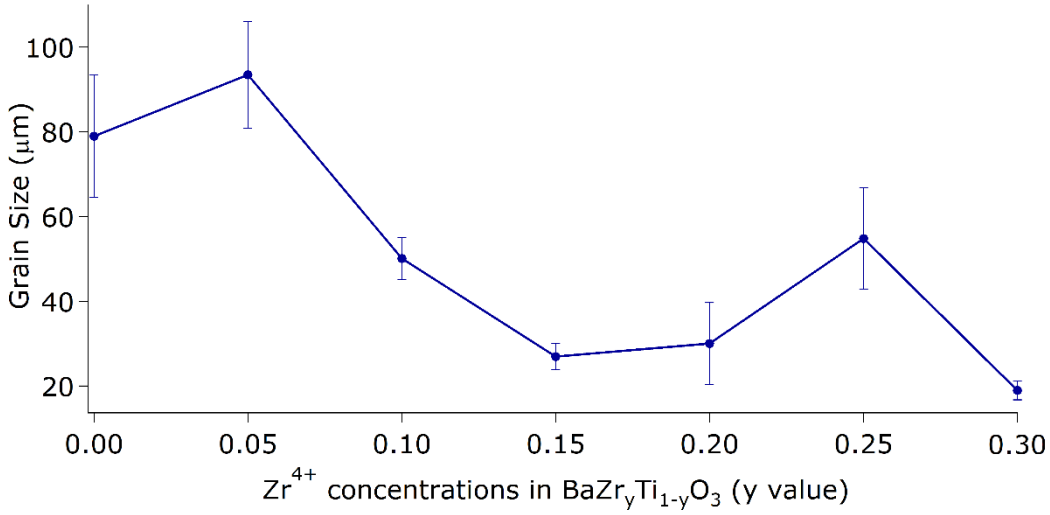

Figure 6.4. Grain sizes of sintered $BaZr_yTi_{1-y}O_3$ (y=0-0.30) ceramics.

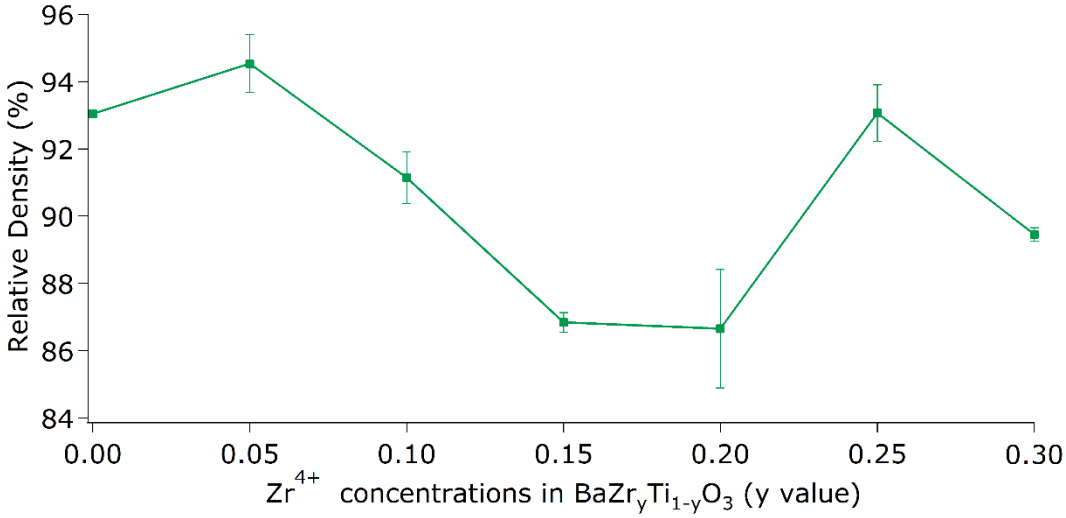

Figure 6.5. Relative density of sintered $BaZr_yTi_{1-y}O_3$ (y=0-0.30) ceramics.

6.2 Structural study of $BaTiO_3$ ceramics by Raman spectroscopy

6.2.1 Raman spectra of $BaTiO_3$ ceramics

The Raman spectra of $BaTiO_3$ powders were presented in section 5.1.2. As a precursor to studying the effect of the Zr^{4+}-substituted materials reported in this chapter, the Raman

spectra of sintered $BaTiO_3$ ceramics were studied for comparison and calibration of phase transition temperature for sintered ceramics. Figure 6.6 shows the Raman spectra of sintered $BaTiO_3$ ceramics measured at four temperatures: (A) 114 K (Rhombohedral), (B) 223 K (Orthorhombic), (C) 298 K (Tetragonal) and (D) 473 K (Cubic). This shows that the $BaTiO_3$ ceramics has similar vibration modes as powder samples (shown in Figure 5.2) in each phase. A general sharpening of peaks has been observed in ceramic samples. The [E(TO+LO), B_1] mode observed as a peak around 310 cm^{-1} in the tetragonal phase is taken as an example to understand this sharpening phenomena. Table 6.2 lists the peak position and half width half maximum (HWHM, peak width Γ) of the [E(TO+LO), B_1] mode measured at room temperature for both $BaTiO_3$ powders and ceramics. The sintered ceramics have undergone two heat treatments resulting in better ordered and more homogeneous grains, therefore it is easier for oxygen atoms to vibrate in the same direction, resulting in less disordered vibrations (shaper peak). As shown in Table 6.2, the ceramic sample has a larger unit cell volume in the tetragonal phase, derived from the room temperature measured XRD, where the Ti-O bond is consequently longer and weaker. Therefore, the Ti-O bond vibration could be achieved by a lower energy in the ceramic sample, which also contributes to a lower peak position.

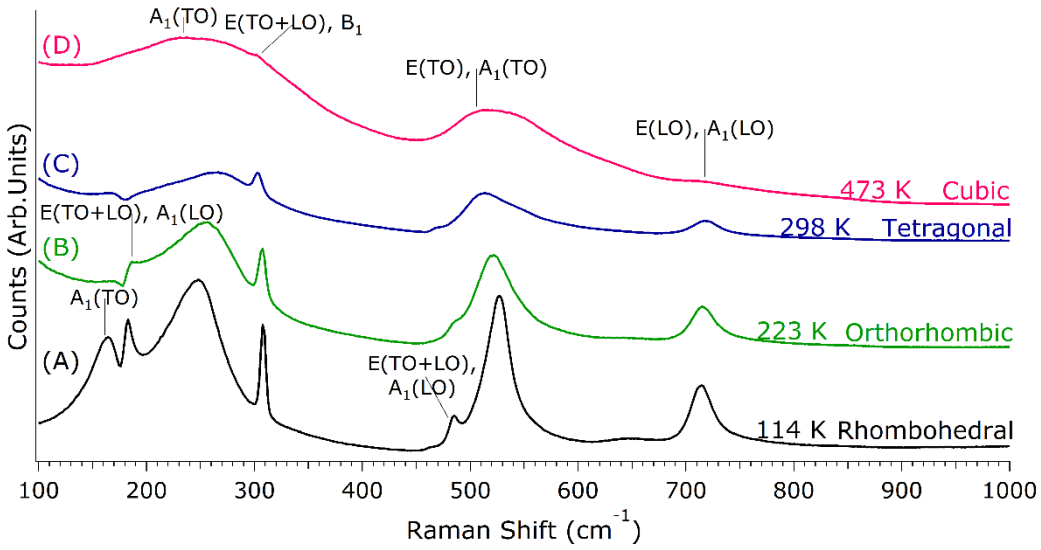

Figure 6.6. Raman spectra of $BaTiO_3$ ceramics at (A) 114 K (Rhombohedral), (B) 223 K (Orthorhombic), (C) 298 K (Tetragonal) and (D) 473 K (Cubic).

Table 6.2. Crystal structure parameters of tetragonal $BaTiO_3$ powders and ceramics.

Sample name	**Raman peak ~ 310 cm^{-1}**		**Unit cell volume**
	Peak position ω (cm^{-1})	**Peak width Γ (cm^{-1})**	**($Å^3$)**
$BaTiO_3$ powders	309.8±0.1	6.96±0.25	64.402±0.002
$BaTiO_3$ ceramics	302.7±0.1	6.83±0.22	64.426±0.003

6.2.2 Phase transitions of $BaTiO_3$ ceramics by Raman spectroscopy

In section 5.1.4, the [E(TO+LO), B_1] mode (peak around 310 cm^{-1}) was used to identify the phase transition temperatures for the $BaTiO_3$ powder sample and A-site doped $(Ba,Ca)TiO_3$ samples. In this section, the changes of peak position (ω) and half width half maximum (HWHM, peak width Γ) of the [E(TO+LO), B_1] modes are also used for the $BaTiO_3$ ceramics, and are shown in Figure 6.7 (A).

Upon heating, there is a general increase in peak width with increasing temperature, the

change in gradient has been identified as the *R-O* and *T-C* phase transition at 166 K and 423 K, respectively. The decrease in peak position indicates the *O-T* (284 K) phase transition and an increase in peak position the *T-C* (423 K) phase.

When comparing ceramic to powder samples the phase transitions in $BaTiO_3$ (section 5.1.4), the *R-O* transition occurs at lower temperature in ceramics sample, however, the *O-T* and *T-C* transitions are at higher temperature. This difference could be attributed to the induced internal stress in the ceramic samples, caused by the cubic to tetragonal phase transition during cooling down to room temperature through the Curie temperature [63].

It has been reported that the 310 cm^{-1} peak is not present in some Zr^{4+}-substituted $BaTiO_3$ [75], so therefore the peaks around 528 cm^{-1} and 715 cm^{-1} were also used to identify the phase transitions in the $BaTiO_3$ ceramics for a better understanding of the phase transitions of $BaZr_yTi_{1-y}O_3$ system.

Table 6.3 lists the phase transition temperatures of $BaTiO_3$ ceramics identified by the 310 cm^{-1}, 528 cm^{-1} and 715 cm^{-1} peaks. As the variations of transition temperatures from different peaks are small, the averaged values are identified as the phase transition temperatures of $BaTiO_3$ ceramics: T_{R-O} is 166.2 K, T_{O-T} is 282.8 K and T_{T-C} is 423.4 K, shown in Table 6.3. This achieves good agreement with literature [225]. As mentioned in section 3.3.1, the calibration of phase transition temperatures in $BaZr_yTi_{1-y}O_3$ system would be calculated between the data of $BaTiO_3$ ceramics and literature [225].

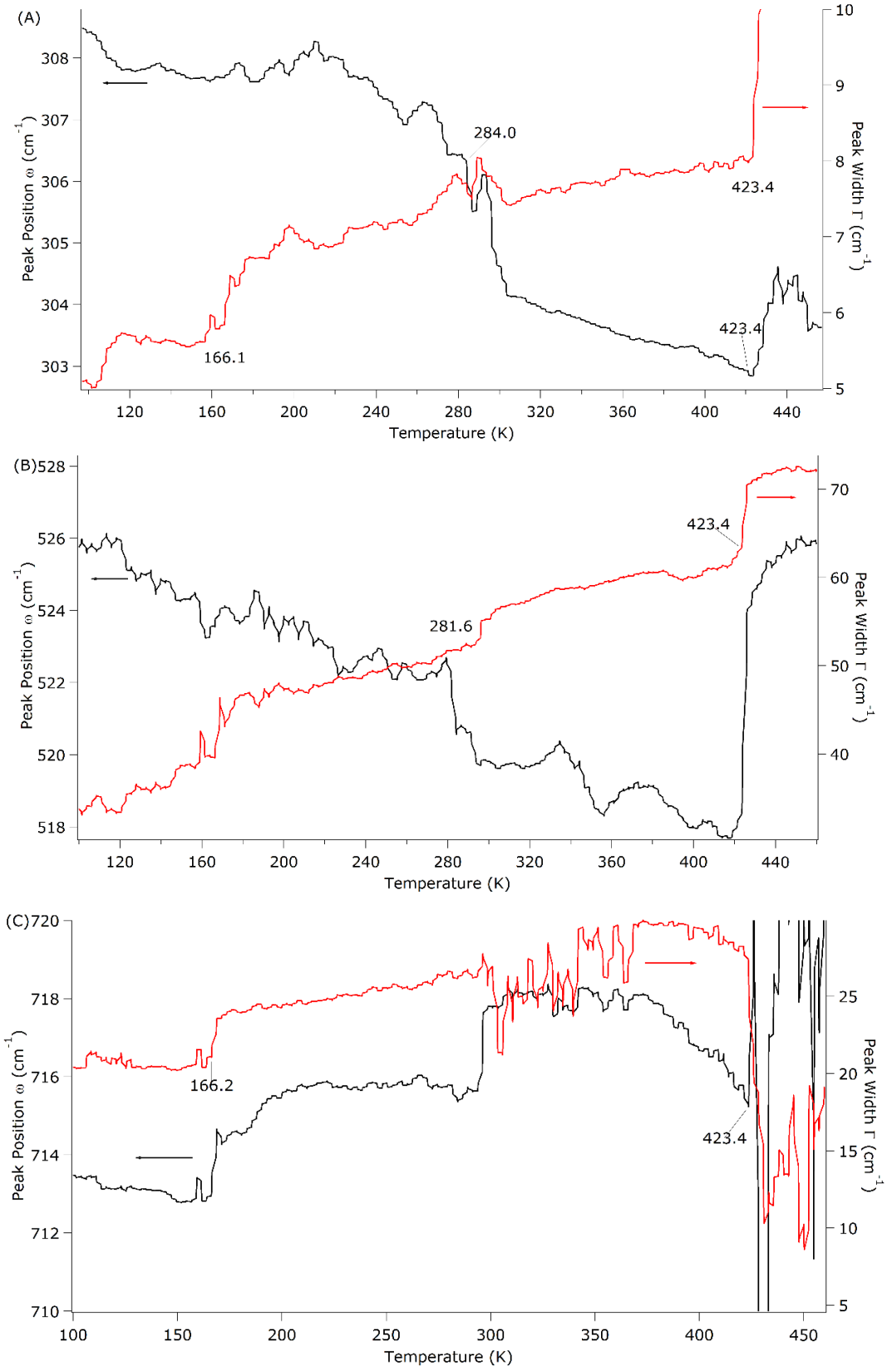

Figure 6.7. The temperature dependence of peak position and peak width changes of peaks around (A) 310 cm^{-1}; (B) 528 cm^{-1}; (C) 715 cm^{-1} for $BaTiO_3$ ceramics.

Table 6.3. The phase transition temperatures of $BaTiO_3$ ceramics identified by different Raman peaks.

Peak name	T_{R-O} (K)	T_{O-T} (K)	T_{T-C} (K)
~ 310 cm^{-1} peak	166.1	284.0	423.4
~ 528 cm^{-1} peak	-	281.6	423.4
~ 715 cm^{-1} peak	166.2	-	423.4
Average	166.2	282.8	423.4

6.3 Structural study of $BaZr_yTi_{1-y}O_3$ (y=0-0.30) ceramics by Raman spectroscopy

6.3.1 Raman spectra of $BaZr_yTi_{1-y}O_3$ (y=0-0.30) ceramics

Figure 6.8 shows the Raman spectra of $BaZr_yTi_{1-y}O_3$ (y=0-0.30) ceramics measured at 114 K, where all compositions exhibit the rhombohedral phase [227]. Compared with the $BaTiO_3$ spectrum (Figure 6.8 (A), y=0), the Zr^{4+}-doped samples (Figure 6.8 (B)-(G)) possess a weaker dip around 180 cm^{-1} as well as an extra peak and dip around 120 cm^{-1}. The 180 cm^{-1} dip in rhombohedral $BaTiO_3$ originates from the anti-resonance effect arising from the coupling between a sharp [A_1(TO)] mode (~160 cm^{-1}) and a broad [A_1(TO)] mode (~ 250 cm^{-1}) [72, 74]. The sharp [A_1(TO)] mode arises from the Ti^{4+} vibrating against the oxygen cage, and the heavier and larger Zr^{4+} substitution into Ti^{4+} site results in a lower frequency of this mode [72]. Therefore, the additional peak and dip around 120 cm^{-1} in $BaZr_yTi_{1-y}O_3$ (y=0.05-0.30) are a consequence of a shift of the 160 cm^{-1} peak and 180 cm^{-1} dip, which are responsible for vibrations between the Zr^{4+} and oxygen cage. Consequently, a higher Zr^{4+} content leads to stronger 120 cm^{-1} peaks

and dips, and less intense 160 cm^{-1} peak and 180 cm^{-1} dip, as more Zr^{4+}- O^{2-} cage vibrations compete with the degradation of Ti^{4+}-O^{2-} cage vibrations. Thus the peak and dip around 120 cm^{-1} could be considered as Zr^{4+}-related features. The presence of 120, 160 and 190 cm^{-1} peaks could then be considered as characteristic modes for the rhombohedral $BaZr_yTi_{1-y}O_3$ (y=0.05-0.30) phase.

The peak around 715 cm^{-1} [E(LO), A_1(LO)] in $BaTiO_3$ originates from the [TiO_6] octahedral breathing, which can also be seen in the Zr^{4+} substituted samples. Another peak around 780 cm^{-1} is only observed in Zr^{4+} substituted compositions. According to the previous reports, this is the A_{1g} asymmetric mode caused by more than one B-site species in the structure [110], but also originates from the movement of [BO_6] octahedral, with shifts resulting from the B-site substitution [75]. With increasing Zr^{4+} content the peaks broaden due to the increased disorder within the structure caused by substitution. The disappearance of peaks around 310 cm^{-1} and 489 cm^{-1} with higher Zr^{4+} content ($y \geq 0.15$) could be attributed to the broadening of the larger peaks around 270 cm^{-1} and 528 cm^{-1} respectively masking the smaller peaks. The progressive disappearance of the modes around 160 cm^{-1}, 180 cm^{-1} and 489 cm^{-1} with Zr^{4+} addition indicates a gradual loss of rhombohedral symmetry [75].

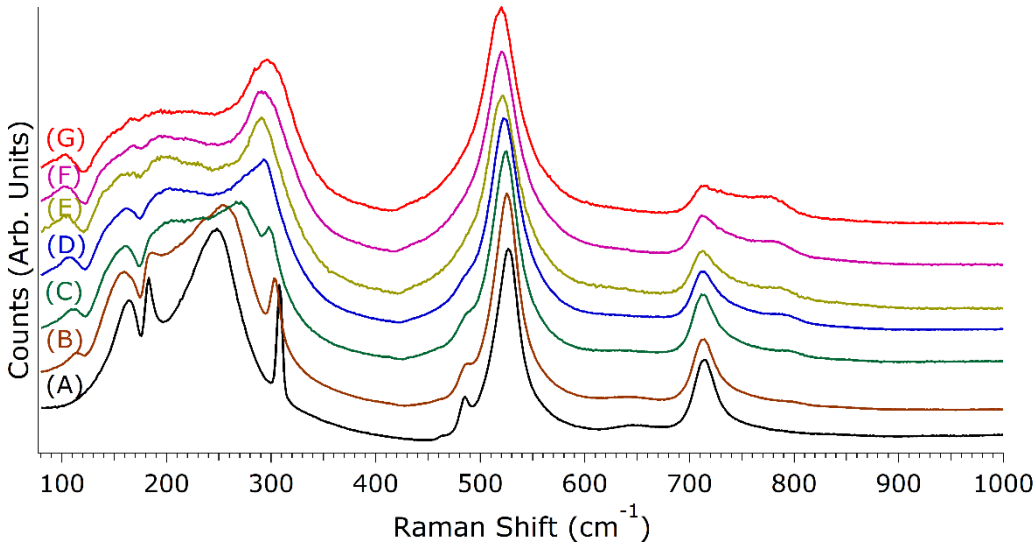

Figure 6.8. The Raman spectra of $BaZr_yTi_{1-y}O_3$ ceramics measured at 114 K: (A) y=0 ($BaTiO_3$), (B) y=0.05, (C) y=0.10, (D) y=0.15, (E) y=0.20, (F) y=0.25 and (G) y=0.30.

The Raman spectra of $BaZr_yTi_{1-y}O_3$ (y=0-0.30) samples measured at room temperature (298 K) are shown in Figure 6.9. An additional weak peak around 188 cm^{-1} in $BaZr_yTi_{1-y}O_3$ (y=0.05) is observed (Figure 6.9 (B)) compared to $BaTiO_3$ (Figure 6.9 (A)) similar to that of the orthorhombic phase in $BaTiO_3$. This suggests that $BaZr_yTi_{1-y}O_3$ (y=0.05) exists in the orthorhombic phase at room temperature. Further increases in Zr^{4+} content, show a dip around 120 cm^{-1} and a peak around 780 cm^{-1} when $BaZr_yTi_{1-y}O_3$ (y=0.10, 0.15) in Figure 6.9 (C), (D), indicating that these samples are rhombohedral at room temperature. The disappearance of the peak around 310 cm^{-1} is first noticed in Figure 6.10 (D) for y=0.15, which may be due to this composition lying close to the diffuse phase transition between the rhombohedral and cubic phases, and suggesting a slight weakening of the rhombohedral structure [75]. When the Zr^{4+} content is 0.20, the Raman peaks become much broader indicating a further loss of rhombohedral symmetry, as shown in Figure 6.10 (E). The existence of the weak dip at 180 cm^{-1} still confirms the

rhombohedral symmetry for this composition. Zr^{4+} contents greater than 0.20, should result in the Raman inactive cubic phase at room temperature [227], however, broad peaks are observed in the Raman spectra. Similar to the broad peaks in cubic $BaTiO_3$ (Figure 5.2 and Figure 6.6), these could be attributed to short range distortions in the oxygen octahedra away from perfect cubic symmetry, within an otherwise ordered cubic structure.

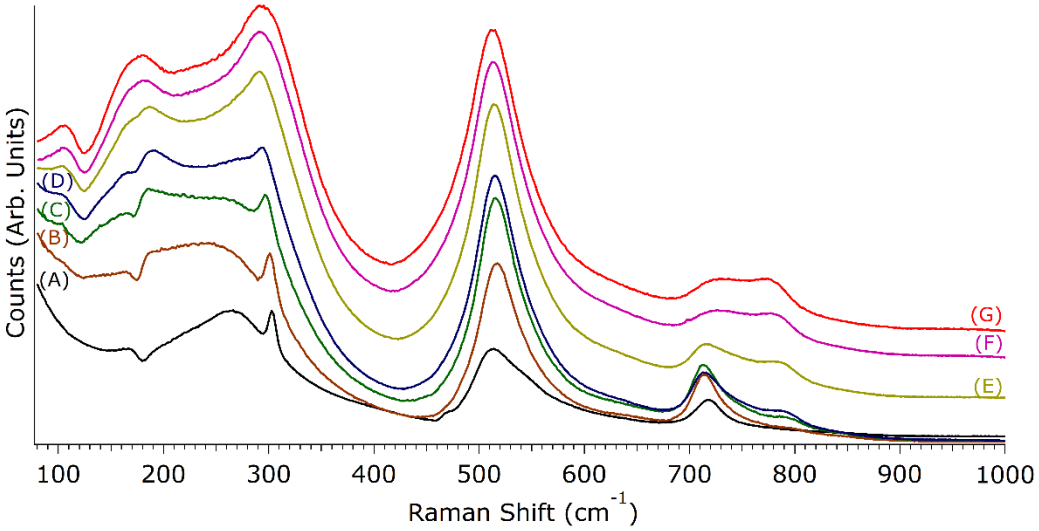

Figure 6.9. The Raman spectra of $BaZr_yTi_{1-y}O_3$ ceramics measured at room temperature (298 K): (A) y=0 ($BaTiO_3$), (B) y=0.05, (C) y=0.10, (D) y=0.15, (E) y=0.20, (F) y=0.25 and (G) y=0.30.

6.3.2 Phase transitions of $BaZr_yTi_{1-y}O_3$ (y=0-0.30) ceramics by Raman spectroscopy

A combination of Raman peaks around 310 cm^{-1}, 528 cm^{-1} and 715 cm^{-1} were used to investigate the phase transitions of $BaZr_yTi_{1-y}O_3$ (y=0-0.30). The onset temperatures are identified as the phase transition temperatures of $BaZr_yTi_{1-y}O_3$ (y=0-0.30), and are listed in Table 6.4. The determined temperatures are in good agreement with literatures [72, 145].The phase diagram of $BaZr_yTi_{1-y}O_3$ (y=0-0.30) is then shown in Figure 6.10, where

the rhombohedral to orthorhombic ($T_{R\text{-}O}$) and orthorhombic to tetragonal ($T_{O\text{-}T}$) phase transition temperatures increase with increasing Zr^{4+} content, however, the Curie temperature ($T_{T\text{-}C}$ or $T_{R\text{-}C}$) decreases.

Table 6.4. Onset temperatures for the phase transition of $BaZr_yTi_{1-y}O_3$ (y=0-0.30) determined by analysis of Raman spectra.

Sample Name	$T_{R\text{-}O}$ (K)	$T_{O\text{-}T}$ (K)	$T_{T\text{-}C}/T_{R\text{-}C}$ (K)
y=0	182.9±0.1	278.1±1.7	393.0
y=0.05	267.8±1.4	317.1±5.8	373.2±2.4
y=0.10	325.7±1.6	335.7±0.3	352.4±2.7
y=0.15			319.3±1.4
y=0.20			290.5±0.3
y=0.25			251.7±0.1
y=0.30			221.4

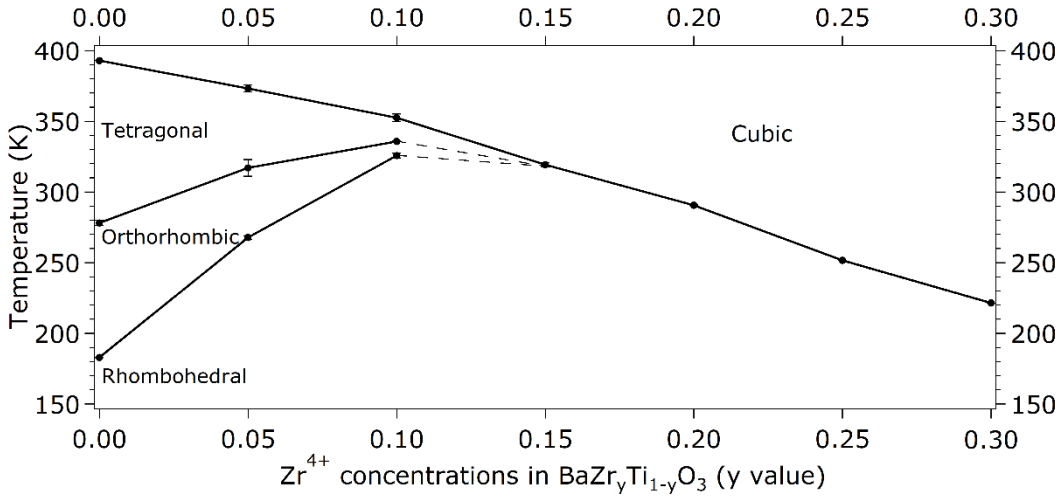

Figure 6.10. Phase diagram of $BaZr_yTi_{1-y}O_3$ (y=0-0.30) derived from Raman spectroscopy measurement.

6.4 Functional properties of $BaZr_yTi_{1-y}O_3$ (y=0-0.30) ceramics

6.4.1 Functional properties of $BaZr_yTi_{1-y}O_3$ (y=0-0.30) ceramics (measured at room temperature)

The relative permittivity (ε_r) and dielectric loss ($tan\delta$) of unpoled and poled $BaZr_yTi_{1-y}O_3$ (y=0-0.30) ceramics are shown in Figure 6.11. It shows insignificant changes in relative permittivity for $BaZr_yTi_{1-y}O_3$ (y=0-0.30) ceramics before and after poling, which has been reported in literature for coarse-grained $BaTiO_3$ ceramics (≥20 μm) [51]. The relative permittivity keeps nearly constant in $BaZr_yTi_{1-y}O_3$ (y=0-0.15) before raising to the highest values at y=0.25 (10915±336 and 10816±324 for unpoled and poled ceramics, respectively) and then decrease again when y=0.30. The highest relative permittivity at y=0.25 (12500) has also been reported by Tang et al [148]. When increasing the Zr^{4+} concentration, the dielectric loss of unpoled and poled $BaZr_yTi_{1-y}O_3$ (y=0-0.15) ceramics generally increases in the ferroelectric phases as a result of more disorder and defects induced by the Zr^{4+} addition, followed by a decrease when $BaZr_yTi_{1-y}O_3$ approaches the cubic phase region (y=0.20-0.30).

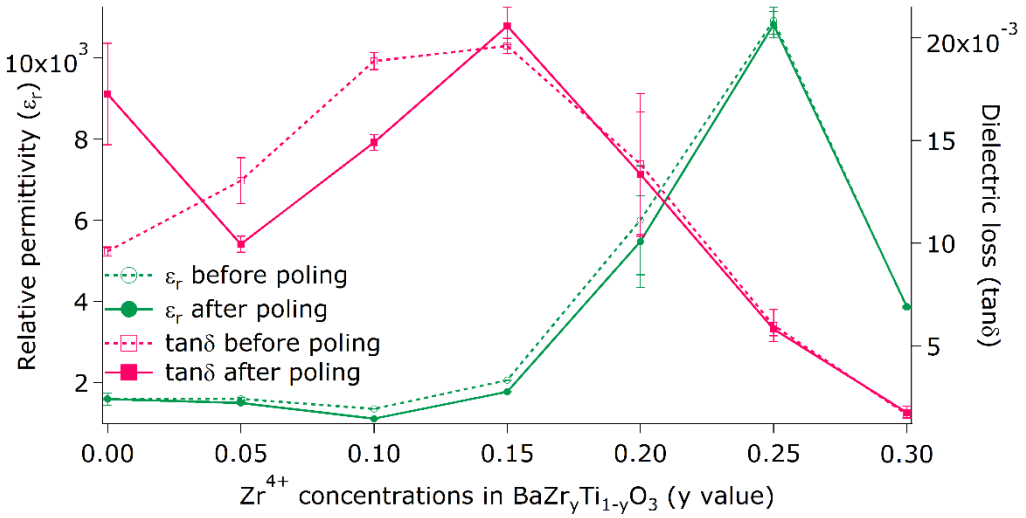

Figure 6.11. Dielectric properties of $BaZr_yTi_{1-y}O_3$ (y=0-0.30) ceramics at room temperature.

The polarization-electric field loops (P-E loop) of $BaZr_yTi_{1-y}O_3$ (y=0-0.30) ceramics measured at room temperature are shown in Figure 6.12. The remanent polarization (P_r) and coercive field (E_c) as a function of Zr^{4+} concentration are reproduced in Figure 6.13. The remanent polarization of $BaZr_yTi_{1-y}O_3$ ceramics is 9.11±0.39 μC/cm^2 at y=0 and then increases to its maximum value at y=0.05 (13.22±0.46 μC/cm^2), followed by decreasing with further Zr^{4+} substitution (y=0.10-0.30). A maximum in remanent polarization at the y=0.05 composition has also been observed in previous research [141, 168, 227]. One of the possible reasons is that orthorhombic $BaZr_yTi_{1-y}O_3$ (y=0.05) has more possible polarization directions resulting in the higher observed value of the spontaneous polarisation and higher remanent polarization after removing the applied electric field [168]. Similarly, the remanent polarization of rhombohedral $BaZr_yTi_{1-y}O_3$ (y=0.10) ceramics is higher than tetragonal $BaTiO_3$ (y=0) and lower than orthorhombic $BaZr_yTi_{1-y}O_3$ (y=0.05) ceramics. On the other hand, the higher remanent polarization could be benefiting from the larger grain size, where the domain walls could switch more

easily with changes to the applied electric field [163]. Within ferroelectric ceramics, it is not possible to fully separate the influence of grain size and composition within a specific range of materials; the relative higher remanent polarizations in $BaZr_yTi_{1-y}O_3$ (y=0-0.10) therefore will be influenced by the larger average grain sizes (≥50 μm) compared to y=0.15 (~27 μm). The further decrease of remanent polarization with increasing Zr^{4+} content (y=0.20-0.30) is a result of approaching and crossing the cubic phase boundary (Table 6.1) [160].

The coercive field of $BaZr_yTi_{1-y}O_3$ (y=0-0.30) decreases with increasing Zr^{4+} content from 3.92±0.15 kV/cm (y=0) to nearly zero (y=0.25 and 0.30). The similar trend has also been observed previously without further explanations of this phenomenon [139, 141, 160]. In this study, it could be speculated that as the Zr^{4+} addition in ferroelectric $BaZr_yTi_{1-y}O_3$ (y=0-0.20) ceramics causes an expansion of the unit cell resulting in a lengthening and weakening of the Ti-O bond, this would weaken the Ti-O bonds thus allowing a reverse in polarization to be achieved under a lower coercive field. In cubic $BaZr_yTi_{1-y}O_3$ (y=0.25-0.30) ceramics, as would be expected, the nonlinear *P-E* loop contributes to lowest coercive field (~ 0 kV/cm).

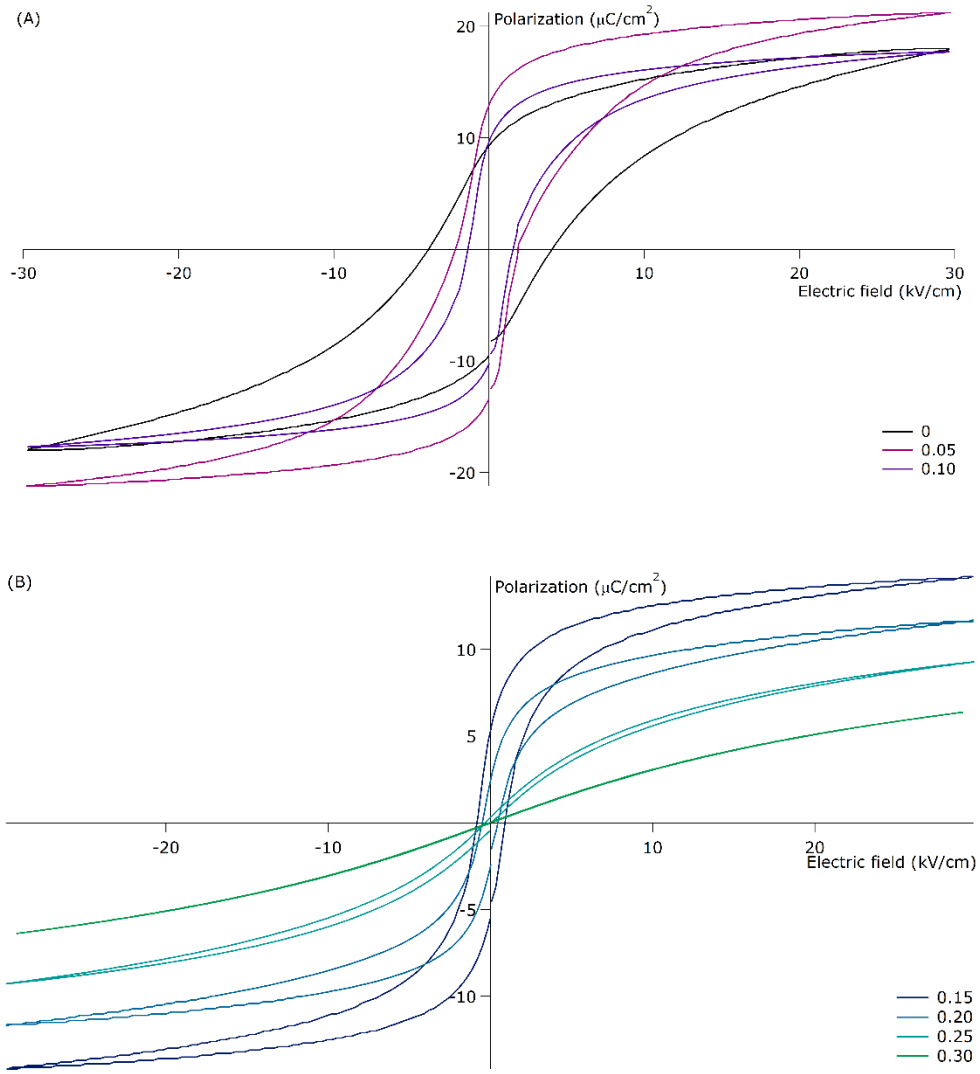

Figure 6.12. The *P-E* loops of $BaZr_yTi_{1-y}O_3$ ceramics at room temperature: (A) *y*=0-0.10; (B) *y*=0.15-0.30 (note different scales on the two polarisation axes).

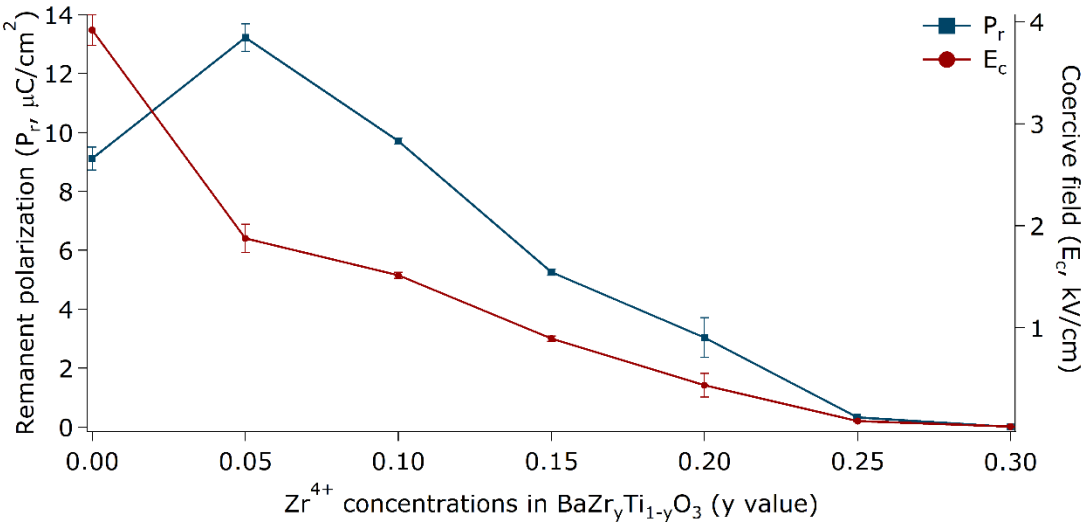

Figure 6.13. The remanent polarization (P_r) and coercive field (E_c) of $BaZr_yTi_{1-y}O_3$ (y=0-0.30) ceramics at room temperature.

The piezoelectric charge coefficient (d_{33}) and electromechanical planar coupling coefficient (k_p) of $BaZr_yTi_{1-y}O_3$ (y=0-0.30) ceramics are shown in Figure 6.14. The maximum d_{33} (286±9 pC/N) and k_p (0.53±<0.01) are both obtained for the y=0.05 composition, with comparative values for pure $BaTiO_3$ ceramics being d_{33}=233±2 pC/N and k_p=0.37±0.01. This has also been reported in previous study [139, 141, 145, 168]. The highest piezoelectric response and best electromechanical property in $BaZr_yTi_{1-y}O_3$ (y=0.05) ceramics are benefited from its relative higher remanent polarization (Figure 6.13) [141]. Both d_{33} and k_p go to zero in $BaZr_yTi_{1-y}O_3$ (y=0.25 and 0.30) ceramics, as consistent with the cubic phase.

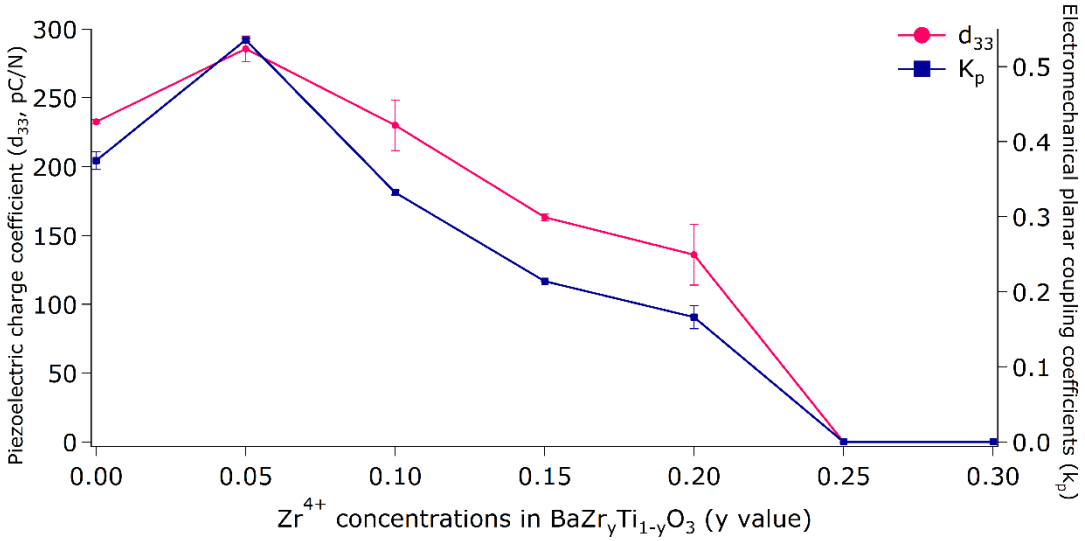

Figure 6.14. Piezoelectric properties of $BaZr_yTi_{1-y}O_3$ (y=0-0.30) ceramics at room temperature.

6.4.2 Phase transitions of $BaZr_yTi_{1-y}O_3$ (y=0-0.30) ceramics by temperature dependent functional property measurements

The relative permittivity of $BaZr_yTi_{1-y}O_3$ (y=0-0.30) ceramics measured at 1 kHz (by IFM measurement, as described in section 3.3.2) as a function of temperature (ε_r-T) is shown in Figure 6.15. There are three distinct peaks in relative permittivity of $BaZr_yTi_{1-y}O_3$ (y=0) upon heating, which derive from the phase transitions from rhombohedral to orthorhombic (R-O), then to tetragonal (O-T), and finally to cubic (T-C). The corresponding phase transition temperatures, T_{R-O}, T_{O-T} and T_{T-C}, are sensitive to Zr^{4+} concentrations. The three peaks in ε_r-T corresponding to the phase transitions become less defined and begin to overlap with increasing Zr^{4+} content. For y=0.05 three transitions are clearly observed, however, for y=0.10 the R-O and O-T transition become less clear, and with Zr^{4+} contents above 0.15 only one phase transition peak is observed.

The maximum values of relative permittivity (ε_{rmax}) are dependent on the Zr^{4+}

concentrations, which can be divided in to two regions: in region I ($0 \leq y \leq 0.10$), ε_{rmax} increases with increasing Zr^{4+} content; ε_{rmax} changes irregularly with Zr^{4+} concentration in region II ($0.15 \leq y \leq 0.30$), however the ε_{rmax} peak becomes broader with greater Zr^{4+} content.

As shown in Figure 6.15, in region I, the relative permittivity of $BaZr_yTi_{1-y}O_3$ ceramics with higher Zr^{4+} content is generally higher in a wide temperature range, therefore a higher ε_{rmax}. This enhanced dielectric response could be attributed to orientational polarization and ionic polarization from small amount Zr^{4+} substitution ($0 \leq y \leq 0.18$) [145]. As for the orientational polarization, non-180º domains are developed to release the internal stress induced by Zr^{4+} substitution, which is similar to development of 90º domains in $BaTiO_3$ ceramics during phase transition [6]. The increased non-180º domain areas contribute to more domain wall vibrations, which therefore improve the dielectric response in $BaZr_yTi_{1-y}O_3$ ceramics [145]. This type of behaviour has been discussed in the context of compositional inhomogeneities. The existence of paraelectric $BaZrO_3$ regions in $BaZr_yTi_{1-y}O_3$ ceramics yields distortion in a long-range ferroelectric $BaTiO_3$ structure. These distortions are stabilized in Zr^{4+}-rich areas, where the dipole interaction becomes weaker and therefore more dipole polarization could be achieved under the application of external electric field (*i.e.* higher dielectric response) [145].

In region II, each $BaZr_yTi_{1-y}O_3$ ($0.15 \leq y \leq 0.30$) ceramic possess only one relative permittivity peak (ε_{rmax} peak), which occurs at the phase transition between the ferroelectric rhombohedral phase and the paraelectric cubic phase. Yu et al. has also

observed the broad ε_{rmax} peak in $BaZr_yTi_{1-y}O_3$ ($0.15 \leq y \leq 0.30$) ceramics, however, they divided region II into two regions based on the measurement of frequency dependent ε_r-T curves [166]. They reported that the frequency dispersion in $BaZr_yTi_{1-y}O_3$ ($0.15 \leq y \leq 0.30$) ceramics is not present until y=0.30, where ferroelectric relaxor behaviour is observed [166]. The relaxor behaviour and frequency dependence are out of scope of this project, however, the broadness of ε_{rmax} peak with increasing Zr^{4+} content (Figure 6.15) does indicate a diffuse phase transition phenomenon at the Curie temperature. This diffuse phase transition is consistent with composition-induced behaviour, which is sensitively dependent on Zr^{4+} concentrations [148, 160]. The existence of non-polar $BaZrO_3$ regions in the long-range polar $BaTiO_3$ structure could again cause distortions in $BaTiO_3$ and break the $BaTiO_3$ macro-domains into some small micro-domains according to various Zr^{4+} amounts, which yields disorders both at the macro- and micro-levels and therefore contributes to the diffuse phase transition behaviour (*i.e.* broad ε_{rmax} peak) [145]. The irregularly changed ε_{rmax} in region II could be potentially attributed to their domain (wall) structures, which are controlled by both the grain size variations and Zr^{4+} concentrations in ceramics [166]. A future work that investigates the microstructure and domain structure of $BaZr_yTi_{1-y}O_3$ system would be helpful to understand this mechanism in more details.

The relative permittivity at room temperature (~298 K) which is obtained from temperature dependent measurements (Figure 6.15) implies the same variations as those measured solely at room temperature (Figure 6.11). The highest relative permittivity at y=0.25 is attributed to its high ε_{rmax} and its Curie temperature close to room temperature

[148]. Ignoring any relaxor behaviour, which has not been considered in this project, the temperature at which the ε_{rmax} peak occurs for each composition has been taken as the Curie temperature (T_C). The obtained phase transition temperatures ($T_{R\text{-}O}$, $T_{O\text{-}T}$ and T_C) from temperature dependent relative permittivity in Figure 6.15 are listed in Table 6.5.

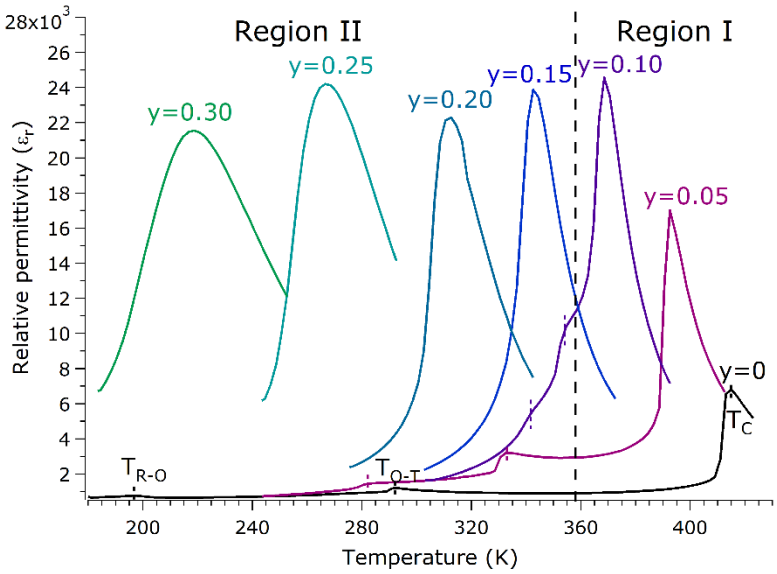

Figure 6.15. The temperature dependence of relative permittivity at 1kHz of $BaZr_yTi_{1-y}O_3$ (y=0-0.30) ceramics.

Table 6.5. Phase transition temperatures of $BaZr_yTi_{1-y}O_3$ (y=0-0.30) identified by relative permittivity peaks in ε_r-T curves.[5]

Sample Name	$T_{R\text{-}O}$ (K)	$T_{O\text{-}T}$ (K)	$T_{T\text{-}C}/T_{R\text{-}C}$ (K)
y=0	184	276	394
y=0.05	266	316	375
y=0.10	326	336	351
y=0.15			326
y=0.20			297
y=0.25			252
y=0.30			206

[5] In this table, the phase transition temperature of each composition was determined from single set measurements, therefore no error bar is displayed (as described in section 3.3).

The temperature dependent *P-E* loops of $BaZr_yTi_{1-y}O_3$ (y=0-0.30) ceramics were measured during both heating and cooling. The obtained remanent polarization and coercive field at 10 K below T_C are shown in Figure 6.16. Combined with Table 6.5, there are two different ferroelectric phases of $BaZr_yTi_{1-y}O_3$ (y=0-0.30) ceramics at 10 K below T_C: tetragonal phase (y=0-0.10) and rhombohedral phase (y=0.15-0.30). As shown in Figure 6.16, the remanent polarization and coercive field decrease with increasing Zr^{4+} content in the tetragonal phase, however, keep nearly constant in rhombohedral phase.

The 310 cm^{-1} peak in temperature dependent Raman spectroscopy of $BaTiO_3$ (Figure 6.7 (A)) indicates that Ti-O bond is stronger in the rhombohedral phase than in the tetragonal phase, with higher vibration energy (higher peak position) and less freedom for movement (lower peak width). Along with data presented in Figure 6.16, it is believed that in the tetragonal phase the Ti-O bond strength could be weakened in the unit cells expanded by Zr^{4+} substitution. This then induces a lower energy to reverse the polarization directions, resulting in lower remanent polarization and coercive field. Whilst in the rhombohedral phase, the higher energy to weaken Ti-O bond could not be induced by the unit cell expansion from the Zr^{4+} substitution. Therefore, less fluctuation in remanent polarization and coercive field is observed.

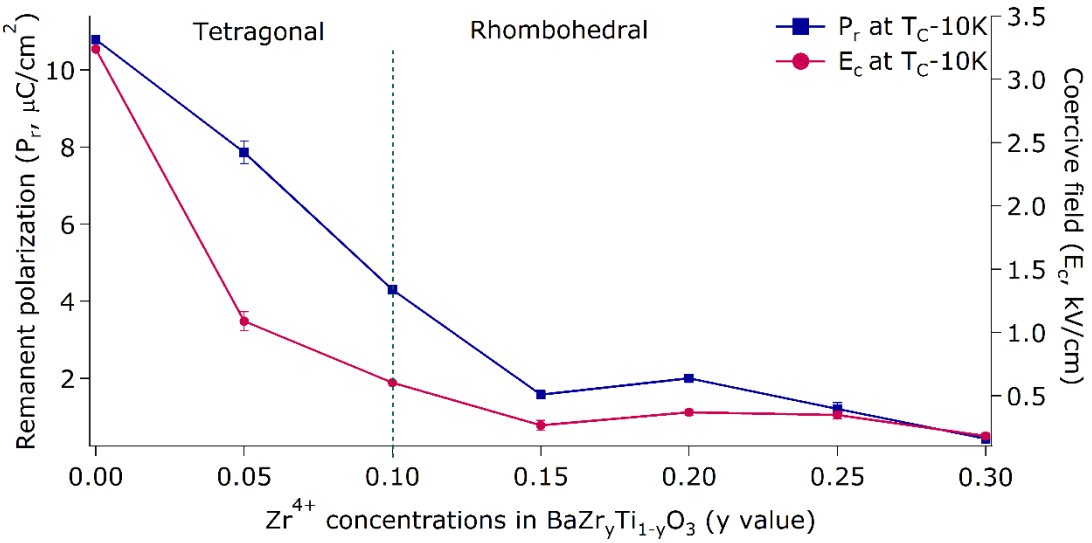

Figure 6.16. The remanent polarization (P_r) and coercive field (E_c) of $BaZr_yTi_{1-y}O_3$ (y=0-0.30) ceramics at 10 K below T_C.

The measured remanent polarizations as a function of temperatures (P_r-T) are shown in Figure 6.17. The heating and cooling curves in the $BaZr_yTi_{1-y}O_3$ (y=0.05-0.30) ceramics match well with each other. Therefore, the variations of P_r with heating in $BaZr_yTi_{1-y}O_3$ (y=0) ceramics have been indicated solely with a measurement during cooling.

Upon heating, there are two distinct P_r peaks in the P_r-T curve of $BaZr_yTi_{1-y}O_3$ (y=0) ceramics below room temperature, which are associated with the improved possible polarization directions at the phase transitions between two ferroelectric phases (R-O and O-T) [6]. The corresponding temperatures are considered as phase transition temperatures $T_{R\text{-}O}$ and $T_{O\text{-}T}$. The other P_r peak is reached at the vicinity of phase transition between the ferroelectric tetragonal and paraelectric cubic phases followed by a sudden drop to a minimum value of P_r (P_{rmin}). The corresponding temperature is considered as $T_{T\text{-}C}$ or Curie temperature (T_C).

The $BaZr_yTi_{1-y}O_3$ (y=0.05) ceramics similarly exhibit two P_r peaks for the *R-O* and *O-T* transitions as in the $BaZr_yTi_{1-y}O_3$ (y=0) ceramics. However, the substitution of Zr^{4+} into $BaTiO_3$ causes the absence of the third peak near T_C, which may be due to a lower ferroelectric character caused by the presence of paraelectric [ZrO_6] clusters within the $BaZr_yTi_{1-y}O_3$ (y=0.05) structure. As the phase transitions of $BaZr_yTi_{1-y}O_3$ (y=0.10) ceramics occurs at a short temperature range (~35 K), the diffuse phase transitions contribute to unclear peaks in the P_r-T curve, therefore the gradient changes in P_r have been taken to indicate the phase transitions.

As for $BaZr_yTi_{1-y}O_3$ (y=0.15-0.30) ceramics, the only phase transition from ferroelectric rhombohedral to paraelectric cubic phase (*R-C*) could be identified by slowing down the decreasing rate of P_r. The stabilization of small P_r values (~ 0 μC/cm^2) indicates no net polarization structure (*i.e.* cubic phase).

As active modes have been observed in the Raman spectra of cubic $BaZr_yTi_{1-y}O_3$ ceramics (Figure 6.6 and Figure 6.7), *i.e.* at temperature over T_C, this implies that the $BaZr_yTi_{1-y}O_3$ ceramics are only cubic phase on average with some ferroelectric (tetragonal or rhombohedral) clusters. It is noticeable in Figure 6.17 that the remanent polarization even increases after the tetragonal to cubic transition (y=0-0.10) whilst remains stable (~0 μC/cm^2) after rhombohedral to cubic transition (y=0.15-0.30). The *P-E* loops of $BaZr_yTi_{1-y}O_3$ (y=0 and 0.30) ceramics are shown in Figure 6.18 as examples to compare *P-E* loop behaviour of transitions to the cubic phase from tetragonal and rhombohedral transitions respectively. This is not a hysteresis loop for $BaZr_yTi_{1-y}O_3$ (y=0.30) ceramics

over T_C, which contributes to low stable remanent polarization after transition from rhombohedral phase. However, the *P-E* loop of cubic $BaZr_yTi_{1-y}O_3$ (y=0) ceramics is swelling, where the maximum value of polarization is not at the highest electric field. One assumption for the appearance of this *P-E* loop could be the existence of electric conductivity in the cubic $BaZr_yTi_{1-y}O_3$ (y=0) ceramics after transferring from tetragonal phase [233]. This conductivity may also be related to the high measurement temperature, where the swelling *P-E* loop of $BaTiO_3$ was measured at 423 K whereas the highest measurement temperature for $BaZr_yTi_{1-y}O_3$ (y=0.30) ceramics was 251 K. The mechanism of this electric conductivity needs some further investigation in future work.

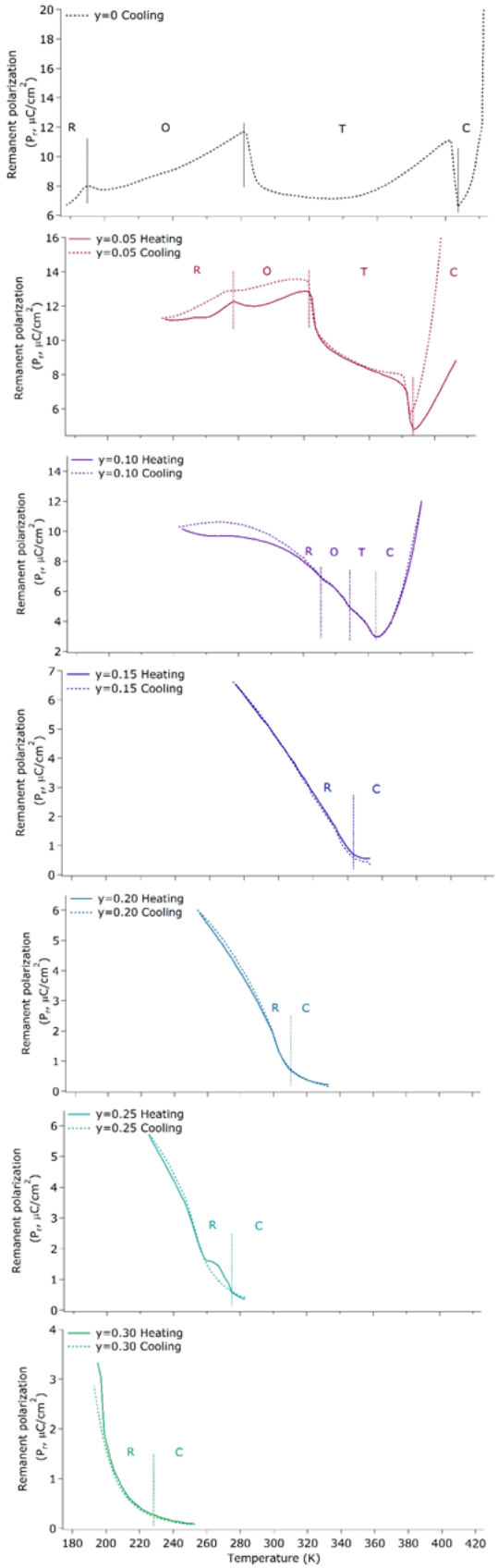

Figure 6.17. The temperature dependence of remanent polarization of $BaZr_yTi_{1-y}O_3$ (y=0-0.30) ceramics.

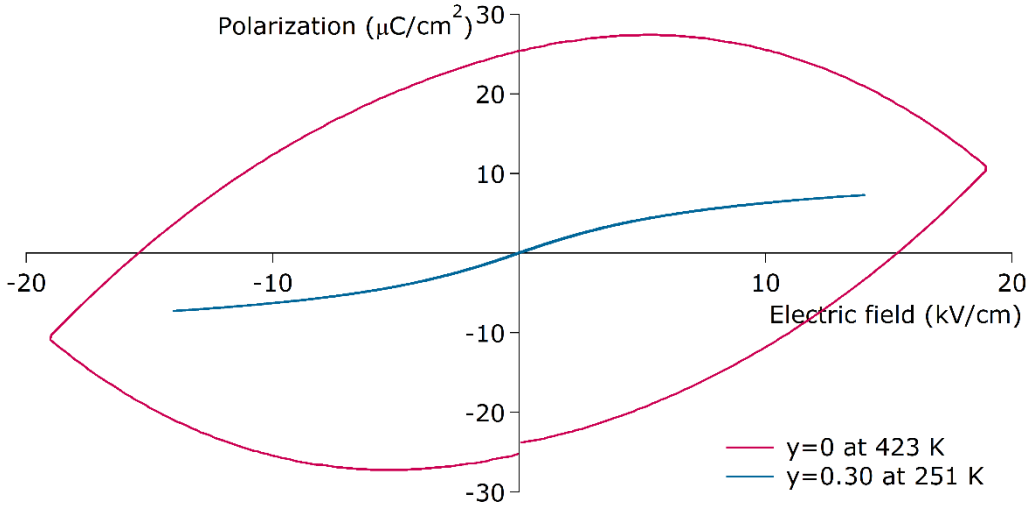

Figure 6.18. *P-E* loops of cubic $BaZr_yTi_{1-y}O_3$ (y=0) at 423 K and $BaZr_yTi_{1-y}O_3$ (y=0.30) at 251 K ceramics.

Based on the discussions above, the phase transitions could also be identified by both the relative permittivity data and the P_r-T curves. The obtained transition temperatures have been added as pink and green markers, respectively, in the $BaZr_yTi_{1-y}O_3$ (y=0-0.30) phase diagram in Figure 6.19. Therefore, the temperature dependent Raman spectroscopy, dielectric and ferroelectric property measurements can all be used to determine the phase diagrams for piezoceramics systems, and achieves good agreement in the $BaZr_yTi_{1-y}O_3$ (y=0-0.30) system investigated here.

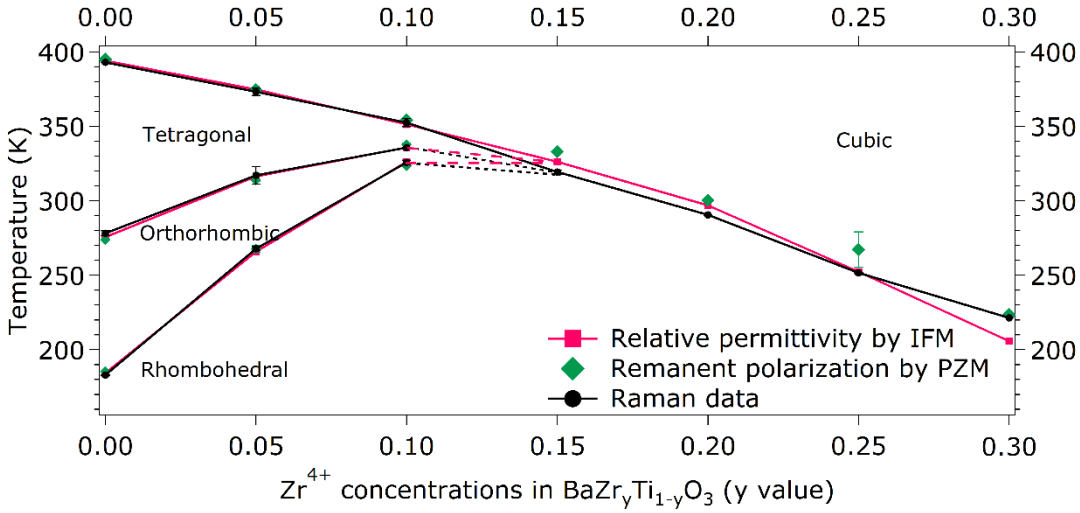

Figure 6.19. Phase diagram of $BaZr_yTi_{1-y}O_3$ (y=0-0.30) derived from Raman spectroscopy (black), relative permittivity (pink) and remanent polarization (green).

6.5 Summary

In summary, a systematic study of $BaZr_yTi_{1-y}O_3$ (y=0-0.30) ceramics has been reported and discussed in this chapter. At room temperature, with increasing Zr^{4+} concentrations in $BaZr_yTi_{1-y}O_3$ (y=0-0.30) ceramics, the phase structure transfers from tetragonal ($BaTiO_3$, y=0) to orthorhombic (y=0.05) to rhombohedral (y=0.10-0.20) and finally to cubic symmetry (y=0.25-0.30). A linear relationship between the Zr^{4+} concentration and the corresponding unit cell volume is fulfilled for the $BaZr_yTi_{1-y}O_3$ (y=0-0.30) system, being independent of the Zr^{4+}-induced phase transition behaviour at room temperature. Therefore, this relationship (V=9.3721y+64.402) can be described by Vegard's law, and used to identify Zr^{4+} content in the $BaZr_yTi_{1-y}O_3$ system in future studies.

A general decrease in average grain size was observed with increasing Zr^{4+} content in $BaZr_yTi_{1-y}O_3$ (y=0-0.30) ceramics. This could be attributed to the inhibited grain growth due to the slower diffusion of Zr^{4+} compared to Ti^{4+}. However, there is a variation at

$BaZr_yTi_{1-y}O_3$ (y=0.25) ceramics with a slight increase in grain size. It is interesting to notice in this project that the effect of Zr^{4+} additions on relative density shows the same trend as that on grain size. Reasons for this similar trend and apparent peak at y=0.25 are unclear based on the current study.

The room temperature functional property measurements of $BaZr_yTi_{1-y}O_3$ (y=0-0.30) ceramics indicate that the highest dielectric properties (ε_r>10000) are observed in $BaZr_yTi_{1-y}O_3$ (y=0.25) ceramics. This is attributed to room temperature being in the vicinity of the phase transition temperature between rhombohedral and cubic phase for this composition, with a corresponding maximum in the relative permittivity. The highest ferroelectric properties (P_r=13.22±0.46 μC/cm^2) and piezoelectric properties (d_{33}=286±9 pC/N, k_p=0.53) are observed in $BaZr_yTi_{1-y}O_3$ (y=0.05) ceramics. Possible explanations for this phenomenon are: more potential polarization rotations in its orthorhombic structure; and a larger-grained microstructure. The coercive field (E_c) of $BaZr_yTi_{1-y}O_3$ (y=0-0.30) ceramics decrease with increasing Zr^{4+} content. This indicates an easier depolarization procedure in $BaZr_yTi_{1-y}O_3$ (y=0-0.30) ceramics due to the weakening of the Ti-O bond caused by an increase in the unit cell volume.

The Raman spectra of $BaTiO_3$ ceramics have similar modes to $BaTiO_3$ powder sample (section 5.1.2), except for slight sharpening and shift to lower energy of modes. This difference is attributed to the more ordered structure in ceramic samples after an extra high temperature sintering step. The temperature dependent Raman spectroscopy measurement of $BaTiO_3$ ceramics also reveals the phase transition points, with $T_{R\text{-}O}$

occurring at a lower temperature, whereas T_{O-T} and T_{T-C} occur at higher temperatures than for the powder samples. This could be related to sintering induced internal stress in the ceramic samples. In this chapter, a phase diagram of the $BaZr_yTi_{1-y}O_3$ (y=0-0.30) system has been constructed based on the changes of ~310 cm^{-1}, ~528 cm^{-1} and ~715 cm^{-1} modes against temperature by measuring temperature dependent Raman spectroscopy.

At 114 K, all the $BaZr_yTi_{1-y}O_3$ (y=0-0.30) ceramics have a rhombohedral structure. The introduction of Zr^{4+} into $BaTiO_3$ induced a more disordered structure and therefore broader Raman modes. The presence of the three modes at ~120 cm^{-1}, ~160 cm^{-1} and ~190 cm^{-1} in $BaZr_yTi_{1-y}O_3$ (y=0.05-0.30) ceramics is considered a rhombohedral characteristic, which is referred to in the analysis of the more complicated zBCT-(1-z)BZT system (section 7.1.2).

The temperature dependent dielectric properties of $BaZr_yTi_{1-y}O_3$ (y=0-0.30) ceramics imply that the maximum relative permittivity (ε_{rmax}) increases with small amounts of Zr^{4+} additions (y=0-0.10, region I). This enhanced dielectric response could be ascribed to orientational polarization and ionic polarization from Zr^{4+} substitution. However, the ε_{rmax} becomes independent of Zr^{4+} concentration with more Zr^{4+} substituted in $BaZr_yTi_{1-y}O_3$ (y=0.15-0.30) samples. In addition, diffuse phase transition behaviour has been observed with the presence of broader ε_r-T peak with increasing Zr^{4+} concentration in $BaZr_yTi_{1-y}O_3$ (y=0.15-0.30) ceramics. This diffuse phase transition behaviour is out of scope of this project and the future work on frequency dependent dielectric property measurements is suggested.

The temperature dependent ferroelectric property measurements indicate a swelling *P-E* loop at high temperatures for samples transformed from tetragonal to cubic structure. One possible explanation for this phenomenon is the existence of electric conductivity; future work is needed to understand this mechanism.

The peaks of ε_r-T curve and peaks or valleys of P_r-T curve are identified as phase transition points for $BaZr_yTi_{1-y}O_3$ (y=0-0.30) ceramics by measuring functional properties, achieving good agreement with Raman spectroscopy measurement that the Zr^{4+} addition induces merged phase transition behaviour from three phase transitions in $BaZr_yTi_{1-y}O_3$ (y=0-0.10) to only one phase transition in $BaZr_yTi_{1-y}O_3$ (y≥0.15). The good agreement between the data derived from the structural and functional property measurements, and the resultant phase diagram then inspired the phase transition study in the complex zBCT-(1-z)BZT system (reported in the next chapter).

Chapter 7 A study of the z($Ba_{0.70}Ca_{0.30}TiO_3$)-(1-z)($BaZr_{0.20}Ti_{0.80}O_3$) (zBCT-(1-z)BZT) system

The preceding chapters have reported investigations of the separate $Ba_{1-x*}Ca_{x*}TiO_3$ (Chapter 5) and $BaZr_yTi_{1-y}O_3$ (Chapter 6) systems. In this chapter, an investigation of a combination of these two systems is reported. A series of $zBa_{0.70}Ca_{0.30}TiO_3$-(1-z)$BaZr_{0.20}Ti_{0.80}O_3$ (abbreviated as zBCT-(1-z)BZT) ceramics for $0 \leq z \leq 1$ were fabricated as detailed in section 3.1.4, combining mixtures of the end member compositions which had been calcined individually at 1250 ºC, followed by sintering of the mixtures at temperatures between 1300 ºC-1500 ºC for 4 hours. The characterisation of the sintered zBCT-(1-z)BZT ceramics is reported and discussed to investigate the effects of sintering temperatures and compositions on the crystal structure, microstructure and the resulting functional properties of the ceramics. The data of end member compositions (BZT, z=0 and BCT, z=1) are same as in Chapter 4 and included here for completeness.

7.1 Characterisation of zBCT-(1-z)BZT ceramics

7.1.1 X-ray diffraction of sintered zBCT-(1-z)BZT ceramics

For completeness, a full set of the X-ray diffraction patterns of sintered zBCT-(1-z)BZT (z=0-1) ceramics are shown in Appendix III for the three sintering temperatures, and only selected features are reproduced and discussed in this section. For ceramics sintered at

1500 ºC a single perovskite phase is observed for all compositions, but at lower sintering temperatures small amounts of secondary phase are observed in the BCT-rich ceramics (z=0.6-1.0 ceramics sintered at 1300 ºC and 1400 ºC), as exampled in Figure 7.1 for z=0.8 ceramics. This secondary phase is identified as a pseudo-cubic (Ba,Ca)(Ti,Zr)O_3 phase, which shows the same reflections as pseudo-cubic Ca-rich (Ba,Ca)TiO_3 phase in z=1 composition (as described in Chapter 4, Figure 4.7 (B)). Therefore, the X-ray diffraction data of 1500 ºC sintered ceramics is used to study the composition induced phase transitions in the zBCT-(1-z)BZT system. A detailed view of $(002)_{pc}$, $(220)_{pc}$ and $(222)_{pc}$ (pc refers to pseudo-cubic symmetry) reflections of zBCT-(1-z)BZT (z=0-1) ceramics sintered at 1500 ºC is shown in Figure 7.2. The splitting in each Miller plane reflections is caused by the different wavelengths of the $K_{\alpha 1}$ and $K_{\alpha 2}$ X-ray radiation.

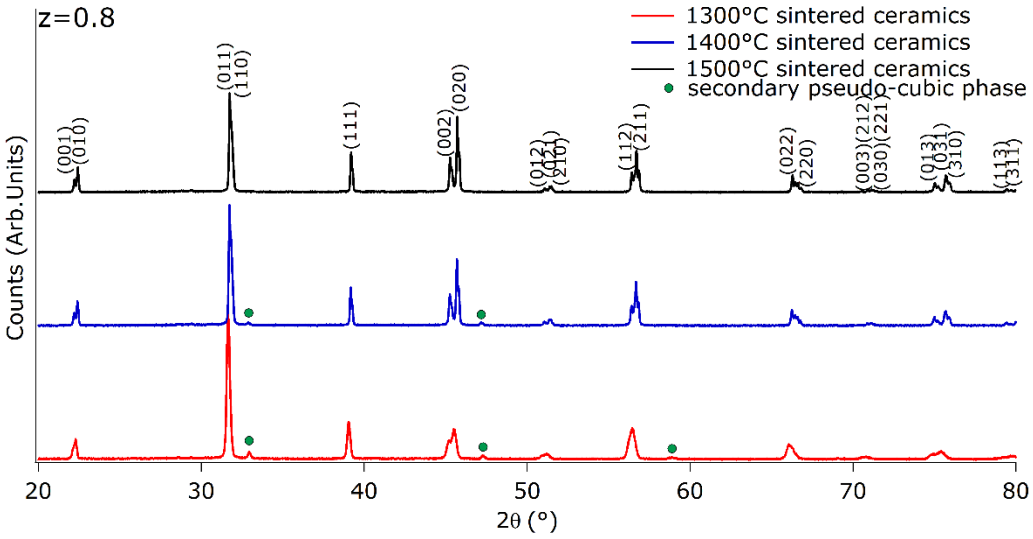

Figure 7.1. The XRD patterns of zBCT-(1-z)BZT (z=0.8) ceramics.

The single $(002)_{pc}$ reflection as well as the splitting of the $(220)_{pc}$ and $(222)_{pc}$ reflections indicates the rhombohedral symmetry for z=0-0.4 ceramics. On the other hand, the

tetragonal symmetry is identified for z=0.6-1 ceramics based on the splitting of the $(002)_{pc}$ and $(220)_{pc}$ reflections and the single $(222)_{pc}$ reflection. However, it becomes more complex to identify the symmetry for z=0.5 ceramics due to doublets in all these reflections. As previous studies have not reached an agreement on the presence of the orthorhombic (*Amm2*) phase in the zBCT-(1-z)BZT system (section 2.5) [28, 204], therefore in this project, pseudo-Rietveld refinement was performed on the X-ray diffraction data from z=0.5 ceramics by using the crystal structure with (1) single orthorhombic (*Amm2*) phase; (2) mixture of tetragonal (*P4mm*) and rhombohedral (*R3m*) phases; (3) mixture of tetragonal (*P4mm*) and orthorhombic (*Amm2*) phases. The refined $(002)_{pc}$ reflections are shown in Figure 7.3 and the consequent values of the R_{wp} (weighted profile R-factor) [234] are (1) 15.26 % with pure orthorhombic phase; (2) 13.48 % with 67.4 wt. % tetragonal phase and 32.6 wt. % rhombohedral phase and (3) 13.61 % with 92.0 wt. % tetragonal phase and 8.0 wt. % orthorhombic phase. As shown in Figure 7.3, all these refinements result in a similar refined $(002)_{pc}$ reflection (indicated as the red line) and none of them achieves a perfect fit with the measured data (blue line). This could be caused by the resolution and multi-chromatic X-ray radiation used in the lab based Bruker D8 Advance X-ray diffractometer, and unrefined atomic coordinates in this project. Therefore, it is impossible to achieve accurate refinement of the site occupancies of each ion or weight fraction of each phase. Hence, the crystal symmetry of z=0.5 ceramics could not be concluded based on this X-ray diffraction data and further investigations were performed by using Raman spectroscopy. And a measurement from synchrotron X-ray

diffraction is under investigation.

In addition, with reference to the XRD patterns of sintered zBCT-(1-z)BZT (z=0-1) ceramics (shown in Appendix III), it is interesting to notice that the relative intensity of reflections in 2θ=44-47º is enhanced with increasing sintering temperature. This could indicate some preferred orientation in the sintered ceramics along (002) in the rhombohedral phase or (002) and (020) in the tetragonal phase. This preferred orientation is not related to the phase identification, however, the origination of this phenomenon in polycrystalline ceramics has not been investigated further in this project.

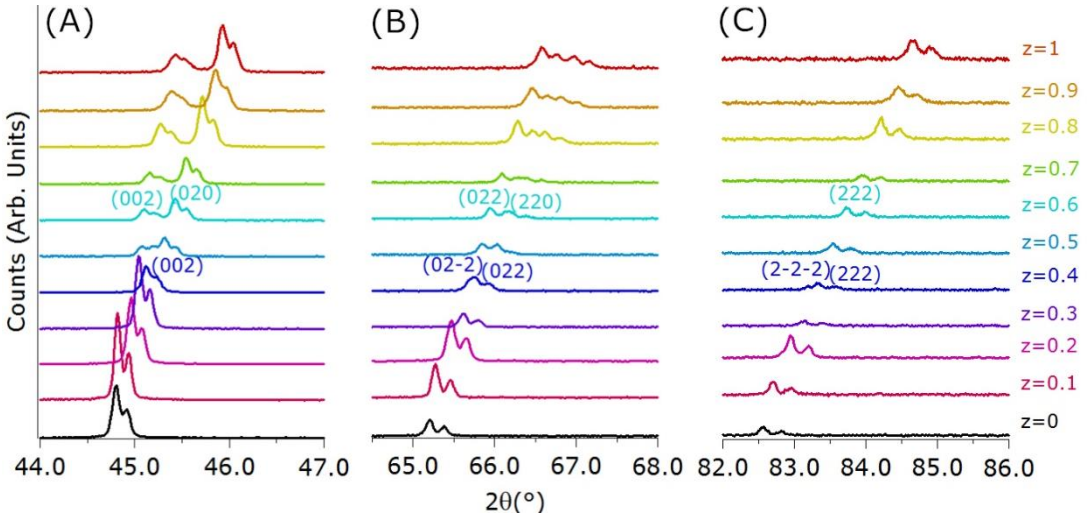

Figure 7.2. XRD data of zBCT-(1-z)BZT (z=0-1) ceramics sintered at 1500 ºC for the (A) $(002)_{pc}$, (B) $(220)_{pc}$ and (C) $(222)_{pc}$ reflections.

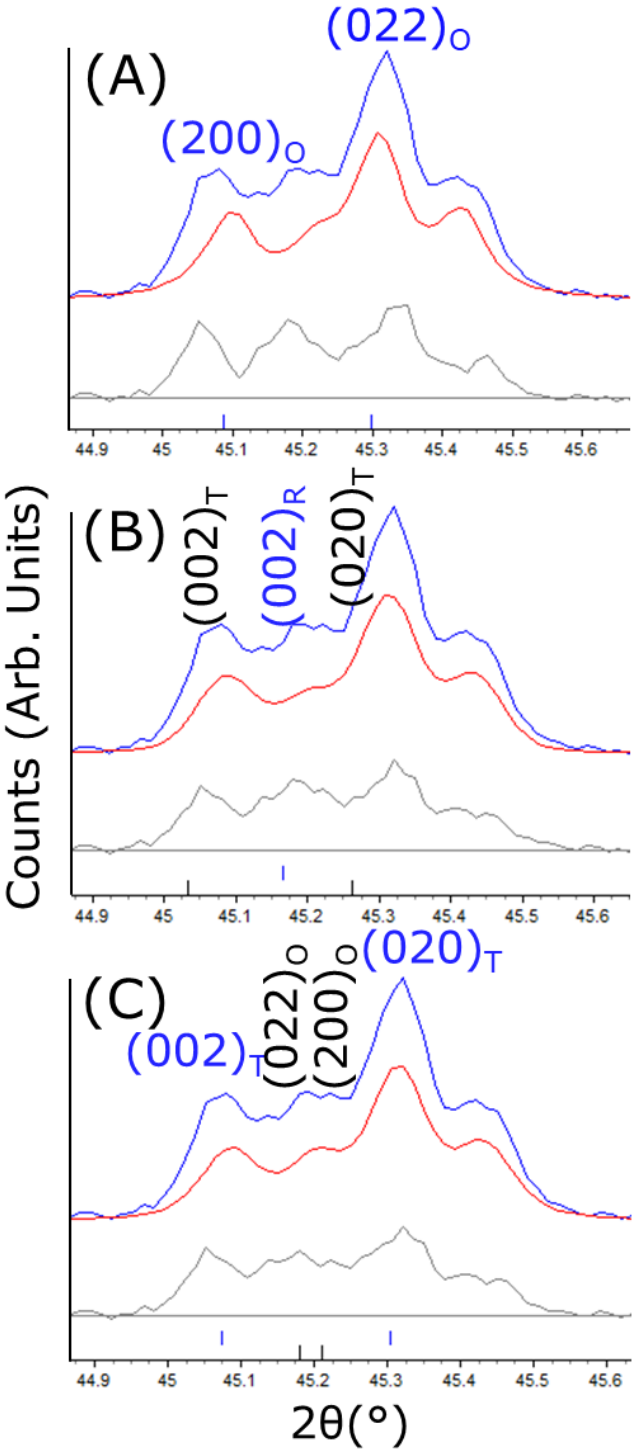

Figure 7.3. Rietveld refinement results of the $(002)_{pc}$ reflection for z=0.5 ceramics sintered at 1500 ºC using crystal symmetry of (A) single orthorhombic phase; (B) mixture of rhombohedral and tetragonal phases; (C) mixture of orthorhombic and tetragonal phases (blue line: measured, red line: refined and grey line: difference between measurement and refinement).

Refinement of the XRD patterns for ceramics sintered at lower temperatures (1300 and

1400 ºC) have rhombohedral structure for the z=0-0.4 ceramics, tetragonal structure for the z=0.6-1 ceramics, and all mentioned possibilities for the z=0.5 ceramics. Figure 7.4 presents unit cell volumes of zBCT-(1-z)BZT (z=0-1) ceramics sintered at 1300 ºC-1500 ºC against BCT (z) content. As shown in Figure 7.4 (A) and (B), there is a small amount of pseudo-cubic phase (≤16.0 wt. %) in BCT-rich ceramics (z=0.6-1) sintered at lower temperatures, which is similar to $Ba_{0.70}Ca_{0.30}TiO_3$ ceramics (section 4.2.3). Compared with ceramics (z=0.6-1) sintered at 1300 ºC, the disappearance of the pseudo-cubic phase in ceramics (z=0.6 and 0.7) sintered at 1400 ºC and in all the ceramic compositions sintered at1500 ºC, implies greater homogeneity with higher temperature sintering. This is attributed to greater Ca^{2+} diffusion into the Ba-site at higher sintering temperature (as discussed in Chapter 4). In addition, the unit cell volume of the predominant ferroelectric phase decreases and the weighted average unit cell volume drops approximately linearly with BCT additions in ceramics sintered at 1300 ºC and 1400 ºC. It is noticeable that a more linear relationship between unit cell volume of ferroelectric phase and BCT content is obtained with increasing sintering temperature, and finally a linear relationship, V=66.272-3.9458z, has been fitted for ceramics sintered at 1500 ºC (Figure 7.4 (C)). As this linear relationship is independent to crystal symmetry, Vegard's relationship could be used, showing that the zBCT-(1-z)BZT can be treated as a pseudo-binary system.

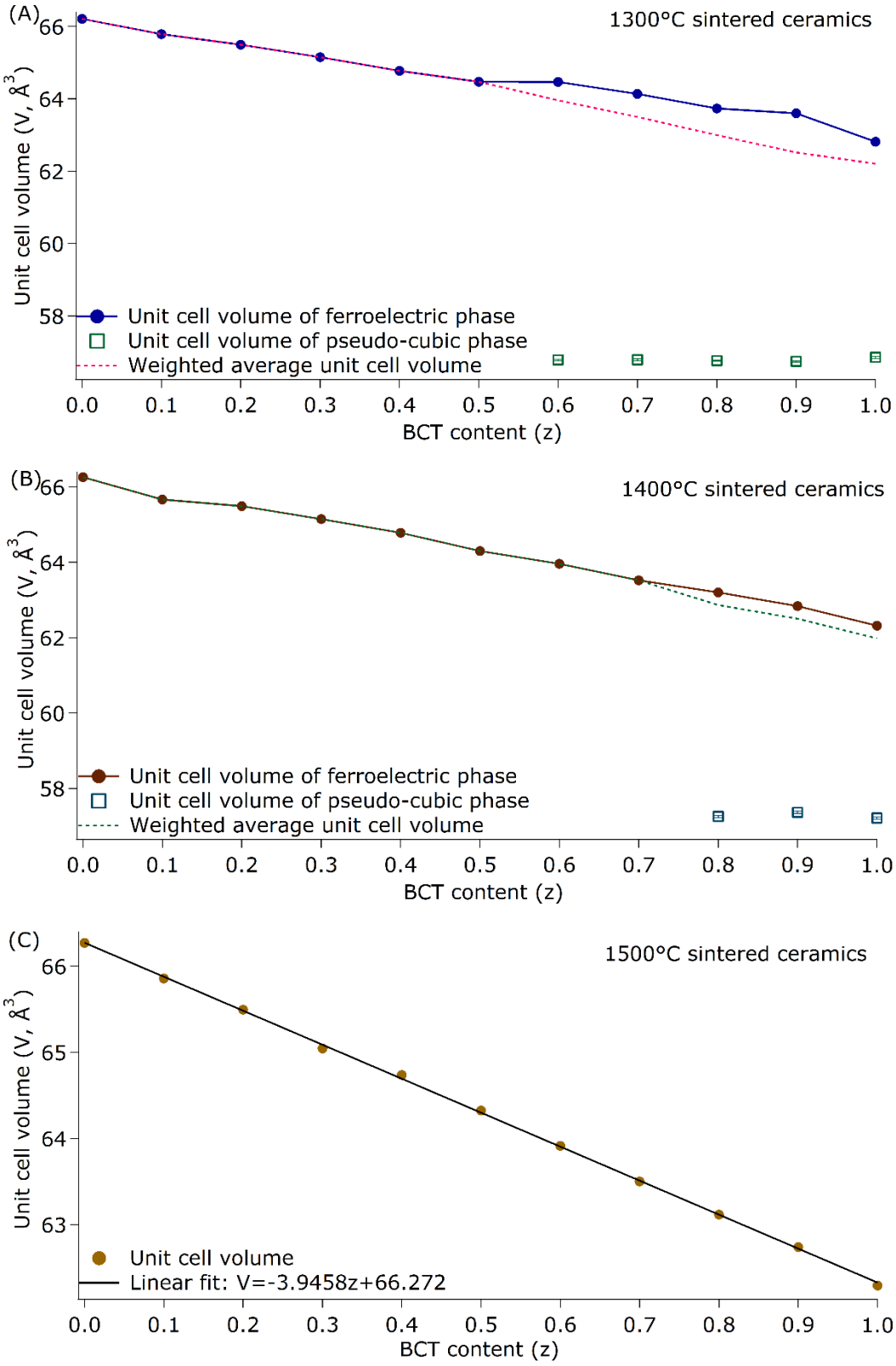

Figure 7.4. The pseudo-Rietveld refined unit cell volume of (A) 1300 ºC, (B) 1400 ºC and (C) 1500 ºC sintered zBCT-(1-z)BZT (*z*=0-1) ceramics from X-ray diffraction data.

Figure 7.5 indicates changes in unit cell volumes of $BaTiO_3$ caused by only Ca^{2+} substitution into Ba-site (pink line) or only Zr^{4+} substitution into Ti-site (green line). These unit cell volumes were calculated based on Vegard's relationships in $Ba_{1-x}Ca_xTiO_3$ (V=64.568-7.4836x) [94] and $BaZr_yTi_{1-y}O_3$ (V=9.3721y+64.402, section 6.1) system. Based on these two linear relationships, the theoretically calculated unit cell volumes of zBCT-(1-z)BZT with both Ba- and Ti- site substitution is shown as a blue dotted line lying between these two lines in Figure 7.5. The calculated unit cell volumes from the derived Vegard's relationship (V=66.272-3.9458z) as well as the measured unit cell volumes of 1500 ºC sintered zBCT-(1-z)BZT ceramics (Figure 7.4 (C)) is plotted as an orange dashed line and black dots respectively in Figure 7.5. The residuals of measured unit cell volumes compared with calculated data from multiple-site substitution (blue) and Vegard's law (orange) are illustrated on the top in Figure 7.5, where the measured data agrees well with calculated data from both methods. This further confirms the full substitution of Ca^{2+} into the Ba-site and Zr^{4+} into the Ti-site in ceramics sintered at 1500 ºC. The zBCT-(1-z)BZT system can thus be considered as a binary solid solution system between BCT and BZT, and composition can be represented by the BCT content (z) in the zBCT-(1-z)BZT phase diagram.

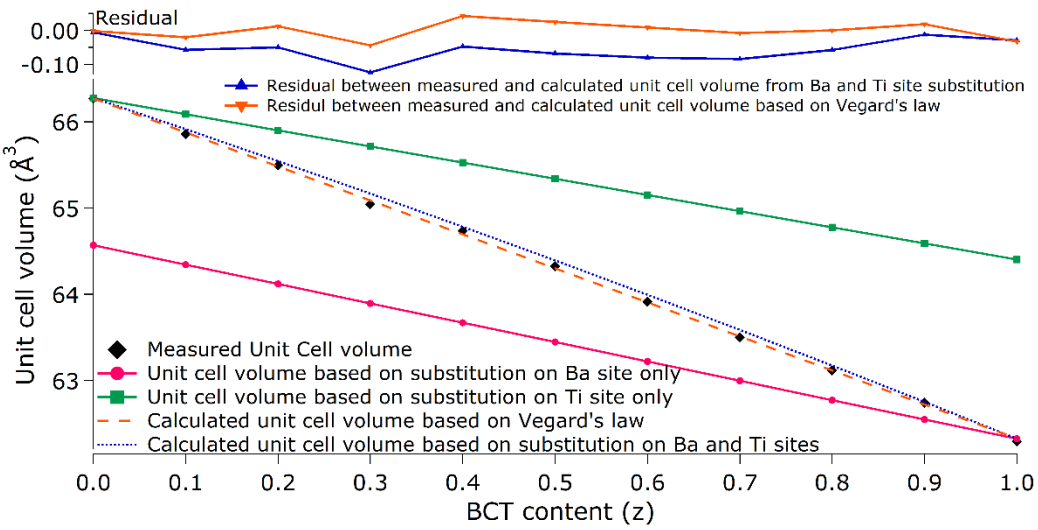

Figure 7.5. Measured and calculated unit cell volume of zBCT-(1-z)BZT ceramics sintered at 1500ºC: pink line for unit cell volume for Ca^{2+} (x*) substituting Ba-site in $BaTiO_3$ (V=64.568-7.4836x*) [94]; green line for unit cell volume for Zr^{4+} (y) substituting Ti-site in $BaTiO_3$ (V=9.3721y+64.402, section 6.1); blue dashed line for calculated unit cell volume for simultaneously substituting Ca^{2+} and Zr^{4+} in $BaTiO_3$ based pink and green lines, residual to measured data is shown as blue solid line; orange dashed line for calculated unit cell volume based on Vegard's law (V=66.272-3.9458z, Figure 7.4 (C)), residual to measured data is shown as orange solid line.

7.1.2 Raman spectroscopy of zBCT-(1-z)BZT ceramics sintered at 1500 ºC

It was shown in sections 5.1.3 and 6.3.1 that the Raman modes of $BaTiO_3$ are strongly affected by single site substitution from both Ca^{2+} and Zr^{4+}, therefore shifts and broadenings in Raman modes of the co-substituted zBCT-(1-z)BZT system were expected to be complicated, due to the simultaneous increasing Ca^{2+} content and reducing Zr^{4+} content as the BCT content increases. This might be a reason for the sparsity of Raman spectroscopy investigations in previous reports on this system. However, as a sensitive and successful detector to ferroelectric phase transitions in its end member systems ($Ba_{1-x*}Ca_{x*}TiO_3$ and $BaZr_yTi_{1-y}O_3$) in preceding chapters, Raman spectroscopy for the

zBCT-(1-z)BZT system has been used in this project, in order to investigate the phase transition behaviour and the corresponding crystal symmetry of each zBCT-(1-z)BZT composition.

The Raman spectra of monophasic zBCT-(1-z)BZT ceramics sintered at 1500 ºC were firstly investigated at low temperature (87 K) to detect the existence of the various ferroelectric symmetries, and the spectra are shown in Figure 7.6 (A). Similar to the $Ba_{1-x*}Ca_{x*}TiO_3$ system (section 5.1.3), BCT addition (*i.e.* Ca^{2+} addition) induces shifts of the ~520 cm^{-1} [E(TO), A_1(TO)] and ~720 cm^{-1} [E(LO), A_1(LO)] modes to higher frequency in the zBCT-(1-z)BZT system. Additionally, the weak shoulder at ~300 cm^{-1} [E(TO+LO), B_1] and weak peak at ~460 cm^{-1} [E(TO+LO), A_1(LO)] start to appear at z=0.4 and z=0.8 respectively with the reduction of BZT content (*i.e.* reduction of Zr^{4+} content), which is analogous to the $BaZr_yTi_{1-y}O_3$ system (section 6.3.1). In addition, the A_{1g} asymmetric mode (~780 cm^{-1}) is only present in BZT-rich compositions (z=0-0.4), and with further increase in the BCT content ($Zr^{4+}\leq0.10$), it is masked with the adjacent ~720 cm^{-1} mode which becomes quite broad. This dependence of the A_{1g} asymmetric mode on Zr^{4+} content has also been observed in the $BaZr_yTi_{1-y}O_3$ system (as discussed in section 6.3.1) [75, 110].

The polymorphic phase transitions reported for the $Ba_{1-x*}Ca_{x*}TiO_3$ and $BaZr_yTi_{1-y}O_3$ systems revealed that the Raman modes in the region 80-300 cm^{-1} are those mostly affected by the compositional changes, therefore an expansion of this region is shown in Figure 7.6 (B). The coexistence of Raman modes at ~120 cm^{-1}, ~150 cm^{-1} [A_1(TO)] and

~200 cm^{-1} [E(TO+LO), A_1(LO)] is present in the *z*=0-0.7 compositions, indicating the characteristics for rhombohedral symmetry, where the ~120 cm^{-1} mode is related to Zr-O motion (as in the $BaZr_yTi_{1-y}O_3$ system) [75]. It is noticeable that the appearance of a weak shoulder at ~300 cm^{-1} [E(TO+LO), B_1] accompanied with a [A_1(TO)] mode at ~260 cm^{-1} in the *z*=0.4-0.7 compositions could be a result of the split of the broad ~300 cm^{-1} mode observed in the *z*=0-0.3 composition.

Further increasing the BCT content to *z*=0.8-1, those modes characteristic of the rhombohedral structure vanish, indicating the loss of rhombohedral symmetry. Based on the findings in the $BaZr_yTi_{1-y}O_3$ system that the Zr^{4+}-related ~125 cm^{-1} dip only occurred in the rhombohedral and orthorhombic phases [72, 153, 154], the absence of ~125 cm^{-1} dip in BCT-rich compositions (*z*=0.8-1) may indicate the corresponding tetragonal symmetry. This phase transition is also accompanied with the degradation of the ~150 cm^{-1} mode. The other change in tetragonal spectra of zBCT-(1-z)BZT (*z*=0.8-1) is the presence of a broad peak around 290 cm^{-1}, which is believed to be merged from a broad ~260 cm^{-1} [A_1(TO)] mode and the weak ~300 cm^{-1} shoulder. Similar to the $Ba_{1-x*}Ca_{x*}TiO_3$ system (section 5.1.3), this mixed mode shifts to a lower frequency with increasing BCT content (*i.e.* Ca^{2+} content).

In the discussion above, the Raman spectroscopy measurements at 87 K did not indicate the existence of orthorhombic symmetry in zBCT-(1-z)BZT (*z*=0-1) ceramics, investigating in compositional steps of *z*=0.1. This could be attributed to either the orthorhombic symmetry not being present, or the *z*=0.1 step being larger than any

orthorhombic phase region at 87 K. Therefore, it was necessary to investigate Raman spectroscopy at room temperature to identify the composition induced phase transitions in the zBCT-(1-z)BZT system and clarify the uncertain phase structure of z=0.5 composition from the X-ray diffraction data presented in section 7.1.1.

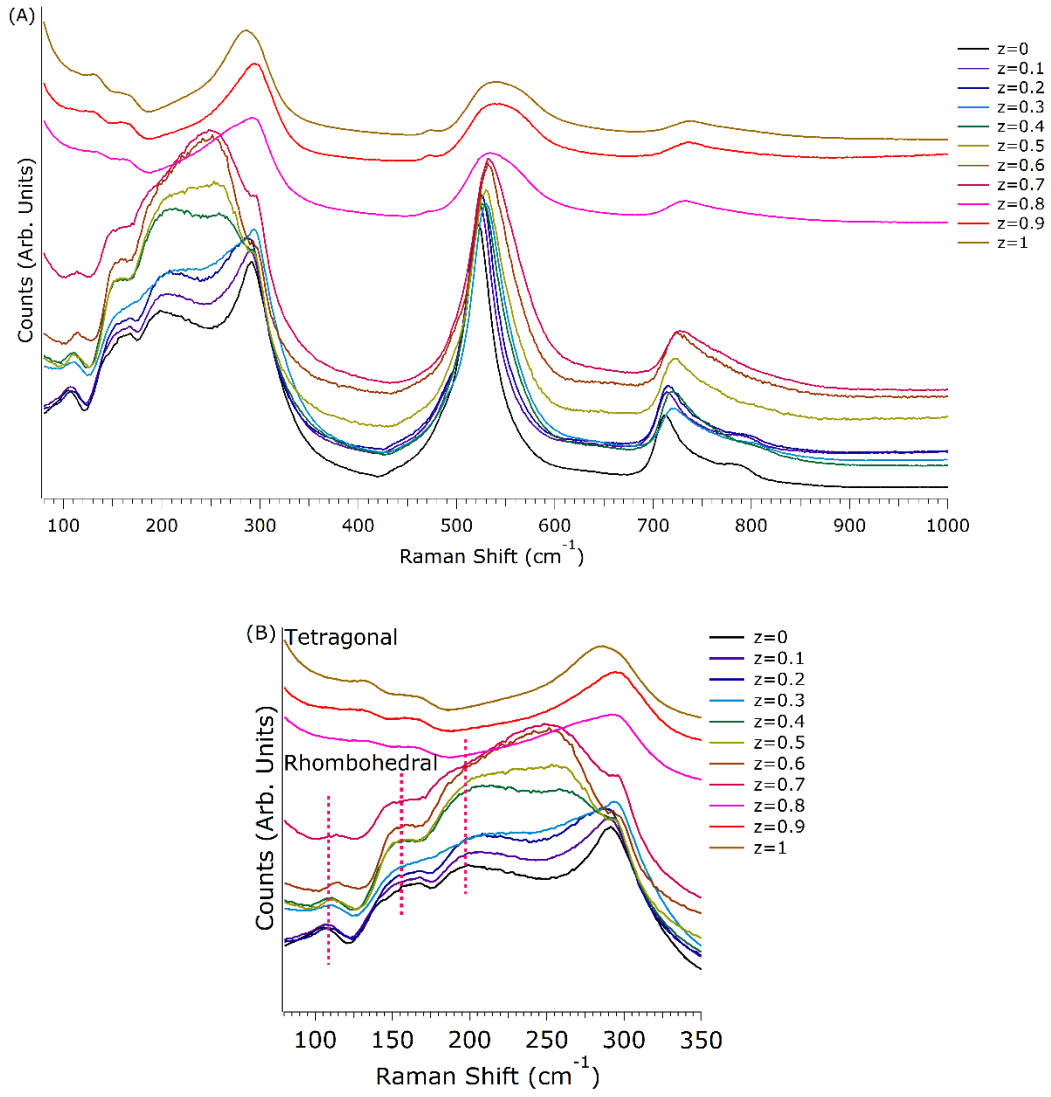

Figure 7.6. Raman spectra of zBCT-(1-z)BZT (z=0-1) ceramics sintered at 1500 ºC and measured at 87 K (A) with broad shifts range; (B) detailed view of 100-350 cm^{-1} region, dotted pink line indicates the rhombohedral characteristic modes.

Compared with the 87 K spectra (Figure 7.6), the room temperature Raman modes (shown

in Figure 7.7) are broader and possess a general shift to lower frequency as a result of the larger molecular vibrations at higher temperature. Therefore, the phase transition identification at room temperature is similar to that at low temperature except for the position of each mode.

Figure 7.7 shows the weakening of the typical rhombohedral modes (~105 cm^{-1}, ~150 cm^{-1} and ~180 cm^{-1}) in the z=0-0.4 compositions compared to the data measured at 87 K indicates the gradual loss of rhombohedral symmetry at room temperature. However, the presence of the ~180 cm^{-1} mode suggests the rhombohedral structure of z=0-0.4 ceramics at room temperature. For the z=0.5 ceramics, the rhombohedral modes are weakened, especially the ~180 cm^{-1} mode which is replaced by a broad mode at ~210 cm^{-1}, which is considered as a feature of orthorhombic spectra [144, 155]. A shift of this ~210 cm^{-1} mode to higher frequency (~230 cm^{-1}) as well as the weakening and disappearance of the ~120 cm^{-1} dip and ~150 cm^{-1} mode reveals the transition to the tetragonal phase for ceramics with compositions of z=0.6-1, which is similar to the observation in $BaZr_yTi_{1-y}O_3$ system (section 6.3.1, Figure 6.9) [72, 153, 154].

Therefore, the room temperature Raman spectra are consistent with the existence of orthorhombic symmetry in ceramics with composition z=0.5, and indicates that the failure to detect this phase at 87 K may be a result of it only occurring over a small compositional range (less than the z=0.1 step size). The composition induced phase transitions in zBCT-(1-z)BZT system at room temperature are therefore from rhombohedral symmetry at the BZT-rich end (z=0-0.4) to orthorhombic symmetry at z=0.5 and finally to tetragonal

symmetry at the BCT-rich end (z=0.6-1).

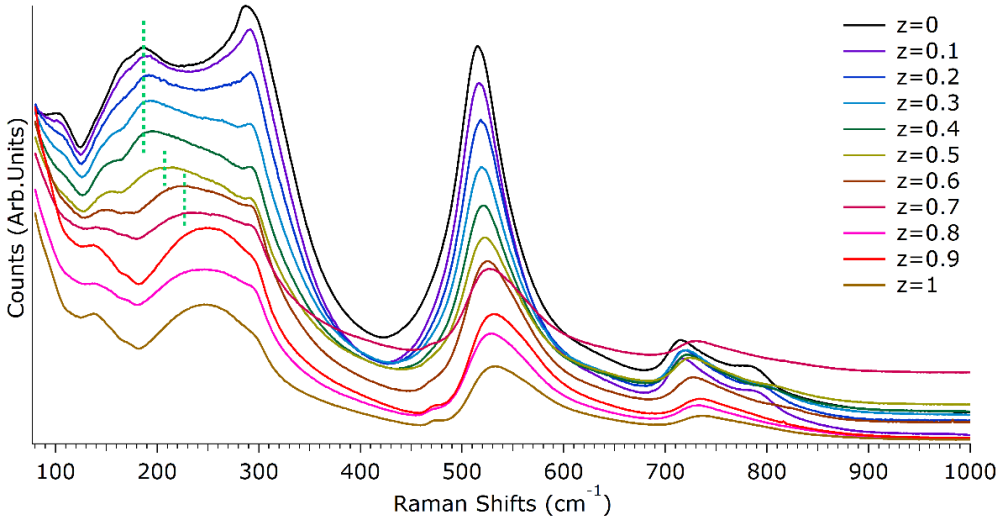

Figure 7.7. Raman spectra of zBCT-(1-z)BZT (z=0-1) ceramics sintered at 1500 ºC and measured at room temperature, dotted green line indicates the replacement of ~180 cm^{-1} mode in rhombohedral symmetry into broad ~210 cm^{-1} mode in orthorhombic symmetry and then shift to ~230 cm^{-1} in tetragonal symmetry.

7.1.3 Microstructure and physical properties of sintered zBCT-(1-z)BZT ceramics

The micrographs of sintered zBCT-(1-z)BZT (z=0.4 and 0.6) ceramics are shown in Figure 7.8, as representatives for BZT-rich and BCT-rich ceramics in the solid solution. Being similar to the end-member ceramics (BZT and BCT, shown in Figure 4.20 and Figure 4.8), both of these compositions, when sintered at 1300 ºC, possess small grains between 1-2 µm in size. According to the XRD data (Figure 7.4 (A)) and micrographs of the low temperature sintered BCT ceramics (Figure 4.8 (C) and (D)), submicron-sized grains in z=0.6 ceramics sintered at 1300 ºC (Figure 7.8 (Bi)) are associated with a second pseudo-cubic phase, which disappears after sintering at higher temperature due to better homogeneity being achieved. When increasing the sintering temperature to 1400 ºC and

1500 ºC, both *z*=0.4 and 0.6 ceramics possess dense microstructure and larger grains (>10 μm).

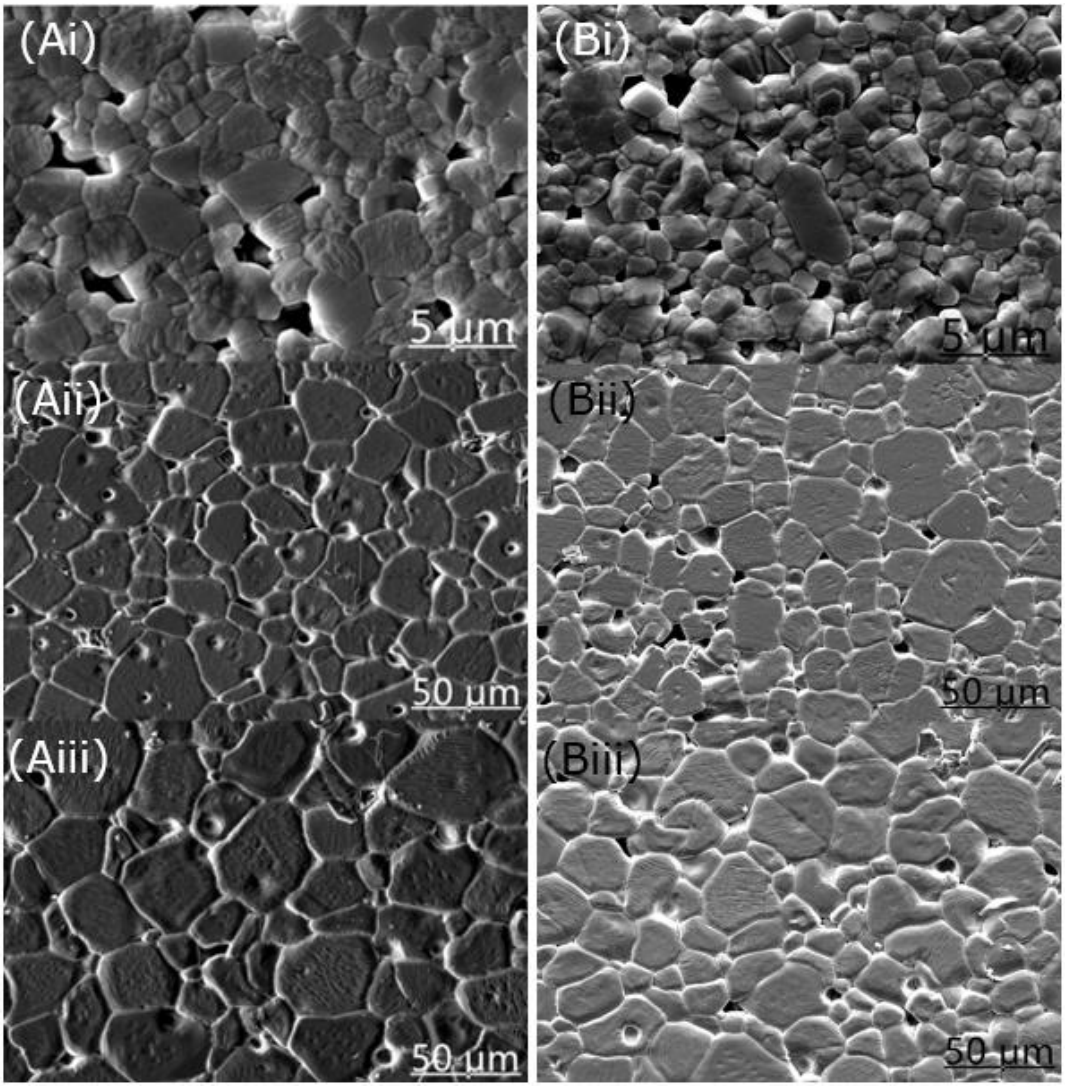

Figure 7.8. Micrographs of sintered zBCT-(1-z)BZT ceramics: (A) *z*=0.4 and (B) *z*=0.6. And (i), (ii) and (iii) refer to sintering temperatures of 1300 ºC, 1400 ºC and 1500 ºC respectively.

The grain sizes of all sintered zBCT-(1-z)BZT (*z*=0-1) ceramics are illustrated in Figure 7.9, where it can be seen that the grain sizes of ceramics sintered at 1300 ºC and 1400 ºC are almost independent of composition, lying in the ranges of 1-2 μm and 8-20 μm respectively. However, the grain size of ceramics sintered at 1500 ºC gradually decreases

with increasing BCT content (z value). With reference to $BaZr_yTi_{1-y}O_3$ (y=0-0.20) ceramics sintered at 1500 ºC (section 6.1, Figure 6.4), reducing Zr^{4+} concentrations contribute to larger grains. Therefore, this decrease in grain size with BCT addition (*i.e.* Ca^{2+} addition and Zr^{4+} reduction) appears to be more affected by Ca^{2+} addition. Additionally, the resultant difference in grain sizes between ceramics sintered at 1400 ºC and 1500 ºC is larger at the BZT end (~20 μm) and reduces with BCT addition. In BCT-rich ceramics (z=0.6-1), this variation vanishes and ceramics sintered at 1400 ºC and 1500 ºC possess similar grain sizes. Combined with the corresponding relative density (shown in Figure 7.10), sintering at 1400 ºC is sufficient to produce BCT-rich ceramics with grain growth and high relative density (>90 %) [3]. It is worth noting that both grain size and relative density are independent of composition and sintering temperature (1400 and 1500 ºC) in BCT-rich ceramics. This composition induced effect is possibly related to different sintering mechanisms between the Ca^{2+} and Zr^{4+} additions. In BCT-rich ceramics, the lower melting point (~1580-1620 ºC for $Ba_{1-x*}Ca_{x*}TiO_3$ (x*≤0.30) [89] and the observed melting phenomenon in section 4.2.3) and the lower Zr^{4+} content (y≤0.08) contributes to the easier diffusion of atoms at any particular heat treatment temperatures, as the formation of $BaZr_yTi_{1-y}O_3$ needs higher heating temperature (≥1500 °C) to achieve homogeneous diffusion of Zr^{4+} into $BaTiO_3$ [129, 131]. Therefore, a lower sintering temperature is required for obtaining denser BCT-rich ceramics compared to BZT-rich ceramics.

In terms of the ceramics sintered at 1300 ºC, as shown in Figure 7.10, higher relative

densities are obtained for the central compositions (z=0.2-0.8). The addition of BCT into BZT or the other way round improves the atomic movement from new dopant (Ca^{2+} or Zr^{4+}) in the solid solution, offering chemical potential as an additional driving force (other than thermal energy) for sintering [235]. This is likely to promote the densification procedure in these central compositions.

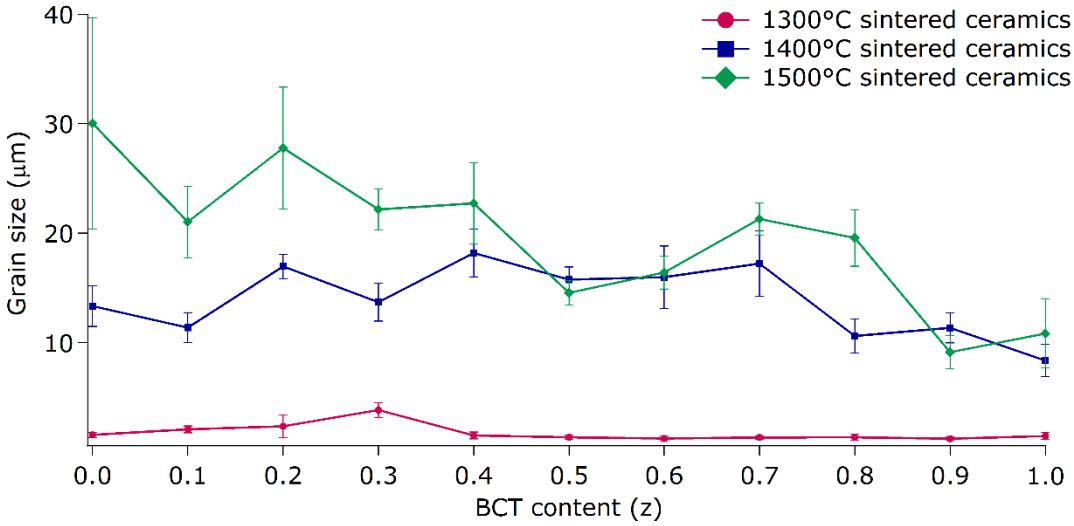

Figure 7.9. Grain sizes of zBCT-(1-z)BZT (z=0-1) ceramics sintered at 1300 ºC-1500 ºC.

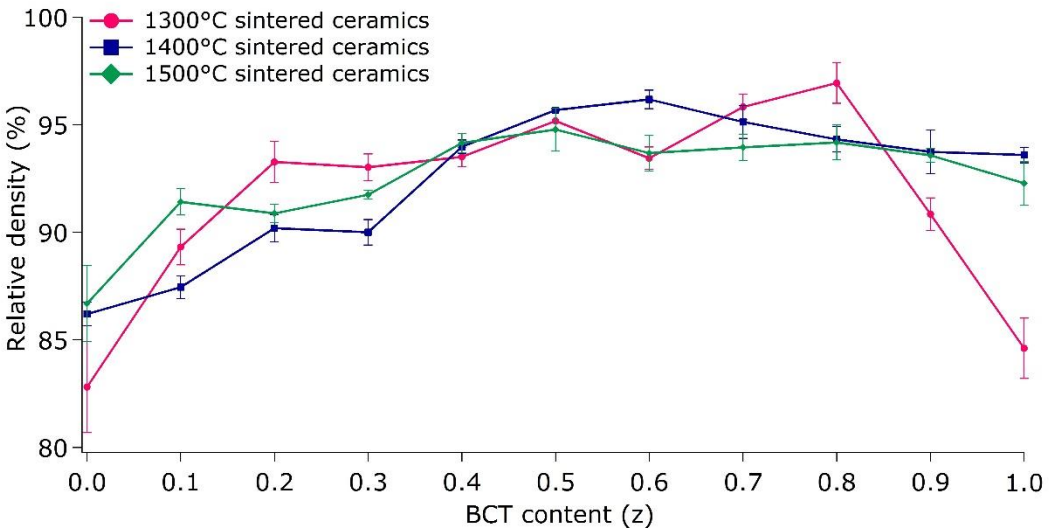

Figure 7.10. Relative density of zBCT-(1-z)BZT (z=0-1) ceramics sintered at 1300 ºC-1500 ºC.

The micrographs of zBCT-(1-z)BZT (z=0-1) ceramics sintered at 1400 ºC are shown in Figure 7.11. A good consistency between relative density and microstructure is achieved for 1400 ºC sintered ceramics. As shown in Figure 7.11 (A)-(E), the porosity decreases with more BCT addition in BZT-rich ceramics. As for BCT-rich ceramics, shown in Figure 7.11 (G)-(K), the microstructure is denser than that of BZT-rich ceramics with constantly higher relative density (94 %-96 %). The insufficient densification in BZT-rich ceramics and improved densification in BCT-rich ceramics further prove the previously mentioned assumption that the required sintering temperature is dropped with BCT additions.

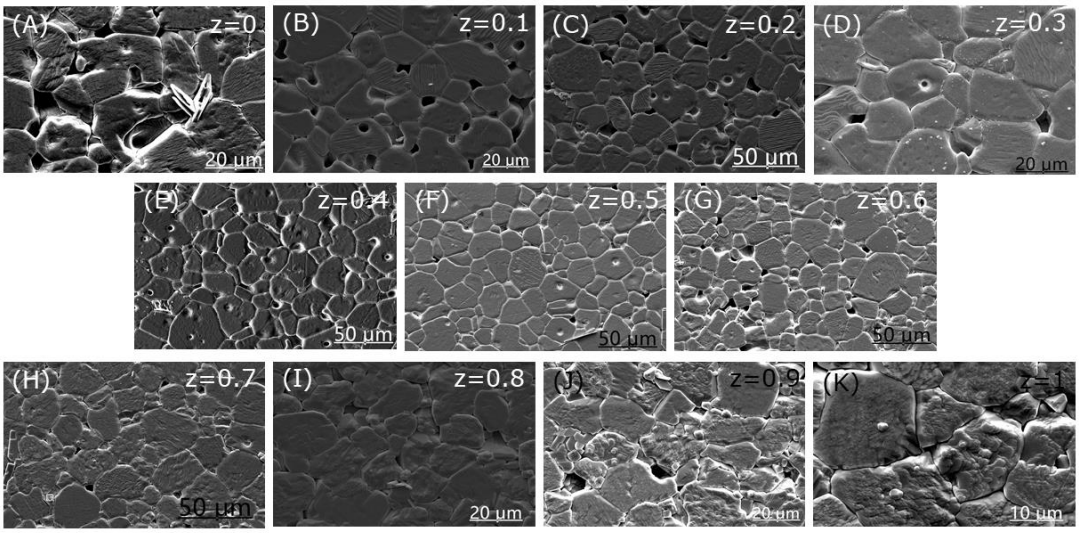

Figure 7.11. Micrographs of zBCT-(1-z)BZT ceramics sintered at 1400 ºC, where (A)-(K) refer to compositions of z=0-1 in steps of 0.1.

7.1.4 Functional properties of sintered zBCT-(1-z)BZT ceramics (measured at room temperature)

The dielectric properties of sintered zBCT-(1-z)BZT ceramics are shown in Figure 7.12.

It can be seen in Figure 7.12 (A) that the relative permittivity of ceramics sintered at 1300 ºC is generally slightly larger than that of those sintered at 1400 ºC and 1500 ºC, the exceptions being for z=0 and z=0.5, although the differences are small. The exception for the z=0 sample (relative permittivity ~3500) may be due to its lower relative density (~82 %, Figure 7.10). The largest relative permittivity value for the ceramics sintered at 1300 ºC occurs for the z=0.1 composition (~5000) and then falls with increasing z to a value of ~700 for z=1.0 (BCT). One possible contribution to higher relative permittivity in the ceramics sintered at 1300 ºC is the grain size (1-2 μm) being similar to the optimal grain size of $BaTiO_3$ ceramics (0.7-1 μm) to produce high dielectric properties [49]. In addition, the broader XRD peaks (Figure 4.7 (Bi) and Figure 4.19 (Bi)), the presence of secondary phase in XRD patterns of BCT-rich ceramics (Figure 4.7 (Bi) and Figure 7.1, Appendix III (G)-(K)) and ε_r-T peak (Figure 5.10) of 1300 ºC sintered ceramics indicate the existence of heterogeneity, which is believed to promote the ionic polarization and dipole polarization in ceramics by the presence of disorders and defects distorting the long-range ferroelectric structure and weakening dipole interactions [145]. Therefore, ceramics sintered at 1300 ºC tend to exhibit higher relative permittivity and relative higher dielectric loss (shown in Figure 7.12 (B)).

Compositional variations in the dielectric properties are also observed for the ceramics sintered at higher sintering temperatures. The ceramics sintered at 1500 ºC, with full ionic diffusion and a single perovskite phase, are chosen to illustrate this effect. Figure 7.12 (A) reveals that the largest relative permittivity (~5500) is obtained for z=0. This is ascribed

to the measurement temperature (room temperature) being in the vicinity of the Curie temperature of this composition (see section 6.4.2). With the addition of BCT into the solid solution, as a low-permittivity phase [125], the relative permittivity decreases, which is analogous to Ca^{2+} addition reducing the relative permittivity in the $Ba_{1-x*}Ca_{x*}TiO_3$ system (see section 5.2.1). The observed anomaly at z=0.5 (~3000) is also reported in previous literature, as a result of this being the 'MPB composition' [28]. This enhancement in relative permittivity, which is superior to other lead-free piezoelectric systems, is believed to be attributed to increased potential polarization orientations in the vicinity of the orthorhombic to tetragonal phase boundary [206]. This coincides with the corresponding largest dielectric loss at z=0.5 (Figure 7.12 (B)).

As described in section 6.4.1, the unploed and poled $BaZr_yTi_{1-y}O_3$ (y=0-0.30) ceramics indicates insignificant difference in relative permittivity. The same observation is shown in zBCT-(1-z)BZT ceramics (Figure 7.12 (A)). This might be a characteristic of $BaTiO_3$-based ceramics, which is observed in coarse-grained $BaTiO_3$ ceramics in previous report [51], and in finer-grained 1300 °C sintered zBCT-(1-z)BZT ceramics (1-2 μm, shown in Figure 7.9) in this project.

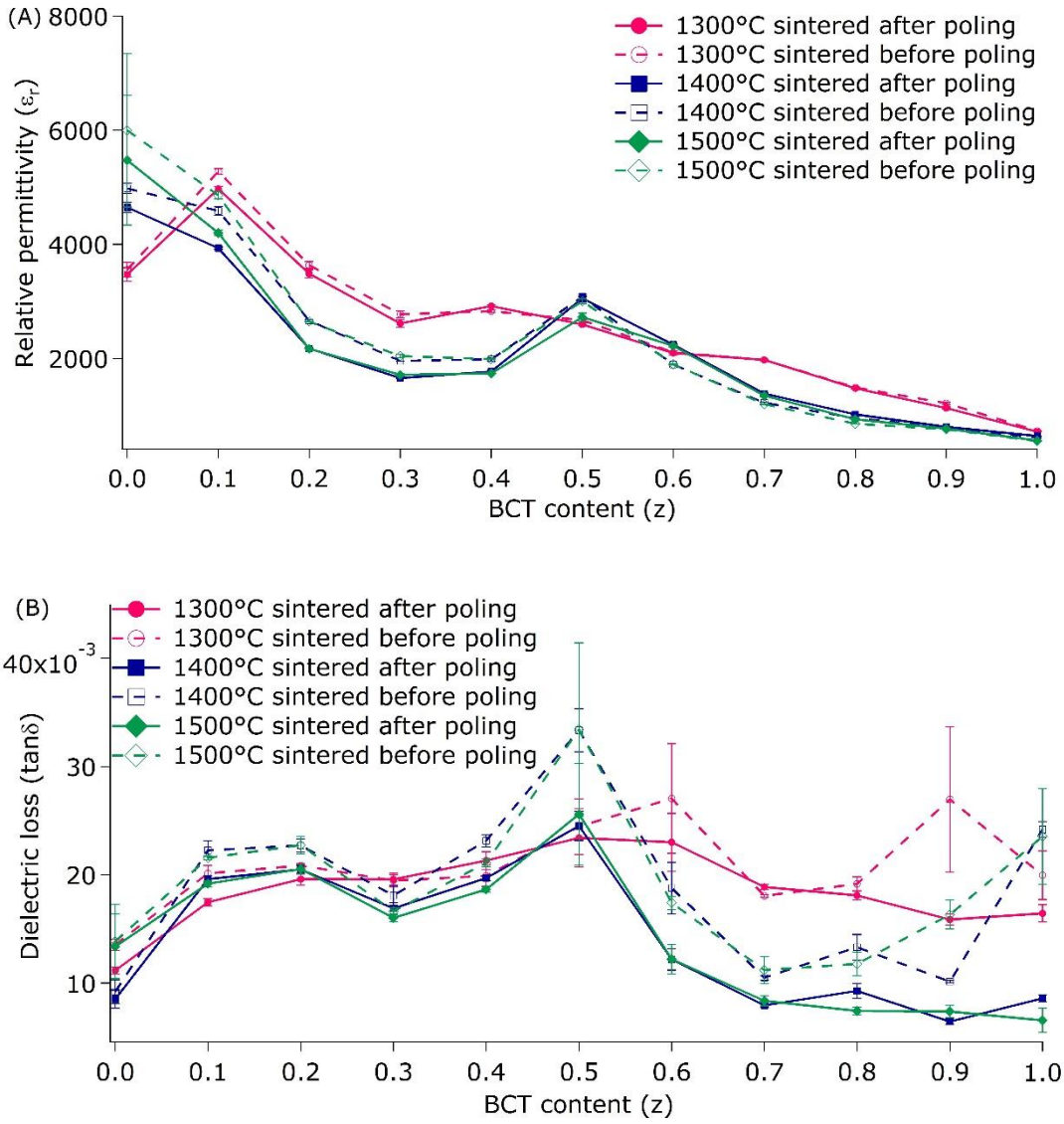

Figure 7.12. Dielectric properties of sintered zBCT-(1-z)BZT ceramics measured at room temperature: (A) relative permittivity; (B) dielectric loss.

As in previous chapters, the remanent polarisation and coercive field have been chosen to illustrate the ferroelectric properties of sintered zBCT-(1-z)BZT ceramics, and these are shown in Figure 7.13. It can be seen in Figure 7.13 (A) that the remanent polarization in ceramics sintered at 1300 ºC is smaller than that for the higher sintering temperatures across the whole composition range. This may be a result of limited polarization reversal in the smaller grains. Increasing the sintering temperature to 1400 ºC and 1500 ºC

promotes the remanent polarization values due to larger grain sizes.

Similar to the dielectric properties, the ferroelectric properties also vary across the composition range. The BZT end ceramic (z=0) possesses the lowest remanent polarization (P_r=3.04±0.68 μC/cm^2) as room temperature is close to the Curie temperature for this composition. In BZT-rich ceramics (z=0-0.4), the remanent polarization is raised by BCT addition with Zr^{4+} content (y value) dropping from 0.20 to 0.08. This behaviour is similar to rhombohedral $BaZr_yTi_{1-y}O_3$ ceramics, where higher remanent polarization is measured in compositions with lower Zr^{4+} contents (section 6.4.1). With further increasing BCT content (z=0.5-1), the remanent polarization becomes independent of compositional variations. The tetragonality distortion (c/a) of BCT-rich ceramics (z=0.6-1.0) is shown in Figure 7.14 and increases with increasing z value, which is estimated to yield higher spontaneous and remanent polarization values. However, the constant remanent polarization in this composition range (P_r~10 μC/cm^2) does not match this expectation. This constant remanent polarization is possibly restricted by the grain size (≤25 μm). Therefore, it is hard to separate grain size and composition effects on the remanent polarization in zBCT-(1-z)BZT ceramics. It is interesting to note that the linear increase in tetragonality of zBCT-(1-z)BZT system rather than the invariance in the $Ba_{1-x}Ca_xTiO_3$ system with Ca^{2+} addition is induced by Zr^{4+} substitution in the B-site [3, 94].

Figure 7.13 (B) reveals the compositional induced changes in the coercive field where it can be seen that the there is a general trend of the coercive field increasing with increasing

z values. In BZT-rich ceramics (z=0-0.4), the compositional dependence is small with ceramics sintered at all temperatures (1300 ºC-1500 ºC) having similar values of coercive field in the range E_c=0.4-2.3 kV/cm. On the contrary, in BCT-rich ceramics (z=0.6-1), much higher coercivity values are measured, and the ceramics sintered at 1300 ºC have lower coercive field values, indicative of an easier domain switching procedure, than those sintered at higher temperatures. This may be related to the presence of small amounts of pseudo-cubic phase in the low temperature sintered BCT-rich ceramics (Figure 7.1 and Figure 7.4). Similar to $Ba_{1-x}*Ca_x*TiO_3$ system (section 5.2.1), the consequence of the reduction of numbers of tetragonal domains and smaller tetragonality (Figure 7.14) yield a reduction in polarization as well as coercive field for BCT-rich ceramics sintered at 1300ºC. In general, zBCT-(1-z)BZT ceramics are 'softer' in BZT-rich compositions and become 'harder' with BCT addition. Combined with high relative permittivity (~3000, Figure 7.12 (A)), the relative high remanent polarization (P_r=8.94±0.18 μC/cm^2) and small coercive field (E_c=2.65±0.08 kV/mm) for the z=0.5 composition, agree with previous reports that z=0.5 ceramics are 'soft' lead-free piezoceramics [28].

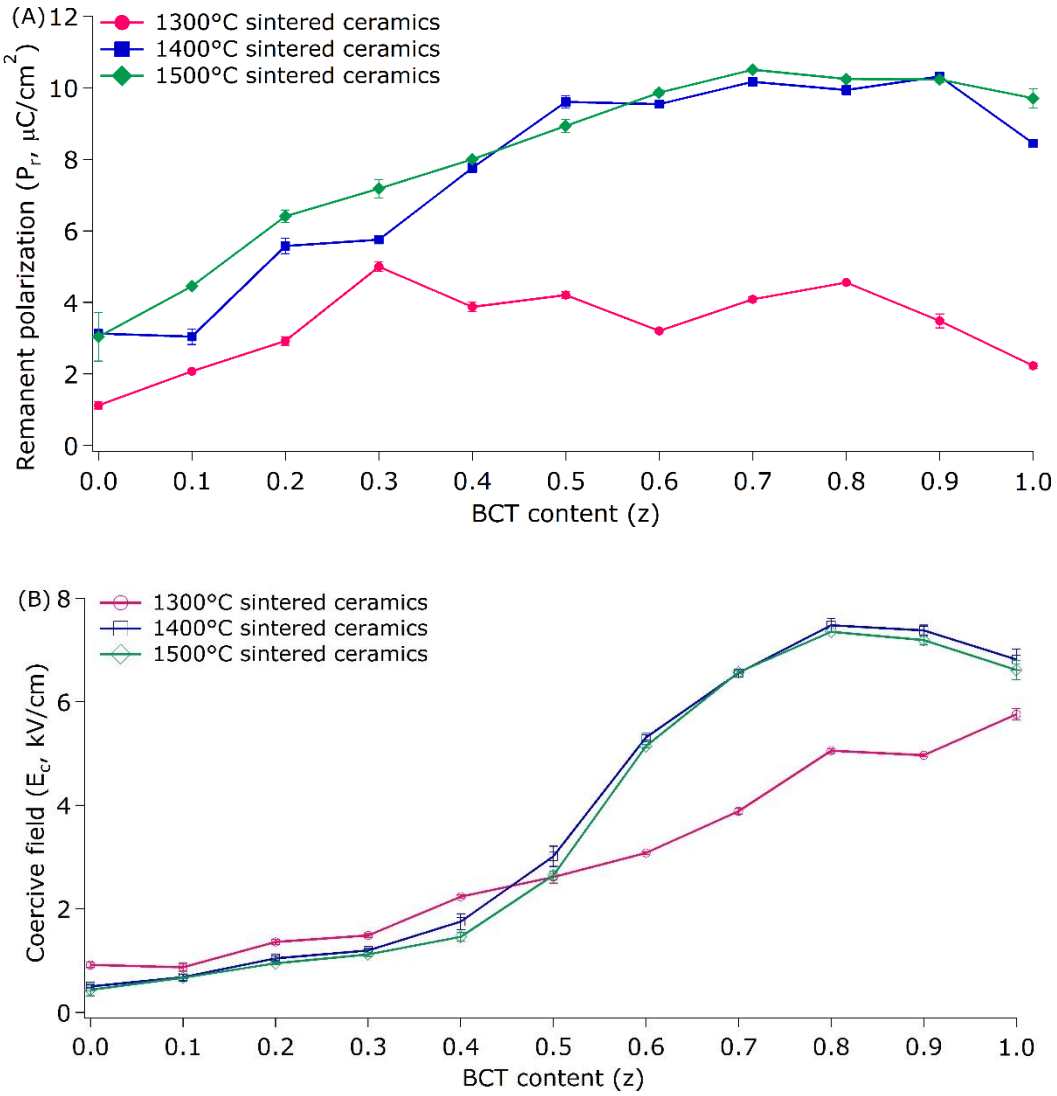

Figure 7.13. Ferroelectric properties of sintered zBCT-(1-z)BZT ceramics at room temperature: (A) remanent polarization (P_r); (B) coercive field (E_c).

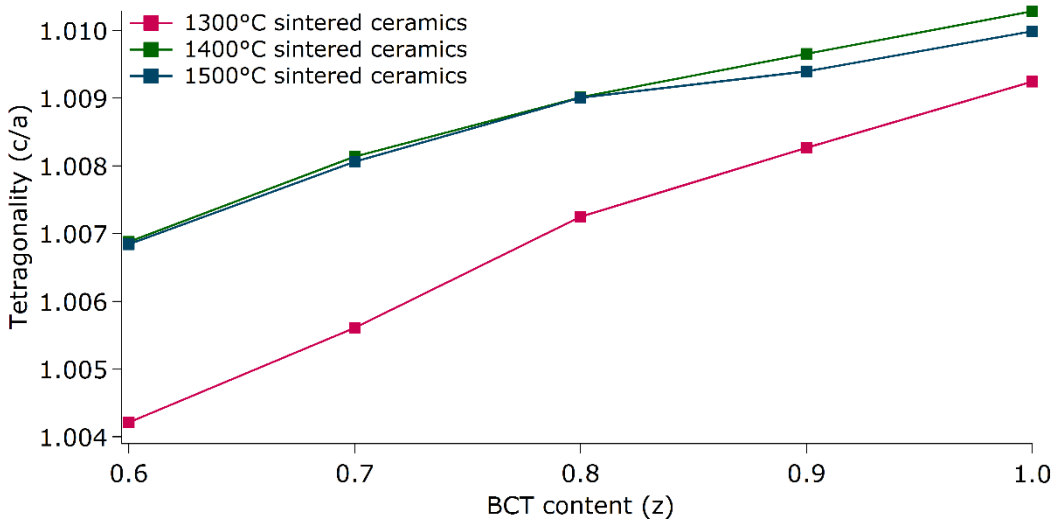

Figure 7.14. Tetragonality of the tetragonal phase in BCT-rich zBCT-(1-z)BZT (z=0.6-1) ceramics (determined by XRD).

Figure 7.15 reveals the piezoelectric properties of zBCT-(1-z)BZT ceramics, where it can be seen that the ceramics sintered at 1300 ºC exhibit the poorest piezoelectric properties (d_{33}≤100 pC/N, k_p≤0.2). This weak piezoelectric performance could be a result of the small grain size (*i.e.* less domain wall motion) and heterogeneity (*i.e.* less ferroelectric phase) [3]. On the other hand, ceramics sintered at 1400 ºC and 1500 ºC possess larger grains (10-40 μm), and exhibit better piezoelectric performance. These results are in good agreement with previous studies that 10 μm is a critical grain size value to maintain sufficient domain wall motion and polarization reversal and therefore enhance piezoelectric properties in zBCT-(1-z)BZT ceramics [210, 214].

As the grain size was considered to have a major effect on piezoelectric properties in dense zBCT-(1-z)BZT ceramics in previous studies [3, 210], and the fact that the piezoelectric performance of 1400 ºC and 1500 ºC sintered ceramics are similar in this project, the compositional induced effect on piezoelectric properties is discussed in

relation to ceramics sintered at 1400 ºC . In BZT-rich ceramics, the enhancement of piezoelectric properties with BCT addition is caused by enhanced ferroelectricity at room temperature due to increased Curie temperature. In BCT-rich ceramics, the promoted piezoelectric properties by BZT addition are originated from increased 90º domain wall motion in less tetragonal distorted compositions [203]. The consequent maximum in z=0.5 (d_{33}=281 pC/N, k_p=0.43) is associated with the increased potential polarization directions in the vicinity of the *O*-*T* phase transition boundary [206]. The higher values of piezoelectric properties reported elsewhere for z=0.5 ceramics (d_{33}=617 pC/N, k_p=0.54 [214]) compared to this project could be attributed to different fabrication procedures, slightly higher relative densities and optimisation of grain size [214].

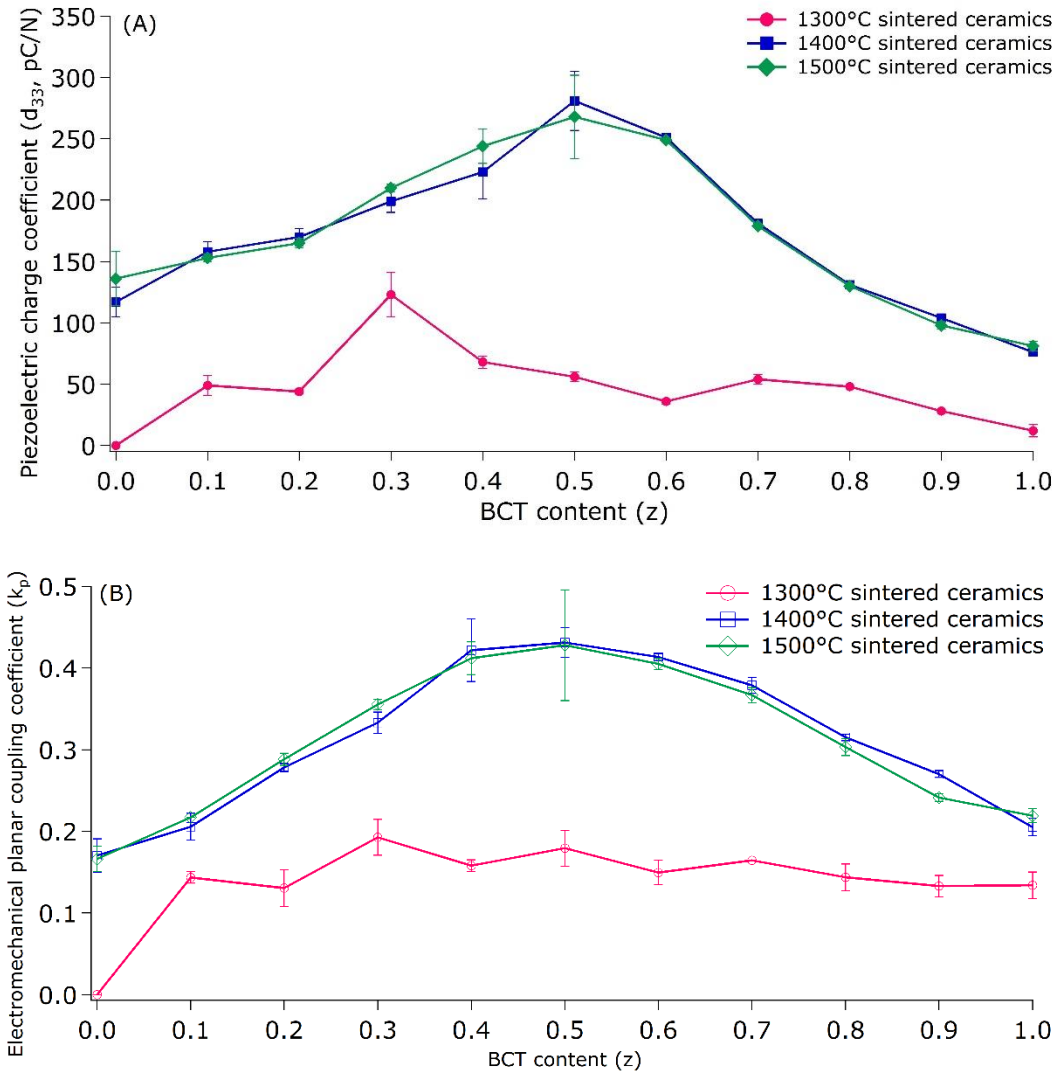

Figure 7.15. Piezoelectric properties of sintered zBCT-(1-z)BZT ceramics: (A) piezoelectric charge coefficient (d_{33}); (B) electromechanical planar coupling coefficient (k_p).

Therefore, the functional properties of sintered zBCT-(1-z)BZT ceramics are mainly controlled by grain size and compositional variations. It is difficult to fully separate these two effects based on the current study, however, it would be worthy to develop future work on investigating single variance (grain size or composition) in a wide compositional range for this system.

7.2 Temperature dependent characterisation of zBCT-(1-z)BZT ceramics

As mentioned in section 3.3, the temperature dependent characterisations of zBCT-(1-z)BZT ceramics were only investigated on ceramics sintered at 1500 ºC due to their desirable homogeneity for phase transition study. Therefore, all ceramics mentioned in this section refer to samples sintered at 1500 ºC. In this section, both temperature dependent structural variations and functional properties are investigated to identify the phase diagram of zBCT-(1-z)BZT system via different techniques.

7.2.1 Temperature dependent Raman spectroscopy of zBCT-(1-z)BZT ceramics

As stated in section 7.1.2, although the Raman modes of zBCT-(1-z)BZT ceramics are broad with many overlaps, the detection of compositional induced phase transitions (both at 87 K and room temperature) could be achieved via Raman spectroscopy by investigating variations in Raman modes in the region 80-300 cm^{-1}. This inspired the investigation of temperature induced phase transitions in the zBCT-(1-z)BZT system via Raman spectroscopy in this project. In this section, z=0.5 ceramics were taken as representative for temperature dependent Raman spectroscopy studies, as this composition going through the full range of phase transitions from rhombohedral to orthorhombic to tetragonal and cubic phases upon heating.

Figure 7.16 shows the Raman spectra of z=0.5 ceramics at temperatures of (A) 189 K, (B)

295 K, (C) 324 K and (D) 382 K. With reference to Figure 7.6, the coexistence of Raman modes at ~120 cm^{-1}, ~150 cm^{-1} [A_1(TO)] and ~200 cm^{-1} [E(TO+LO), A_1(LO)] in Figure 7.16 (A) confirms the rhombohedral symmetry of z=0.5 ceramics at 189 K. Upon heating, as shown in Figure 7.16 (B), all these three rhombohedral characteristic modes are weakened at 295 K, especially the disappearance of the mode at ~120 cm^{-1} which, together with the appearance of a broad peak at ~210 cm^{-1}, is indicative of orthorhombic symmetry. In addition, the ~150 cm^{-1} mode is weaker after transferring from rhombohedral to orthorhombic symmetry. With further heating to 324 K, the ~150 cm^{-1} mode nearly vanishes, implying the existence of tetragonal symmetry (Figure 7.16 (C)). At 382 K, the ceramics are believed to have cubic symmetry with broad peaks around 220 cm^{-1}, 530 cm^{-1} and 720 cm^{-1}, which is similar to the Raman spectra for cubic $BaTiO_3$ (Figure 5.2 and Figure 6.6).

In spite of variations in ~120 cm^{-1} and ~150 cm^{-1} modes, the weak shoulder at ~300 cm^{-1} is also dependent on phase transitions, and becomes broader and weaker in the higher symmetry phases and finally disappears in the cubic phase. As mentioned in sections 5.1.4 and 6.3.2, the ~300 cm^{-1} mode is a sharp peak in the $Ba_{1-x*}Ca_{x*}TiO_3$ (x*=0-0.30) system and low Zr^{4+}-containing $BaZr_yTi_{1-y}O_3$ (y=0-0.10) compositions, where temperature dependent peak position and peak width could indicate subtle structural changes in the ferroelectric phase transitions. However, in the zBCT-(1-z)BZT system, the 300 cm^{-1} mode is only present as a weak shoulder in the z=0.4-0.7 ceramics. Also, there are a few overlapped modes in the adjacent broad ~250 cm^{-1} peak, which makes it more difficult to

achieve reliable curve fitting for the weak ~300 cm^{-1} shoulder. Hence, the identification of phase transitions could not be achieved by curve fitting the ~300 cm^{-1} mode in this system.

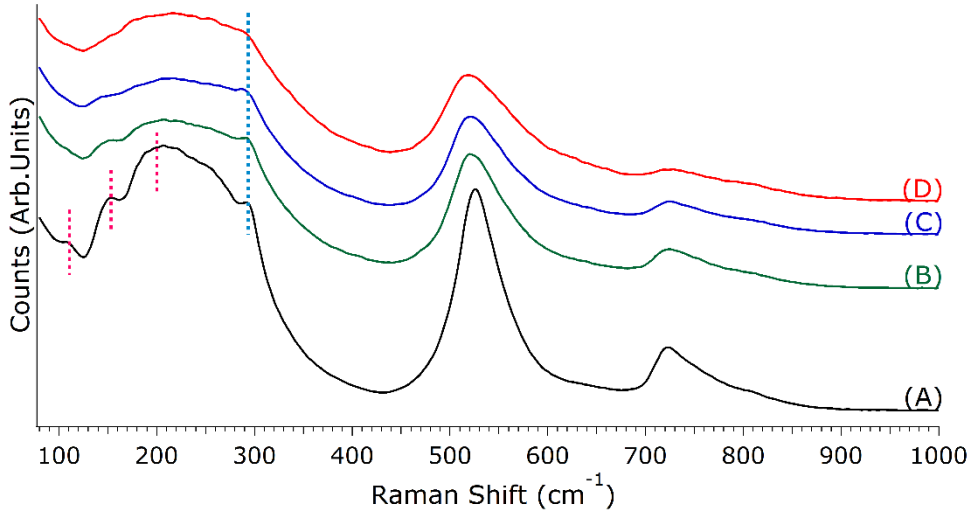

Figure 7.16. Raman spectra of zBCT-(1-z)BZT (z=0.5) ceramics sintered at 1500 ºC and measured at (A) 189 K; (B) 295 K; (C) 324 K; (D) 382 K: pink dotted lines indicate the rhombohedral characteristic modes at 189 K and blue dotted line indicate the ~300 cm^{-1} mode.

Therefore, the weakening of the ~120 cm^{-1} and ~150 cm^{-1} modes with approach to higher symmetry has been investigated to determine the phase transitions in the zBCT-(1-z)BZT system. Reliable curve fitting for the weak ~120 cm^{-1} mode has not been achieved in this project, however, the disappearance of this rhombohedral mode is considered as an indication of a phase transition to orthorhombic symmetry. In z=0.5 ceramics, the ~120 cm^{-1} mode vanishes between 257-267 K (*i.e. R-O* transition temperature). The weakening of the ~150 cm^{-1} mode in z=0.5 ceramics as a function of temperature is shown in Figure 7.17. Upon heating from 180 K to 250 K, the intensity of the ~150 cm^{-1} mode decreases gradually, followed by a sudden degradation between 257 K-267 K, which

could also imply an *R-O* transition and be in good agreement with the ~120 cm^{-1} mode identification. The intensity of the ~150 cm^{-1} mode decreases further when heating to 295-305 K, after which it is too weak to obtain curve fitting. This drop in intensity is considered as indicative of the transition to the tetragonal phase (*O-T*). Therefore, the ~120 cm^{-1} mode could identify the *R-O* transition and the ~150 cm^{-1} mode could determine comprehensive ferroelectric phase transitions (*R-O* and *O-T*) in the zBCT-(1-z)BZT system.

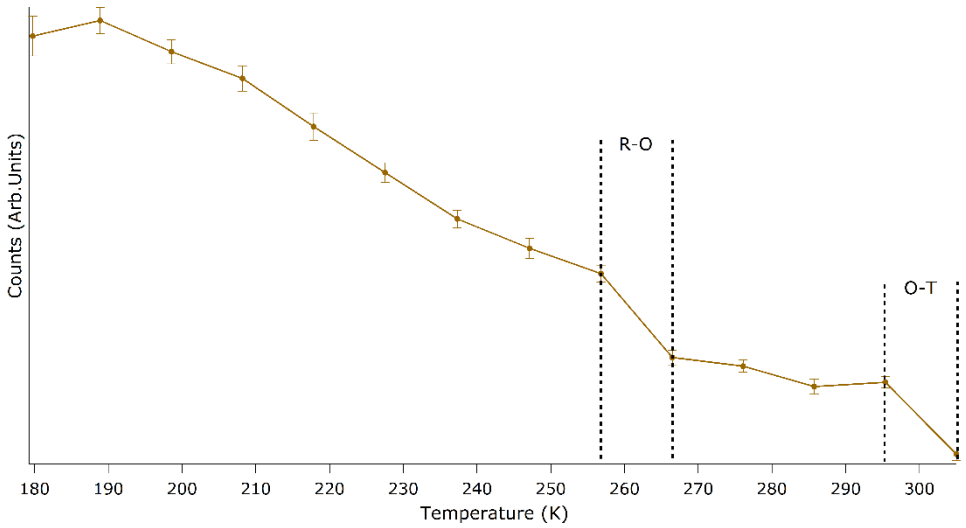

Figure 7.17. Intensity of the ~150 cm^{-1} Raman mode in *z*=0.5 ceramics measured as a function of temperature.

Similar to the $BaZr_yTi_{1-y}O_3$ (*y*=0-0.30) system (Figure 6.7 (C)), the ferroelectric to paraelectric phase transition (T_{R-C} or T_{T-C}) in the zBCT-(1-z)BZT system can be determined by the broadening and shift of the 720 cm^{-1} mode. The resulting calibrated phase transition temperatures identified by the ~120 cm^{-1}, ~150 cm^{-1} and 720 cm^{-1} modes are listed in Table 7.1. And the corresponding phase diagram is shown in Figure 7.18, where the estimated *R-O* and *O-T* phase boundaries at low temperature and the triple

critical point are represented as dotted lines. It can be seen, therefore, that Raman spectroscopy reveals an orthorhombic phase region in the zBCT-(1-z)BZT system, separating the rhombohedral and tetragonal phases.

Table 7.1. Onset temperatures for the phase transition of zBCT-(1-z)BZT (z=0-1) ceramics determined by analysis of Raman spectra.

Sample Name	$T_{R\text{-}O}$ **(K)**	$T_{O\text{-}T}$ **(K)**	$T_{R\text{-}C}/T_{T\text{-}C}$ **(K)**
z=0			299
z=0.1			305
z=0.2			313
z=0.3			336
z=0.4	293±2.5	321±3.5	346±2.3
z=0.5	261±5.0	290±2.8	353
z=0.6	225±4.8	257±4.8	359
z=0.7	121±1.0	185±4.8	368
z=0.8			367
z=0.9			367±1.4
z=1			375

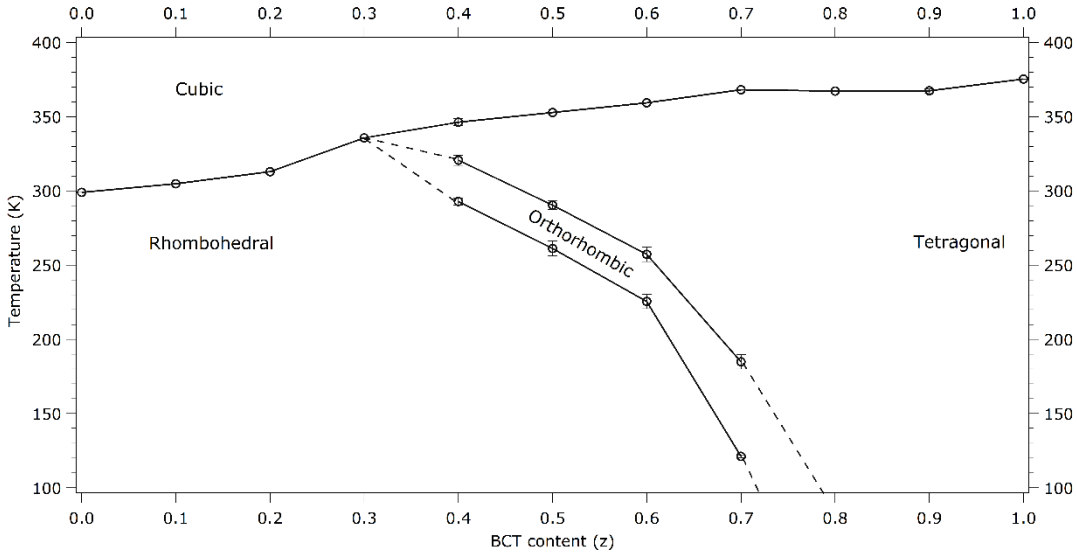

Figure 7.18. Phase diagram of zBCT-(1-z)BZT (*z*=0-1) system derived from Raman spectroscopy measurements.

Combining this phase diagram with the two end member binary systems, $Ba_{1-x*}Ca_{x*}TiO_3$ (section 5.1.4, Figure 5.7) and $BaZr_yTi_{1-y}O_3$ (section 6.3.2, Figure 6.10), a three-dimensional phase diagram of ternary $Ba_{1-x*}Ca_{x*}TiO_3$-$BaZr_yTi_{1-y}O_3$-[zBCT-(1-z)BZT] system could therefore be determined by Raman spectroscopy and is shown as Figure 7.19. Instead of traversing directly from $BaZr_yTi_{1-y}O_3$ (y=0.20) (*i.e.* z=0) to $Ba_{1-x*}Ca_{x*}TiO_3$ (x*=0.30) (*i.e.* z=1) in zBCT-(1-z)BZT system, the three-dimensional phase diagram offers a view to compare the zBCT-(1-z)BZT system with the parent $BaTiO_3$ (BTO) phase. Where the Zr^{4+}-induced pinching phase transition effect and Ca^{2+}-induced stabilization of the tetragonal phase occur simultaneously in the zBCT-(1-z)BZT system, resulting in the presence of a vertical orthorhombic region [204].

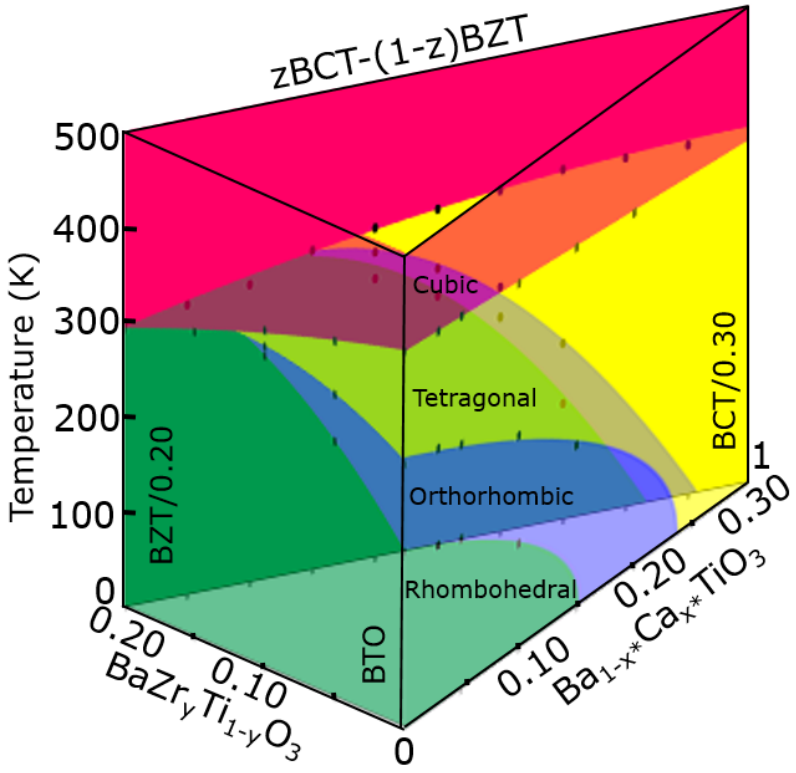

Figure 7.19. Three-dimensional phase diagram of $Ba_{1-x}*Ca_x*TiO_3$-$BaZr_yTi_{1-y}O_3$-zBCT-(1-z)BZT system determined by Raman spectroscopy.

7.2.2 Temperature dependent functional properties of zBCT-(1-z)BZT ceramics

The relative permittivity of zBCT-(1-z)BZT ceramics at 1 kHz (ε_r-*T*) as a function of temperature (173 K-423 K) is shown in Figure 7.20, where the relative permittivity at 298 K as a function of BCT content (*z* values) follows the same trend as shown in Figure 7.12 (A). There is only one ε_r-*T* peak for *z*=0-0.3 and *z*=0.8-1 ceramics, which refers to the rhombohedral-cubic (*R*-*C*) and tetragonal-cubic (*T*-*C*) phase transitions respectively. As for z=0.4-0.6 ceramics, there are three ε_r-*T* peaks, representing the phase transitions from rhombohedral to orthorhombic (*R*-*O*), orthorhombic to tetragonal (*O*-*T*) and tetragonal to cubic (*T*-*C*) phase respectively. As the *R*-*O* peaks are weaker than the *O*-*T*

and *T*-*C* peaks, the identification of the *R*-*O* transition temperature has been obtained from the gradient changes in the $1/\varepsilon_r$-*T* curve. As the *O*-*T* transition in *z*=0.7 (Figure 7.20 (C)) is in the vicinity of the lowest measured temperature (173 K), therefore this transition temperature is also determined from the $1/\varepsilon_r$-*T* curve. The calibrated phase transition temperatures derived from temperature dependent relative permittivity measurements are listed in Table 7.2.

In Figure 7.20, the highest ε_{rmax} value is observed for the *z*=0 composition rather than for *z*=0.3 as reported near the tricritical composition [28]. This variation is possibly related to the effect of grain size on the dielectric properties. The $BaZr_yTi_{1-y}O_3$ (*y*=0.20) ceramics reported in Chapter 6 were fabricated via the same procedure and designed to be the same composition as the *z*=0 ceramics described in this chapter. However, grain size values were measured to be 22.9±4.1 μm and 38.6±6.7 μm, respectively, indicating quite a large variability and being the cause of the large error bars shown for the average grain size values in Figure 7.9. The corresponding ε_{rmax} values are ~23000 and ~26000 as shown in Figure 6.15 for *y*=0.20 ceramics and Figure 7.20 for the *z*=0 ceramics respectively. This is further evidence of the grain size effect on ε_{rmax} values. It should also be noted that the grain sizes corresponding to the dielectric properties reported in reference [1] are not given. In general, the ε_{rmax} value is similar in BZT-end ceramics (*z*=0-0.3) and higher than BCT-end ceramics (*z*=0.8-1), further proving that BCT ceramics have lower permittivity values.

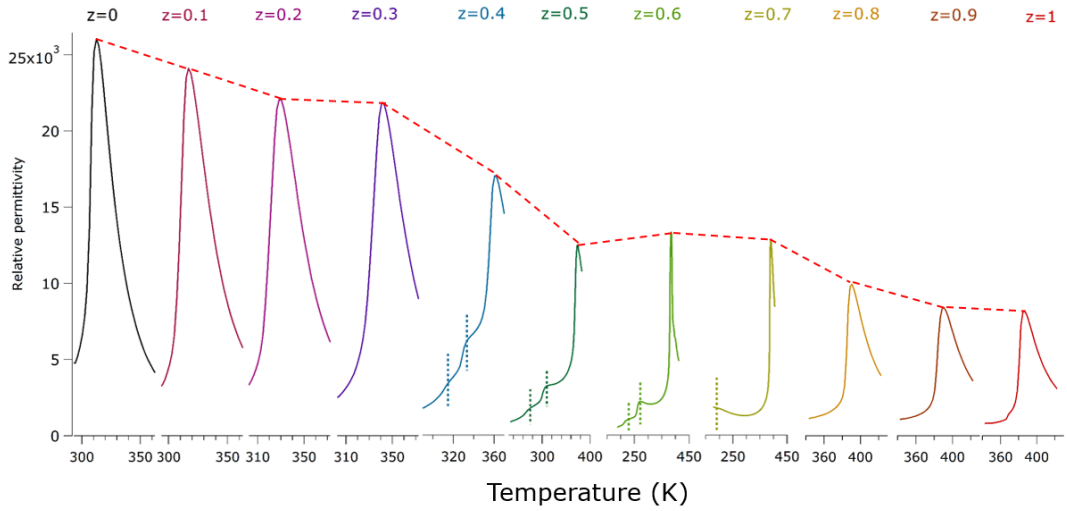

Figure 7.20. Selected temperature dependent relative permittivity measurements at 1 kHz of zBCT-(1-z)BZT (z=0-1) ceramics sintered at 1500 °C: the vertical dotted lines indicate ferroelectric phase transitions in zBCT-(1-z)BZT (z=0.4-0.7) and the red dotted line shows the change of ε_{rmax} value to z content.

Table 7.2. Phase transition temperatures of zBCT-(1-z)BZT (z=0-1) ceramics sintered at 1500 °C identified by temperature dependent relative permittivity.[6]

Sample Name	$T_{R\text{-}O}$ (K)	$T_{O\text{-}T}$ (K)	$T_{R\text{-}C}/T_{T\text{-}C}$ (K)
z=0			297
z=0.1			301
z=0.2			312
z=0.3			326
z=0.4	301	316	343
z=0.5	262	291	357
z=0.6	212	252	367
z=0.7		176	373
z=0.8			373
z=0.9			373
z=1			369

[6] In this table, the phase transition temperature of each composition was determined from single set measurements, therefore no error bar is displayed (as described in section 3.3).

According to the results presented in Chapter 5 and Chapter 6 (section 5.2.3 and 6.4.2), determinations of phase transitions in $Ba_{1-x*}Ca_{x*}TiO_3$ (x*=0.2 and 0.30) and $BaZr_yTi_{1-y}O_3$ (y=0-0.30) ceramics can also be achieved by measuring the temperature dependent remanent polarization (P_r-T), where the ferroelectric to paraelectric phase transition is determined as a minimum P_r value or the slowing down in the rate of decrease of P_r. Regarding the $BaZr_yTi_{1-y}O_3$ (y=0.10) ceramics, whose comprehensive phase transitions occur within a short temperature range (40 K), the gradient changes in the P_r-T curve are considered as phase transition points. In the zBCT-(1-z)BZT system, this measurement is also applied to identify phase transitions. The remanent polarization of z=0.5 ceramics as a function of temperature is shown in Figure 7.21, as a representative figure to demonstrate the phase transition determination. The phase transitions are shown as green dotted lines based on gradient changes. The higher P_r value in the orthorhombic phase is attributed to its more potential polarization orientations (twelve) than rhombohedral (eight) and tetragonal (six) phases. Therefore, the P_r-T curve could also imply phase transitions in zBCT-(1-z)BZT system.

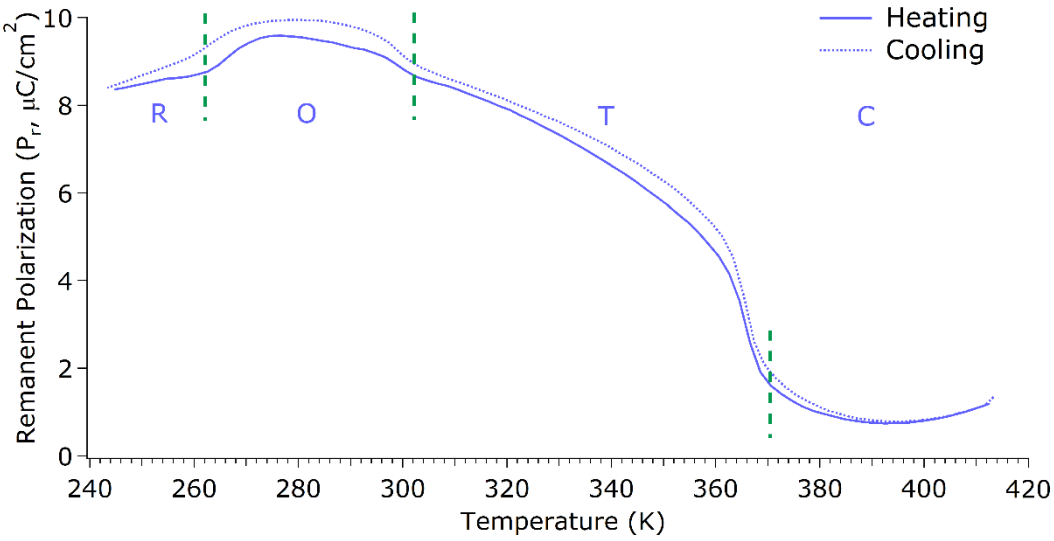

Figure 7.21. Temperature dependent remanent polarization of z=0.5 ceramics sintered at 1500 °C: green dotted line indicates the phase transitions.

The corresponding *P-E* loops of z=0.5 ceramics from 253 K to 373 K (20 K as step) are shown in Figure 7.22. With increasing temperature, the *P-E* loop becomes slimmer and the corresponding remanent polarization decreases, with small variations at 273 K and 293 K (as orthorhombic phase). At 373 K, the ceramics possess cubic symmetry, indicating a slim but not closed *P-E* loop. This implies that ceramics only show an averaged paraelectric symmetry with the presence of local polar clusters, which is further evidenced by the existence of broad 220 cm^{-1}, 530 cm^{-1} and 720 cm^{-1} Raman modes in the cubic phase (Figure 7.16). Therefore, the corresponding P_r value in the cubic phase does not drop to zero (Figure 7.21).

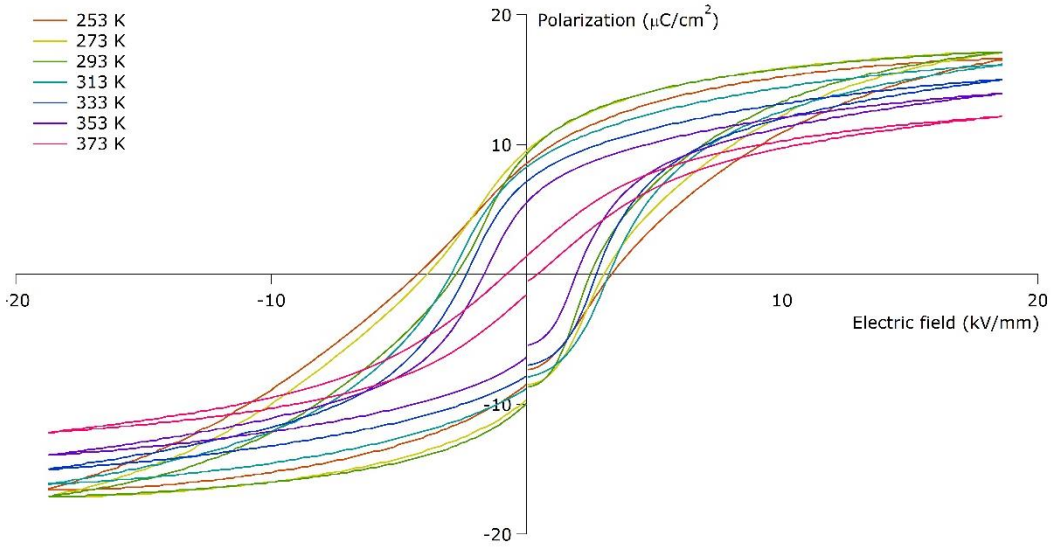

Figure 7.22. *P-E* loops of *z*=0.5 ceramics sintered at 1500 °C measured at various temperatures.

7.3 Summary

In this chapter, an investigation of the zBCT-(1-z)BZT (*z*=0-1) system is reported, based on previous studies on the $Ba_{1-x*}Ca_{x*}TiO_3$ (*x**=0-0.30) and $BaZr_yTi_{1-y}O_3$ (*y*=0-0.30) systems presented in Chapter 5 and Chapter 6. The BCT-rich (*z*=0.6-1) ceramics sintered at 1300 °C and 1400 °C are heterogeneous with the presence of a secondary pseudo-cubic phase. The room temperature XRD measurements for zBCT-(1-z)BZT ceramics sintered at higher temperature (1500 °C) indicate a single rhombohedral structure for *z*=0-0.4 ceramics and single tetragonal structure for *z*=0.6-1 ceramics, whereas the crystal structure of *z*=0.5 ceramics could not be identified by the lab-based XRD. However, a linear relationship between unit cell volume and BCT content (*V*=66.272-3.9458*z*) has been established as a linear Vegard's relationship for homogeneous zBCT-(1-z)BZT ceramics, indicating that the zBCT-(1-z)BZT system can be treated as a pseudo-binary system.

The Raman spectroscopy measurements at 87 K indicate the rhombohedral structure for z=0-0.7 ceramics and the tetragonal structure for z=0.8-1 ceramics, and the measurements at room temperature clarify the existence of an orthorhombic structure for z=0.5 ceramics. The variations in Raman modes ~120 cm^{-1}, ~150 cm^{-1} and 720 cm^{-1} upon heating have been used to identify phase transitions in zBCT-(1-z)BZT ceramics.

The temperature dependent relative permittivity and *P-E* loops have been measured and used to determine the phase transition points in zBCT-(1-z)BZT ceramics. A combined phase diagram of the zBCT-(1-z)BZT system derived from Raman spectroscopy (black), relative permittivity (pink) and remanent polarization (green) is summarised in Figure 7.23, where a good agreement among different measurements is achieved. It can be seen that the existence of an orthorhombic phase separating the rhombohedral and tetragonal phases is confirmed. The maximum piezoelectric properties at room temperature (d_{33}=281 pC/N, k_p=0.43) are therefore observed in z=0.5 ceramics due to the composition in the vicinity of *O-T* phase boundary at this temperature.

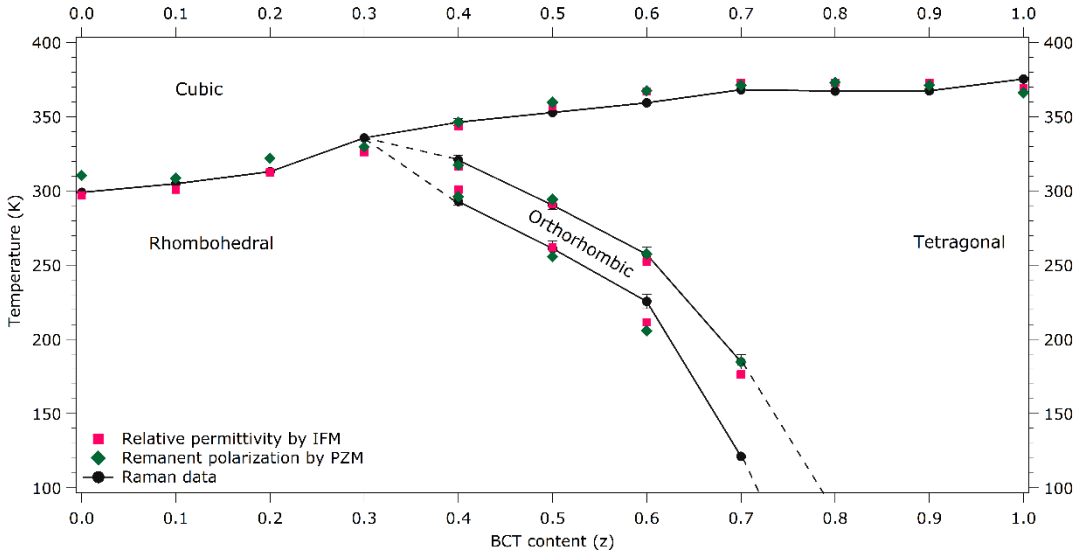

Figure 7.23. Phase diagram of zBCT-(1-z)BZT system combined measured data from Raman spectroscopy (black), relative permittivity (pink) and remanent polarization (green).

The microstructure of zBCT-(1-z)BZT ceramics are related to sintering temperatures and compositions: the ceramics sintered at 1300 °C have small grains (1-2 μm) and a generally porous microstructure; the ceramics sintered at 1400 °C and 1500 °C have larger grains (8-40 μm), and the grain size is more sensitive to sintering temperature in BZT-rich ceramics (z=0-0.4) than BCT-rich ceramics (z=0.6-1). In this project, the functional properties of zBCT-(1-z)BZT are found to be sensitive to variations in grain size and composition. Future work is needed to separate those variations and investigate the grain size or the composition induced effect on the functional properties of the zBCT-(1-z)BZT system.

Chapter 8 Conclusions and future work

The focus of the work reported in this thesis has been a systematic study of the promising lead-free zBCT-(1-z)BZT (z=0-1) system fabricated from mixtures of the end member $Ba_{0.70}Ca_{0.30}TiO_3$ and $BaZr_{0.20}Ti_{0.80}O_3$ compositions. This has involved firstly a study of the $Ba_{0.70}Ca_{0.30}TiO_3$ and $BaZr_{0.20}Ti_{0.80}O_3$ end members and the influence of the individual dopant ions (Ca^{2+} or Zr^{4+}) on the parent $BaTiO_3$ composition. This understanding has enabled a more detailed interpretation of the co-doped zBCT-(1-z)BZT system to be made and help link an understanding of the functional properties with their corresponding structural properties. It now remains to summarise the main outcomes of this investigation in the context of the aims and objectives set out in section 2.6 and propose areas of potential future work.

8.1 Conclusions

Optimisation studies of the fabrication of $Ba_{0.70}Ca_{0.30}TiO_3$ ceramics have been carried out by mixing stoichiometric amounts of $BaCO_3$, $CaCO_3$ and TiO_2 powders, followed by calcination at 1250 ºC (2 hours) and sintering at 1300 ºC, 1400 ºC and 1500 ºC (4 hours). The calcined powders and ceramics sintered at 1300 ºC and 1400 ºC exhibit two distinct phases: a majority of a Ba-rich tetragonal phase (86-95 wt. %) and a minority of a Ca-rich pseudo-cubic phase (5-14 wt. %). Increasing sintering temperature to 1500 ºC promotes homogeneity between those two phases and yields a single tetragonal phase $Ba_{0.70}Ca_{0.30}TiO_3$ ceramic.

Similarly, $BaZr_{0.20}Ti_{0.80}O_3$ ceramics have been formed by calcining stoichiometric mixtures of $BaCO_3$, ZrO_2 and TiO_2 powders at 1250 ºC (2 hours) and then sintering at 1300 ºC, 1400 ºC and 1500 ºC (4 hours). The calcined powders consist of tetragonal $BaTiO_3$, Zr-rich cubic $Ba(Zr,Ti)O_3$ and Ti-rich cubic $Ba(Zr,Ti)O_3$ phases, which homogenise into a single $BaZr_{0.20}Ti_{0.80}O_3$ phase during sintering. This indicates that the substitution of Zr^{4+} into the Ti-site is easier than Ca^{2+} into the Ba-site in $BaTiO_3$. The greatest compositional homogeneity of Zr^{4+} into $BaTiO_3$ is achieved in the ceramics sintered at 1500 ºC, which is evidenced by its sharpest XRD diffraction peaks.

Thus, increasing sintering temperature is able to promote diffusion for both Ca^{2+} and Zr^{4+} into $BaTiO_3$, and calcination at 1250 ºC followed by sintering at 1500 ºC yields the formation of homogeneous and monophasic $Ba_{0.70}Ca_{0.30}TiO_3$ and $BaZr_{0.20}Ti_{0.80}O_3$ ceramics.

In this project, the investigation of the reaction mechanism of $BaCO_3$, $CaCO_3$ and TiO_2 mixtures was firstly carried out and published. It suggests that $CaCO_3$ and $BaCO_3$ decompose first, followed by the formation of Ba_2TiO_4 and an unknown phase (XRD diffraction peaks at 2θ=26.7º) as intermediate phases and the final formation of $(Ba,Ca)TiO_3$. Comparing the reaction between $BaCO_3$ and TiO_2 with $CaCO_3$ and TiO_2, the formed $CaTiO_3$ actually inhibits the mobility of Ca^{2+} into $BaTiO_3$ (*i.e.* the formation of $(Ba,Ca)TiO_3$ phase). This further confirms that fabrication procedures should use $CaCO_3$ rather than $CaTiO_3$ as a reagent to form monophasic $Ba_{0.70}Ca_{0.30}TiO_3$ ceramics. In addition, the diffusion mechanism of Ca^{2+} into $BaTiO_3$ was firstly investigated by creating

a $BaTiO_3$-$CaTiO_3$ diffusion couple and using Raman imaging. To form a (Ba,Ca)TiO_3 phase from $BaTiO_3$ and $CaTiO_3$, the Ca^{2+} firstly diffuses along the $BaTiO_3$ grain boundaries, leaving a core of $BaTiO_3$ surrounded by a (Ba,Ca)TiO_3 shell, followed by a slower and gradual diffusion of Ca^{2+} into the core.

Quantitative XRD analysis of the Ba-rich tetragonal phase ($Ba_{1-x*}Ca_{x*}TiO_3$) has enabled the identification of the Ca^{2+} content ($x*$, $\leq \pm$ 0.007), based on a published relationship for the $Ba_{1-x}Ca_xTiO_3$ system. XRD and Raman spectroscopy measurements indicate that when Ca^{2+} ($x*$=0-0.30) substitutes into the Ba-site in $BaTiO_3$, the corresponding $Ba_{1-x*}Ca_{x*}TiO_3$ phase has a tetragonal symmetry at room temperature and its unit cell dimension contracts with the Ca^{2+} addition. Also, the Ca^{2+} addition induces disorder in the Ti^{4+} positions in $BaTiO_3$, giving rise to shifts and broadenings in the Raman modes.

A lower relative permittivity is observed in $Ba_{1-x*}Ca_{x*}TiO_3$ ($x*$=0.30) than $x*$=0.20 ceramics due to higher Ca^{2+} content. However, $Ba_{1-x*}Ca_{x*}TiO_3$ ($x*$=0.30) exhibits a more saturated *P-E* loop and better piezoelectric properties, resulting from increased concentrations of the tetragonal phase. A diffuse phase transition (DPT) behaviour is observed in $Ba_{1-x*}Ca_{x*}TiO_3$ ($x*$=0.20) bulk ceramics due to its poor homogeneity. Raman spectroscopy of $Ba_{1-x*}Ca_{x*}TiO_3$ ($x*$=0.30) ceramics indicates lower vibration energy for the Ti-O bond, implying an easier polarization reversal procedure (*i.e.* lower coercive field). This contradicts with a measured higher coercive field in the *P-E* loop. This discrepancy is thought to arise because Raman spectroscopy focuses on measuring the tetragonal phase whereas the *P-E* loop is obtained by measuring both ferroelectric

tetragonal phase and paraelectric pseudo-cubic phase present in the bulk ceramics.

Thus, this project suggests the difficult formation of end member $Ba_{0.70}Ca_{0.30}TiO_3$ phase via solid-state method with the observation of single phase only after 1250 °C calcination and 1500 °C sintering. The corresponding reaction mechanism and diffusion mechanism between the reagents ($BaCO_3$, $CaCO_3$ and TiO_2) were firstly investigated and published. The observed tetragonal $Ba_{1-x}Ca_xTiO_3$ (x*=0-0.30) phases were used for the construction of phase diagram. The future work on fabrication pure $Ba_{1-x}Ca_xTiO_3$ (x=0-0.30) ceramics is suggested to understand more about Ca^{2+} doping effect on functional properties, and its linkage to structural properties could refer back to this study.

A series of $BaZr_yTi_{1-y}O_3$ (y=0-0.30) ceramics with single phase has shown that Zr^{4+} addition into $BaTiO_3$ induces a phase transition from tetragonal (y=0) to orthorhombic (y=0.05) to rhombohedral (y=0.10-0.20) and cubic (y=0.25-0.30) phases. The corresponding unit cell volumes of each phase have been expanded by Zr^{4+} substitution, and fulfils a linear relationship (V=9.3721y+64.402) independent of crystal symmetry. This well-correlated relationship is firstly promoted in this project and enables the quantitative determination of the Zr^{4+} concentrations in $BaTiO_3$. An overall decrease in relative density and grain size with increasing Zr^{4+} content is observed in $BaZr_yTi_{1-y}O_3$ (y=0-0.30) ceramics, with a small variation at y=0.25. Among all $BaZr_yTi_{1-y}O_3$ (y=0-0.30) ceramics, $BaZr_yTi_{1-y}O_3$ (y=0.25) exhibits the highest relative permittivity (ε_r=10816) and $BaZr_yTi_{1-y}O_3$ (y=0.05) has best ferroelectric (P_r=13.22±0.46 μC/cm^2) and piezoelectric properties (d_{33}=286±9 pC/N and k_p=0.53±<0.01). These optimised functional properties

are in agreement with literature, and are a result of room temperature lying close to the *R*-*C* transition for *y*=0.25 and the existence of more potential polarization rotations in orthorhombic structure and larger-grained *y*=0.05 ceramics.

After fabricating end member $Ba_{0.70}Ca_{0.30}TiO_3$ (*z*=1) and $BaZr_{0.20}Ti_{0.80}O_3$ (*z*=0) ceramics, a novel fabrication procedure has been taken to fabricate the zBCT-(1-z)BZT (*z*=0.1-0.9) ceramics by stoichiometric mixing of 1250 ºC calcined $Ba_{0.70}Ca_{0.30}TiO_3$ and $BaZr_{0.20}Ti_{0.80}O_3$ ceramic powders followed by sintering at 1300 ºC, 1400 ºC and 1500 ºC for 4 hours. There are two distinct phases present in low temperature sintered BCT-rich ceramics (*z*=0.6-1), as predominant tetragonal phase and a minority of pseudo-cubic phase, which then homogenate and become single phase after 1500 ºC sintering. Therefore, similar to forming the end member $Ba_{0.70}Ca_{0.30}TiO_3$ (*z*=1) ceramics, increasing sintering temperature promotes diffusion and homogeneity between Ba^{2+} and Ca^{2+} in BCT-rich (*z*=0.6-1) ceramics. On the other hand, all 1300 ºC, 1400 ºC and 1500 ºC sintered zBCT-(1-z)BZT (*z*=0-0.5) ceramics exhibit a monophasic perovskite structure. The XRD measurement on 1500ºC sintered zBCT-(1-z)BZT (*z*=0-1) ceramics (*i.e.* those with greatest homogeneity) reveals rhombohedral symmetry for BZT-rich (*z*=0-0.4) and tetragonal symmetry for BCT-rich (*z*=0.6-1) ceramics, where the uncertain crystal symmetry of *z*=0.5 ceramics has been clarified as orthorhombic by Raman spectroscopy measurements. This is achieved by comparing its Raman spectrum with rhombohedral and tetragonal end member systems, and this identification from Raman spectra is firstly reported in this project owing to the systematic fabrication of all zBCT-(1-z)BZT

compositions. A linear relationship between unit cell volume and BCT content for 1500 ºC sintered zBCT-(1-z)BZT (z=0-1) ceramics has been determined by XRD measurements and is independent of crystal symmetry. This relationship is firstly published in this project and therefore confirms zBCT-(1-z)BZT (z=0-1) as a pseudo-binary solid solution system between BCT and BZT and enables quantitative determination of BCT content in the system.

All zBCT-(1-z)BZT (z=0-1) ceramics sintered at 1300 ºC have small grains (1-2 μm), contributing to relative better dielectric properties and poorer ferroelectric and piezoelectric properties than ceramics sintered at 1400 ºC and 1500 ºC. The microstructure and relative density of ceramics sintered at 1400 ºC and 1500 ºC indicate that a lower sintering temperature is required for producing denser BCT-rich (z=0.6-1) ceramics than that for BZT-rich ceramics (z=0-0.4).

The functional properties of zBCT-(1-z)BZT (z=0-1) ceramics sintered at 1500 ºC are sensitive to BCT content (z value). The addition of BCT (*i.e.* addition of Ca^{2+}) induces a general decrease in relative permittivity with a variation at z=0.5 (ε_r~3000). This anomaly agrees with literature and is believed to be caused by increased potential polarization orientations at the vicinity of *O-T* phase transition boundary. Consequently, the corresponding dielectric loss is highest among all compositions. Additionally, the best piezoelectric performance (d_{33}=281 pC/N, k_p=0.43) is observed in this composition (z=0.5), which is also associated with promoted polarization rotations. This enhancement in piezoelectric properties at z=0.5 coincides with the literature, however, in this project,

the piezoelectric coefficients are lower than in other reports. This is thought to be caused by different fabrication procedures and the variations in resulting grain size. The remanent polarization of BZT-rich (z=0-0.4) ceramics increases with increased BCT concentrations, which is similar to $BaZr_yTi_{1-y}O_3$ (y=0.08-0.20) where reducing Zr^{4+} content yields an increase in remanent polarization. In the BCT-rich (z=0.6-1) ceramics, although the higher z values exhibit larger tetragonality, implying a higher spontaneous polarization, the corresponding remanent polarization is independent of z value, which is thought to be restricted by the grain sizes (≤25 μm) of the BCT-rich (z=0.6-1) ceramics.

In this project, systematic and consecutive characterisations on zBCT-(1-z)BZT (z=0-1) ceramics at room temperature have been investigated, where it is difficult to separate the effect of compositional variations (z value) and microstructure on the corresponding functional properties.

Temperature dependent measurements of the tetragonal $Ba_{1-x*}Ca_{x*}TiO_3$ (x*=0-0.30) phase, monophasic $BaZr_yTi_{1-y}O_3$ (y=0-0.30) ceramics and monophasic zBCT-(1-z)BZT (z=0-1) ceramics have also been investigated for these three solid solution systems, in order to determine changes in phase transition behaviours with Ca^{2+} addition, Zr^{4+} addition and BCT addition (increasing Ca^{2+} and reducing Zr^{4+} simultaneously). In situ Raman spectroscopy, which is sensitive to molecular vibrations, has been applied systematically as a pioneering work, to identify phase transitions in these piezoelectric systems. A three-dimensional structural phase diagram of the ternary $Ba_{1-x*}Ca_{x*}TiO_3$-$BaZr_yTi_{1-y}O_3$-[zBCT-(1-z)BZT] (x*=0-0.30, y=0-0.20, z=0-1) system has been firstly

derived. In $Ba_{1-x*}Ca_{x*}TiO_3$ ($x*$=0-0.30), Ca^{2+} addition reduces the phase transition temperatures for the rhombohedral to orthorhombic (*R*-*O*) and orthorhombic to tetragonal (*O*-*T*) phase changes, but the tetragonal to cubic transition (*T*-*C*) appears approximately independent of composition. This first structural phase diagram study in the $Ba_{1-x*}Ca_{x*}TiO_3$ ($x*$=0-0.30) system agrees well with phase diagram in literature based on dielectric properties. On the contrary, in $BaZr_yTi_{1-y}O_3$ (y=0-0.30), Zr^{4+} addition raises phase transition temperatures for *R*-*O* and *O*-*T* whereas *R*-*C* decreases. Therefore, those three phase transitions are pinched around y=0.15, achieving good agreements with literature. In zBCT-(1-z)BZT (z=0-1), the Ca^{2+}-induced stabilization of the tetragonal phase and Zr^{4+}-induced pinching of the phase transition effect occur simultaneously, resulting in the presence of a vertical orthorhombic phase region separating the rhombohedral and tetragonal phases. The existence of orthorhombic structure in the zBCT-(1-z)BZT (z=0-1) system answers the previous debate on crystal symmetry for the morphotropic phase boundary (MPB) region in the literature.

The temperature dependent dielectric and ferroelectric properties have been measured on all bulk ceramics: $Ba_{1-x*}Ca_{x*}TiO_3$ ($x*$=0.20 and 0.30), $BaZr_yTi_{1-y}O_3$ (y=0-0.30) and zBCT-(1-z)BZT (z=0-1), which are also able to reveal the corresponding phase transition points. The phase diagrams based on these functional properties coincide extremely well with the phase diagram derived from Raman spectroscopy measurements, giving increased confidence in the data presented.

8.2 Future work

Based on investigations in this project, some interesting future work could be proposed as discussed below:

It would be worthy to fabricate monophasic $Ba_{1-x}Ca_xTiO_3$ (x=0-0.30) ceramics, in order to further investigate how microstructure and functional properties of $Ba_{1-x}Ca_xTiO_3$ (x=0-0.30) changes against Ca^{2+} content. Also, the temperature dependent dielectric properties under various frequencies should also be investigated to further confirm the observed diffuse phase transition in $Ba_{1-x*}Ca_{x*}TiO_3$ (x*=0.20) ceramics. The fabrication procedure for these $Ba_{1-x}Ca_xTiO_3$ (x=0-0.30) ceramics needs to be optimised, considering the difficult homogenisation procedure between Ba^{2+} and Ca^{2+} and its melting point being dependent on the Ca^{2+} concentration.

Similar to the investigation of the diffusion mechanism between Ca^{2+} and Ba^{2+} reported in this thesis, a diffusion couple of $BaZrO_3$-$BaTiO_3$ and even $BaZrO_3$-$BaTiO_3$-$CaTiO_3$ could be created, in order to investigate the diffusion mechanism between Zr^{4+} and Ti^{4+}, or even simultaneous diffusion of Ca^{2+}-Ba^{2+}, Zr^{4+}-Ti^{4+} at phase boundaries. However, it would be a challenge to conquer the different sintering shrinkages of each phase during co-sintering.

As the functional properties of zBCT-(1-z)BZT ceramics are sensitive to processing procedure, the fabrication of the z=0.5 composition ($Ba_{0.85}Ca_{0.15}Zr_{0.10}Ti_{0.90}O_3$) in powder form could be investigated from stoichiometric mixing and heating of (1) $BaCO_3$, $CaCO_3$,

ZrO_2 and TiO_2; (2) $BaCO_3$, $CaCO_3$, preformed $BaZrO_3$ and TiO_2 and (3) 1250 ºC calcined $Ba_{0.70}Ca_{0.30}TiO_3$ and $BaZr_{0.20}Ti_{0.80}O_3$ powders, with the aim to understand how processing procedure affects reaction mechanism for this composition.

According to the observation of a broad relative permittivity peak in the temperature dependent dielectric properties measurements for $BaZr_yTi_{1-y}O_3$ (y=0.20-0.30) ceramics, the diffuse phase transition and ferroelectric relaxor behaviour of $BaZr_yTi_{1-y}O_3$ (y=0.20-0.30) ceramics could be further investigated by measuring temperature dependent dielectric properties at different frequencies. This could be potentially linked to the presence of Zr^{4+}-related Raman mode at ~800 cm^{-1}.

As it has been difficult to completely separate compositional and microstructural effects on the functional properties of $BaZr_yTi_{1-y}O_3$ (y=0-0.30) and zBCT-(1-z)BZT (z=0-1) ceramics in this project. Alternative fabrication methods (such as two-step sintering) could be carried. In this way, the effect of grain size of $BaZr_yTi_{1-y}O_3$ (y=0-0.30) and zBCT-(1-z)BZT (z=0-1) ceramics on functional properties could be studied to further elucidate the complex composition, grain size and functional property relationships.

Further compositions at the vicinity of the converged phase transition regions in $BaZr_yTi_{1-y}O_3$ (y~0.15) and zBCT-(1-z)BZT (z~0.3) ceramics should be fabricated and characterised to further confirm accurate compositions for those converged points and clarify the estimated dotted lines in the phase diagrams presented in this thesis.

Temperature dependent high-energy X-ray powder diffraction measurements could be

carried out to determine phase transitions in the zBCT-(1-z)BZT (z=0-1) system as another structural measurement, which conquers the limitation of lab-based XRD and is able to determine precise crystal symmetry and phase compositions of zBCT-(1-z)BZT (z=0-1) ceramics at various temperatures.

Appendix I. Examples of XRD analysis via jEdit and Topas-Academic.

1. XRD analysis of $Ba_{0.70}Ca_{0.30}TiO_3$ (1100 °C calcined and 1300 °C sintered)

Most of fabricated $Ba_{0.70}Ca_{0.30}TiO_3$ ceramics consisted of two distinct phases, the 1100°C calcined and 1300°C sintered $Ba_{0.70}Ca_{0.30}TiO_3$ ceramics was chosen as example to demonstrate the quantitative phase analysis of those multiphasic compositions.

1.1 The .inp file from jEdit

'==========

'1. DIFFRACTION FILE - Your selected PXRD file

'==========

xdd "BCT 1100-1300.raw" → File Name: Open the .raw file from XRD measurement

'Your TOPAS INPut File will be saved under the same name

'This feature currently only works with .XYE and .RAW files

'==========

'2. FILE HEADER - Contains statistics from Rietlevd Refienement

'==========

r_wp 5.34171318 r_exp 2.87721856 r_p 3.91919302 r_wp_dash 17.5508099 r_p_dash 18.8749972 r_exp_dash 9.45343081 weighted_Durbin_Watson 0.580601297 gof 1.85655454

iters 100000 'Maximum number of iterations of refinement

chi2_convergence_criteria 0.001 'Stop criteria for refinement

do_errors 'Reports errors for each refined value

'conserve_memory 'Increases computation time by about 20% but reduces memory useage

Good of fitness: the closer to 1, the better fit

'==========

'3. DIFFRACTION FILE PREPARATION - Contains data needed by TOPAS on the diffraction file

'==========

x_calculation_step = Yobs_dx_at(Xo); 'Sets the calculation step size for Rietveld refinement. This function used the step size of the measured diffraction pattern

'==========

'4. BACKGROUND FUNCTIONS - Background profiles

'==========

bkg @ 1003.00858`_2.93766329 181.947578`_4.88659486 124.446531`_3.44040121

99.3284133`_2.17455867 -34.7936523`_1.58796158 30.7111392`_1.59076531

'==

'5. RADIATION SOURCE - Information on the profile of D8 with Gobel Mirror

'==

lam

ymin_on_ymax 0.0001

la 0.66050 lo 1.540598 lh 0.5

la 0.33950 lo 1.544426 lh 0.5

Information of incident X-rays

LP_Factor(!th2_monochromator, 0) 'Lorentz-Polarisation factor. Change the monochromator angle as required

Simple_Axial_Model(@, 10.74542`_0.59168)

Zero_Error(@,-0.00844`_0.02392)

Specimen_Displacement(@,-0.06585`_0.03946)

'==

'7. RIETVELD REFINEMENT PHASE - Phase information for Reitveld Refinement

'==

str

a @ 3.968540`_0.000167)

b =Get(a);

c @ 4.004520`_0.000219)

al 90.

be 90.

ga 90.

volume 63.34

space_group "P4mm"

site Ba1 x 0 y 0 z 0 occ Ba+2 0.799988

site Ca1 x 0 y 0 z 0 occ Ca+2 0.200012

site Ti1 x 0.5 y 0.5 z 0.5204 occ Ti+4 1.

site O1 x 0.5 y 0.5 z -.0204 occ O-2 1.

site O2 x 0 y 0.5 z 0.4763 occ O-2 1.

Lattice parameters from .cif file (based on tetragonal $BaTiO_3$);
Then refinement in Topas to obtain those refined data with error bars

Elemental fractions on Ba-site, calculated by revised linear relationship: V=64.568-7.4836, where V is unit cell volume 63.068±0.006 $Å^3$ here, x is the Ca^{2+} content

'Place @ before values to be refined in Rietveld refinement

'You may need to replace a, b, c, al, be and ga parameters with the appropriate Cubic/Tetrahedral etc. function from 'vi. lattice parameters' below

phase_name "Tetra Ba0.80Ca0.20TiO3"

scale @ 0.00661500727`_2.789e-005

PV_Peak_Type(@, 0.00010`_0.10221_LIMIT_MIN_0.0001,@,  0.42633`_0.06104,@, 0.12739`_0.11593,@,  0.31766`_0.21595,@, 0.00010`_0.15948_LIMIT_MIN_0.0001,@, 0.00010`_0.25378_LIMIT_MIN_0.0001)

cell_mass 213.741 'Calculates the cell mass

cell_volume 63.068`_0.006 'Calculates the cell volume

Theoretical density of tetragonal phase

Phase_Density_g_on_cm3(5.62763`_0.00057) 'Calculates the phase density
weight_percent 87.887`_0.312 'Calculated weight fraction

Calculated weight fraction of tetragonal phase

'==========

'7. RIETVELD REFINEMENT PHASE - Phase information for Reitveld Refinement

'==========

str

a @ 3.836218`_0.000385

b =Get(a);

c =Get(a);

al 90.

be 90.

ga 90.

volume 54.66

space_group "Pm-3m"

Lattice parameters from .cif file (based on cubic $CaTiO_3$);
Then refinement in Topas to obtain those refined data with error bars

Elemental fractions on Ba-site, calculated by Vegard's law: V'=64.54-9.88x', where V' is unit cell volume 56.456±0.017 $Å^3$ here, x' is the Ca^{2+} content

site Ba1 x 0.5 y 0.5 z 0.5 occ Ba+2 0.179767

site Ca1 x 0.5 y 0.5 z 0.5 occ Ca+2 0.820233

site Ti1 x 0 y 0 z 0 occ Ti+4 1.

site O1 x 0.5 y 0 z 0 occ O-2 1.

'Place @ before values to be refined in Rietveld refinement

'You may need to replace a, b, c, al, be and ga parameters with the appropriate Cubic/Tetrahedral etc. function from 'vi. lattice parameters' below

phase_name "Cubic Ba0.18Ca0.82TiO3"

scale @ 0.00141889344`_4.115e-005

PV_Peak_Type(@, 0.00010`_0.51943_LIMIT_MIN_0.0001,@, 0.49192`_0.28667,@, 0.06246`_0.57847_LIMIT_MIN_0.0001,@, 0.87750`_1.85655_LIMIT_MIN_0.0001,@, 0.30500`_1.85655_LIMIT_MIN_0.0001,@, 0.30500`_1.85655_LIMIT_MIN_0.0001)

cell_mass 153.425 'Calculates the cell mass

cell_volume 56.456`_0.017 'Calculates the cell volume

Theoretical density of pseudo-cubic phase

Phase_Density_g_on_cm3(4.51270`_0.00136) 'Calculates the phase density

weight_percent 12.113`_0.312 'Calculated weight fraction

Calculated weight fraction of pseudo-cubic phase

xo_Is

xo @ 16.2286919`_0.0216685492 I @ 102.37764`_2.21693

PV_Peak_Type(@, 2.17977`,@, 7.13475`,@, 2.17316`,@, 0.87750`,@, 0.30500`,@, 0.30500`)

xo @ 29.3717872`_0.0510215664 I @ 139.83215`_5.38299

PV_Peak_Type(@,3.83104`_542147.49951,@,0.00010`_109327.55106_LIMIT_MIN_0.0001, @,2.29230`_552150.83382,@, 0.87750`_1.85655_LIMIT_MIN_0.0001,@,0.30500`_1.85655_LIMIT_MIN_0.0001,@,0.30500`_1.85655_LIMIT_MIN_0.0001)

Unindexed peaks

1.2 The refined pattern in Topas

As shown in Figure I.1, the measured pattern (blue) indicated two distinct phases. The measured pattern (as blue) and refined pattern (as red) were shown together in Topas, where the difference was shown as grey line at the bottom, indicating a good fitness between measured and calculated data. The weight fractions of each phases and calculated elemental fractions were also shown on the right corner.

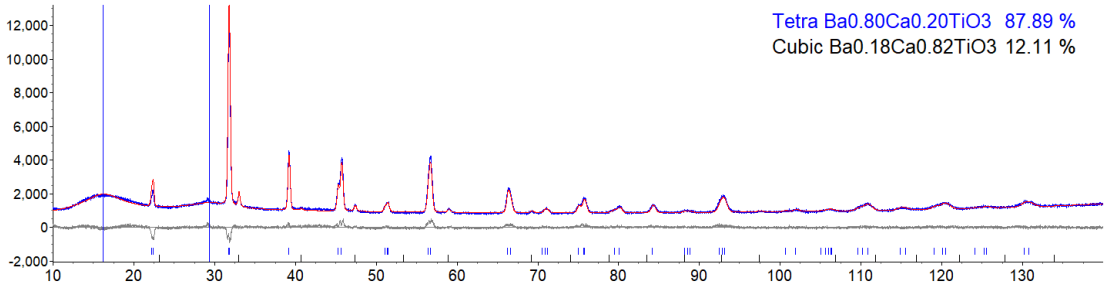

Figure I.1. Refinement of "BCT 1100-1300" pattern in Topas.

1.3 Calculation of elemental fractions

The elemental fractions in two distinct phases were calculated separately.

In Ba-rich tetragonal phase:

The calculation of Ba-rich tetragonal phase is based on previous work by Fu et al. [94], showing a revised linear relationship for $Ba_{1-x}Ca_xTiO_3$ system (V= 64.568-7.4836x), as shown in Figure I.2.

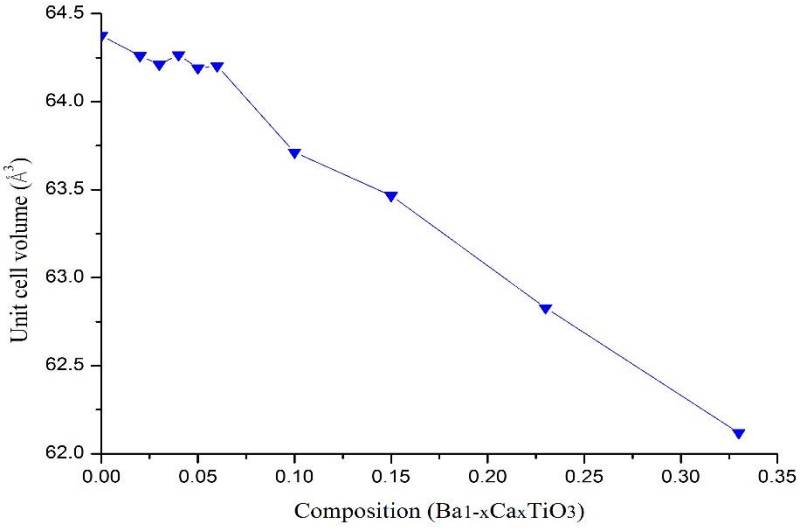

Figure I.2. Refined linear relationship from Fu et al [94].

Putting the highlighted unit cell volume of Ba-rich phase (63.068 Å) into the formula, figuring out x=0.20 (as Ca^{2+} concentrations). And the weight percent of Ba-rich phase is calculated by jEdit and Topas, highlighted in the .inp file. Thus, the tetragonal phase is $Ba_{0.80}Ca_{0.20}TiO_3$ with 87.887±0.312 wt.% (quoted as 89.9±0.3 wt.%).

In Ca-rich pseduo-cubic phase:

The Vegard's relationship of Ca-rich phase is worked out by the unit cell volume of psedo-cubic $BaTiO_3$ (x'=0) and $CaTiO_3$ (x'=1) from cif. file [236, 237], with the formula: V'= 64.54-9.88x'. Using the highlighted cell volume for Ca-rich phase (V'=56.456 Å) to figure out x'= 0.82 (as Ca^{2+} concentrations). Similarly, the weight percent of this phase is highlighted in .inp file. Hence, the psedo-cubic phase is $Ba_{0.18}Ca_{0.82}TiO_3$ with 12.113±0.312 wt.% (quotoed as 12.1±0.3 wt.%).

In conclusion, a quantitative phase analysis of designed $Ba_{0.70}Ca_{0.30}TiO_3$ phase could be achieved by using refinement through jEdit and Topas. For this 1100°C calcined and 1300°C sintered ceramics, it consists of a predominant tetragonal $Ba_{0.80}Ca_{0.20}TiO_3$ (89.9±0.3 wt.%) and a minority of psedo-cubic $Ba_{0.18}Ca_{0.82}TiO_3$ phase with 12.1±0.3 wt.%.

2. XRD analysis of $BaZr_{0.20}Ti_{0.80}O_3$ (1250 °C calcined and 1500 °C sintered)

The sintered $BaZr_{0.20}Ti_{0.80}O_3$ ceramics were single phase. As the designed composition was in vicinity of rhombohedral to cubic phase boundary at room temperature and the best homogeneity was achieved under 1250°C calcination and 1500°C sintering, therefore, the ceramics fabricated at this condition was chosen to demonstrate the identification of crystal structure in $BaZr_{0.20}Ti_{0.80}O_3$ samples. The calculation of Zr^{4+} concentrations based on Vegard's law would also be discussed.

2.1 The .inp file from jEdit

'==========

'1. DIFFRACTION FILE - Your selected PXRD file

'==========

xdd "BZT 1250-1500.raw"

File name

'Your TOPAS INPut File will be saved under the same name

'This feature currently only works with .XYE and .RAW files

'==========

'2. FILE HEADER - Contains statistics from Rietlevd Refienement

'==========

r_wp 21.0037175 r_exp 13.892735 r_p 15.9492722 r_wp_dash 48.1002115 r_p_dash 53.4194503 r_exp_dash 31.8154866 weighted_Durbin_Watson 0.947618118 gof 1.511849

Good of fitness

iters 100000 'Maximum number of iterations of refinement

chi2_convergence_criteria 0.001 'Stop criteria for refinement

do_errors 'Reports errors for each refined value

'conserve_memory 'Increases computation time by about 20% but reduces memory useage

'==

'3. DIFFRACTION FILE PREPARATION - Contains data needed by TOPAS on the diffraction file

'==

x_calculation_step = Yobs_dx_at(Xo); 'Sets the calculation step size for Rietveld refinement. This function used the step size of the measured diffraction pattern

start_X 20 'Removes lower 2th values from future calculations

Refinement start from 2θ=20°

'==

'4. BACKGROUND FUNCTIONS - Background profiles

'==

bkg @ 46.6083`_0.157389943 -31.4833773`_0.28715626 20.3143791`_0.248579835 -13.2240798`_0.235248926 6.80028884`_0.187807494 -3.29779466`_0.178851567

'==

'5. RADIATION SOURCE - Information on the profile of D8 with Monochromator

'==

lam

ymin_on_ymax 0.0001

la 1 lo 1.540596 lh 0.5

LP_Factor(!th2_monochromator, 26.6) 'Lorentz-Polarisation factor. Change the monochromator angle as required

use_tube_dispersion_coefficients

Simple_Axial_Model(@, 10.27487`_0.13908)

Zero_Error(@,-0.08726`_0.00765)

Specimen_Displacement(@,-0.24494`_0.01232)

/*

Silent this part: as refinement based on cubic .cif file

'==

'7. RIETVELD REFINEMENT PHASE - Phase information for Reitveld Refinement

'==

str

a @ 4.045751

b =Get(a);

c =Get(a);

al 90.

be 90.

ga 90.

volume 64.29

space_group "Pm-3m"

.cif file for cubic phase: single phase with Zr^{4+} concentrations calculated as 0.18; Good of fitness=1.5332541

site Ba1 x 0 y 0 z 0 occ Ba+2 1.

site Ti1 x 0.5 y 0.5 z 0.5 occ Ti+4 0.82

site Zr1 x 0.5 y 0.5 z 0.5 occ Zr+4 0.18

site O1 x 0.5 y 0.5 z 0 occ O-2 1.

```
'Place @ before values to be refined in Rietveld refinement
'You may need to replace a, b, c, al, be and ga parameters with the appropriate Cubic/Tetrahedral etc. function from 'vi. lattice parameters' below
            phase_name "C BaZr0.18Ti0.82O3"
            scale @    0.00033297641
            PV_Peak_Type(@,       0.00056_LIMIT_MIN_0.0001,@,       0.05076,@,       0.03334,@, 0.87750_LIMIT_MIN_0.0001,@, 0.30500_LIMIT_MIN_0.0001,@, 0.30500_LIMIT_MIN_0.0001)
            cell_mass    240.996 'Calculates the cell mass
            cell_volume    66.221 'Calculates the cell volume
            Phase_Density_g_on_cm3( 6.04314) 'Calculates the phase density
            weight_percent    100.000 'Calculated weight fraction
*/

'=======================================================================
'7. RIETVELD REFINEMENT PHASE - Phase information for Reitveld Refinement
'=======================================================================
      str
            a @    4.045646`_0.000033
            b =Get(a);
            c =Get(a);
            al @    90.03158`_0.00115
            be =Get(al);
            ga =Get(al);
            volume 64.05
            space_group "R3mR"
            site Ba1       x 0.013              y 0.013              z 0.013              occ Ba+2 1.
            site Ti1       x 0.5                y 0.5                z 0.5                occ Ti+4 0.82
            site Zr1       x 0.5                y 0.5                z 0.5                occ Zr+4 0.18
            site O1        x 0.524              y 0.524              z 0.031              occ O-2    1.
'Place @ before values to be refined in Rietveld refinement
'You may need to replace a, b, c, al, be and ga parameters with the appropriate Cubic/Tetrahedral etc. function from 'vi. lattice parameters' below
            phase_name "R BaZr0.18Ti0.82O3"
            scale @    0.000333246109`_2.181e-006
            PV_Peak_Type(@,    0.00132`_0.01444_LIMIT_MIN_0.0001,@,    0.02679`_0.01162,@, 0.03711`_0.01748,@,                0.87750`_1.51185_LIMIT_MIN_0.0001,@, 0.30500`_1.51185_LIMIT_MIN_0.0001,@, 0.30500`_1.51185_LIMIT_MIN_0.0001)
            cell_mass    240.996 'Calculates the cell mass
            cell_volume    66.216`_0.002 'Calculates the cell volume
            Phase_Density_g_on_cm3( 6.04361`_0.00015) 'Calculates the phase density
            weight_percent    100.000`_0.000 'Calculated weight fraction
```

.cif file for rhombohedral phase: single phase with Zr^{4+} concentrations calculated as 0.18.
It worthy mention that lattice parameters obtained for rhombohedral phase is similar to cubic phase (as silent above). As the rhombohedral fitting has better value of good of fitness, the refinement by rhombohedral phase is showing here.

Unit cell volume to calculate Zr^{4+} concentrations as 0.18

Theoretical density as rhombohedral phase

2.2 The refined pattern in Topas

The refinements of 1250°C calcined and 1500°C sintered $BaZr_{0.20}Ti_{0.80}O_3$ ceramics by cubic and rhombohedral symmetry were shown in Figure I.3 and I.4 respectively, where the measured pattern (blue) indicated the formation of single phase in the ceramics. In both cases, the difference (grey) between refined pattern (red) and measured pattern were small with good of fitness around 1.5, which implied the good refinement results from both symmetries. Based on XRD analysis here, the rhombohedral refinement had better fitness (gof=1.51) than the cubic refinement (gof=1.53), therefore the sintered $BaZr_{0.20}Ti_{0.80}O_3$ ceramics was believed to be rhombohedral symmetry. The more discussion on determining its crystal structure was detailed in section 6.1 and 6.3.1.

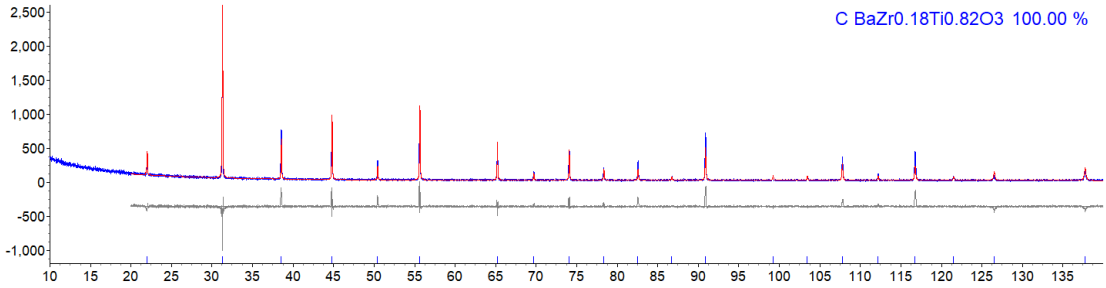

Figure I.3. Refinement of "BZT 1250-1500" by cubic symmetry.

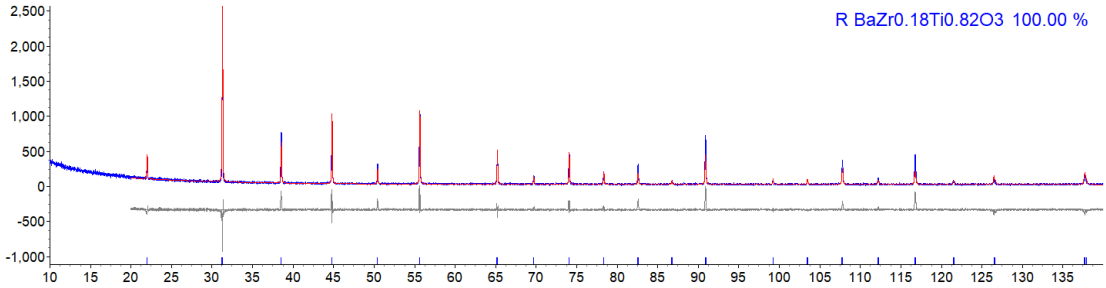

Figure I.4. Refinement of "BZT 1250-1500" by rhombohedral symmetry.

2.3 Calculation of elemental fractions

The $BaZr_yTi_{1-y}O_3$ system was believed to fulfil the Vegard's law (section 2.4.4). Therefore, Zr^{4+} concentrations (y) and unit cell volume (V) were referenced from literature, and a linear relationship was calculated as the Vegard's relationship for $BaZr_yTi_{1-y}O_3$ system: V=9.2799y+64.543 [223]. As shown in .inp file, the unit cell volume was 66.216 $Å^3$, thus the Zr^{4+} concentrations (y) was calculated as 0.18. This difference from the designed concentration (y=0.20) was believed to related to the accuracy of referenced relationship. Based on XRD and refinement of fabricated single $BaZr_yTi_{1-y}O_3$ (y=0-0.30) phases, a new relationship was established in this study (section 6.1).

3. XRD analysis of $0.5Ba_{0.70}Ca_{0.30}TiO_3$-$0.5BaZr_{0.20}Ti_{0.80}O_3$ (1250 °C calcined and 1500 °C sintered)

The $zBa_{0.70}Ca_{0.30}TiO_3$-$(1-z)BaZr_{0.20}Ti_{0.80}O_3$ ceramics were sintered at 1300-1500°C, where the low temperature sintered ceramics (z=0.6-1) had two distinct phases, being similar to fabricated

$Ba_{0.70}Ca_{0.30}TiO_3$ ceramics. The 1500°C sintered ceramics were all single phasic. The crystal structure of z=0-0.4 and z=0.6-1 could be easily identified as rhombohedral and tetragonal phase respectively. However, the crystal structure of the z=0.5 composition was difficult to determine. This appendix shows the refinement of this composition to be single orthorhombic symmetry, rhombohedral and tetragonal symmetry, or orthorhombic and tetragonal symmetry.

3.1 The refinement from orthorhombic phase

3.1.1 The .inp file from jEdit

'==========
'1. DIFFRACTION FILE - Your selected PXRD file
'==========
xdd "5-5 BCZT 1500.raw"
'Your TOPAS INPut File will be saved under the same name
'This feature currently only works with .XYE and .RAW files

'==========
'2. FILE HEADER - Contains statistics from Rietlevd Refienement
'==========
r_wp 15.262346 r_exp 7.62179684 r_p 11.0565101 r_wp_dash 45.3542051 r_p_dash 50.9251881 r_exp_dash 22.64924 weighted_Durbin_Watson 0.539812308 gof 2.00246035
iters 100000 'Maximum number of iterations of refinement
chi2_convergence_criteria 0.001 'Stop criteria for refinement
do_errors 'Reports errors for each refined value
'conserve_memory 'Increases computation time by about 20% but reduces memory useage

Not very good fitness

'==========
'3. DIFFRACTION FILE PREPARATION - Contains data needed by TOPAS on the diffraction file
'==========
x_calculation_step = Yobs_dx_at(Xo); 'Sets the calculation step size for Rietveld refinement. This function used the step size of the measured diffraction pattern

'==========
'4. BACKGROUND FUNCTIONS - Background profiles
'==========
bkg @ 146.259224`_0.324337715 -2.50564918`_0.566234617 10.1929154`_0.506504847 19.6949076`_0.509871402 -12.6794059`_0.438186155 5.17012424`_0.428927371

'==========
'5. RADIATION SOURCE - Information on the profile of D8 with Gobel Mirror
'==========

```
    lam
        ymin_on_ymax 0.0001
        la 0.66050 lo 1.540598    lh 0.5
        la 0.33950 lo 1.544426    lh 0.5
LP_Factor(!th2_monochromator, 0) 'Lorentz-Polarisation factor. Change the monochromator angle as required
Simple_Axial_Model(@, 9.25503`_0.20964)
Zero_Error(@, 0.02107`_0.01343)
Specimen_Displacement(@,-0.00119`_0.02126)


'======================================================================
'7. RIETVELD REFINEMENT PHASE - Phase information for Reitveld Refinement
'======================================================================
    str
        a @    4.018431`_0.000106
        b @    5.655716`_0.000243
        c @    5.659928`_0.000218
        al 90.
        be 90.
        ga 90.
        volume 127.09
        space_group "Amm2"
        site Ba1      x 0          y 0          z 0          occ Ba+2 0.85
        site Ca1      x 0          y 0          z 0          occ Ca+2 0.15
        site Ti1      x 0.5        y 0          z 0.5100     occ Ti+4 0.90
        site Zr1      x 0.5        y 0          z 0.5100     occ Zr+4 0.10
        site O1       x 0.5        y 0.5        z 0.4900     occ O-2    1.
        site O2       x 0.5        y 0.7525     z 0.7396     occ O-2    1.
'Place @ before values to be refined in Rietveld refinement
'You may need to replace a, b, c, al, be and ga parameters with the appropriate Cubic/Tetrahedral etc. function from 'vi. lattice parameters' below
        phase_name "O Ba0.85Ca0.15Zr0.10Ti0.90O3"
        scale @    0.000262136853`_1.56e-006
        PV_Peak_Type(@,    0.00010`_0.03031_LIMIT_MIN_0.0001,@,    0.07204`_0.01919,@, 0.03486`_0.03444,@,    0.87750`_2.00246_LIMIT_MIN_0.0001,@, 0.30500`_2.00246_LIMIT_MIN_0.0001,@, 0.30500`_2.00246_LIMIT_MIN_0.0001)
        cell_mass    445.881 'Calculates the cell mass
        cell_volume    128.634`_0.008 'Calculates the cell volume
        Phase_Density_g_on_cm3( 5.75590`_0.00037) 'Calculates the phase density
```

As Ca^{2+} and Zr^{4+} substitute into $BaTiO_3$ simultaneously, the accurate determination of elemental fractions cannot be achieved, the occupancies shown here were indexed as designed values in this single phase (with fully homogeneity).

3.1.2 The refined pattern in Topas

The refined pattern (red) based on single orthorhombic symmetry was shown in Figure I.5. The difference (grey) to the measured pattern (blue) was quite large at 2θ=45°. A more detailed view were shown and discussed in section 7.1.1.

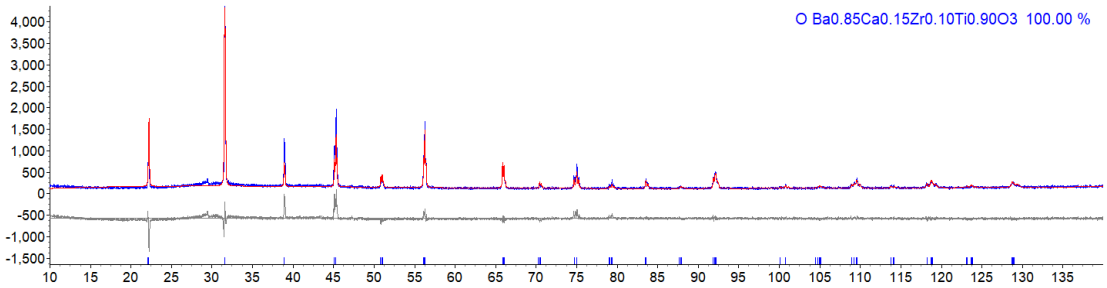

Figure I.5. The refinement of $0.5Ba_{0.70}Ca_{0.30}TiO_3$-$0.5BaZr_{0.20}Ti_{0.80}O_3$ ceramics by single orthorhombic phase.

3.2 The refinement from rhombohedral and tetragonal phases

3.2.1 The .inp file from jEdit

'==========
'1. DIFFRACTION FILE - Your selected PXRD file
'==========
xdd "5-5 BCZT 1500.raw"
'Your TOPAS INPut File will be saved under the same name
'This feature currently only works with .XYE and .RAW files

'==========
'2. FILE HEADER - Contains statistics from Rietlevd Refienement
'==========
r_wp 13.4748417 r_exp 7.61846272 r_p 10.2553529 r_wp_dash 39.8952611 r_p_dash 46.8607913 r_exp_dash 22.5561507 weighted_Durbin_Watson 0.670618105 gof 1.76870876
iters 100000 'Maximum number of iterations of refinement
chi2_convergence_criteria 0.001 'Stop criteria for refinement
do_errors 'Reports errors for each refined value
'conserve_memory 'Increases computation time by about 20% but reduces memory useage

Best fitness among three refinement

'==========
'3. DIFFRACTION FILE PREPARATION - Contains data needed by TOPAS on the diffraction file
'==========
x_calculation_step = Yobs_dx_at(Xo); 'Sets the calculation step size for Rietveld refinement. This function used the step size of the measured diffraction pattern

'==========

'4. BACKGROUND FUNCTIONS - Background profiles

'==========

bkg @ 145.603267`_0.29968638 -2.9063635`_0.508465339 11.0389229`_0.457791235 19.0559801`_0.465362033 -12.1002312`_0.393381586 5.04383371`_0.385499783

'==========

'5. RADIATION SOURCE - Information on the profile of D8 with Gobel Mirror

'==========

lam

ymin_on_ymax 0.0001

la 0.66050 lo 1.540598 lh 0.5

la 0.33950 lo 1.544426 lh 0.5

LP_Factor(!th2_monochromator, 0) 'Lorentz-Polarisation factor. Change the monochromator angle as required

Simple_Axial_Model(@, 6.63269`_0.47877)

Zero_Error(@, 0.33561`_0.01304)

Specimen_Displacement(@, 0.45419`_0.02131)

'==========

'7. RIETVELD REFINEMENT PHASE - Phase information for Reitveld Refinement

'==========

str

a @ 4.011814`_0.000372

b =Get(a);

c =Get(a);

al @ 89.94707`_0.03165

be =Get(al);

ga =Get(al);

volume 64.05

space_group "R3mR"

.cif file for rhombohedral $BaTiO_3$, no determination of elemental fractions was applied.

site Ba1 x 0.013 y 0.013 z 0.013 occ Ba+2 1.

site Ti1 x 0.5 y 0.5 z 0.5 occ Ti+4 1.

site O1 x 0.524 y 0.524 z 0.031 occ O-2 1.

'Place @ before values to be refined in Rietveld refinement

'You may need to replace a, b, c, al, be and ga parameters with the appropriate Cubic/Tetrahedral etc. function from 'vi. lattice parameters' below

phase_name "Rhom BaTiO3"

scale @ 0.000319236957`_4.442e-005

PV_Peak_Type(@, 0.00010`_0.32895_LIMIT_MIN_0.0001,@, 0.00010`_0.24940_LIMIT_MIN_0.0001,@, 0.22839`_0.39002,@, 0.87826`_1.76871_LIMIT_MIN_0.0001,@, 0.01261`_1.76871_LIMIT_MIN_0.0001,@, 0.18277`_1.76871_LIMIT_MIN_0.0001)

```
        cell_mass    233.192 'Calculates the cell mass
        cell_volume    64.569`_0.018 'Calculates the cell volume
        Phase_Density_g_on_cm3( 5.99710`_0.00167) 'Calculates the phase density
        weight_percent    32.548`_3.349 'Calculated weight fraction
```

```
'=======================================================================
'7. RIETVELD REFINEMENT PHASE - Phase information for Reitveld Refinement
'=======================================================================
    str
        a @    4.003577`_0.000094
        b =Get(a);
        c @    4.022915`_0.000127
        al 90.
        be 90.
        ga 90.
        volume 64.27
        space_group "P4mm"
        site Ba1      x 0          y 0          z 0          occ Ba+2 1.
        site Ti1      x 0.5        y 0.5        z 0.5224     occ Ti+4 1.
        site O1       x 0.5        y 0.5        z -.0244     occ O-2  1.
        site O2       x 0.5        y 0          z 0.4895     occ O-2  1.
'Place @ before values to be refined in Rietveld refinement
'You may need to replace a, b, c, al, be and ga parameters with the appropriate Cubic/Tetrahedral etc.
function from 'vi. lattice parameters' below
          phase_name "Tetra BaTiO3"
        scale @    0.000662460945`_4.167e-005
        PV_Peak_Type(@,    0.00010`_0.04347_LIMIT_MIN_0.0001,@,    0.10594`_0.02756,@,
0.03961`_0.04997,@,                    0.00010`_0.74851_LIMIT_MIN_0.0001,@,
0.16621`_0.60500_LIMIT_MIN_0.0001,@, 0.00010`_0.89528_LIMIT_MIN_0.0001)
        cell_mass    233.192 'Calculates the cell mass
        cell_volume    64.482`_0.004 'Calculates the cell volume
        Phase_Density_g_on_cm3( 6.00518`_0.00034) 'Calculates the phase density
        weight_percent    67.452`_3.349 'Calculated weight fraction
```

.cif file for tetragonal $BaTiO_3$, no determination of elemental fractions was applied.

3.2.2 The refined pattern in Topas

As shown in Figure I.6, the rhombohedral and tetragonal $BaTiO_3$ phases were used to refine the measured pattern. The weight percent of each phase was obtained, however, determination of the elemental fraction was not achieved, due to the lack of reference relationship to figure out the multiple dopants in $BaTiO_3$. It is also noticeable that the intensity variations at $2\theta=45°$ was quite large, which

was discussed in section 7.1.1.

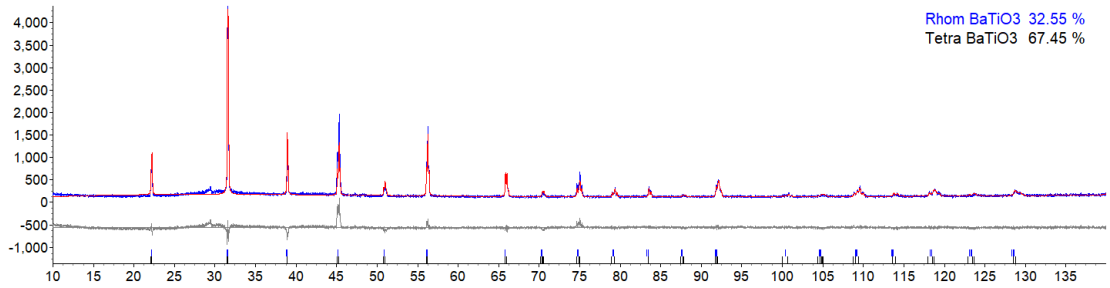

Figure I.6. The refinement of $0.5Ba_{0.70}Ca_{0.30}TiO_3$-$0.5BaZr_{0.20}Ti_{0.80}O_3$ ceramics by rhombohedral and tetragonal phase.

3.3 The refinement from orthorhombic and tetragonal phases

3.3.1 The .inp file from jEdit

'==========

'1. DIFFRACTION FILE - Your selected PXRD file

'==========

xdd "5-5 BCZT 1500.raw"

'Your TOPAS INPut File will be saved under the same name

'This feature currently only works with .XYE and .RAW files

'==========

'2. FILE HEADER - Contains statistics from Rietlevd Refienement

'==========

r_wp 13.6142275 r_exp 7.61804585 r_p 10.3602573 r_wp_dash 40.3737676 r_p_dash 47.4856664 r_exp_dash 22.5917492 weighted_Durbin_Watson 0.656860944 gof 1.78710233

iters 100000 'Maximum number of iterations of refinement

chi2_convergence_criteria 0.001 'Stop criteria for refinement

do_errors 'Reports errors for each refined value

'conserve_memory 'Increases computation time by about 20% but reduces memory useage

'==========

'3. DIFFRACTION FILE PREPARATION - Contains data needed by TOPAS on the diffraction file

'==========

x_calculation_step = Yobs_dx_at(Xo); 'Sets the calculation step size for Rietveld refinement. This function used the step size of the measured diffraction pattern

'==========

'4. BACKGROUND FUNCTIONS - Background profiles

'==========

```
bkg   @      146.021395`_0.291221872   -3.03299817`_0.506449923      10.8412026`_0.455659224
20.0457465`_0.457019624 -12.5088059`_0.393276648    5.52963958`_0.384182421

'==========================================================================
'5. RADIATION SOURCE - Information on the profile of D8 with Gobel Mirror
'==========================================================================
      lam
            ymin_on_ymax 0.0001
            la 0.66050 lo 1.540598    lh 0.5
            la 0.33950 lo 1.544426    lh 0.5
LP_Factor(!th2_monochromator, 0) 'Lorentz-Polarisation factor. Change the monochromator angle as
required
Simple_Axial_Model(@, 5.42758`_0.92375)
Zero_Error(@, 0.02906`_0.01578)
Specimen_Displacement(@, 0.02198`_0.02757)


'==========================================================================
'7. RIETVELD REFINEMENT PHASE - Phase information for Reitveld Refinement
'==========================================================================
      str
            a @    4.000207`_0.000090
            b =Get(a);
            c @    4.019410`_0.000119
            al 90.
            be 90.
            ga 90.
            volume 64.27
            space_group "P4mm"
            site Ba1       x 0                  y 0                  z 0                  occ Ba+2 1.
            site Ti1       x 0.5                y 0.5                z 0.5224             occ Ti+4 1.
            site O1        x 0.5                y 0.5                z -.0244             occ O-2  1.
            site O2        x 0.5                y 0                  z 0.4895             occ O-2  1.
'Place @ before values to be refined in Rietveld refinement
'You may need to replace a, b, c, al, be and ga parameters with the appropriate Cubic/Tetrahedral etc.
function from 'vi. lattice parameters' below
             phase_name "Tetra BaTiO3"
            scale @    0.000873555733`_1.347e-005
            PV_Peak_Type(@,   0.01025`_0.05453,@,   0.08166`_0.03761,@,   0.04336`_0.06438,@,
0.29260`_0.49005,@, 0.00010`_0.38174_LIMIT_MIN_0.0001,@, 0.29682`_0.58856)
            cell_mass    233.192 'Calculates the cell mass
            cell_volume    64.317`_0.003 'Calculates the cell volume
            Phase_Density_g_on_cm3( 6.02055`_0.00032) 'Calculates the phase density
```

.cif file for tetragonal $BaTiO_3$, no determination of elemental fractions was applied.

```
        weight_percent    92.023`_1.190 'Calculated weight fraction


'=======================================================================
'7. RIETVELD REFINEMENT PHASE - Phase information for Reitveld Refinement
'=======================================================================
    str
        a @    4.007903`_0.000649
        b @    5.677966`_0.000886
        c @    5.665410`_0.000942
        al 90.
        be 90.
        ga 90.
        volume 127.09
        space_group "Amm2"
        site Ba1      x 0          y 0          z 0          occ Ba+2 1.
        site Ti1      x 0.5        y 0          z 0.5100     occ Ti+4 1.
        site O1       x 0.5        y 0.5        z 0.4900     occ O-2  1.
        site O2       x 0.5        y 0.7525     z 0.7396     occ O-2  1.
'Place @ before values to be refined in Rietveld refinement
'You may need to replace a, b, c, al, be and ga parameters with the appropriate Cubic/Tetrahedral etc.
function from 'vi. lattice parameters' below
          phase_name "Orth BaTiO3"
        scale @    1.88890311e-005`_3.05e-006
        PV_Peak_Type(@,                    0.00011`_0.16645_LIMIT_MIN_0.0001,@,
0.00027`_0.11278_LIMIT_MIN_0.0001,@,                    0.04758`_0.19167,@,
0.87750`_1.78710_LIMIT_MIN_0.0001,@,          0.30500`_1.78710_LIMIT_MIN_0.0001,@,
0.30500`_1.78710_LIMIT_MIN_0.0001)
        cell_mass    466.384 'Calculates the cell mass
        cell_volume    128.926`_0.036 'Calculates the cell volume
        Phase_Density_g_on_cm3( 6.00692`_0.00168) 'Calculates the phase density
        weight_percent    7.977`_1.190 'Calculated weight fraction
```

.cif file for orthorhombic $BaTiO_3$, no determination of elemental fractions was applied.

3.3.2 The refined pattern in Topas

Figure I.7 shows the refinement of measured pattern from coexistence of tetragonal and orthorhombic phases. A better fitness (gof=1.79) was achieved than fitting single orthorhombic phase (gof>2), however, there was still a large difference between refined and measured data at 2θ=45°. Also, the accurate identification of elemental fractions was not achieved.

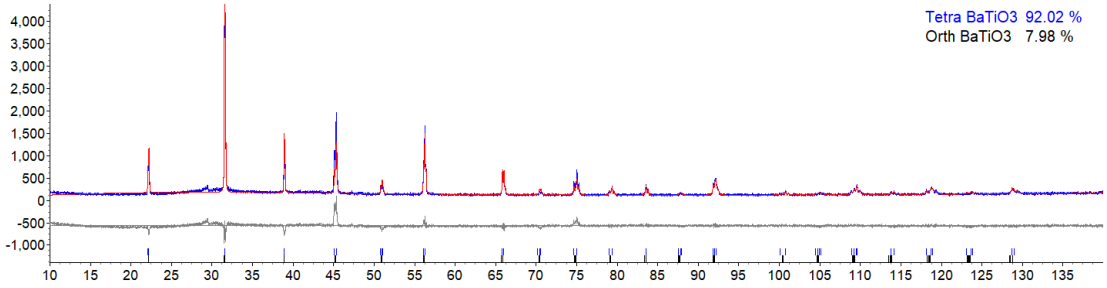

Figure I.7. The refinement of $0.5Ba_{0.70}Ca_{0.30}TiO_3$-$0.5BaZr_{0.20}Ti_{0.80}O_3$ ceramics by orthorhombic and tetragonal phase.

3.4 Summary

In conclusion, the quantitative phase analysis from XRD measurements and refinements could reveal the general phase compositions of multiphasic $zBa_{0.70}Ca_{0.30}TiO_3$-(1-z) $BaZr_{0.20}Ti_{0.80}O_3$ ceramics (with two distinct phases), whereas the elemental concentrations were not able to be worked out based on the current study. The quantitative phase analysis also enabled the identification of rhombohedral and tetragonal symmetry for z=0-0.4 and z=0.6-1 ceramics, where the elemental fractions in those single phasic ceramics were assumed to be the same as the designed compositions. However, the accurate identification of the crystal structure of z=0.5 ceramics was not achieved by lab-based XRD measurement and the lack of determination of elemental fractions in ceramics. Therefore, it is difficult to conclude the crystal structure for this composition at this stage.

In this project, the aim of investigating XRD data for 1500°C sintered $zBa_{0.70}Ca_{0.30}TiO_3$-(1-z)$BaZr_{0.20}Ti_{0.80}O_3$ was to confirm the formation of single phase. This was considered as the fundamental to figure out a relationship between $Ba_{0.70}Ca_{0.30}TiO_3$ concentrations (z) and the unit cell volume (V) and to further confirm that $zBa_{0.70}Ca_{0.30}TiO_3$-(1-z)$BaZr_{0.20}Ti_{0.80}O_3$ is a pseudo-binary system between $Ba_{0.70}Ca_{0.30}TiO_3$ and $BaZr_{0.20}Ti_{0.80}O_3$ (discussed in section 7.1.1).

Appendix II. Analysis of temperature dependent Raman spectra data.

As described in section 3.3.1, the temperature dependent Raman spectroscopy was carried out on Renishaw InVia Reflex Raman spectrometer. During the measurement, the sample was heating at 1 °C/min, and the Raman spectra was collected at every 30 seconds (*i.e.* 0.5 °C). Therefore, the measured data contains hundreds of data set.

In order to analyse the multiple Raman spectra, the measured data was firstly loaded in Wire 4.1, and then saved as '.txt' files in a same folder, as described in the flow diagram below. As each '.txt' file was named with measuring time, the MATLAB was then used to read the '.txt' file name and pick up the n^{th} Raman spectrum. A MATLAB peak fitting tool was applied to analyse the peak information, using a non-linear optimization algorithm to decompose a complex, overlapping-peak signal into its component parts [238]. The corresponding peak position, peak width and peak intensity of each Raman spectrum were obtained. After repeating this process for all data set by MATLAB, the peak information was output and plotted as a function of temperature, in order to identify the phase transition behaviour.

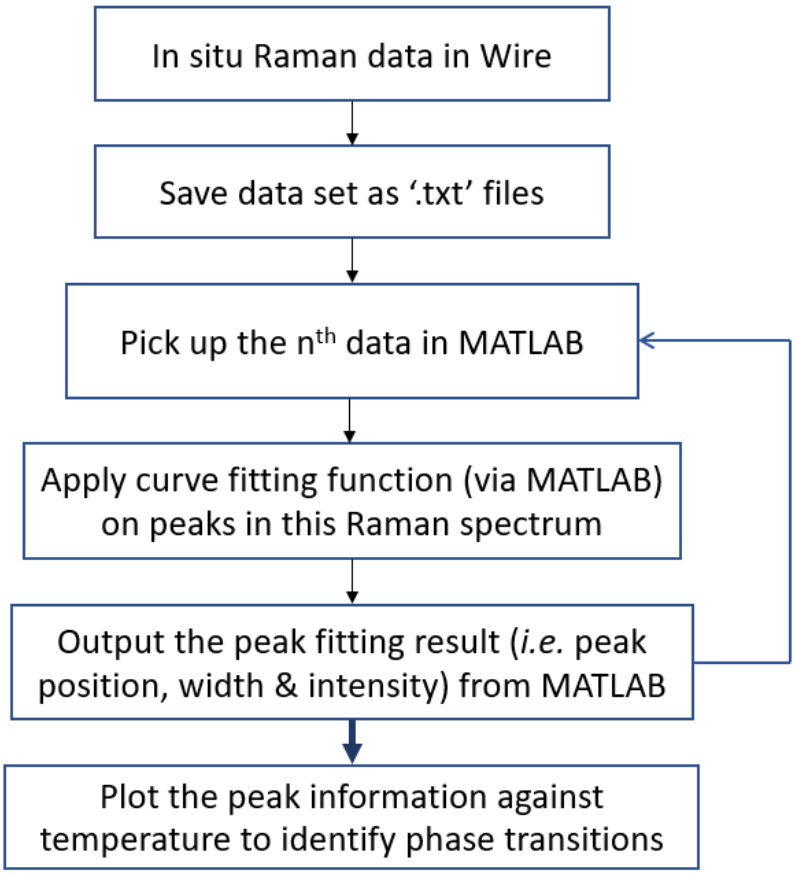

Appendix III. XRD patterns of sintered zBCT-(1-z)BZT (*z*=0-1) ceramics.

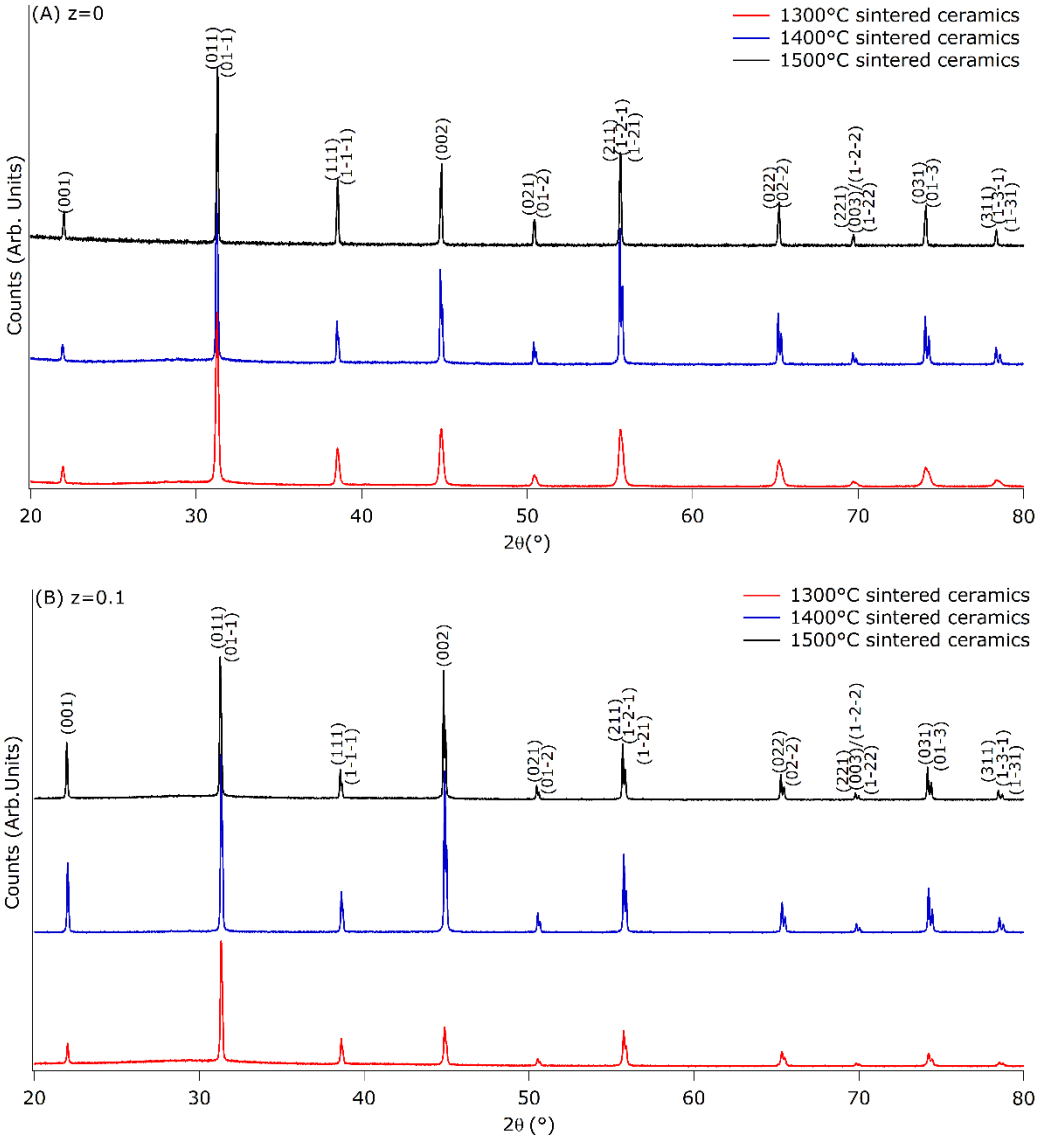

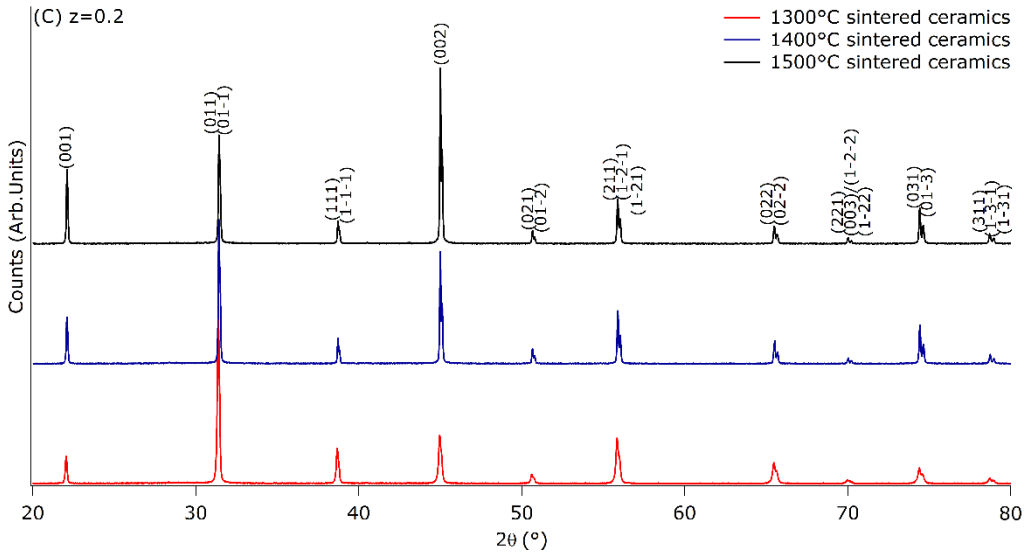
(C) z=0.2
1300°C sintered ceramics
1400°C sintered ceramics
1500°C sintered ceramics
Counts (Arb.Units)
2θ (°)
(001)
(011)
(01-1)
(111)
(1-1-1)
(002)
(021)
(01-2)
(211)
(1-2-1)
(1-21)
(022)
(02-2)
(221)
(003)
(1-2-2)
(1-22)
(031)
(01-3)
(311)
(1-3-1)
(1-31)

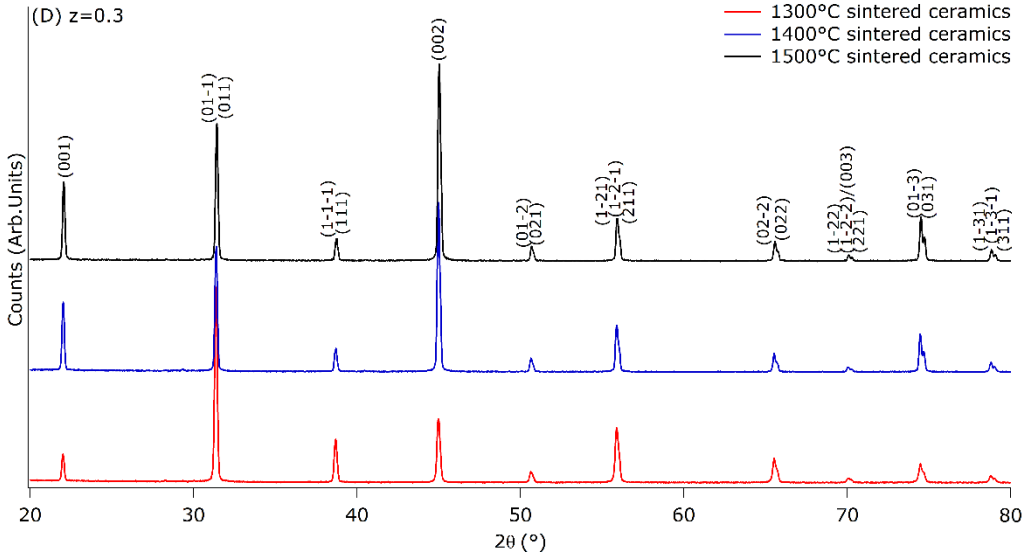
(D) z=0.3
1300°C sintered ceramics
1400°C sintered ceramics
1500°C sintered ceramics
Counts (Arb.Units)
2θ (°)
(001)
(01-1)
(011)
(1-1-1)
(111)
(002)
(01-2)
(021)
(1-21)
(1-2-1)
(211)
(02-2)
(022)
(1-22)
(1-2-2)
(221)
(003)
(01-3)
(031)
(1-31)
(1-3-1)
(311)

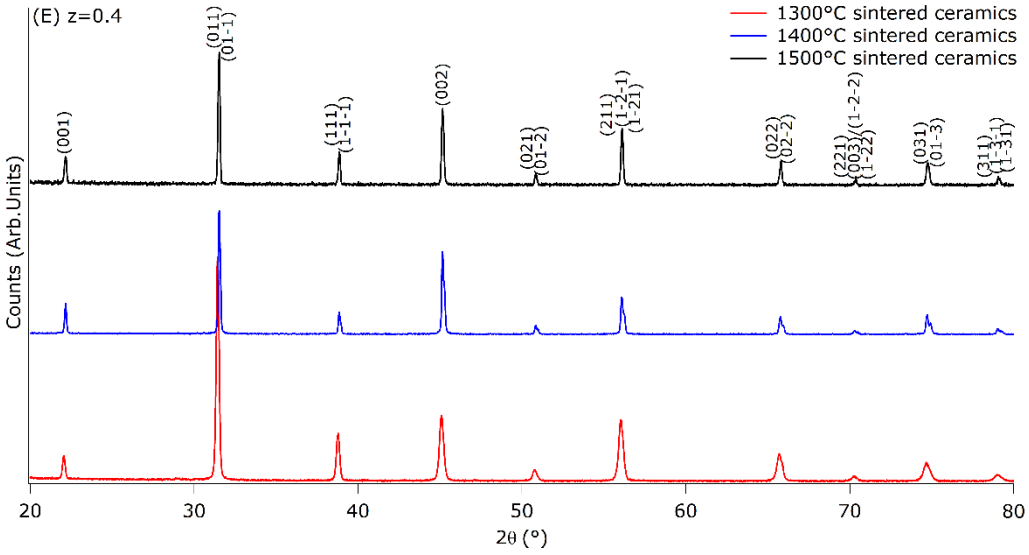
(E) z=0.4
1300°C sintered ceramics
1400°C sintered ceramics
1500°C sintered ceramics
Counts (Arb.Units)
2θ (°)
(001)
(011)
(01-1)
(111)
(1-1-1)
(002)
(021)
(01-2)
(211)
(1-2-1)
(1-21)
(022)
(02-2)
(221)
(003)
(1-2-2)
(1-22)
(031)
(01-3)
(311)
(1-3-1)
(1-31)

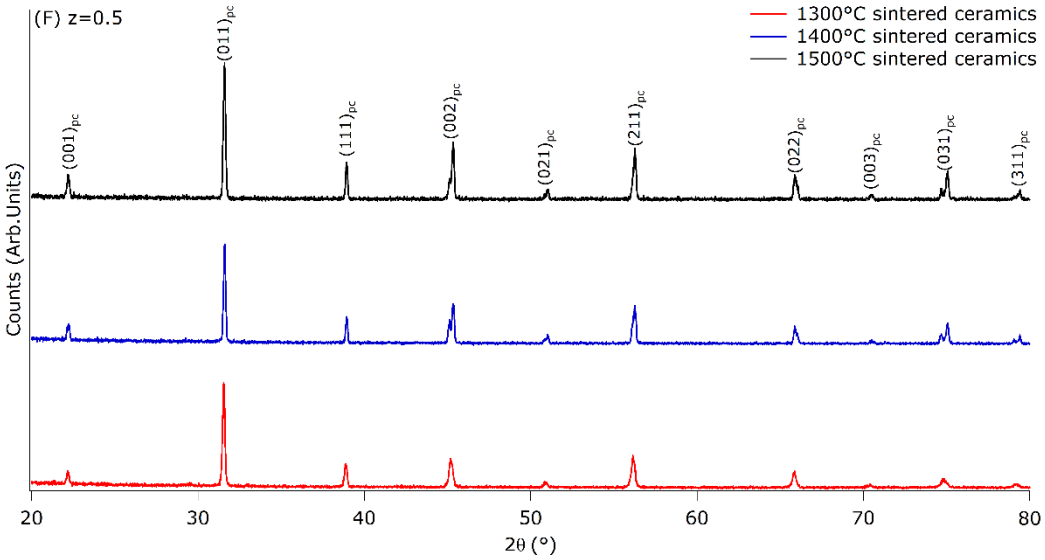
(F) z=0.5
1300°C sintered ceramics
1400°C sintered ceramics
1500°C sintered ceramics
(001)pc
(011)pc
(111)pc
(002)pc
(021)pc
(211)pc
(022)pc
(003)pc
(031)pc
(311)pc
Counts (Arb.Units)
20
30
40
50
60
70
80
2θ (°)

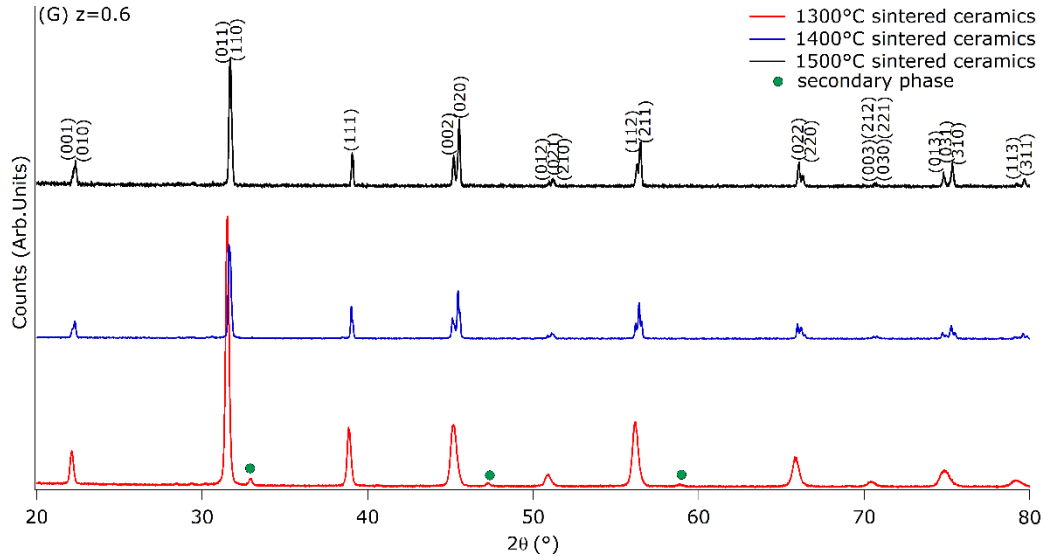
(G) z=0.6
1300°C sintered ceramics
1400°C sintered ceramics
1500°C sintered ceramics
secondary phase
(001)
(010)
(011)
(110)
(111)
(002)
(020)
(012)
(021)
(210)
(112)
(211)
(022)
(220)
(003)(212)
(030)(221)
(013)
(031)
(310)
(113)
(311)
Counts (Arb.Units)
20
30
40
50
60
70
80
2θ (°)

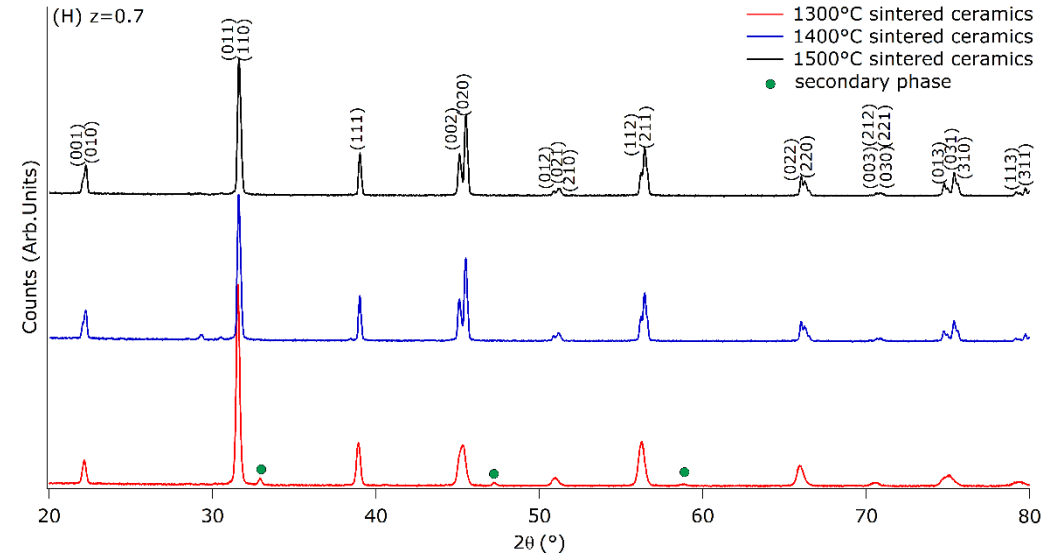
(H) z=0.7
1300°C sintered ceramics
1400°C sintered ceramics
1500°C sintered ceramics
secondary phase
(001)
(010)
(011)
(110)
(111)
(002)
(020)
(012)
(021)
(210)
(112)
(211)
(022)
(220)
(003)(212)
(030)(221)
(013)
(031)
(310)
(113)
(311)
Counts (Arb.Units)
20
30
40
50
60
70
80
2θ (°)

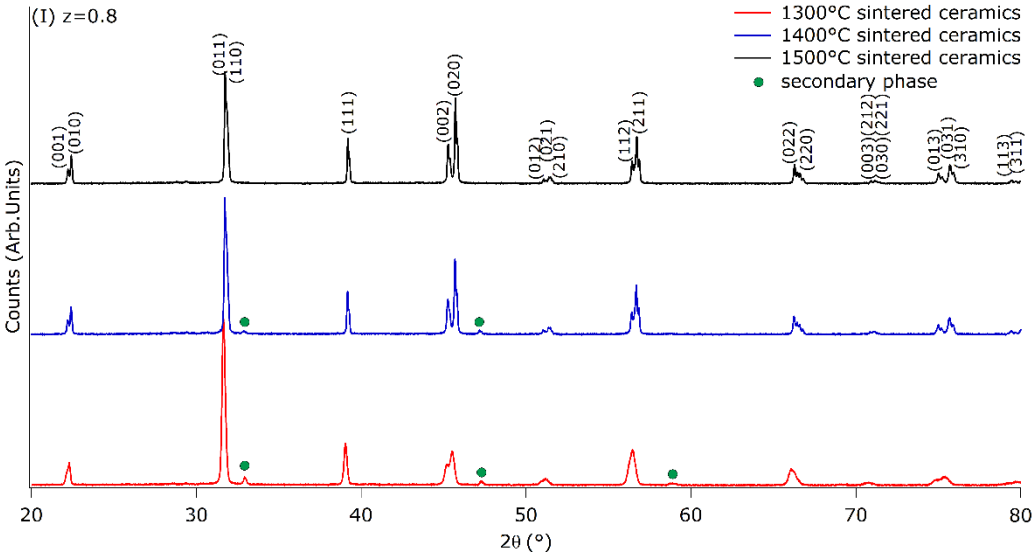
(I) z=0.8
1300°C sintered ceramics
1400°C sintered ceramics
1500°C sintered ceramics
secondary phase
Counts (Arb.Units)
2θ (°)
(001)
(010)
(011)
(110)
(111)
(002)
(020)
(012)
(021)
(210)
(112)
(211)
(022)
(220)
(003)(212)
(030)(221)
(013)
(031)
(310)
(113)
(311)

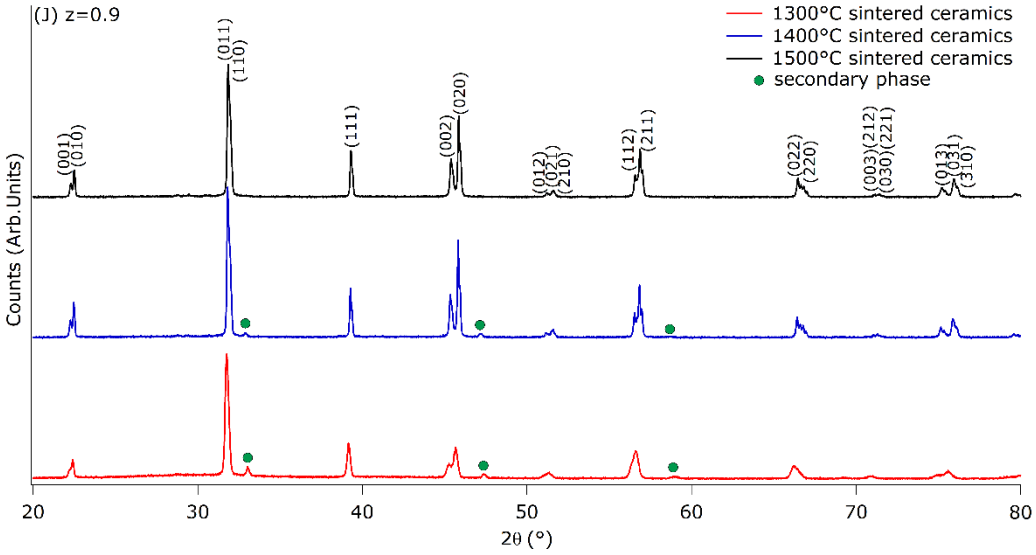
(J) z=0.9
1300°C sintered ceramics
1400°C sintered ceramics
1500°C sintered ceramics
secondary phase
Counts (Arb.Units)
2θ (°)
(001)
(010)
(011)
(110)
(111)
(002)
(020)
(012)
(021)
(210)
(112)
(211)
(022)
(220)
(003)(212)
(030)(221)
(013)
(031)
(310)

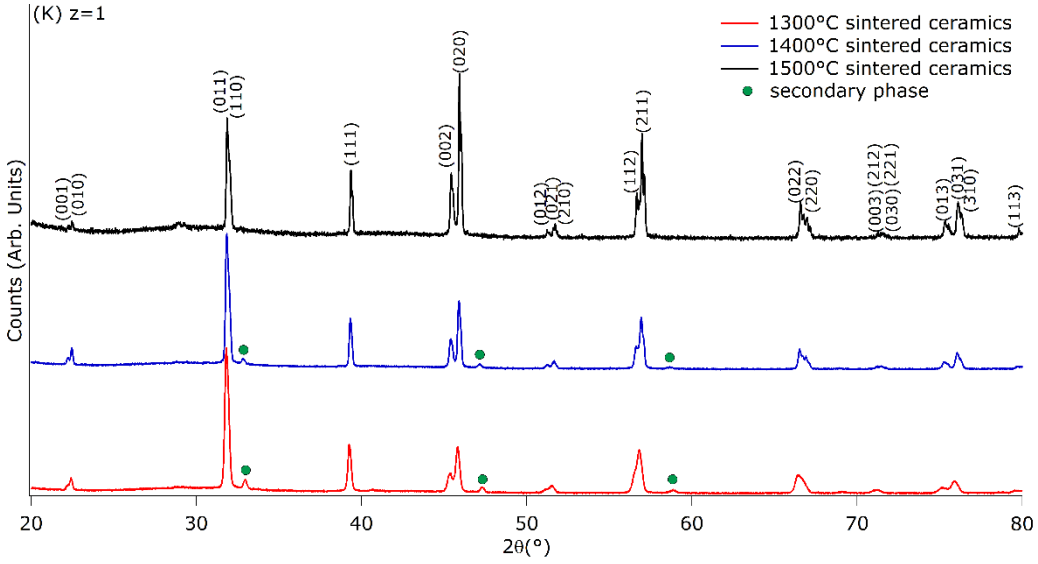
(K) z=1
1300°C sintered ceramics
1400°C sintered ceramics
1500°C sintered ceramics
secondary phase
Counts (Arb. Units)
2θ(°)
(001)
(010)
(011)
(110)
(111)
(002)
(020)
(012)
(021)
(210)
(112)
(211)
(022)
(220)
(003)(212)
(030)(221)
(013)
(031)
(310)
(113)

Appendix IV. Publications

Chang Shu, Daniel Reed, Tim W Button, Mechanism of Ca-Ba diffusion in lead-free (Ba,Ca)TiO_3 piezoelectrics, MRS Proceedings, 1782: 23-28, 2015.
DOI:10.1557/opl.2015.668

Chang Shu, Daniel Reed, Tim W Button, A phase diagram of $Ba_{1-x}Ca_xTiO_3$ (x=0-0.30) piezoceramics by Raman spectroscopy, Journal of the American Ceramic Society, 00: 1-5, 2018.
DOI: https://doi.org/10.1111/jace.15415

List of References

1. *EU-Directive 2002/95/EC: restriction of the use of certain hazardous sub-stances in electrical and electronic equipment (RoHS).* Office Journal of the European Union, 2003. **46**: p. 19-37.
2. *EU-Directive 2011/65/EC: restriction of the use of certain hazardous substances in electrical and electronic equipment (RoHS).* Office Journal of the European Union, 2011. **54**: p. 88-110.
3. Bai, Y., et al., *(Ba,Ca)(Zr,Ti)O_3 lead-free piezoelectric ceramics—The critical role of processing on properties.* Journal of the European Ceramic Society, 2015. **35**(13): p. 3445-3456.
4. Callister, W.D. and D.G. Rethwisch, *Materials Science and Engineering: An Introduction, 8th Edition*. 2009: Wiley.
5. Barsoum, M.W., *Fundamentals of ceramics*. Vol. McGraw-Hill series in materials science and engineering. 2003, Bristol: IOP.
6. Moulson, A.J., Herbert, J.M., *Electroceramics Materials, Properties, Applications*. 1990, London: Cambridge: University Press.
7. Bottcher, C.J.F., *Chapter II - Some Concepts and Problems of Electrostatics*, in *Theory of Electric Polarization (Second Edition)*. 1973, Elsevier: Amsterdam. p. 59-89.
8. Dineva, P., et al., *Piezoelectric Materials.* 2014. **212**: p. 7-32.
9. Kholkin, A.L., N.A. Pertsev, and A.V. Goltsev, *Piezoelectricity and Crystal Symmetry*, in *Piezoelectric and Acoustic Materials for Transducer Applications*, A. Safari and E.K. Akdoğan, Editors. 2008, Springer US: Boston, MA. p. 17-38.
10. Fialka, J.r. and P. Beneš, *Comparison of Methods for the Measurement of Piezoelectric Coeeficients.* IEEE Transactions on Instrumentation and Measurement, 2013. **62**(5).
11. Shrout, T.R. and S.J. Zhang, *Lead-free piezoelectric ceramics: Alternatives for PZT?* Journal of Electroceramics, 2007. **19**(1): p. 113-126.
12. Jaffe, B., W.R. Cook Jr, and H. Jaffe, *Chapter 7 - Solid Solutions of Pb(Ti, Zr, Sn, Hf)O_3*, in *Piezoelectric Ceramics*. 1971, Academic Press. p. 135-183.
13. Jaffe, B., R.S. Roth, and S. Marzullo, *Piezoelectric Properties of Lead Zirconate-Lead Titanate Solid-Solution Ceramics.* Journal of Applied Physics, 1954. **25**(6): p. 809-810.
14. Gordon, J.N., A. Taylor, and P.N. Bennett, *Lead poisoning: case studies.* British Journal of Clinical Pharmacology, 2002. **53**(5): p. 451-458.
15. Aksel, E. and J.L. Jones, *Advances in Lead-Free Piezoelectric Materials for Sensors and Actuators.* Sensors, 2010. **10**(3): p. 1935.
16. *EU-Directive 2000/53/EC of the European Parliament and of the Council of 18 September 2000 on end-of life vehicles.* Office Journal of the European Union, 2000. **269**: p. 34-42.
17. *EU-Directive 2002/96/EC: Waste Electrical and Electronic Equipment (WEEE).* Office Journal of the European Union, 2003. **46**: p. 24-38.

18. Rödel, J., et al., *Perspective on the Development of Lead-free Piezoceramics.* Journal of the American Ceramic Society, 2009. **92**(6): p. 1153-1177.
19. Ahn, Z.S. and W.A. Schulze, *Conventionally Sintered $(Na_{0.5},K_{0.5})NbO_3$ with Barium Additions.* Journal of the American Ceramic Society, 1987. **70**(1): p. C-18-C-21.
20. Jaeger, R.E. and L. Egerton, *Hot Pressing of Potassium-Sodium Niobates.* Journal of the American Ceramic Society, 1962. **45**(5): p. 209-213.
21. Kosec, M. and D. Kolar, *On activated sintering and electrical properties of $NaKNbO_3$.* Materials Research Bulletin, 1975. **10**(5): p. 335-339.
22. Egerton, L. and D.M. Dillon, *Piezoelectric and Dielectric Properties of Ceramics in the System Potassium—Sodium Niobate.* Journal of the American Ceramic Society, 1959. **42**(9): p. 438-442.
23. Coondoo, I., N. Panwar, and A. Kholkin, *Lead-free piezoelectrics: Current status and perspectives.* Journal of Advanced Dielectrics, 2013. **03**(02): p. 1330002.
24. G. A. Smolenskii, et al., *New ferroelectrics of complex composition.* Soviet Physics, Solid State, 1961. **2**: p. 2651.
25. Li, Y., et al., *Dielectric and piezoelecrtic properties of lead-free $(Na_{0.5}Bi_{0.5})TiO_3$–$NaNbO_3$ ceramics.* Materials Science and Engineering: B, 2004. **112**(1): p. 5-9.
26. Panda, P.K., *Review: environmental friendly lead-free piezoelectric materials.* Journal of Materials Science, 2009. **44**(19): p. 5049-5062.
27. Tadashi, T., M. Kei-ichi, and S. Koichiro, *$(Bi_{1/2}Na_{1/2})TiO_3$-$BaTiO_3$ System for Lead-Free Piezoelectric Ceramics.* Japanese Journal of Applied Physics, 1991. **30**(9S): p. 2236.
28. Liu, W. and X. Ren, *Large Piezoelectric Effect in Pb-Free Ceramics.* Physical Review Letters, 2009. **103**(25).
29. Rödel, J., et al., *Transferring lead-free piezoelectric ceramics into application.* Journal of the European Ceramic Society, 2015. **35**(6): p. 1659-1681.
30. Jaffe, B., W.R. Cook Jr, and H. Jaffe, *Chapter 5 - Barium Titanate*, in *Piezoelectric Ceramics*. 1971, Academic Press. p. 53-114.
31. Trolier-McKinstry, S., *Crystal Chemistry of Piezoelectric Materials*, in *Piezoelectric and Acoustic Materials for Transducer Applications*, A. Safari and E.K. Akdoğan, Editors. 2008, Springer US: Boston, MA. p. 39-56.
32. M.M., V., B. J.D., and S. B.D., *History and challenges of barium titanate: Part I.* Science of Sintering, 2008.
33. M.M., V., B. J.D., and S. B.D., *History and challenges of barium titanate: Part II.* Science of Sintering, 2008.
34. Uchino, K., E. Sadanaga, and T. Hirose, *Dependence of the Crystal Structure on Particle Size in Barium Titanate.* Journal of the American Ceramic Society, 1989. **72**(8): p. 1555-1558.
35. Beauger, A., J.C. Mutin, and J.C. Niepce, *Synthesis reaction of metatitanate $BaTiO_3$ Part 1.* Journal of Materials Science, 1983. **18**(10): p. 3041-3046.
36. Beauger, A., J.C. Mutin, and J.C. Niepce, *Synthesis reaction of metatitanate $BaTiO_3$ Part 2.* Journal of Materials Science, 1983. **18**(12): p. 3543-3550.

37. Simon-Seveyrat, L., et al., *Re-investigation of synthesis of $BaTiO_3$ by conventional solid-state reaction and oxalate coprecipitation route for piezoelectric applications.* Ceramics International, 2007. **33**(1): p. 35-40.
38. Gomez-Yañez, C., C. Benitez, and H. Balmori-Ramirez, *Mechanical activation of the synthesis reaction of $BaTiO_3$ from a mixture of $BaCO_3$ and TiO_2 powders.* Ceramics International, 2000. **26**(3): p. 271-277.
39. H.-T. Kim, et al., *Effect of starting materials on the properties of solid-state reacted barium titanate powder.* Journal of Ceramic Processing Research, 2009. **10**(6): p. 753-757.
40. Ryu, S. S., S. K. Lee, and D. H. Yoon, *Synthesis of fine Ca-doped $BaTiO_3$ powders by solid-state reaction method—Part I: Mechanical activation of starting materials.* Journal of Electroceramics, 2007. **18**(3): p. 243-250.
41. Brzozowski, E. and M.S. Castro, *Lowering the synthesis temperature of high-purity $BaTiO_3$ powders by modifications in the processing conditions.* Thermochimica Acta, 2003. **398**(1–2): p. 123-129.
42. Yamaguchi, T., et al., *Effects of raw materials and mixing methods on the solid state reactions involved in fabrication of electronic ceramics.* Ceramurgia International, 1976. **2**(2): p. 76-80.
43. Tsuzuku, K. and M. Couzi, *In situ investigation of chemical reactions between $BaCO_3$ and anatase or rutile TiO_2.* Journal of Materials Science, 2012. **47**(10): p. 4481-4487.
44. Berbenni, V., A. Marini, and G. Bruni, *Effect of mechanical milling on solid state formation of $BaTiO_3$ from $BaCO_3$–TiO_2 (rutile) mixtures.* Thermochimica Acta, 2001. **374**(2): p. 151-158.
45. Brzozowski, E. and M.S. Castro, *Synthesis of barium titanate improved by modifications in the kinetics of the solid state reaction.* Journal of the European Ceramic Society, 2000. **20**(14–15): p. 2347-2351.
46. V.P., P., et al., *Synthesis of $BaTiO_3$ from a mechanically activated $BaCO_3$-TiO_2 system.* Science of Sintering, 2008. **40**(1): p. 21-26.
47. Othman, K.I., et al., *Formation Mechanism of Barium Titanate by Solid-State Reactions.* International Journal of Scientific & Engineering Research, 2014. **5**(7): p. 1460-1465.
48. Lee, J. K., K. S. Hong, and J. W. Jang, *Roles of Ba/Ti Ratios in the Dielectric Properties of $BaTiO_3$ Ceramics.* Journal of the American Ceramic Society, 2001. **84**(9): p. 2001-2006.
49. Arlt, G., D. Hennings, and G. de With, *Dielectric properties of fine-grained barium titanate ceramics.* Journal of Applied Physics, 1985. **58**(4): p. 1619-1625.
50. Guo, F.Q., et al., *Grain size effects on piezoelectric properties of $BaTiO_3$ ceramics prepared by spark plasma sintering.* Journal of Materials Science: Materials in Electronics, 2016. **27**(6): p. 5967-5971.
51. Zheng, P., et al., *Grain-size effects on dielectric and piezoelectric properties of poled $BaTiO_3$ ceramics.* Acta Materialia, 2012. **60**(13–14): p. 5022-5030.
52. Huan, Y., et al., *Grain size effect on piezoelectric and ferroelectric properties of*

$BaTiO_3$ ceramics. Journal of the European Ceramic Society, 2014. **34**(5): p. 1445-1448.
53. Shihua, D., et al., *Effect of Grain Size of $BaTiO_3$ Ceramics on Dielectric Properties.* Ferroelectrics, 2010. **402**(1): p. 55-59.
54. Hoshina, T., et al., *Size Effect and Domain-Wall Contribution of Barium Titanate Ceramics.* Ferroelectrics, 2010. **402**(1): p. 29-36.
55. Buscaglia, V., et al., *Grain size and grain boundary-related effects on the properties of nanocrystalline barium titanate ceramics.* Journal of the European Ceramic Society, 2006. **26**(14): p. 2889-2898.
56. Wang, X. H., et al., *The grain size effect on dielectric properties of $BaTiO_3$ based ceramics.* Materials Science and Engineering: B, 2003. **99**(1–3): p. 199-202.
57. Kanata, T., T. Yoshikawa, and K. Kubota, *Grain-size effects on dielectric phase transition of $BaTiO_3$ ceramics.* Solid State Communications, 1987. **62**(11): p. 765-767.
58. Huan, Y., et al., *Grain Size Effects on Piezoelectric Properties and Domain Structure of $BaTiO_3$ Ceramics Prepared by Two-Step Sintering.* Journal of the American Ceramic Society, 2013. **96**(11): p. 3369-3371.
59. Shoufu, S., et al., *High piezoelectric properties and domain configuration in $BaTiO_3$ ceramics obtained through the solid-state reaction route.* Journal of Physics D: Applied Physics, 2008. **41**(12): p. 125408.
60. Ma, N., et al., *Phase structure and nano-domain in high performance of $BaTiO_3$ piezoelectric ceramics.* Journal of the European Ceramic Society, 2012. **32**(5): p. 1059-1066.
61. Tomoaki, K., Y. Kang, and A. Masatoshi, *Barium Titanate Piezoelectric Ceramics Manufactured by Two-Step Sintering.* Japanese Journal of Applied Physics, 2007. **46**(10S): p. 7035.
62. Smith, E. and G. Dent, *Modern Raman Spectroscopy: A Practical Approach*. 2005: Wiley.
63. Shiratori, Y., et al., *Raman scattering studies on nanocrystalline $BaTiO_3$ Part I—isolated particles and aggregates.* Journal of Raman Spectroscopy, 2007. **38**(10): p. 1288-1299.
64. DiDomenico, M., et al., *Raman Spectrum of Single-Domain $BaTiO_3$.* Physical Review, 1968. **174**(2): p. 522-530.
65. Pavlovic, V.P., et al., *Raman Responses in Mechanically Activated $BaTiO_3$.* Journal of the American Ceramic Society, 2014. **97**(2): p. 601-608.
66. Lazarevica, Z., et al. *Characterization of barium titanate ceramic powders by Raman spectroscopy*. in *Proceedings of the Tenth Annual Conference of the Materials Research Society of Serbia*. 2008.
67. Xiao, C.J., et al., *The phase transitions and ferroelectric behavior of dense nanocrystalline $BaTiO_3$ ceramics fabricated by pressure assisted sintering.* Journal of Physics and Chemistry of Solids, 2007. **68**(2): p. 311-314.
68. Venkateswaran, U.D., V.M. Naik, and R. Naik, *High-pressure Raman studies of polycrystalline $BaTiO_3$.* Physical Review B (Condensed Matter), 1998. **58**(21): p.

14256-60.
69. Gajović, A., et al., *Temperature-dependent Raman spectroscopy of $BaTiO_3$ nanorods synthesized by using a template-assisted sol–gel procedure.* Journal of Raman Spectroscopy, 2013. **44**(3): p. 412-420.
70. Baskaran, N., et al., *Phase transformation studies of ceramic $BaTiO_3$ using thermo-Raman and dielectric constant measurements.* Journal of Applied Physics, 2002. **91**(12): p. 10038.
71. Han, W., et al., *Phase transitions in nanoparticles of $BaTiO_3$ as functions of temperature and pressure.* Journal of Applied Physics, 2013. **113**(19): p. 193513.
72. Dobal, P.S., et al., *Micro-Raman scattering and dielectric investigations of phase transition behavior in the $BaTiO_3$–$BaZrO_3$ system.* Journal of Applied Physics, 2001. **89**(12): p. 8085.
73. Freire, J.D. and R.S. Katiyar, *Lattice dynamics of crystals with tetragonal $BaTiO_3$ structure.* Phys Rev B Condens Matter, 1988. **37**(4): p. 2074-2085.
74. Karan, N.K., et al., *Raman spectral studies of Zr^{4+}-rich $BaZr_xTi_{1-x}O_3(0.5 \leqslant x \leqslant 1.00)$ phase diagram.* Journal of Raman Spectroscopy, 2009. **40**(4): p. 370-375.
75. Buscaglia, V., et al., *Average and local atomic-scale structure in $BaZr_xTi_{(1-x)}O_3$ (x =0.10, 0.20, 0.40) ceramics by high-energy x-ray diffraction and Raman spectroscopy.* J Phys Condens Matter, 2014. **26**(6): p. 065901.
76. Fleury, P.A. and P.D. Lazay, *Acoustic Soft-Optic Mode Interactions in Ferroelectric $BaTiO_3$.* Physical Review Letters, 1971. **26**(21): p. 1331-1334.
77. Scalabrin, A., et al., *Temperature dependence of the A1 and E optical phonons in $BaTiO_3$.* physica status solidi (b), 1977. **79**(2): p. 731-742.
78. Mejía-Uriarte, E.V., et al., *Determination of Phase Transition by Principal Component Analysis Applied to Raman Spectra of Polycristalline $BaTiO_3$ at Low and High Temperature.* Journal of applied research and technology, 2012. **10**: p. 57-62.
79. Xiaohui, W., et al., *Phase transition and high dielectric constant of bulk dense nanograin barium titanate ceramics.* Applied Physics Letters, 2006: p. Medium: X; Size: page(s) 162902-162902.3.
80. Aoyama, M., Hasegawa, T., Ogita, N., Nakajima, N., Maruyama, H., Kurokawa, H., Udagawa, M., *Raman scattering study of nano-particle $BaTiO_3$.* Chinese J. Phys, 2011. **49**: p. 49-55.
81. Perry, C.H. and D.B. Hall, *Temperature Dependence of the Raman Spectrum of $BaTiO_3$.* Physical Review Letters, 1965. **15**(17): p. 700-702.
82. Smith, M.B., et al., *Crystal Structure and the Paraelectric-to-Ferroelectric Phase Transition of Nanoscale $BaTiO_3$.* Journal of the American Chemical Society, 2008. **130**(22): p. 6955-6963.
83. Rehrig, P.W., et al., *Piezoelectric properties of zirconium-doped barium titanate single crystals grown by templated grain growth.* Journal of Applied Physics, 1999. **86**(3): p. 1657.
84. Hayashi, H., T. Nakamura, and T. Ebina, *In-situ Raman spectroscopy of $BaTiO_3$ particles for tetragonal–cubic transformation.* Journal of Physics and Chemistry

of Solids, 2013. **74**(7): p. 957-962.
85. Shiratori, Y., et al., *Raman scattering studies on nanocrystalline $BaTiO_3$ Part II—consolidated polycrystalline ceramics.* Journal of Raman Spectroscopy, 2007. **38**(10): p. 1300-1306.
86. Wang, X., H. Yamada, and C.-N. Xu, *Large electrostriction near the solubility limit in $BaTiO_3$–$CaTiO_3$ ceramics.* Applied Physics Letters, 2005. **86**(2): p. 022905.
87. Chen, X.M., T. Wang, and J. Li, *Dielectric characteristics and their field dependence of (Ba, Ca)TiO_3 ceramics.* Materials Science and Engineering: B, 2004. **113**(2): p. 117-120.
88. Cheng, X. and M. Shen, *Different microstructure and dielectric properties of $Ba_{1-x}Ca_xTiO_3$ ceramics and pulsed-laser-ablated films.* Materials Research Bulletin, 2007. **42**(9): p. 1662-1668.
89. DeVries, R.C. and R. Roy, *Phase Equilibria in the System $BaTiO_3$—$CaTiO_3$.* Journal of the American Ceramic Society, 1955. **38**(4): p. 142-146.
90. Tiwari, V.S. and D. Pandey, *Structure and Properties of (Ba,Ca)TiO_3 Ceramics Prepared Using (Ba,Ca)CO_3 Precursors: II, Diffuse Phase Transition Behavior.* Journal of the American Ceramic Society, 1994. **77**(7): p. 1819-1824.
91. Panigrahi, M.R. and S. Panigrahi, *Structural analysis of 100% relative intense peak of $Ba_{1-x}Ca_xTiO_3$ ceramics by X-ray powder diffraction method.* Physica B: Condensed Matter, 2010. **405**(7): p. 1787-1791.
92. Li, C.-X., et al., *Effects of sintering temperature and poling conditions on the electrical properties of $Ba_{0.70}Ca_{0.30}TiO_3$ diphasic piezoelectric ceramics.* Ceramics International, 2013. **39**(3): p. 2967-2973.
93. Puli, V.S., et al., *Investigations on structure, ferroelectric, piezoelectric and energy storage properties of barium calcium titanate (BCT) ceramics.* Journal of Alloys and Compounds, 2014. **584**: p. 369-373.
94. Fu, D., M. Itoh, and S.Y. Koshihara, *Invariant lattice strain and polarization in $BaTiO_3$-$CaTiO_3$ ferroelectric alloys.* J Phys Condens Matter, 2010. **22**(5): p. 052204.
95. Fu, D., M. Itoh, and S.-y. Koshihara, *Crystal growth and piezoelectricity of $BaTiO_3$–$CaTiO_3$ solid solution.* Applied Physics Letters, 2008. **93**(1): p. 012904.
96. Zhang, W., Z. Shen, and J. Chen, *Preparation and characterization of nanosized barium calcium titanate crystallites by low temperature direct synthesis.* Journal of Materials Science, 2006. **41**(17): p. 5743-5745.
97. Tiwari, V.S., N. Singh, and D. Pandey, *Structure and Properties of (Ba,Ca) TiO_3 Ceramics Prepared Using (Ba,Ca)TiO_3 Ceramics I, Crystallographic and Microstructural Studies.* Journal of the American Ceramic Society, 1994. **77**(7): p. 1813-1818.
98. Pullar, R.C., et al., *Dielectric measurements on a novel $Ba_{1-x}Ca_xTiO_3$ (BCT) bulk ceramic combinatorial library.* Journal of Electroceramics, 2009. **22**(1-3): p. 245-251.
99. Park, J. S., et al., *Structural study of Ca doped barium titanate.* Nuclear

Instruments and Methods in Physics Research Section B: Beam Interactions with Materials and Atoms, 2012. **284**: p. 44-48.
100. Panigrahi, M.R. and S. Panigrahi, *Synthesis and microstructure of Ca-doped $BaTiO_3$ ceramics prepared by high-energy ball-milling.* Physica B: Condensed Matter, 2009. **404**(21): p. 4267-4272.
101. Zhang, X.W., et al., *Defect Chemistry of $BaTiO_3$ with Additions of $CaTiO_3$.* Journal of the American Ceramic Society, 1987. **70**(2): p. 100-103.
102. Jayanthi, S. and T.R.N. Kutty, *Extended phase homogeneity and electrical properties of barium calcium titanate prepared by the wet chemical methods.* Materials Science and Engineering: B, 2004. **110**(2): p. 202-212.
103. Lin, T. F., et al., *The microstructure developments and electrical properties of calcium-modified barium titanate ceramics.* Journal of Materials Science, 1991. **26**(2): p. 491-496.
104. Krishna, P.S.R., et al., *Effect of powder synthesis procedure on calcium site occupancies in barium calcium titanate: A Rietveld analysis.* Applied Physics Letters, 1993. **62**(3): p. 231-233.
105. Tiwari, V.S., et al., *Neutron diffraction study of ferroelectric $Ba_{0.88}Ca_{0.12}TiO_3$.* Physica B: Condensed Matter, 1991. **174**(1): p. 112-116.
106. Yukio, S., et al., *Dielectric Properties of Fine-Grained $BaTiO_3$ Ceramics Doped with CaO.* Japanese Journal of Applied Physics, 2002. **41**(11S): p. 6922.
107. Han, Y.H., J.B. Appleby, and D.M. Smyth, *Calcium as an Acceptor Impurity in $BaTiO_3$.* Journal of the American Ceramic Society, 1987. **70**(2): p. 96-100.
108. Chang, M.C. and S.C. Yu, *Raman study for $(Ba_{1-x}Ca_x)TiO_3$ and $Ba(Ti_{1-y}Ca_y)O_3$ crystalline ceramics.* Journal of Materials Science Letters, 2000. **19**(15): p. 1323-1325.
109. Pasha, U.M., et al., *In situ Raman spectroscopy of A-site doped barium titanate.* Applied Physics Letters, 2007. **91**(6): p. 062908.
110. Pokorny, J., et al., *Use of Raman spectroscopy to determine the site occupancy of dopants in $BaTiO_3$.* Journal of Applied Physics, 2011. **109**(11): p. 114110 (5 pp.).
111. Vegard, L., *Die Konstitution der Mischkristalle und die Raumfüllung der Atome.* Zeitschrift für Physik, 1921. **5**(1): p. 17-26.
112. Mitsui, T. and W.B. Westphal, *Dielectric and X-Ray Studies of $Ca_xBa_{1-x}TiO_3$ and $Ca_xSr_{1-x}TiO_3$.* Physical Review, 1961. **124**(5): p. 1354-1359.
113. Shannon, R., *Revised effective ionic radii and systematic studies of interatomic distances in halides and chalcogenides.* Acta Crystallographica Section A, 1976. **32**(5): p. 751-767.
114. Levin, I., V. Krayzman, and J.C. Woicik, *Local-structure origins of the sustained Curie temperature in $(Ba,Ca)TiO_3$ ferroelectrics.* Applied Physics Letters, 2013. **102**(16): p. 162906.
115. Lee, S. and C.A. Randall, *A modified Vegard's law for multisite occupancy of Ca in $BaTiO_3$–$CaTiO_3$ solid solutions.* Applied Physics Letters, 2008. **92**(11): p. 111904.
116. Zhuang, Z.Q., et al. *The Effect of Octahedrally-Coordinated Calcium on the*

Ferroelectric Transition of $BaTiO_3$. in *Applications of Ferroelectrics. 1986 Sixth IEEE International Symposium on*. 1986.
117. Fu, D., et al., *Anomalous phase diagram of ferroelectric (Ba,Ca)TiO_3 single crystals with giant electromechanical response.* Phys Rev Lett, 2008. **100**(22): p. 227601.
118. Dawson, J.A., et al., *A-Site Strain and Displacement in $Ba_{1-x}Ca_xTiO_3$ and $Ba_{1-x}Sr_xTiO_3$ and the Consequences for the Curie Temperature.* Chemistry of Materials, 2014. **26**(21): p. 6104-6112.
119. Iwata, M., et al., *Consideration on the Phase Diagrams of Ferroelectric (Ba,Ca)TiO_3.* Journal of the Physical Society of Japan, 2009. **78**(5): p. 054706.
120. Lin, J.N. and T.B. Wu, *Effects of isovalent substitutions on lattice softening and transition character of $BaTiO_3$ solid solutions.* Journal of Applied Physics, 1990. **68**(3): p. 985-993.
121. Kazaoui, S. and J. Ravez, *Hyperfrequency dielectric relaxation in ferroelectric ceramics with composition $(Ba_{1-y}Ca_y)TiO_3$.* physica status solidi (a), 1992. **130**(1): p. 227-237.
122. C. Sinclair, D. and J. Paul Attfield, *The influence of A-cation disorder on the Curie temperature of ferroelectric $ATiO_3$ perovskites.* Chemical Communications, 1999(16): p. 1497-1498.
123. Imura, R., et al., *Polarization properties and crystal structures of ferroelectric (Ba,Ca)TiO_3 single crystals.* Journal of Advanced Dielectrics, 2014. **04**(01): p. 1450003.
124. Koopmans, H.J.A., G.M.H. van de Velde, and P.J. Gellings, *Powder neutron diffraction study of the perovskite $CaTiO_3$ and $CaZrO_3$.* Acta Cryst., 1983. **C39**: p. 1323-1325.
125. Varatharajan, R., et al., *Ferroelectric characterization studies on barium calcium titanate single crystals.* Materials Characterization, 2000. **45**(2): p. 89-93.
126. Kumar, P., et al., *Influence of calcium substitution on structural and electrical properties of substituted barium titanate.* Ceramics International, 2011. **37**(5): p. 1697-1700.
127. Li, L.-Y. and X.-G. Tang, *Effect of electric field on the dielectric properties and ferroelectric phase transition of sol–gel derived $(Ba_{0.90}Ca_{0.10})TiO_3$ ceramics.* Materials Chemistry and Physics, 2009. **115**(2–3): p. 507-511.
128. Han, L., et al., *Preparation and ferroelectric properties of $(Ba_{0.7}Ca_{0.3})TiO_3$ ceramics.* Advanced Materials Research, 2011. **148-149**: p. 1016-1020.
129. Bera, J. and S.K. Rout, *On the formation mechanism of $BaTiO_3$–$BaZrO_3$ solid solution through solid-oxide reaction.* Materials Letters, 2005. **59**(1): p. 135-138.
130. Thananatthanachon, T., *Synthesis and Characterization of a Perovskite Barium Zirconate ($BaZrO_3$): An Experiment for an Advanced Inorganic Chemistry Laboratory.* Journal of Chemical Education, 2016. **93**(6): p. 1120-1123.
131. Vasilescu, C.A., et al., *Phase formation, microstructure and functional properties of some $BaTi_{1-x}Zr_xO_3$ ceramics.* UPB Scientific Bulletin, Series B, 2015. **77**(1): p. 95-106.

132. Suslov, A.N., et al., *Synthesis and dielectric and nonlinear properties of $BaTi_{1-x}Zr_xO_3$ ceramics.* Inorganic Materials, 2014. **50**(11): p. 1125-1130.
133. Mahesh, M.L.V., V.V. Bhanuprasad, and A.R. James, *Enhanced Piezoelectric Properties and Tunability of Lead-Free Ceramics Prepared by High-Energy Ball Milling.* Journal of Electronic Materials, 2013. **42**(12): p. 3547-3551.
134. Takuya, H., et al., *Grain Size Effect on Dielectric Properties of $Ba(Zr,Ti)O_3$ Ceramics.* Japanese Journal of Applied Physics, 2012. **51**(9S1): p. 09LC04.
135. Sateesh, P., et al., *Studies of phase transition and impedance behavior of $Ba(Zr,Ti)O_3$ ceramics.* Journal of Advanced Dielectrics, 2015. **05**(01): p. 1550002.
136. Chen, X., et al., *Synthesis and morphology of $Ba(Zr_{0.20}Ti_{0.80})O_3$ powders obtained by sol–gel method.* Journal of Sol-Gel Science and Technology, 2011. **57**(2): p. 149-156.
137. Jha, P.A. and A.K. Jha, *Effect of sintering temperature on the grain growth and electrical properties of barium zirconate titanate ferroelectric ceramics.* Journal of Materials Science: Materials in Electronics, 2012. **24**(5): p. 1511-1518.
138. Jha, P.A. and A.K. Jha, *Influence of processing conditions on the grain growth and electrical properties of barium zirconate titanate ferroelectric ceramics.* Journal of Alloys and Compounds, 2011.
139. Yu, Z., et al., *Piezoelectric and strain properties of $Ba(Ti_{1-x}Zr_x)O_3$ ceramics.* Journal of Applied Physics, 2002. **92**(3): p. 1489-1493.
140. Elbasset, A., et al., *Influence of Zr on Structure and Dielectric Behavior of $BaTiO_3$ Ceramics*. 2015. 2015.
141. Li, et al., *Dielectric and piezoelectric properties of $Ba(Zr_xTi_{1-x})O_3$ lead-free ceramics.* Brazilian Journal of Physics, 2010.
142. Mahajan, S., et al., *Effect of Zr on dielectric, ferroelectric and impedance properties of $BaTiO_3$ ceramic.* Bulletin of Materials Science, 2011. **34**(7): p. 1483-1489.
143. Huang, H.-H., et al., *Tetragonality and Properties of $Ba(Zr_xTi_{1-x})O_3$ Ceramics Determined Using the Rietveld Method.* Metallurgical and Materials Transactions A, 2008. **39**(13): p. 3276-3282.
144. Miao, S., et al., *Polar order and diffuse scatter in $Ba(Ti_{1-x}Zr_x)O_3$ ceramics.* Journal of Applied Physics, 2009. **106**(11): p. 114111.
145. Dong, L., D.S. Stone, and R.S. Lakes, *Enhanced dielectric and piezoelectric properties of $xBaZrO_3$-$(1-x)BaTiO_3$ ceramics.* Journal of Applied Physics, 2012. **111**(8): p. 084107.
146. Garbarz-Glos, B., K. Bormanis, and D. Sitko, *Effect of Zr^{4+} Doping on the Electrical Properties of $BaTiO_3$ Ceramics.* Ferroelectrics, 2011. **417**(1): p. 118-123.
147. Aghayan, M., et al., *Sol–gel combustion synthesis of Zr-doped $BaTiO_3$ nanopowders and ceramics: Dielectric and ferroelectric studies.* Ceramics International, 2014. **40**(10, Part B): p. 16141-16146.
148. Tang, X.G., K.H. Chew, and H.L.W. Chan, *Diffuse phase transition and dielectric tunability of $Ba(Zr_yTi_{1-y})O_3$ relaxor ferroelectric ceramics.* Acta Materialia, 2004.

52(17): p. 5177-5183.
149. Gupta, K. and P.C. Jana, *Study of structural, dielectric and electrical properties of sol-gel prepared Zr-modified $BaTiO_3$ ceramic.* Materials Science: An Indian Journal, 2007. **3**(4): p. 265-269.
150. Tang, X.G., et al., *Effects of grain size on the dielectric properties and tunabilities of sol–gel derived $Ba(Zr_{0.2}Ti_{0.8})O_3$ ceramics.* Solid State Communications, 2004. **131**(3-4): p. 163-168.
151. Cai, W.E.I., et al., *Microstructure and Dielectric Properties of Barium Zirconate Titanate Ceramics by Two Methods.* Integrated Ferroelectrics, 2010. **113**(1): p. 83-94.
152. Nanakorn, N., et al., *Dielectric and ferroelectric properties of $Ba(Zr_xTi_{1-x})O_3$ ceramics.* Ceramics International, 2008. **34**(4): p. 779-782.
153. Farhi, R., et al., *A Raman and dielectric study of ferroelectric $Ba(Ti_{1-x}Zr_x)O_3$ ceramics.* Eur. Phys. J. B, 1999. **9**(4): p. 599-604.
154. Dobal, P.S., et al. *Raman study of overlap of phase transitions in Zr-doped barium titanate ceramics*. in *Smart Structures and Materials 2001: Active Materials: Behavior and Mechanics, 5-8 March 2001*. 2001. USA: SPIE-Int. Soc. Opt. Eng.
155. Deluca, M., et al., *Investigation of the composition-dependent properties of $BaTi_{1-x}Zr_xO_3$ ceramics prepared by the modified Pechini method.* Journal of the European Ceramic Society, 2012. **32**(13): p. 3551-3566.
156. Parida, S., et al., *Structural investigation and improvement of photoluminescence properties in $Ba(Zr_xTi_{1-x})O_3$ powders synthesized by the solid state reaction method.* Materials Chemistry and Physics, 2013. **142**(1): p. 70-76.
157. Moura, F., et al., *Dielectric and ferroelectric characteristics of barium zirconate titanate ceramics prepared from mixed oxide method.* Journal of Alloys and Compounds, 2008. **462**(1-2): p. 129-134.
158. Wirunchit, S., et al., *The Effect of Zirconium on the Perovskite Phase Formation of Barium Zirconium Titanate Nanoparticles by the Sonochemical Method.* Ferroelectrics, 2016. **491**(1): p. 54-64.
159. Levin, I., et al., *Local structure of $Ba(Ti,Zr)O_3$ perovskite-like solid solutions and its relation to the band-gap behavior.* Physical Review B, 2011. **83**(9): p. 094122.
160. Chen, H., et al., *Microstructure and dielectric properties of $BaZr_xTi_{1-x}O_3$ ceramics.* Journal of Materials Science: Materials in Electronics, 2008. **19**(4): p. 379-382.
161. Huang, Z., et al., *Synthesis and characterization of BST and BZT solid solutions through the homogeneous phase precipitation route.* ACTA Chimica Sinica, 2005. **63**(15): p. 1439-1443.
162. Maiwa, H., *Preparation and Properties of $BaTiO_3$ and $Ba(Zr,Ti)O_3$ Ceramics by Spark Plasma Sintering*. 2011: InTech.
163. Jiwei, Z., et al., *Structural and dielectric properties of $Ba(Zr_xTi_{1-x})O_3$ thin films prepared by the sol–gel process.* Journal of Physics D: Applied Physics, 2004. **37**(5): p. 748.
164. Ciomaga, C., et al., *Preparation and characterisation of the $Ba(Zr,Ti)O_3$ ceramics with relaxor properties.* Journal of the European Ceramic Society, 2007. **27**(13–

15): p. 4061-4064.
165. Dixit, A., et al., *Phase transition studies of sol–gel deposited barium zirconate titanate thin films.* Thin Solid Films, 2004. **447–448**: p. 284-288.
166. Yu, Z., et al., *Dielectric properties of $Ba(Ti_{1-x}Zr_x)O_3$ solid solutions.* Materials Letters, 2007. **61**(2): p. 326-329.
167. Choudhury, S. and S. Akter, *Structural, Dielectric and Electrical Properties of Zirconium Doped Barium Titanate Perovskite.* Journal of Bangladesh Academy of Science, 2008. **32**(2).
168. Binhayeeniyi, N., et al., *Physical and electromechanical properties of barium zirconium titanate synthesized at low-sintering temperature.* Materials Letters, 2010. **64**(3): p. 305-308.
169. Julphunthong, P., S. Chootin, and T. Bongkarn, *Phase formation and electrical properties of $Ba(Zr_xTi1_{-x})O_3$ ceramics synthesized through a novel combustion technique.* Ceramics International, 2013. **39, Supplement 1**: p. S415-S419.
170. Pisitpipathsin, N., et al., *Influence of Ca substitution on microstructure and electrical properties of $Ba(Zr,Ti)O_3$ ceramics.* Ceramics International, 2013. **39, Supplement 1**: p. S35-S39.
171. Li, W., et al., *Piezoelectric and Dielectric Properties of $(Ba_{1-x}Ca_x)(Ti_{0.95}Zr_{0.05})O_3$ Lead-Free Ceramics.* Journal of the American Ceramic Society, 2010. **93**(10): p. 2942-2944.
172. Li, W., et al., *Structural and dielectric properties in the $(Ba_{1-x}Ca_x)(Ti_{0.95}Zr_{0.05})O_3$ ceramics.* Current Applied Physics, 2012. **12**(3): p. 748-751.
173. Jain, K., et al., *Investigation of dielectric and structural behaviour of lead free $(Ba_{1-x}Ca_x)(Zr_{0.05}Ti_{0.95})O_3$ ceramics.* AIP Conference Proceedings, 2013. **1512**(1): p. 42-43.
174. Singh, G., V.S. Tiwari, and P.K. Gupta, *Thermal stability of piezoelectric coefficients in $(Ba_{1-x}Ca_x)(Zr_{0.05}Ti_{0.95})O_3$: A lead-free piezoelectric ceramic.* Applied Physics Letters, 2013. **102**(16): p. 162905.
175. Singh, G., V.S. Tiwari, and P.K. Gupta, *Evaluating the polymorphic phase transition in calcium-doped $Ba(Zr_{0.05}Ti_{0.95})O_3$: a lead-free piezoelectric ceramic.* Journal of Applied Crystallography, 2013. **46**(2): p. 324-331.
176. Singh, G., V. Sathe, and V.S. Tiwari, *Investigation of orthorhombic-to-tetragonal structural phase transition in $(Ba_{1-x}Ca_x)(Zr_{0.05}Ti_{0.95})O_3$ ferroelectric ceramics using micro-Raman scattering.* Journal of Applied Physics, 2014. **115**(4): p. 044103.
177. Li, W., et al., *High piezoelectric d_{33} coefficient in $(Ba_{1-x}Ca_x)(Ti_{0.98}Zr_{0.02})O_3$ lead-free ceramics with relative high Curie temperature.* Materials Letters, 2010. **64**(21): p. 2325-2327.
178. Tian, Y., et al., *Polymorphic structure evolution and large piezoelectric response of lead-free $(Ba,Ca)(Zr,Ti)O_3$ ceramics.* Applied Physics Letters, 2014. **104**(11): p. 112901.
179. Ye, S., J. Fuh, and L. Lu, *Effects of Ca substitution on structure, piezoelectric properties, and relaxor behavior of lead-free $Ba(Ti_{0.9}Zr_{0.1})O_3$ piezoelectric*

ceramics. Journal of Alloys and Compounds, 2012. **541**: p. 396-402.
180. Desheng, F., et al., *Phase diagram and piezoelectric response of* $(Ba_{1-x}Ca_x)(Zr_{0.1}Ti_{0.9})O_3$ *solid solution.* Journal of Physics: Condensed Matter, 2013. **25**(42): p. 425901.
181. Tian, Y., et al., *Phase transition behavior and electrical properties of lead-free* $(Ba_{1-x}Ca_x)(Zr_{0.1}Ti_{0.9})O_3$ *piezoelectric ceramics.* Journal of Applied Physics, 2013. **113**(18): p. 184107.
182. Li, W., et al., *Polymorphic phase transition and piezoelectric properties of* $(Ba_{1-x}Ca_x)(Ti_{0.9}Zr_{0.1})O_3$ *lead-free ceramics.* Physica B: Condensed Matter, 2010. **405**(21): p. 4513-4516.
183. Fu, D. and M. Itoh, *Role of Ca off-Centering in Tuning Ferroelectric Phase Transitions in* $Ba(Zr,Ti)O_3$ *System.* 2015.
184. Zhang, S.-W., et al., *Phase-transition behavior and piezoelectric properties of lead-free* $(Ba_{0.95}Ca_{0.05})(Ti_{1-x}Zr_x)O_3$ *ceramics.* Journal of Alloys and Compounds, 2010. **506**(1): p. 131-135.
185. Sindhu, M., et al., *Effect of Zr substitution on phase transformation and dielectric properties of* $Ba_{0.9}Ca_{0.1}TiO_3$ *ceramics.* Journal of Applied Physics, 2013. **114**(16): p. 164106.
186. Ravez, J. and A. Simon, *Spontaneous transition from relaxor to ferroelectric state in new lead-free perovskite ceramics.* Ferroelectrics, 2000. **240**(1): p. 1579-1586.
187. Sciau, P., G. Calvarin, and J. Ravez, *X-ray diffraction study of* $BaTi_{0.65}Zr_{0.35}O_3$ *and* $Ba_{0.92}Ca_{0.08}Ti_{0.75}Zr_{0.25}O_3$ *compositions: influence of electric field.* Solid State Communications, 1999. **113**(2): p. 77-82.
188. Tang, X. G. and H.L. W. Chan, *Effect of grain size on the electrical properties of* $(Ba,Ca)(Zr,Ti)O_3$ *relaxor ferroelectric ceramics.* Journal of Applied Physics, 2005. **97**(3): p. 034109.
189. Zeng, Y., et al., *Growth and characterization of lead-free* $Ba_{(1-x)}Ca_xTi_{(1-y)}Zr_yO_3$ *single crystal.* Journal of Crystal Growth, 2012. **343**(1): p. 17-20.
190. Liu, L., et al., *Structure and piezoelectric properties of* $(1-0.5x)BaTiO_3–0.5x(0.4BaZrO_3–0.6CaTiO_3)$ *ceramics.* Journal of Physics D: Applied Physics, 2012. **45**(29): p. 295403.
191. Damjanovic, D., *A morphotropic phase boundary system based on polarization rotation and polarization extension.* Applied Physics Letters, 2010. **97**(6): p. 062906.
192. Benabdallah, F., et al., *Linking large piezoelectric coefficients to highly flexible polarization of lead free* $BaTiO_3$-$CaTiO_3$-$BaZrO_3$ *ceramics.* Journal of Applied Physics, 2011. **109**(12): p. 124116.
193. Ehmke, M.C., et al., *Reduction of the piezoelectric performance in lead-free* $(1-x)Ba(Zr_{0.2}Ti_{0.8})O_3-x(Ba_{0.7}Ca_{0.3})TiO_3$ *piezoceramics under uniaxial compressive stress.* Journal of Applied Physics, 2012. **112**(11): p. 114108.
194. Xue, D., et al., *Elastic, piezoelectric, and dielectric properties of* $Ba(Zr_{0.2}Ti_{0.8})O_3$-$50(Ba_{0.7}Ca_{0.3})TiO_3$ *Pb-free ceramic at the morphotropic phase boundary.* Journal of Applied Physics, 2011. **109**(5): p. 054110.

195. Jeong, I.K. and J.S. Ahn, *The atomic structure of lead-free $Ba(Zr_{0.2}Ti_{0.8})O_3$-$(Ba_{0.7}Ca_{0.3})TiO_3$ by using neutron total scattering analysis.* Applied Physics Letters, 2012. **101**(24): p. 242901.
196. Gao, J., et al., *Microstructure basis for strong piezoelectricity in Pb-free $Ba(Zr_{0.2}Ti_{0.8})O_3$-$(Ba_{0.7}Ca_{0.3})TiO_3$ ceramics.* Applied Physics Letters, 2011. **99**(9): p. 092901.
197. Gao, J., et al., *Symmetry determination on Pb-free piezoceramic $0.5Ba(Zr_{0.2}Ti_{0.8})O_3$-$0.5(Ba_{0.7}Ca_{0.3})TiO_3$ using convergent beam electron diffraction method.* Journal of Applied Physics, 2014. **115**(5): p. 054108.
198. Gao, J., et al., *Major contributor to the large piezoelectric response in $(1-x)Ba(Zr_{0.2}Ti_{0.8})O_3$ $-x(Ba_{0.7}Ca_{0.3})TiO_3$ ceramics: Domain wall motion.* Applied Physics Letters, 2014. **104**(25): p. 252909.
199. Lu, S., et al., *Temperature driven nano-domain evolution in lead-free $Ba(Zr_{0.2}Ti_{0.8})O_3$-$50(Ba_{0.7}Ca_{0.3})TiO_3$ piezoceramics.* Applied Physics Letters, 2014. **105**(3): p. 032903.
200. Tutuncu, G., et al., *Domain wall motion and electromechanical strain in lead-free piezoelectrics: Insight from the model system $(1-x)Ba(Zr_{0.2}Ti_{0.8})O_3$–$x(Ba_{0.7}Ca_{0.3})TiO_3$ using in situ high-energy X-ray diffraction during application of electric fields.* Journal of Applied Physics, 2014. **115**(14): p. 144104.
201. Damjanovic, D., et al., *Elastic, dielectric, and piezoelectric anomalies and Raman spectroscopy of $0.5Ba(Ti_{0.8}Zr_{0.2})O_3$-$0.5(Ba_{0.7}Ca_{0.3})TiO_3$.* Applied Physics Letters, 2012. **100**(19): p. 192907.
202. Bjørnetun Haugen, A., et al., *Structure and phase transitions in $0.5(Ba_{0.7}Ca_{0.3}TiO_3)$-$0.5(BaZr_{0.2}Ti_{0.8}O_3)$ from −100 °C to 150 °C.* Journal of Applied Physics, 2013. **113**(1): p. 014103.
203. Ehmke, M.C., et al., *Phase coexistence and ferroelastic texture in high strain $(1-x)Ba(Zr_{0.2}Ti_{0.8})O_3$–$x(Ba_{0.7}Ca_{0.3})TiO_3$ piezoceramics.* Journal of Applied Physics, 2012. **111**(12): p. 124110.
204. Keeble, D.S., et al., *Revised structural phase diagram of $(Ba_{0.7}Ca_{0.3}TiO_3)$-$(BaZr_{0.2}Ti_{0.8}O_3)$.* Applied Physics Letters, 2013. **102**(9): p. 092903.
205. Xue, D., et al., *Phase transitions and phase diagram of $Ba(Zr_{0.2}Ti_{0.8})O_3$-$x(Ba_{0.7}Ca_{0.3})TiO_3$ Pb-free system by anelastic measurement.* Journal of Applied Physics, 2015. **117**(12): p. 124107.
206. Zhang, L., et al., *Phase transitions and the piezoelectricity around morphotropic phase boundary in $Ba(Zr_{0.2}Ti_{0.8})O_3$-$x(Ba_{0.7}Ca_{0.3})TiO_3$ lead-free solid solution.* Applied Physics Letters, 2014. **105**(16): p. 162908.
207. Puli, V.S., et al., *Barium zirconate-titanate/barium calcium-titanate ceramics via sol–gel process: novel high-energy-density capacitors.* Journal of Physics D: Applied Physics, 2011. **44**(39): p. 395403.
208. Sreenivas Puli, V., et al., *Structure, dielectric tunability, thermal stability and diffuse phase transition behavior of lead free BZT–BCT ceramic capacitors.* Journal of Physics and Chemistry of Solids, 2013. **74**(3): p. 466-475.
209. Puli, V.S., et al., *Structure, dielectric, ferroelectric, and energy density properties*

of (1−x)BZT–xBCT ceramic capacitors for energy storage applications. Journal of Materials Science, 2012. **48**(5): p. 2151-2157.
210. Hao, J., et al., *Correlation Between the Microstructure and Electrical Properties in High-Performance $(Ba_{0.85}Ca_{0.15})(Zr_{0.1}Ti_{0.9})O_3$ Lead-Free Piezoelectric Ceramics.* Journal of the American Ceramic Society, 2012. **95**(6): p. 1998-2006.
211. Ye, S., et al., *Structure and properties of hot-pressed lead-free $(Ba_{0.85}Ca_{0.15})(Zr_{0.1}Ti_{0.9})O_3$ piezoelectric ceramics.* RSC Advances, 2013. **3**(43): p. 20693.
212. Praveen, P.J., K. Kumar, and D. Das, *Structure Property Correlation in Barium Zirconate Titanate–Barium Calcium Titanate Piezoelectric Ceramics.* Transactions of the Indian Institute of Metals, 2013. **66**(4): p. 329-332.
213. Castkova, K., et al., *Chemical Synthesis, Sintering and Piezoelectric Properties of $Ba_{0.85}Ca_{0.15}Zr_{0.1}Ti_{0.9}O_3$ Lead-Free Ceramics.* Journal of the American Ceramic Society, 2015. **98**(8): p. 2373-2380.
214. Chandrakala, E., et al., *Effect of sintering temperature on structural, dielectric, piezoelectric and ferroelectric properties of sol–gel derived BZT-BCT ceramics.* Ceramics International, 2016. **42**(4): p. 4964-4977.
215. Bharathi, P. and K.B.R. Varma, *Grain and the concomitant ferroelectric domain size dependent physical properties of $Ba_{0.85}Ca_{0.15}Zr_{0.1}Ti_{0.9}O_3$ ceramics fabricated using powders derived from oxalate precursor route.* Journal of Applied Physics, 2014. **116**(16): p. 164107.
216. Srinivas, A., et al., *Ferroelectric, piezoelectric and mechanical properties in lead free $(0.5)Ba(Zr_{0.2}Ti_{0.8})O_3$–$(0.5)(Ba_{0.7}Ca_{0.3})TiO_3$ electroceramics.* Ceramics International, 2015. **41**(2): p. 1980-1985.
217. Wang, P., Y. Li, and Y. Lu, *Enhanced piezoelectric properties of $(Ba_{0.85}Ca_{0.15})(Ti_{0.9}Zr_{0.1})O_3$ lead-free ceramics by optimizing calcination and sintering temperature.* Journal of the European Ceramic Society, 2011. **31**(11): p. 2005-2012.
218. Wu, J., et al., *Sintering temperature-induced electrical properties of $(Ba_{0.90}Ca_{0.10})(Ti_{0.85}Zr_{0.15})O_3$ lead-free ceramics.* Materials Research Bulletin, 2012. **47**(5): p. 1281-1284.
219. Mishra, P., Sonia, and P. Kumar, *Effect of sintering temperature on dielectric, piezoelectric and ferroelectric properties of BZT–BCT 50/50 ceramics.* Journal of Alloys and Compounds, 2012. **545**: p. 210-215.
220. E, V.R., et al., *Structure and ferroelectric studies of $(Ba_{0.85}Ca_{0.15})(Ti_{0.9}Zr_{0.1})O_3$ piezoelectric ceramics.* Materials Research Bulletin, 2013. **48**(10): p. 4395-4401.
221. Coondoo, I., et al., *Synthesis and characterization of lead-free $0.5Ba(Zr_{0.2}Ti_{0.8})O_3$-$0.5(Ba_{0.7}Ca_{0.3})TiO_3$ ceramic.* Journal of Applied Physics, 2013. **113**(21): p. 214107.
222. Software, C. *TOPAS-Academic V6*. 2016; Available from: http://www.topas-academic.net/.
223. Cavalcante, L.S., et al., *Local electronic structure, optical bandgap and photoluminescence (PL) properties of $Ba(Zr_{0.75}Ti_{0.25})O_3$ powders.* Materials

Science in Semiconductor Processing, 2013. **16**(3): p. 1035-1045.
224. Hiruma, Y., H. Nagata, and T. Takenaka, *Grain-size effect on electrical properties of $(Bi_{1/2}K_{1/2})TiO_3$ ceramics.* Japanese Journal of Applied Physics Part 1-Regular Papers Brief Communications & Review Papers, 2007. **46**(3A): p. 1081-1084.
225. Shuvalov, L.A., *Electrical Properties of Crystals*, in *Modern Crystallography IV: Physical Properties of Crystals*, L.A. Shuvalov, Editor. 1988, Springer Berlin Heidelberg: Berlin, Heidelberg. p. 178-266.
226. Luxova, J., P. Sulcova, and M. Trojan, *Study of Perovskite Compounds.* Journal of Thermal Analysis and Calorimetry, 2008. **93**(3): p. 823-827.
227. Qian, X.-S., et al., *Giant Electrocaloric Response Over A Broad Temperature Range in Modified $BaTiO_3$ Ceramics.* Advanced Functional Materials, 2014. **24**(9): p. 1300-1305.
228. Hagemann, H., et al., *Raman studies of reorientation motions of $[BH_4]^-$ anionsin alkali borohydrides.* Journal of Alloys and Compounds, 2004. **363**(1–2): p. 129-132.
229. Hagemann, H., et al., *Lattice anharmonicity and structural evolution of $LiBH_4$: an insight from Raman and X-ray diffraction experiments.* Phase Transitions, 2009. **82**(4): p. 344-355.
230. Reed, D. and D. Book, *Recent applications of Raman spectroscopy to the study of complex hydrides for hydrogen storage.* Current Opinion in Solid State and Materials Science, 2011. **15**(2): p. 62-72.
231. Teranishi, T., et al., *Analysis on dipole polarization of $BaTiO_3$-based ferroelectric ceramics by Raman spectroscopy.* Journal of the Ceramic Society of Japan, 2010. **118**(1380): p. 679-682.
232. Buscaglia, M.T., et al., *Synthesis of $BaTiO_3$ Core−Shell Particles and Fabrication of Dielectric Ceramics with Local Graded Structure.* Chemistry of Materials, 2006. **18**(17): p. 4002-4010.
233. YAN, H., et al., *The Contribution of Electrical Conductivity, Dielectric Permittivity and Domain Switching in Ferroelectric Hysteresis Loops.* Journal of Advanced Dielectrics, 2011. **01**(01): p. 107-118.
234. Toby, B.H., *R factors in Rietveld analysis: How good is good enough?* Powder Diffraction, 2012. **21**(1): p. 67-70.
235. Kang, S. J.L., *4 - Initial Stage Sintering*, in *Sintering*. 2005, Butterworth-Heinemann: Oxford. p. 39-55.
236. Kalyani, A.K., et al., *Orthorhombic-tetragonal phase coexistence and enhanced piezo-response at room temperature in Zr, Sn, and Hf modified $BaTiO_3$.* Applied Physics Letters, 2014. **104**(25): p. 252906.
237. Bonshedt-Kupleckaya, E.M., *Some data on the minerals of the perovskite group.* Probl. min. geochim. petr. Acad. Sci. USSR, 1946: p. 43-51.
238. *Peakfit.m-File Exchange-MATLAB Central*. Available from: http://uk.mathworks.com/matlabcentral/fileexchange/23611-peakfit-m?requestedDomain=true&nocookie=true.